

UC San Diego

UC San Diego Electronic Theses and Dissertations

Title

Expanded Tools and Isosteres for Fragment-Based Drug Discovery against Metalloenzymes

Permalink

<https://escholarship.org/uc/item/4mk320fd>

Author

Seo, Hyeonglim

Publication Date

2024

Peer reviewed|Thesis/dissertation

UNIVERSITY OF CALIFORNIA SAN DIEGO

Expanded Tools and Isosteres for Fragment-Based Drug Discovery against Metalloenzymes

A dissertation submitted in partial satisfaction of the
requirements for the degree Doctor of Philosophy

in

Chemistry

by

Hyeonglim Seo

Committee in charge:

Professor Seth M. Cohen, Chair
Professor Carlo Ballatore, Co-Chair
Professor Galia T. Debelouchina
Professor Kamil Godula
Professor Alina M. Schimpf

2024

Copyright

Hyeonglim Seo, 2024

All rights reserved.

The Dissertation of Hyeonglim Seo is approved, and it is acceptable in quality and form for publication on microfilm and electronically.

University of California San Diego

2024

DEDICATION

To my husband, whose unwavering support has sustained me, and
to my loving family, whose endless prayers have lifted me in every endeavor,
I dedicate this thesis with the deepest appreciation.

TABLE OF CONTENTS

Dissertation Approval Page	iii
Dedication.....	iv
Table of Contents	v
List of Figures.....	viii
List of Tables	xiii
List of Abbreviations	v
Acknowledgements	xxii
Vita.....	xxvi
Abstract of the Dissertation	xxix
Chapter 1: Library Design for Metalloenzyme Fragment-based Drug Discovery	1
1.1 Introduction to Metalloenzymes and Metalloenzyme Inhibitors	2
1.2 Fragment-Based Drug Discovery (FBDD).....	5
1.3 FBDD for Metalloenzyme Targets	9
1.4 Bioisosterism	12
1.5 Bioinorganic Model Complexes	15
1.6 Scope of this Dissertation	17
1.7 Acknowledgments	19
1.8 References.....	19
Chapter 2: Developing Metal-binding Isosteres of 8-Hydroxyquinoline (8-HQ) as Metalloenzyme Inhibitor Scaffolds	30
2.1 Introduction.....	31
2.2 Library Design and 8-HQ MBI Synthesis	33
2.3 Physicochemical Properties Analysis	36

2.4 Structural Analysis.....	38
2.5 Metal-binding Isosteres Screening.....	46
2.6 Conclusions.....	50
2.7 Acknowledgments	51
2.8 Appendix: Supporting Information.....	51
2.9 References.....	85
Chapter 3: Evaluating Metal-Ligand Interactions of Metal-Binding Isosteres (MBIs) Using Model Complexes	96
3.1 Introduction.....	97
3.2 Preparation of MBIs and Model Complexes	99
3.3 Structural Analysis.....	101
3.4 Computational Analysis.....	107
3.5 Spectroscopic Analysis	109
3.6 Conclusions.....	112
3.7 Acknowledgments	113
3.8 Appendix: Supporting Information.....	113
3.9 References.....	137
Chapter 4: Masking Thiol Reactivity with Thioamide, Thiourea, and Thiocarbamate-based Metal-Binding Pharmacophores (MBPs)	143
4.1 Introduction.....	144
4.2 Library Design and Preparation	146
4.3 Reactivity Evaluation.....	147
4.4 Structural Analysis.....	150
4.5 Biochemical Evaluation	153

4.6 Protein X-ray Crystallography	155
4.7 Conclusion	158
4.8 Acknowledgements.....	158
4.9 Appendix: Supporting Information.....	159
4.10 References.....	182
Chapter 5: Developing Cu-only Superoxide Dismutase Inhibitors as Novel Antifungals ...	187
5.1 Introduction.....	188
5.2 Assay Protocol and Library Screening Results.....	191
5.3 Inhibitor Development Against Cu-only SOD5	198
5.3.1 7-(1 <i>H</i> -tetrazol-5-yl)-1 <i>H</i> -benzo[d][1,2,3]triazole-based Inhibitors of Cu-only SOD5	199
5.3.2 1-Hydroxypyridine-2(1 <i>H</i>)-thione (1,2-HOPTO)-based Inhibitors of Cu-only SOD5	202
5.3.3 8-Hydroxyquinoline (8-HQ)-based Inhibitors of Cu-only SOD5.....	207
5.4 Future Work	212
5.5 Acknowledgments	214
5.6 Appendix: Supporting Information.....	214
5.7 References.....	223

LIST OF FIGURES

Figure 1.1. FDA-approved metalloenzyme inhibitors containing MBPs. MBPs containing donor atoms are highlighted in red. Adapted from reference 1.....	4
Figure 1.2. a) HTS hits may bind by virtue of numerous suboptimal interactions. By contrast, Fragment hits are more ligand efficient and involve fewer but more optimized interactions. b) General workflow of the fragment-based approach, indicating the process of taking validated fragments through to a lead series	7
Figure 1.3. Fragment optimization approaches	8
Figure 1.4. Representative MBP fragments specifically designed for FBDD against metalloenzyme targets	9
Figure 1.5. a) Chemical structure of baloxavir acid, which is an active agent of baloxavir marboxil, a reported metal-binding inhibitor of PA _N endonuclease. b) FBDD for the development of influenza endonuclease inhibitor	11
Figure 1.6. Representation of isosteric replacement. In this example, triazole was introduced as a carboxylic acid isostere in the design of AT1 receptor antagonists (both highlighted in blue)	13
Figure 1.7. Isosteric replacement on picolinic acid has successfully developed into MBIs. Each coordinating group was replaced with a) carboxylic acid isosteres, b) heteroarene isosteres, and c) both carboxylic acid and heteroarene isosteres, respectively	14
Figure 1.8. a) a) [(Tp ^{Ph,Me})Zn(OH)] as a bioinorganic model system of hydrolytic Zn(II)-dependent metalloenzymes. Chemical structures (<i>Left</i>) and X-ray crystallographic (<i>Right</i>) structure of [(Tp ^{Ph,Me})Zn(OH)]. b) X-ray crystallographic structures of the active site of carbonic anhydrase (<i>Left</i>) (PDB: 1CA2) and MMP (<i>Right</i>) (PDB: 2OXU)	16
Figure 2.1. a) Quinoline and examples of its isosteres that are frequently used in drug discovery. b) The hydroxyl group (blue) and the quinoline ring scaffold (red) were replaced with various isosteres. c) Library of 8-HQ MBIs.....	35
Figure 2.2. Crystal structure of [Tp ^{Ph,Me} Zn(MBI)] complexes with 6,6-membered ring MBIs. (ORTEP, 50% probability ellipsoids). Hydrogen atoms and phenyl groups from the Tp ^{Ph,Me} ligand were removed for clarity. Color scheme: carbon = gray, nitrogen = blue, oxygen = red, boron = pink, and zinc = green.....	39
Figure 2.3. Crystal structure of [Tp ^{Ph,Me} Zn(MBI)] complexes with 6,5-membered ring MBIs. (ORTEP, 50% probability ellipsoids). Angle a is defined between the 5- and 6-membered ligand rings and angles a and b together are used to describe overall internal ligand geometry on the binding modes of MBI 2.6 , 2.7 , and 2.11	41

Figure 2.4. Crystal structure of $[\text{Tp}^{\text{Ph,Me}}\text{Zn}(\text{MBI})]$ complexes with sulfonamide MBIs. (ORTEP, 50% probability ellipsoids). N1 and N2 are labeled to identify nitrogen atoms that are position to participate in bidentate coordination to Zn(II) center. Hydrogen atoms and phenyl groups from the $\text{Tp}^{\text{Ph,Me}}$ ligand were removed for clarity..... 43

Figure 2.5. Crystal structure of $[\text{Tp}^{\text{Ph,Me}}\text{Zn}(\text{MBI})]$ complexes with 6,6,5-membered ring MBIs. (ORTEP, 50% probability ellipsoids). Angle **a** is defined between the 5- and 6-membered ligand rings and is used to describe overall internal ligand geometry on the binding modes of the MBIs..... 45

Figure 2.S1. Crystal structure of $[\text{Zn}(\mathbf{2.22})_2]$ complex. (ORTEP, 50% probability ellipsoids). Hydrogen atoms were removed for clarity. Color scheme: carbon = gray, nitrogen = blue, oxygen = red, sulfur = yellow, and zinc = green 81

Figure 2.S2. IC_{50} curves of 8-HQ, MBI **2.1**, **2.2**, **2.3**, **2.5**, **2.18**, and **2.26** against MMP-2. The assay conditions used to obtain IC_{50} values are the same as the conditions used to measure percent inhibition values..... 82

Figure 3.1. a) Picolinic acid (pic), MBIs of picolinic acid, and 2,2'-bipyridine (bpy). b) Chemical structure of the $[\text{M}(\text{TPA})(\text{MBI})]^+$ model system (TPA = tris(2-pyridylmethyl)amine). c) Chemical structure of the $[(\text{Tp}^{\text{Ph,Me}})\text{Zn}(\text{MBI})]$ model system ($\text{Tp}^{\text{Ph,Me}}$ = hydrotris(5,3-methylphenylpyrazolyl)borate) 98

Figure 3.2. Crystal structures of $[\text{Ni}(\text{TPA})(\text{L})]$ complexes (ORTEP, 50% probability ellipsoids). a) $[\text{Ni}(\text{TPA})(\text{pic})]^+$, b) $[\text{Ni}(\text{TPA})(\mathbf{3.1})]^+$, c) $[\text{Ni}(\text{TPA})(\mathbf{3.2})]^+$, d) $[\text{Ni}(\text{TPA})(\mathbf{3.3})]^+$, e) $[\text{Ni}(\text{TPA})(\mathbf{3.4})]^+$, f) $[\text{Ni}(\text{TPA})(\text{bpy})]^{2+}$. Solvent molecules, counter ions, and hydrogen atoms have been omitted for clarity 102

Figure 3.3. Crystal structures of $[\text{Co}(\text{TPA})(\text{L})]$ complexes (ORTEP, 50% probability ellipsoids). a) $[\text{Co}(\text{TPA})(\text{pic})]^+$, b) $[\text{Co}(\text{TPA})(\mathbf{3.1})]^+$, c) $[\text{Co}(\text{TPA})(\mathbf{3.2})]^+$, d) $[\text{Co}(\text{TPA})(\mathbf{3.3})]^+$, e) $[\text{Co}(\text{TPA})(\mathbf{3.4})]^+$. Solvent molecules, counter ions, and hydrogen atoms have been omitted for clarity. Donor atoms are alphanumerically labelled 103

Figure 3.4. Crystal structures of $[(\text{Tp}^{\text{Ph,Me}})\text{Co}(\text{L})]$ complexes (ORTEP, 50% probability ellipsoids). a) $[(\text{Tp}^{\text{Ph,Me}})\text{Co}(\text{pic})]$, b) $[(\text{Tp}^{\text{Ph,Me}})\text{Co}(\mathbf{3.1})]$, c) $[(\text{Tp}^{\text{Ph,Me}})\text{Co}(\mathbf{3.2})]$, d) $[(\text{Tp}^{\text{Ph,Me}})\text{Co}(\text{bpy})]$. Phenyl groups of $\text{Tp}^{\text{Ph,Me}}$ have been omitted for clarity. Donor atoms are alphanumerically labelled..... 106

Figure 3.5. Computationally optimized structures and relative free Gibbs energy differences of the binding orientation isomers of the MBI **3.1** – **3.4** coordinated to Ni(II) (*left*) or Co(II) (*right*) TPA complexes at the wB97x-D/LanL2DZ level of theory 108

Figure 3.S1. Crystal structure of $[(\text{Tp}^{\text{Ph,Me}})\text{Zn}(\text{bpy})]$ (ORTEP, 50% probability ellipsoids). Color scheme: carbon = gray, oxygen = red, nitrogen = blue, zinc = navy, and boron = pink
..... 130

Figure 3.S2. ^1H NMR spectra of $[\text{Ni}(\text{TPA})(\text{L})]$ system in DMSO. $[\text{Ni}(\text{TPA})(\text{OAc})(\text{H}_2\text{O})]\text{PF}_6$ complex (<i>bottom</i>) was characterized to guide the interpretation of the other complexes	132
Figure 3.S3. ^1H NMR spectra of $[\text{Co}(\text{TPA})(\text{L})]$ system in DMSO. $[\text{Co}(\text{TPA})(\text{OAc})]\text{PF}_6$ complex (<i>bottom</i>) was characterized to guide the interpretation of the other complexes	132
Figure 3.S4. UV-visible spectra of $[\text{Ni}(\text{TPA})(\text{L})]$ complexes (5 mM) in DMSO.....	133
Figure 3.S5. UV-visible spectra of $[\text{Co}(\text{TPA})(\text{L})]$ complexes (5 mM) in DMSO	133
Figure 3.S6. UV-visible spectra of $[(\text{Tp}^{\text{Ph,Me}})\text{Co}(\text{L})]$ complexes (5 mM) in DMSO	134
Figure 3.S7. IR spectra of $[\text{Ni}(\text{TPA})(\text{L})]$ complexes.....	135
Figure 3.S8. IR spectra of $[\text{Co}(\text{TPA})(\text{L})]$ complexes.....	135
Figure 3.S9. IR spectra showing C=O stretching peaks of picolinic acid, $[\text{Ni}(\text{TPA})(\text{L})]$, and $[\text{Co}(\text{TPA})(\text{L})]$ complexes. The carbonyl band of picolinic acid was shifted to a lower wavenumber when bound to the TPA complex	136
Figure 4.1. Thioamide, thiourea, and thiocarbamate MBPs were proposed for use in Zn(II)-dependent metalloenzymes. Compounds 4.9 and 4.10 were utilized as known thione-based MBPs and 2-mercaptophenol (4.11), captopril (4.12), and L-cysteine methyl ester (4.13) were used as representative thiol-based compounds in this paper	146
Figure 4.2. Percent reactivity of compounds 4.1 – 4.12 with DTNB. The molar ratio of compounds tested to DTNB was 1:10 with an incubation time of 90 min. 2-Mercapophenol (4.11) and captopril (4.12) were used as representative thiol-based compounds that showed essential quantitative disulfide formation with DTNB.....	148
Figure 4.3. HPLC traces of the thioamide, thiourea, and thiocarbamate compounds (<i>red</i>), and 1:1 molar mixture of the compounds and L-cysteine methyl ester after 24 h incubation (<i>black</i>)	149
Figure 4.4. Crystal structure of $[\text{Tp}^{\text{Ph,Me}}\text{Zn}(\text{MBP})]$ complexes (ORTEP, 50% probability ellipsoids). Hydrogen atoms and phenyl groups from the $\text{Tp}^{\text{Ph,Me}}$ ligand were removed for clarity. Color scheme: carbon = gray, nitrogen = blue, oxygen = red, sulfur = yellow, boron = pink, and zinc = green	151
Figure 4.5. Reported crystal structure of $[\text{Tp}^{\text{Ph,Me}}\text{Zn}(\text{MBP})]$ complexes (ORTEP, 50% probability ellipsoids). Hydrogen atoms and phenyl groups from the $\text{Tp}^{\text{Ph,Me}}$ ligand were removed for clarity. Color scheme: carbon = gray, nitrogen = blue, oxygen = red, sulfur = yellow, boron = pink, and zinc = green.....	152
Figure 4.6. Crystal structure of a) $[(\text{Tp}^{\text{Ph,Me}})\text{Zn}(\mathbf{5})]$ b) $[\text{Zn}(\text{TPA})(\mathbf{5})]\text{BPh}_4$ complexes (ORTEP, 50% probability ellipsoids). Hydrogen atoms and phenyl groups from the $\text{Tp}^{\text{Ph,Me}}$ ligand were	

removed for clarity. Color scheme: carbon = gray, nitrogen = blue, sulfur = yellow, boron = pink, and zinc = green 152

Figure 4.7. IC₅₀ curves of compounds **4.4**, **4.5**, **4.5a**, **4.7**, and **4.11** against hCAII. The range of concentration of the compounds is between 0.01 and 1000 μM. IC₅₀ values reported in μM with the 95% confidence interval indicated 154

Figure 4.8. IC₅₀ curves of compounds **4.4**, **4.5**, **4.5a**, **4.9**, and **4.10** against MMP-2. The range of concentration of the compounds is between 1 and 1000 μM. IC₅₀ values reported in μM with the 95% confidence interval indicated..... 155

Figure 4.9. Structure of a) **4.4** (PDB: 8FAL) and b) **4.7** (PDB: 8FAU) bound to hCAII. Zn(II) coordination is represented by solid lines and hydrogen bonding is represented by dashed lines. Zn(II) ion and water molecules are shown as green and red spheres, respectively..... 157

Figure 4.10. Structural superposition between compounds a) **4.4** (blue) and **4.11** (green) (PDB: 2OSM), b) **4.7** (red) and **4.11** (green) bound to the hCAII active site. c) Coordination mode of benzenesulfonamide (orange) bound to the hCAII active site (PDB: 2WEJ)..... 157

Figure 4.S1. Standard calibration curve of L-cysteine methyl ester. The final concentration range of L-cysteine methyl ester was between 1 and 500 μM with the fixed concentration of DTNB (500 μM). The whole concentration range (*left*) and the lower concentration range (*right*) of the standard calibration curve 163

Figure 4.S2. ¹H NMR spectra of L-cysteine methyl ester (*top*), the proposed thioamide, thiourea, and thiocarbamate compounds (*middle*), and 1:1 molar mixture of the compounds and L-cysteine methyl ester after 24 h incubation (*bottom*) 165

Figure 4.S3. Co-crystal structures of hCAII with a) **4.4** and b) **4.7**. Details of the coordination modes of c) **4.4** and d) **4.7** bound to the hCAII active site..... 181

Figure 5.1. Fungal Cu-only SOD. a) Cu-only SODs can react with superoxide from both the host and fungal pathogen. b) Overall structure of *C. albicans* SOD5 (PDB: 4N3U). The Cu(II) ion is shown as a green sphere and select active site residues are shown as sticks colored by atom type (carbon, gray; nitrogen, blue; oxygen, red) 189

Figure 5.2. Active site structure of SODs. a) Active site of *C. albicans* Cu-only SOD5 (PDB: 4N3U). b) Active site of *S. cerevisiae* Cu/Zn-SOD1 (PDB: 1AZV). Cu/Zn-SODs The electrostatic loop is shown in yellow and the Zn(II) ion is shown as an orange sphere 190

Figure 5.3. a) Reported SOD5 inhibitors. b) Schematic showing the principle of the SOD assay. c) Titration curves for the reported SOD5 inhibitors, pyrithione zinc and 1-hydroxypyridine-2(1H)-thione (1,2-HOPTO). The IC₅₀ values were determined under the optimized SOD assay condition and validated the assay 192

Figure 5.4. Structures of all fragments in the MBP and MBI library 194

Figure 5.5. Screening of the MBP/MBI fragment library (~380 fragments) against Cu-only SOD5. Percent inhibition of SOD5 activity shown at a fragment concentration of 200 μ M. ~45 fragments showed >50% inhibition activity. Grey cells are compounds that interfered with the assay due to background signal	196
Figure 5.6. IC ₅₀ curves for the representative hits (color-coded) from the MBP/MBI library screen (<i>left</i>). The structure and IC ₅₀ values of the hits are listed (<i>right</i>)	197
Figure 5.7. Binding modes of computationally derived poses for hit compounds (5.1 , 1,2-HOPTO, and 8-HQ) upon docking with MOE. The docking models were prepared using the structure (PDB: 4N3U).....	199
Figure 5.8. Synthetic scheme of compound 5.1	200
Figure 5.9. Proposed synthetic scheme for derivatization of compound 5.1 at the 6-position. The step for Suzuki coupling reaction did not work under different conditions: (1) Pd(PPh ₃) ₄ , tetrakis(triphenylphosphine)palladium(0), Na ₂ CO ₃ , (2) Pd(PPh ₃) ₄ , SPhos Pd G3, Na ₂ CO ₃ , (3) Pd(OAc) ₂ , tri(<i>o</i> -tolyl)phosphine, CsF.....	200
Figure 5.10. Chemical structures and labeling for MBIs of compound 5.1 (<i>top</i>) and percent inhibition against SOD5 at a concentration of 200 μ M (<i>bottom</i>). The tetrazole and benzothiazole moieties were replaced with their isosteres and their combinations were synthesized as MBIs	201
Figure 5.11. Synthetic scheme for sulfonamide derivatives of 1,2-HOPTO.....	203
Figure 5.12. Synthetic pathway illustrating the challenges in the preparation of sulfonamide derivatives of 1,2-HOPTO. This figure outlines each reaction step, conditions, and the resulting products and byproducts.....	205
Figure 5.S1. IC ₅₀ curves of sulfonamide derivatives of 1,2-HOPTO. The IC ₅₀ values of each compound are listed in the curve. IC ₅₀ values reported in log [nM] with the 95% confidence interval indicated	222
Figure 5.S2. IC ₅₀ curves of sulfonamide derivatives of 8-HQ. The IC ₅₀ values of each compound are listed in the curve. IC ₅₀ values reported in log [nM] with the 95% confidence interval indicated	222

LIST OF TABLES

Table 1.1. List of metalloenzymes that are the target of FDA-approved therapeutics. Adapted from reference 1	3
Table 2.1. Measured and calculated pK_a and $\log P/D_{7.4}$ values of 8-HQ MBI library. pK_a values were measured in the range of pH 2.0 – 12.0. All pK_a and $\log P$ experiments yielded standard deviations <0.05. Calculated pK_a and $\log P/D_{7.4}$ values were obtained using Marvin (ChemAxon) software package	37
Table 2.2. Selected bond lengths and angles of $[Tp^{Ph,Me}Zn(MBI)]$ complexes with 6,6-membered ring MBIs.....	40
Table 2.3. Selected bond lengths and angles of $[Tp^{Ph,Me}Zn(MBI)]$ complexes with 6,5-membered ring MBIs.....	42
Table 2.4. Selected bond lengths and angles of $Tp^{Ph,Me}Zn(MBI)$ complexes with 6,6,5-membered fused ring MBIs. ^a Zn-S bond distance. ^b Zn-external nitrogen bond distance. ^c Not bound to the Zn(II) center, measured values based on X-ray crystallographic data	45
Table 2.5. Percent inhibition values of 8-HQ MBIs (200 μ M) against MMP-2, GLO1, and hCAII. Standard deviations from triplicate measurements are given in parentheses.....	47
Table 2.S1. Aromatic heterocycles used to replace quinoline in the design of 8-HQ MBIs. The frequency of occurrence as a substructure in DrugBank database is listed. The listed number of FDA-approved drugs also includes drugs classified as nutraceuticals, illicit, withdrawn, investigational, and experimental.....	68
Table 2.S2. Crystal structures containing 8-HQ and its MBIs bound to metals in Cambridge Crystallographic Data Centre (CCDC) database. The number of structures and refcodes (entry ID) are listed. Maximum five refcodes are shown when the number of result structures are over 10. No result was obtained for MBIs that are not reported below	69
Table 2.S3. Published pK_a values	70
Table 2.S4. Crystal data and structure refinement for $[(Tp^{Ph,Me})Zn(MBI)]$ complexes	72
Table 2.S5. Selected bond lengths and angles of $[Tp^{Ph,Me}Zn(MBI)]$ complexes with sulfonamide MBIs	81
Table 2.S6. Percent inhibition values of 8-HQ MBIs against GLO1. Whole library of 8-HQ MBIs was screened at 50 μ M final concentration against GLO1. The MBIs having less than 5% inhibition activity were omitted in this table. Standard deviations are given in parentheses. Cells are color-coded by percent inhibition: white (<20%), yellow (20–50%), and red (>50%)	83

Table 2.S7. Inhibition and binding data on select 8-HQ MBIs against GLO1 and hCAII. Select MBIs (200 μ M final concentration) and reference compounds (50 μ M final concentration) were prepared for enzymatic assay and thermal shift assay.....	84
Table 3.1. Selected bond lengths and angles for $[\text{Ni}(\text{TPA})(\text{L})]^{+/2+}$. Structures with more than one complex in the asymmetric unit are marked with an asterisk.....	104
Table 3.2. Selected bond lengths and angles for $[\text{Co}(\text{TPA})(\text{L})]^+$. Structures with more than one complex in the asymmetric unit are marked with an asterisk.....	104
Table 3.3. Selected bond lengths and angles for $[(\text{Tp}^{\text{Ph,Me}})\text{Co}(\text{L})]^{0/+}$	106
Table 3.4. UV-visible and magnetic moment data for $[\text{M}(\text{TPA})(\text{L})]^{+/2+}$	111
Table 3.5. UV-visible and magnetic moment data for $[(\text{Tp}^{\text{Ph,Me}})\text{Co}(\text{L})]^{0/+}$	112
Table 3.S1. Crystal data and structure refinement for $[\text{Ni}(\text{TPA})(\text{L})]$ complexes	123
Table 3.S2. Crystal data and structure refinement for $[\text{Co}(\text{TPA})(\text{L})]$ complexes	125
Table 3.S3. Crystal data and structure refinement for $[(\text{Tp}^{\text{Ph,Me}})\text{Co}(\text{L})]$ complexes	127
Table 3.S4. Crystal data and structure refinement for $[(\text{Tp}^{\text{Ph,Me}})\text{Zn}(\text{bpy})]$ complex	129
Table 3.S5. Selected bond lengths for $[\text{Ni}(\text{TPA})(\text{L})]$ (N1: amine nitrogen of TPA, N2-4: pyridyl nitrogen of TPA). Structures with more than one complex in the asymmetric unit are marked with an asterisk	130
Table 3.S6. Selected bond lengths for $[\text{Co}(\text{TPA})(\text{L})]$ (N1: amine nitrogen of TPA, N2-4: pyridyl nitrogen of TPA). Structures with more than one complex in the asymmetric unit are marked with an asterisk	130
Table 3.S7. Bonds lengths and angles for Ni(II) and Co(II) coordinated TPA complexes with the MBIs 3.2 – 3.4 using DFT calculations at the wB97x-D/LanL2DZ level of theory. a = N5 cis to the N1 of TPA, b = N5 trans to the N1 of TPA, * = crystallographically observed conformation.....	131
Table 4.1. IC_{50} values of the proposed compounds against hCAII and MMP-2. IC_{50} values reported in μ M with the 95% confidence interval indicated. IC_{50} titration curves can be found in Figures 4.7 and 4.8	154
Table 4.S1. Percent reactivity of the proposed compounds with DTNB. Excess amount of DTNB was used with different molar ratios (1:2, 1:5, 1:10). 2-Mercapophenol (4.11), captopril (4.12), and L-cysteine methyl ester (4.13) were used as representative free thiol groups and showed almost 100% reactivity with DTNB.....	164

Table 4.S2. Selected bond lengths and angles of [Tp ^{Ph,Me} Zn(MBP)] complexes. *Previously reported structure. Refcodes (entry ID) for the reported compounds are listed below	171
Table 4.S3. Crystal data and structure refinement for [(Tp ^{Ph,Me})Zn(MBP)] complexes	172
Table 4.S4. X-ray crystallographic data collection and refinement statistics.....	180
Table 5.1. IC ₅₀ values of hit compounds against Cu-only SOD5 versus Cu,Zn-SOD1. IC ₅₀ values reported in μM with the 95% confidence interval indicated. ^a ND, not defined; IC ₅₀ for Cu,Zn-SOD1 was not defined due to insufficient or absent inhibition of enzyme activity over the dose range of compounds tested (0.02 – 50 μM)	197
Table 5.2. IC ₅₀ values of compound 1,2-HOPTO and its derivatives against Cu-only SOD5. IC ₅₀ values reported in μM with the 95% confidence interval indicated	206
Table 5.3. Percent inhibition and IC ₅₀ values of 8-HQ derivatives against Cu-only SOD5.	208
Table 5.4. IC ₅₀ values of 8-HQ and its derivatives with 2- or 7-position substituents against Cu-only SOD5. IC ₅₀ values reported in μM with the 95% confidence interval indicated ..	209
Table 5.5. IC ₅₀ values of compound 3 and its derivatives at 5- or 5,7-positions against Cu-only SOD5. IC ₅₀ values reported in μM with the 95% confidence interval indicated	211
Table 5.6. Calculated pK _a values of 8-HQ derivatives. Calculated pK _a values were obtained using Marvin (ChemAxon) software package. ^a ND, not defined in the range of pH 0–14.	211

LIST OF ABBREVIATIONS

Å	Ångström
AcOH	Acetic acid
ACS	American Chemical Society
ADME	Absorption, Distribution, Metabolism, and Excretion
Bn	Benzyl
BnOH	Benzyl alcohol
CCDC	Cambridge Crystallographic Data Centre
(CD ₃) ₂ CO	Deuterated acetone
CD ₃ OD	Deuterated methanol
CDI	Carbonyldiimidazole
clogP	Calculated log P
CI	Confidence Interval
CSD	Cambridge Structural Database
d	Doublet
Da	Daltons
DBU	1,8-Diazabicyclo(5.4.0)undec-7-ene
DCM	Dichloromethane
dd	doublet of doublets
DETC	diethyldithiocarbamic acid
dt	doublet of triplets
DFT	Density Functional Theory
DNA	Deoxyribonucleic acid

DNase	Deoxyribonuclease
DMF	Dimethylformamide
DMSO	Dimethyl Sulfoxide
DTT	Dithiothreitol
EDTA	Ethylenediaminetetraacetic acid
ESI-MS	Electrospray Ionization Mass Spectrometry
Et ₂ O	Diethyl ether
EtOAc	Ethyl Acetate
EtOH	Ethanol
FBDD	Fragment-Based Drug Discovery
FDA	Food and Drug Administration
g	Times Gravity
G	Gibbs Free Energy
h	hours
H	Hydrogen
H ₂ O	Water
hCAII	human Carbonic Anhydrase II
HCl	Hydrochloric acid
Hex	Hexanes
HEPES	4-(2-hydroxyethyl)-1-piperazineethanesulfonic acid
HONH ₂ ·HCl	Hydroxylamine hydrochloride
HPLC	High-Performance Liquid Chromatography
HR-ESI-MS	High-Resolution Electrospray Ionization Mass Spectrometry

HRMS	High Resolution Mass Spectrometry
HTS	High-Throughput Screening
IC ₅₀	Half maximal Inhibitor Concentration
IPTG	β-D-1-thiogalactopyranoside
J	Coupling constant
K	Kelvin
KCl	Potassium Chloride
K ₂ CO ₃	Potassium Carbonate
KDM	Jumonji-domain of Histone Lysine Demethylase
KOH	Potassium hydroxide
L	Liter
LB	Luria broth
LC-TOFMS	Liquid Chromatography Time-of-Flight Mass Spectrometry
LiAlH ₄	Lithium Aluminum Hydride
LiCl	Lithium Chloride
LogP	Octanol-water partition coefficient
m	multiplet
M	Molar
MBI	Metal-Binding Isostere
MBP	Metal-Binding Pharmacophore
MeCN	Acetonitrile
MeOH	Methanol
min	minutes

MM	Molecular Mechanical
MOE	Molecular Operating Environment
mg	Milligram
MgCl ₂	Magnesium Chloride
MgCl ₂ ·6H ₂ O	Magnesium Chloride Hexahydrate
MgSO ₄	Magnesium Sulfate
MHz	Megahertz
mL	milliliters
mM	millimolar
mmol	millimoles
MMP	Matrix Metalloproteinase
MnCl ₂	Manganese Chloride
MW	Molecular Weight
MWCO	Molecular Weight Cutoff
MV	Molecular Volume
m/z	mass-to-charge ratio
n-BuLi	n-Butyllithium
NaBH ₄	Sodium Borohydride
NaCl	Sodium Chloride
NaH	Sodium Hydride
NaN ₃	Sodium azide
NaNO ₂	Sodium Nitrite
NaOAc	Sodium Acetate

NaOH	Sodium Hydroxide
Na ₂ PO ₄	Sodium Phosphate
NEt ₃	Triethylamine
NH ₃	Ammonia
NH ₄ Cl	Ammonium Chloride
nm	nanometer
nM	nanomolar
NMR	Nuclear Magnetic Resonance
PA _N	N-terminal domain of the Polymerase Acidic subunit of the RNA-dependent RNA polymerase of the influenza virus
PK	Pharmacokinetic
pK _a	Acid dissociation constant
PDB	Protein Data Bank
q	quartet
RPM	Revolutions Per Minute
s	singlet
SAR	Structure-Activity Relationship
S _N Ar	Nucleophilic Aromatic Substitution
SOD	Superoxide Dismutase
SPhos Pd G3	(2-Dicyclohexylphosphino-2',6'-dimethoxybiphenyl) [2-(2'-amino-1,1'-biphenyl)]palladium(II) methanesulfonate
t	triplet
TEV	Tobacco Etch Virus protease

TFA	Trifluoro acetic acid
THF	Tetrahydrofuran
TLC	Thin layer chromatography
TMS	Trimethylsilyl
TTM	Tetrathiomolybdate
Tris	Tris(hydroxymethyl)aminomethane
UV	Ultraviolet
VS	Virtual Screening
ZnCl ₂	Zinc Chloride
δ	Chemical shift; ppm
Δ	Difference
ζ	Average of the sum of the deviation of 6 unique metal–ligand bond lengths around the central metal atom
λ	Wavelength
μL	Microliter
μM	Micromolar
τ	Tau

ACKNOWLEDGEMENTS

First, I would like to express my deepest gratitude to my supervisor, Professor Seth M. Cohen, for his invaluable guidance and continuous support during my PhD journey. His mentorship was not only crucial for my development as a scientist but also inspirational, pushing me to always strive for excellence. Seth is an exemplary leader—organized, diligent, and incredibly efficient, embodying the true essence of hard work and dedication in addition to his intelligence. I have learned so much from him, not just about science, but about how to be a better person too. I owe a huge thank you to Seth for his constant encouragement, especially during the challenging times of the COVID-19 pandemic and when he had to mentor us from afar. Despite the distance and global crisis, Seth guided us to stay focused, motivated, and connected. His commitment to our success not only kept the lab moving forward but also brought us closer together as a team. Thank you, Seth, for your incredible leadership and for keeping me on track, even from afar. Your support during those times—and continuing to the present—has been priceless and will always be cherished.

I want to express my gratitude to both past and present members of the Cohen lab for their support throughout my PhD program, professionally and personally. A special shout-out to my cohort lab mates, Alysia J. Kohlbrand and Conor O'Herin, for their friendship and support during my graduate studies. The warm welcome and kindness you provided as I navigated my new life in the US made it truly feel like a second home. Our scientific discussions and everyday conversations have been incredibly inspiring, shaping me into not only a better scientist but also a great team member. I would also like to thank Dr. Kathleen E. Prosser and Dr. Ryjul W. Stokes for their exceptional mentorship in the lab. Your generosity and example have set a standard for what great mentorship looks like, motivating me to offer the same level

of guidance to the next generation in our lab. I'm so grateful to everyone who collaborated with me on various projects and papers. Being part of such an incredible team of motivated postdocs and graduate students has been a privilege, and I look forward to seeing where the Cohen Lab's success leads in the future.

I am deeply thankful to my committee members, Professors Carlo Ballatore, Galia T. Debelouchina, Kamil Godula, and Alina M. Schimpf, for their invaluable guidance, which has been crucial in keeping me on track and moving forward. I'm also grateful to my advisor from my undergraduate and master's research, Professor Youngbok Lee from Hanyang University, whose support helped me to pave the way for my PhD journey. Thanks to Professor Pratip Bhattacharya at MD Anderson Cancer Center for his mentorship, which reinforced my determination to pursue research in the US. Additionally, my gratitude goes to Sierra Gosting and Lan Tran from BD Biosciences for showing me the practical applications of R&D in product development. I also would like to express my appreciation to Dr. Chongwoo Yu for his mentorship at the US FDA, where I gained invaluable knowledge in clinical pharmacology and regulation in drug development. Dr. Yu is one of the most knowledgeable and enthusiastic reviewers I have encountered. Each of you has left a lasting imprint on my professional path, and for that, I am so grateful.

I want to extend my deepest thanks to my family for their endless support and unconditional love over the years. I would like to thank my parents, Jeongbok Nam and Yongcheol Seo, who have always kept me in their prayers, taught me the values of humility and the power of faith during these tough times. I'm grateful to my in-laws, Junghwa Kim and Gihong Lee, for welcoming me into their hearts and making Houston, TX, feel like a second home. Your generous support has been a pillar for me, and I treasure every moment spent with

you. To my brother, Hyunglak Seo, thank you for filling our family's life with joy and love in Korea. Your smile and pure-heartedness are treasures I hold close to my heart.

Finally, I extend a heartfelt thank you to my incredible husband, Sung Jin Lee, for his steadfast support and love throughout my PhD journey. Sung, your dedication to our life together is beyond words. Despite his busy schedule, you have flown from Houston to San Diego every other weekend for the past five years just to be with me for those few precious days. This act of love and sacrifice means everything to me, and I am eternally grateful. You have been my pillar of stability, reminding me that there is more to life than scientific achievements alone. I treasure every moment we share together in San Diego and look forward to all the adventures that await us, anticipating a future filled with love and joy.

Chapter 1, in part, is a reprint of the material as it appears in “Evaluating Metal–Ligand Interactions of Metal-Binding Isosteres Using Model Complexes.” *Inorg. Chem.*, 2021, 60, 22, 17161. The dissertation author was a primary author of this paper and gratefully acknowledges the contributions of coauthors Kathleen E. Prosser, Mark Kalaj, Johannes Karges, Benjamin Dick, and Seth M. Cohen.

Chapter 2 is a reprint of the material as it appears in “Developing Metal-binding Isosteres of 8-Hydroxyquinoline as Metalloenzyme Inhibitor Scaffolds.” *Inorg. Chem.*, 2022, 61, 19, 7631. The dissertation author was a primary author of this paper and gratefully acknowledges the contributions of coauthors Moritz K. Jackl, Mark Kalaj, and Seth M. Cohen.

Chapter 3 is a reprint of the material as it appears in “Evaluating Metal–Ligand Interactions of Metal-Binding Isosteres Using Model Complexes.” *Inorg. Chem.*, 2021, 60, 22, 17161. The dissertation author was a primary author of this paper and gratefully acknowledges

the contributions of coauthors Kathleen E. Prosser, Mark Kalaj, Johannes Karges, Benjamin L. Dick, and Seth M. Cohen.

Chapter 4 is a reprint of the material as it appears in “Masking thiol reactivity with thioamide, thiourea, and thiocarbamate-based MBPs.” *Chem. Comm.*, 2023, 59, 2283. The dissertation author was a primary author of this paper and gratefully acknowledges the contributions of coauthors Alysia J. Kohlbrand, Ryjul W. Stokes, Jeewon Chung, and Seth M. Cohen.

Chapter 5 contains unpublished material that was written with Valeria Culotta and Seth M. Cohen. The dissertation author was the primary author of this chapter. We acknowledge Alysia J. Kohlbrand for the preparation of Cu-only SOD5 and the effort for protein X-ray crystallography. This chapter, in part, is a reprint of the material as it appears in “Salicylate metal-binding isosteres as fragments for metalloenzyme inhibition.” *Chem. Sci.* 2022, 13, 7, 2128. The dissertation author was a primary author of this paper and gratefully acknowledges the contributions of coauthors Moritz K. Jackl, Mark Kalaj, and Seth M. Cohen.

VITA

Education

- 2024 Doctor of Philosophy in Chemistry, University of California San Diego (UCSD)
- 2018 Master of Engineering in Bioengineering, Hanyang University
- 2016 Bachelor of Science in Chemistry, Hanyang University

Professional Experience

- 2023 ORISE Fellow, U.S. Food and Drug Administration (FDA), Silver Spring, MD
- 2022 R&D Intern, BD Biosciences, San Diego, CA
- 2018 Visiting Scholar, MD Anderson Cancer Center, Houston, TX

Honors and Awards

- 2023 MOGAM-KASBP Scholarship, Korean American Society in Biotech and Pharmaceuticals (KASBP)
- 2022 KASBP-YUHAN Fellowship, KASBP
- 2021-22 Teddy Traylor Award, UCSD
- 2021-22 Distinguished Graduate Student Fellowship, UCSD
- 2021 Friends of the International Center Fellowship, UCSD
- 2021 ACS Student Travel Award, American Chemical Society (ACS)
- 2016 KCS President's Award, Korean Chemical Society (KCS)
- 2016 Dean's Award, Hanyang University

Publications

17. Yu, C.; Jiang, W.; Matta, M.; Wang, Rong.; Haidar, S.; Seo, H., Lessons Learned from Regulatory Submissions Involving Endogenous Therapeutic Analyte Bioanalysis. *Bioanalysis* 2024, 16 (3), 171-184.
16. Doyle, M. R.; Dirik, S.; Martinez, A. R.; Sneddon, E. A.; Seo, H.; Cohen, S. M.; Guglielmo, G., Catechol-O-Methyltransferase Inhibition and Alcohol Use Disorder: Evaluating the Efficacy of Tolcapone in Ethanol-Dependent Rats. *Neuropharmacology* 2024, 242, 109770.
15. Seo, H.; Kohlbrand, A. J.; Stokes, R. W.; Chung, J.; Cohen, S. M., Masking thiol reactivity with thioamide, thiourea, and thiocarbamate-based MBPs. *Chem. Commun.* 2023, 59 (16), 2283-2286.
14. Stokes, R. W.; Kohlbrand A. J.; Seo, H.; Sankaran, B.; Karges, J.; Cohen, S. M., Hydroxypyridinone Carboxylic Acid Isosteres as Inhibitors of Influenza Endonuclease. *ACS Med. Chem. Lett.* 2023, 14 (1), 75-82.
13. Seo, H.; Jackl, M. K.; Kalaj, M.; Cohen, S. M., Developing Metal-binding Isosteres of 8-Hydroxyquinoline as Metalloenzyme Inhibitor Scaffolds. *Inorg. Chem.* 2022, 61 (19), 7631-7641.
12. Jackl, M. K.; Seo, H.; Karges, J.; Kalaj, M.; Cohen, S. M., Salicylate Metal-Binding Isosteres as Fragments for Metalloenzyme Inhibition. *Chem. Sci.* 2022, 13 (7), 2128-2136.
11. Cho, C.; Niederholtmeyer, H.; Seo, H.; Bhattacharya, A.; Devaraj, N., Functionalizing lipid sponge droplets with DNA. *ChemSystemsChem* 2022, e202100045.
10. Seo, H.; Prosser, K. E.; Kalaj, M.; Karges, J.; Dick, B.; Cohen, S. M., Evaluating Metal-Ligand Interactions of Metal-Binding Isosteres Using Model Complexes. *Inorg. Chem.* 2021, 60 (22), 17161-17172.
9. Karges, J.; Seo, H.; Cohen, S. M., Synthesis of Tetranuclear Rhenium(I) Tricarbonyl Metallacycles. *Dalton Trans.* 2021, 50 (44), 16147-16155.
8. Prosser, K.; Kohlbrand, A.; Seo, H.; Kalaj, M.; Cohen, S. M., ¹⁹F-Tagged Metal Binding Pharmacophores for NMR Screening of Metalloenzymes. *Chem. Commun.* 2021, 57 (40), 4934-4937.
7. Kim, J.; Jo, D.; Yang, S.; Joo C.; Whiting N.; Pudakalakatti S.; Seo, H.; Son, H. Y.; Min, S.; Bhattacharya, P.; Huh, Y.; Shim, J. H.; Lee, Y., ²⁹Si Isotope-Enriched Silicon Nanoparticles for Efficient Hyperpolarized Magnetic Resonance Imaging Probe. *ACS Appl. Mater. Interfaces* 2021, 13 (48), 56923-56930.
6. Seo, H.; Choi, I.; Whiting, N.; Hu, J.; Luu, Q. S.; Pudakalakatti, S.; McCowan, C.; Kim, Y.; Zacharias, N.; Lee, S.; Bhattacharya, P.; Lee, Y., Hyperpolarized Porous Silicon

Nanoparticles: Potential Theragnostic Material for ^{29}Si Magnetic Resonance Imaging. *ChemPhysChem* 2018, 19 (17), 2143-2147.

5. Seo, H.; Kim, D.; Ahn, H.; Hwang, S.; Luu, Q. S.; Kim, J.; Lee, S.; Lee, Y., Efficient Conversion Method of Bulk Silicon Powders into Porous Silicon Nanoparticles. *Bull. Korean Chem. Soc.* 2018, 39 (12), 1455-1458.
4. Lee, H.; Lee, J.; Min, S.; Seo, H.; Lee, Y.; Rhee, H., Copper(I)-Catalyzed Synthesis of 1,4-Disubstituted 1,2,3-Triazoles from Azidoformates and Aryl Terminal Alkynes. *J. Org. Chem.* 2018, 83 (3), 4805-4811.
3. Ko, H.; Choi, I.; Chang, K.; Jeong, G.; Gong, G.; Seo, H.; Ryu, D.; Lee, K.G.; Choi, D.; Chung, H.; Lee, Y., Amphiphilic metabolites in gallbladder bile: Potential biomarkers for gallbladder diseases. *Appl. Spectrosc. Rev.* 2016, 51 (7-9), 706-717.
2. Jung, G.; Lee, J.W.; Gong, G.; Ko, H.; Choi, I.; Seo, H.; Zacharias, N.; Bhattacharya, P.; Lee, Y., Bio-interfacial Magnetic Resonance Imaging of Hyperpolarized Contrast Agents for Metabolic Flux Interrogation *In Vivo*. *J. Ind. Eng. Chem.* 2016, 36, 224-228.
1. Ko, H.; Jung, G.; Gong, G.; Choi, I.; Seo, H.; Lee, Y., Hyperpolarization: Sensitivity Boost for Magnetic Resonance Spectroscopy and Imaging. *J. Korean Magn. Reason.* 2015, 19 (3), 124-131.

Presentations

6. Seo, H.; Jackl, M.; Kohlbrand, A. J.; Cohen, S. M., Expanding Metal-Binding Pharmacophores for Fragment-Based Drug Discovery: Isosteric Replacement and Reactivity Masking Strategy. *ACS Fall Meeting*. 2023, San Francisco, CA
5. Seo, H.; Kohlbrand, A. J.; Stokes, R. W.; Chung, J.; Cohen, S. M. Masking thiol reactivity with thioamide, thiourea, and thiocarbamate-based MBPs to generate a potent metalloenzyme inhibitor. *UC Chemical Spring Symposium*. 2023, Lake Arrowhead, CA.
4. Seo, H.; Jackl, M.; Kalaj, M.; Cohen, S. M., Novel Scaffold Library Design for Metalloenzyme Fragment-based Drug Discovery. *KASBP Spring Symposium*. 2022, virtual
3. Seo, H.; Jackl, M.; Kalaj, M.; Cohen, S. M., Developing Metal-binding Isosteres as Metalloenzyme Inhibitor Scaffolds. *ACS Spring Meeting*. 2022, San Diego, CA
2. Seo, H.; Hwang, S.; Lee, Y. Real-time Kinetic and Mechanistic Study of Decarboxylation Reaction of Pyruvic Acid Using Hyperpolarization Techniques. *KCS Spring Meeting*. 2017, Gwangju, Korea
1. Seo, H.; Choi, I.; Ko, H.; Gong, G.; Park, H.; Chung, H.; Lee, Y. Hyperpolarized Silicon Nanoparticles as Biocompatible Contrast Agents for ^{29}Si Magnetic Resonance Imaging. *KCS Fall Meeting*. 2016, Busan, Korea

ABSTRACT OF THE DISSERTATION

Expanded Tools and Isosteres for Fragment-Based Drug Discovery against Metalloenzymes

by

Hyeonglim Seo

Doctor of Philosophy in Chemistry

University of California San Diego, 2024

Professor Seth M. Cohen, Chair
Professor Carlo Ballatore, Co-Chair

Fragment-based drug discovery (FBDD) is a powerful approach for identifying molecules that inhibit therapeutically relevant targets, focusing on the elaboration of fragment 'hits' into compounds with enhanced inhibition and desirable pharmaceutical attributes. A significant challenge in metalloenzyme inhibition within FBDD is the repeated use of the same metal-binding pharmacophores (MBPs), which limits the development of novel inhibitors. This

thesis presents innovative strategies for exploring and expanding the fragment library, aimed at developing inhibitors for metalloenzymes and thus overcoming existing limitations. It also demonstrates how the enhanced fragment libraries have facilitated the identification of hit compounds targeting therapeutically relevant metalloenzymes.

Metal-binding isosteres (MBIs) are introduced as a strategy to diversify fragment libraries for metalloenzyme inhibition. Isosteric replacement with 8-hydroxyquinoline was explored to enhance the potency and selectivity of drug-target interactions, as well as to broaden physicochemical properties of the fragments. Subsequently, this thesis includes an exploration of bioinorganic model complexes to study the structural and electronic characteristics of MBIs. MBIs of picolinic acid were investigated within different bioinorganic model systems, offering new insights into their properties. Furthermore, the strategic design of thioamide, thiourea, and thiocarbamate MBPs as potent warheads was showcased. Their potential in addressing the challenges of thiol-based MBPs, specifically against Zn(II)-dependent metalloenzymes, was demonstrated. Lastly, the discovery of small molecule inhibitors against Cu-only Superoxide Dismutase (SOD5) demonstrates the identification and development of MBP/MBI warheads for a novel antifungal target. This significantly advances the quest for antifungal agents, underscoring the thesis's contribution to the development of metalloenzyme inhibitors through fragment-based strategies.

Chapter 1: Library Design for Metalloenzyme Fragment-based Drug Discovery

1.1 Introduction to Metalloenzymes and Metalloenzyme Inhibitors

Enzymes play a pivotal role in facilitating the chemical transformations necessary for sustaining life. A subset of these enzymes, known as metalloenzymes, contains one or more bound metal ions that are essential for enzymatic function. The role of metal ions in metalloenzymes (and metalloproteins more broadly) can be generally classified into two categories: structure and function.¹ Structural metal ions support protein folding, exemplified by zinc finger proteins,² while functional metal ions carry out a roles, including electron transfer and catalysis.³ Metalloenzymes, promote a diverse range of reactions including hydrolytic processes,⁴⁻⁵ oxidation/reductions,⁶⁻⁷ and functional group transfers.⁸⁻⁹ Examples include hydrogenases that catalyze the reversible oxidation of molecular hydrogen,⁶ superoxide dismutases that catalyze the reduction of superoxide anions to hydrogen peroxide,¹⁰ and methylases that transfer methyl group between two molecules.⁸

Due to the many biological processes controlled and regulated by metalloenzymes, they are important therapeutic targets for treating a wide range of diseases including diabetes, cancer, and pathogenic infections, just to name a few.^{1, 11} Some metalloenzymes that are the target of approved therapeutics are summarized in Table 1.1.¹ With 40% to 50% of all enzymes being metal-dependent,¹²⁻¹⁴ metalloenzymes present a vast, and largely untapped target space for novel therapeutic development.

Table 1.1. List of metalloenzymes that are the target of FDA-approved therapeutics. Adapted from reference 1.

Metalloenzyme	Metal Ion	Disease/Condition
Arginase	Mn(II)	Cancer
Histone Deacetylase	Zn(II)	Cancer
Histone Demethylase	Fe(II)	Cancer
Farnesyl Transferase	Zn(II)	Cancer
Glyoxalase I	Zn(II)	Cancer
Carbonic Anhydrases	Zn(II)	Cancer
Rpn11	Zn(II)	Cancer
Methionine Aminopeptidase	Mn(II)/Fe(II)	Cancer, Obesity
Matrix Metalloprotease	Zn(II)	Cancer, Arthritis, Inflammation
LpxC	Zn(II)	Bacterial Infection
Peptide Deformylase	Fe(II)	Bacterial Infection
Metallo- β -lactamase	Zn(II)	Bacterial Infection
<i>Pseudomonas Aeruginosa</i> Elastase	Zn(II)	<i>P. aureginosa</i> Infection
HIV Integrase	Mg(II)	Human Immunodeficiency Virus
Influenza Endonuclease	Mn(II)	Influenza Virus
Angiotensin Converting Enzyme	Zn(II)	Hypertension
Neprilysin	Zn(II)	Hypertension
Lipoxygenase	Fe(II)	Asthma
Insulin Degrading Enzyme	Zn(II)	Diabetes, Alzheimer's
Catechol- <i>O</i> -Methyltransferase	Mg(II)	Parkinson's disease

Despite their prevalence and therapeutic value, fewer than 5% of small molecule drugs target a metalloenzyme.^{1, 15} A barrier for developing metalloenzyme inhibitors has been the longstanding reliance on a limited number of metal-binding pharmacophores (MBPs) to bind to the active site metal ion(s) in these targets. The majority of FDA-approved metalloenzyme inhibitors coordinate to the catalytic active site metal ion via an MBP (Figure 1.1). Numerous crystallographic studies of metalloenzyme inhibitors in complex with their protein targets have validated the importance of metal coordination.¹ However, among clinically used metalloenzyme inhibitors, a limited number of MBPs have been employed to bind the active site metal ions, with a particular overreliance on the hydroxamic acid, carboxylic acid, thiol, and a handful of other MBP functional groups (Figure 1.1). These and other commonly investigated MBPs suffer from pharmacokinetic liabilities such as metabolic instability, poor solubility, and low membrane permeability that ultimately limit the usefulness of many MBPs as lead scaffolds for the development of effective therapeutics.¹⁶⁻²¹

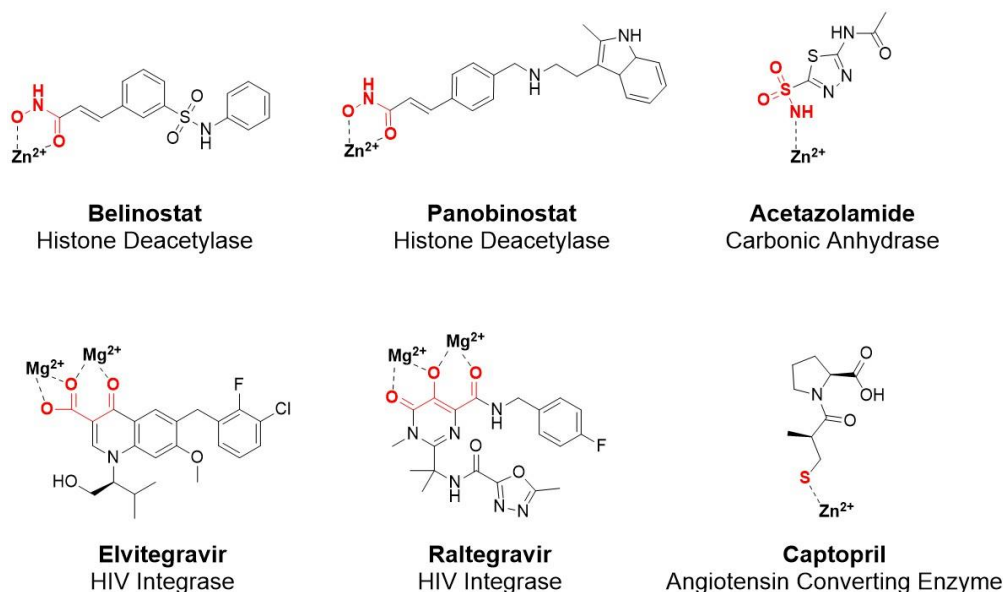


Figure 1.1. FDA-approved metalloenzyme inhibitors containing MBPs. MBPs containing donor atoms are highlighted in red. Adapted from reference 1.

1.2 Fragment-Based Drug Discovery (FBDD)

Fragment-based drug discovery (FBDD) is an established, robust approach for small molecule drug discovery, offering a complementary strategy to more traditional methods such as high-throughput screening (HTS).²²⁻²³ The initial step in FBDD involves screening a fragment library (Figure 1.2), where compounds with generally ≤ 20 heavy atoms are screened against a target protein. Fragment library design tends to follow the ‘rule of three,’²⁴ in which the molecular weight of a fragment is ≤ 300 Da, the number of hydrogen bond donors (HBD) is ≤ 3 , the number of hydrogen bond acceptors (HBA) is ≤ 3 , and the logarithm of the partition or distribution coefficient (LogP/LogD) is ≤ 3 . However, the ‘rule of three’ is not absolute, and successful fragments can often violate at least one of these rules, most commonly by having a higher HBA count.²⁵

FBDD provides several attractive advantages over HTS campaign in target-based drug discovery, including reduced experimental costs, offering diverse hits, and providing multiple pathways for hit-to-lead development.²³ The rationale behind FBDD is that smaller fragments (≤ 300 Da) allow for a more atom-efficient binding interaction with target proteins than larger molecules (> 300 Da) typically screened in HTS.²⁶⁻²⁷ While HTS compounds may initially have impressive affinity through a summation of suboptimal interactions, fragments binding relies on a smaller number of high quality molecular interactions.^{26, 28} As a result, fragment hits leave chemical space to optimize potency, selectivity, and physicochemical properties for the development of lead compounds.²³ Moreover, FBDD typically achieves a higher hit rate (3-5%) compared to HTS ($< 1\%$), meaning that a considerably smaller fragment library ($\sim 10^3$) is required to yield quality hits for a drug discovery program, as opposed to the vast libraries ($\sim 10^6$) used in HTS.²⁷ In essence, the FBDD approach not only enhances the efficiency of the drug discovery

process but also provides a better developmental starting point, leading to a more effective exploration of potential therapeutic agents.

To carry out a fragment screening experiment, the following procedures are usually required (Figure 1.2): selecting a fragment library, setting up screening methods for hits identification, determining structures of fragment-target complexes, conducting structure-activity relationship (SAR) studies, and designing a strategy to elaborate the fragment into a lead inhibitor. The primary challenge associated with FBDD involves identifying fragment hits and confirming the binding of the fragments to the target protein. Binding affinities between fragments and their targets are typically low, with equilibrium dissociation constant (K_d) values ranging from 100 μM to 1 mM, compared with HTS hits, which have K_d values in 10 to 100 μM range.²⁸ The weaker affinities found with fragment hits are usually difficult to measure in standard biochemical assays (e.g., spectrophotometric and fluorescence enzyme-based assays) that are typically used for HTS screens. Therefore, more sensitive biophysical techniques have been used in fragment screening, including nuclear magnetic resonance (NMR), surface plasmon resonance (SPR), X-ray crystallography, and differential scanning fluorimetry (DSF).²⁸⁻²⁹

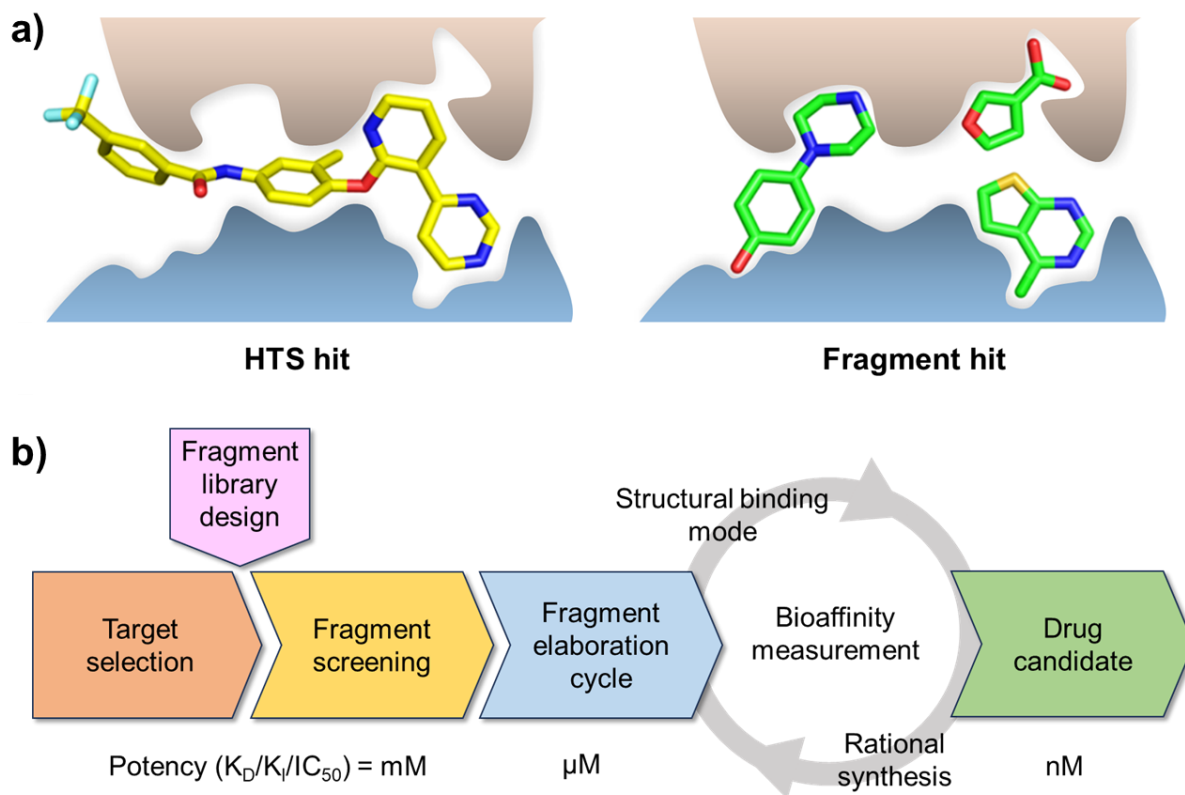


Figure 1.2. a) HTS hits may bind by virtue of numerous suboptimal interactions. By contrast, fragment hits are more ligand efficient and involve fewer but more optimized interactions. b) General workflow of fragment-based drug discovery (FBDD), indicating the process of taking validated fragments through to a lead series. The iterative cycle of design, binding mode determination, and affinity measurement to incrementally improve potency. Adapted from reference 30.

To transform hits into leads with higher affinities and activities against their targets, three strategies are generally employed to enhance the specificity and potency of fragment hits. These strategies include fragment growing, merging, and linking (Figure 1.3),³⁰⁻³¹ with fragment growing being the most used approach. This approach involves growing fragments through chemical synthesis to identify and generate additional interactions with the target. The success of this strategy is evidenced by the development of FDA-approved drugs developed by FBDD, including Pexidartinib,³² Vemurafenib,³³ Venetoclax,³⁴ and Erdafitinib.³⁵ FBDD is often supported by structural data, usually gained through techniques like X-ray crystallography or NMR.³⁶ Decisions

on which fragment hits to further develop are based on multiple factors, including their potency, ligand efficiency, synthetic tractability, and broader medicinal chemistry considerations.³¹

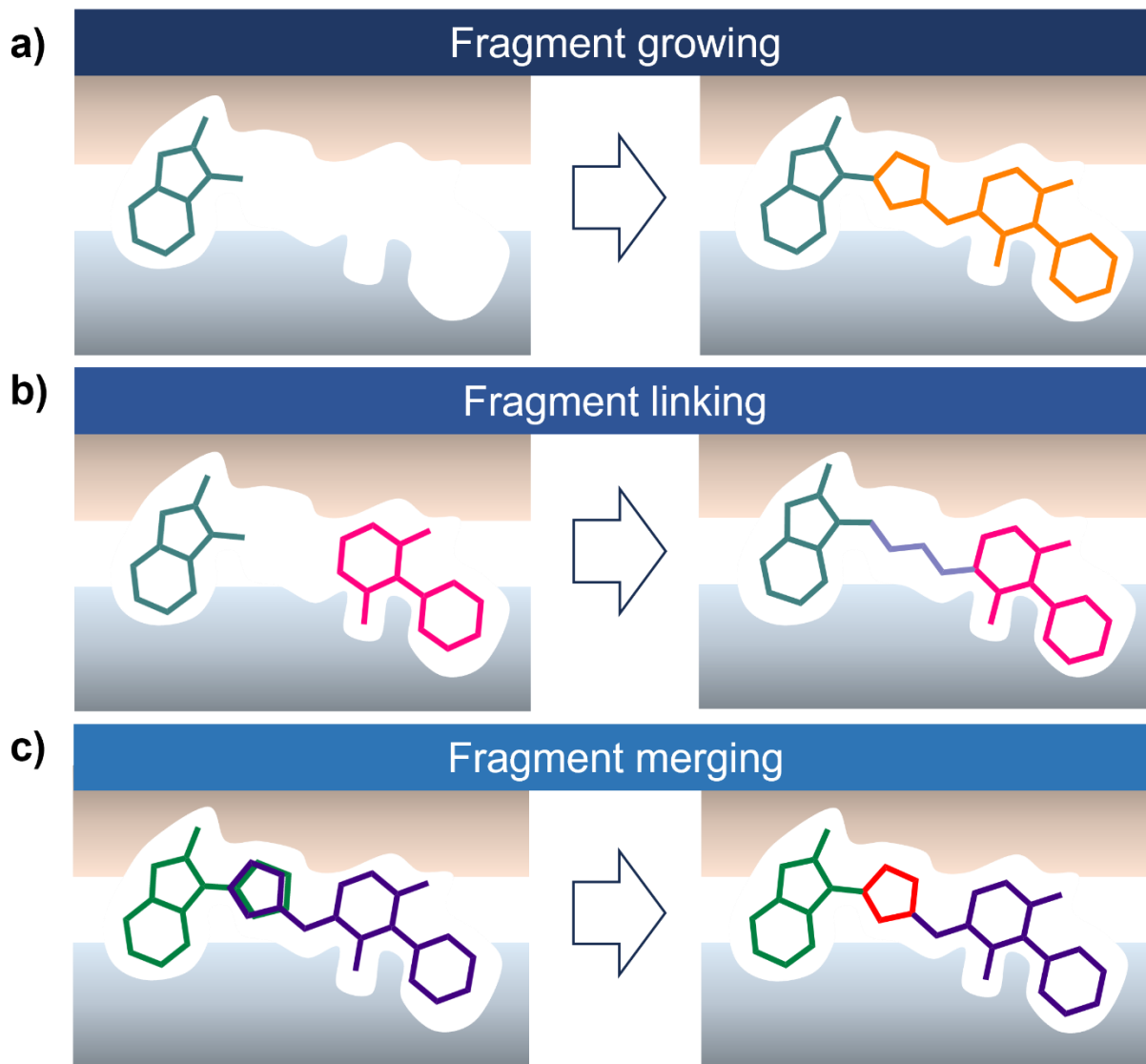


Figure 1.3. FBDD elaboration strategies. a) Fragment growing consists of modifying the fragments to increase their size. b) Fragment linking describes the process of joining two fragments that bind in two different sub-pockets of the binding site with a chemical linker or spacer. c) Fragment merging is used in case where two distinct fragments partially occupy the same region, and the overlapping groups merge the two fragments. Adapted from reference 37.

1.3 FBDD for Metalloenzyme Targets

In the realm of metalloenzyme inhibitor discovery, our laboratory has developed FBDD with the use of MBPs as privileged fragment scaffolds.¹⁵ MBPs are particularly advantageous in this context as they can strongly interact with an active site metal center via metal-ligand coordinate covalent bonds, effectively inhibiting the catalytic activity of metalloenzymes.¹ This approach has led to the development of a novel set of MBP fragment library, moving beyond the conventional scope of hydroxamic acid inhibitors, resulting in a fragment library of ~300 MBP fragments (Figure 1.4).³⁷⁻³⁸ This library serves as an excellent starting point for FBDD, given the small size and high affinity of MBPs for metal ions in target metalloenzymes, and has yielded several hits against therapeutically relevant metalloenzyme targets.³⁹⁻⁴¹

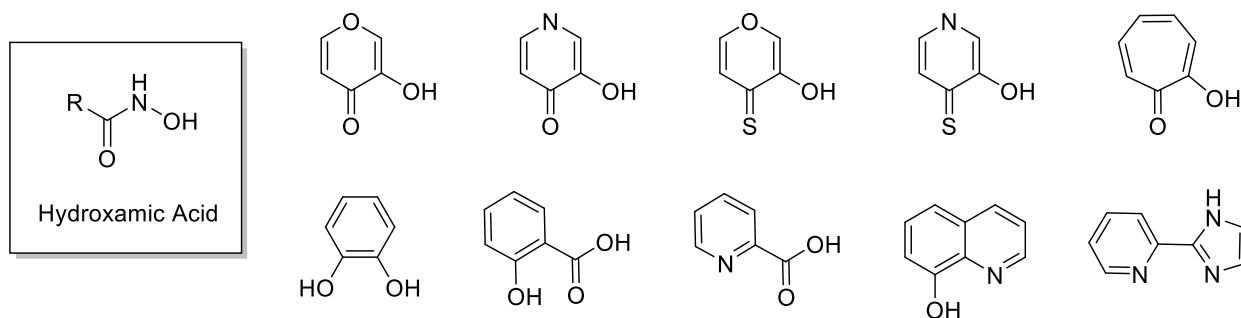


Figure 1.4. Representative MBP fragments specifically designed for FBDD against metalloenzyme targets. Several metalloenzyme inhibitors that had developed showed overreliance on hydroxamic acid functional group. Alternative MBPs were created and this MBP library possesses fragments with a variety of coordination motifs, being capable of monodentate and multidentate coordination to active site metal(s).

Unlike traditional FBDD, which often relies on sensitive biophysical techniques, such as X-ray crystallography, NMR and SPR, to screen fragment libraries, our approach with an MBP library allows the use of simple biochemical, enzyme-based assays including colorimetric, fluorescence, and bioluminescence based methods.⁴²⁻⁴⁴ This advantage originates from the comparatively high affinity of MBPs for metal ions in metalloenzyme active sites, which often

exhibits greater binding constants (IC_{50} or $K_d < 1$ mM) and higher hit rates (>5%) during fragment screening. This highlights that FBDD tailored for metalloenzymes offers significant benefits over conventional FBDD. Specifically, our MBP library streamlines the early stages of drug discovery by providing quality hits that are used for further development through synthetic elaboration to enhance their potency and selectivity for metalloenzyme targets.

Our metalloenzyme-targeted fragment-based drug discovery (mFBDD) has been successful in developing novel and potent metalloenzyme inhibitors, including those targeting RNA-dependent RNA polymerase acidic N-terminal (PA_N) endonuclease of influenza virus (Figure 1.5), among others.^{39, 45-46} In the case of PA_N , the metalloenzyme contains a dinuclear Mg^{2+} or Mn^{2+} active site and has been the target of several recent drug discovery efforts.⁴⁷⁻⁴⁹ In 2018, the compound baloxavir marboxil discovered by Shinogi was approved by FDA for treatment of flu.⁵⁰ In our own efforts, our MBP library was evaluated against PA_N , and MBPs featuring a triad of oxygen donors, particularly those with a free carboxylic acid, were identified as potent fragment hits.^{39, 45-46} These hits exhibited high activities, with IC_{50} values ranging from 0.43 to 13.6 μ M. Subsequent structural elaboration was guided by structural information revealed through X-ray crystallography, and rational SAR trends were established by involving fragment merging and growing techniques. Those efforts ultimately led to the identification of highly active PA_N endonuclease inhibitors. The most potent inhibitor, containing carboxylic acid modified hydroxypyridinone, demonstrated remarkable efficacy, with an IC_{50} of ~47 pM.⁴⁵

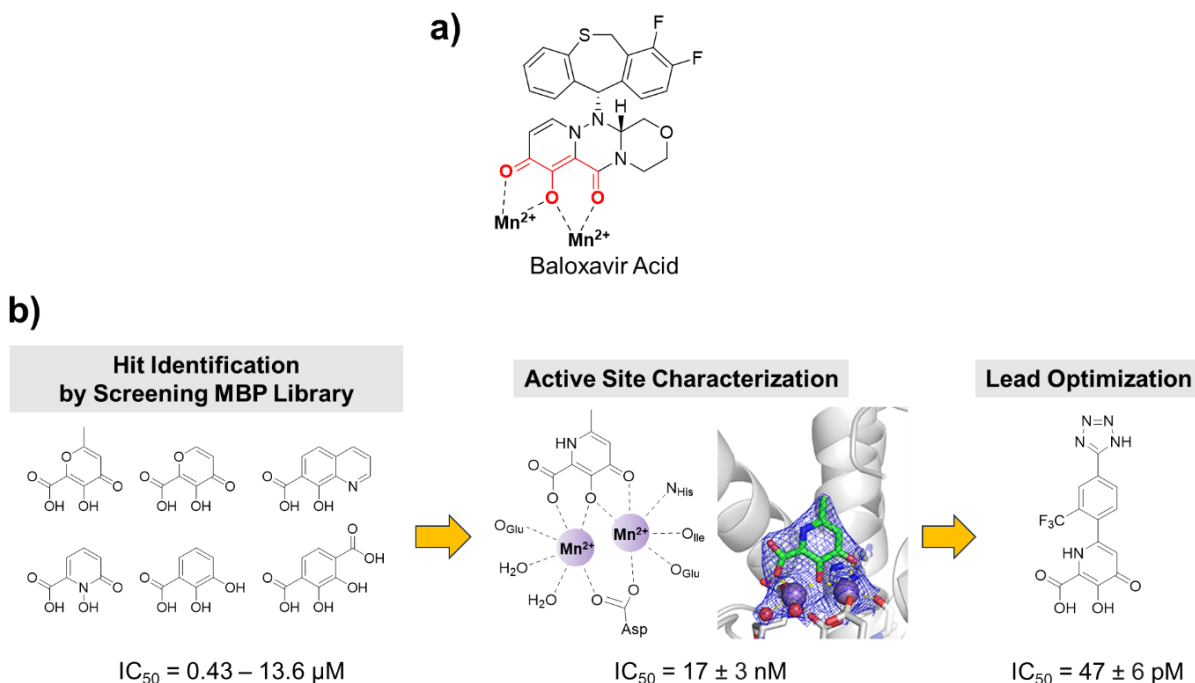


Figure 1.5. a) Chemical structure of baloxavir acid, which is an active agent of baloxavir marboxil, a reported metal-binding inhibitor of PA_N endonuclease. Donor atoms are highlighted in red. b) FBDD for the development of influenza endonuclease inhibitor. Several potent hits were identified by screening the MBP library through the fluorescence-quenching-based biochemical assays. Among the hits, carboxylic acid modified hydroxypyridinone was further studied to determine its binding modes with the active site by X-ray crystallography. The fragment hit were optimized by various medicinal chemistry approaches, resulting in a potent inhibitor with IC_{50} of ~ 47 pM. Adapted from reference 45.

Although the PA_N endonuclease inhibitors showed impressive effectiveness, the carboxylic acid modified hydroxypyridinone and its derivatives exhibited only moderate activity in influenza infected cells.⁴⁵ This disparity between the inhibition of the enzyme and the antiviral effectiveness appears to be a common issue among structurally related compounds with carboxylic acid moieties. This is likely attributed to their low membrane permeability, a consequence of their high polar nature.⁴⁹ This research showed that the presence of carboxylic acid groups as a MBP could pose challenges in drug development due to associated pharmacokinetic liabilities.⁵¹⁻⁵³

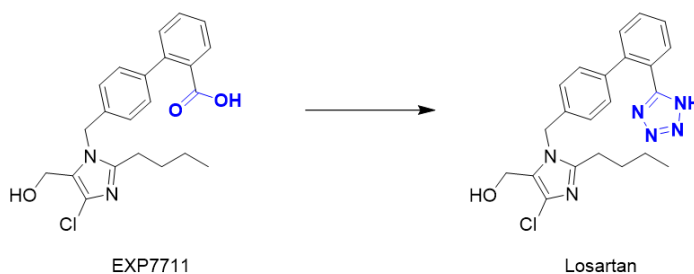
To overcome these challenges, substituting the carboxylic acid group with another metal-binding functional group, which offers similar biochemical interactions but possess different

physicochemical properties, is recommended.⁵³⁻⁵⁴ This strategy entails broadening the scope of novel MBP warheads and re-evaluating current MBPs to refine the existing MBP library.⁵³⁻⁵⁴ Consequently, a major theme of this dissertation is on augmenting the diversity of MBP fragments and designing alternative MBPs that have improved pharmacokinetic characteristics, and aiming to utilize these MBPs in the development of metalloenzyme inhibitors. To achieve these goals, two unique approaches are introduced and will be detailed in subsequent sections.

1.4 Bioisosterism

Bioisosterism has been a longstanding strategy in drug design and continues to be a crucial element in modern medicinal chemistry practices. The term “isostere” was originally recognized by Irving Langmuir in 1919, referring to compounds or groups of atoms with the same number of atoms and electrons such as N₂ and CO.⁵⁵⁻⁵⁷ Today, a broader concept of bioisosterism has evolved to include single atoms, functional groups, or entire molecules that exhibit similar volume, shape, and/or physicochemical properties, producing broadly similar biological effects.⁵⁸ These entities are frequently employed to improve pharmacokinetic properties including oral bioavailability, membrane permeability, and absorption, distribution, metabolism, and excretion (ADME) of drug candidates.⁵⁹ For example, the tetrazole moiety was utilized as a carboxylic acid isostere to develop nonpeptidic angiotensin II type 1 (AT1) receptor antagonists (Figure 1.6).⁶⁰⁻⁶¹ While both carboxylic acid and tetrazole moieties exhibited potent biological activity in vitro, only the tetrazole derivative, Losartan, was found to be effective after oral administration. However, the effectiveness of bioisosteres cannot always be guaranteed and is often context-dependent, relying on less exact structural or physicochemical mimicry to achieve the desired biological effect.^{16, 61-62}

Recent investigations in our laboratory have sought to incorporate the concept of isosteric replacement into the realm of metalloenzyme FBDD.^{53-54, 63-64} Metal-binding isosteres (MBIs) combine the metal-binding features of MBPs with the principles of isosteres/bioisosteres to produce ligands with even greater chemical diversity and potentially improved pharmacokinetic properties of MBPs. Two prior studies have examined MBIs derived from the picolinic acid MBP, examining carboxylic acid isosteres and pyridine ring isosteres of picolinic acid (Figure 1.7).^{53, 64} These studies demonstrated MBIs possess metal-binding ability and their ability to inhibit metalloenzymes, while having a pronounced influence on physicochemical properties of the resulting ligands. Consequently, isosteric replacement combined with MBPs has the potential to be a valuable approach to improving the drug-likeness of small molecule inhibitors of metalloenzyme.



Compound	pK_a estimated	$IC_{50}^{[a]}$ [μM]	Dose ^[b] [$mg\ kg^{-1}$]	
			iv	po
EXP7711	5	0.23	3	11
Losartan	5-6	0.019	0.80	0.59

Figure 1.6. Representation of isosteric replacement. In this example, triazole was introduced as a carboxylic acid isostere in the design of AT1 receptor antagonists (both highlighted in blue). Both compounds demonstrated potent in vitro biological activity, but the tetrazole derivative, Losartan, achieved a more effective oral dose compared to the original molecule. ^[a] Inhibition of specific binding of angiotensin II (2 nM) to rat adrenal cortical microsomes. ^[b] Intravenous (iv) and oral (po) dose at which statistically significant drops in blood pressure were observed (> 15 mm Hg) in renal hypertensive rats. Adapted from references 61 and 62.

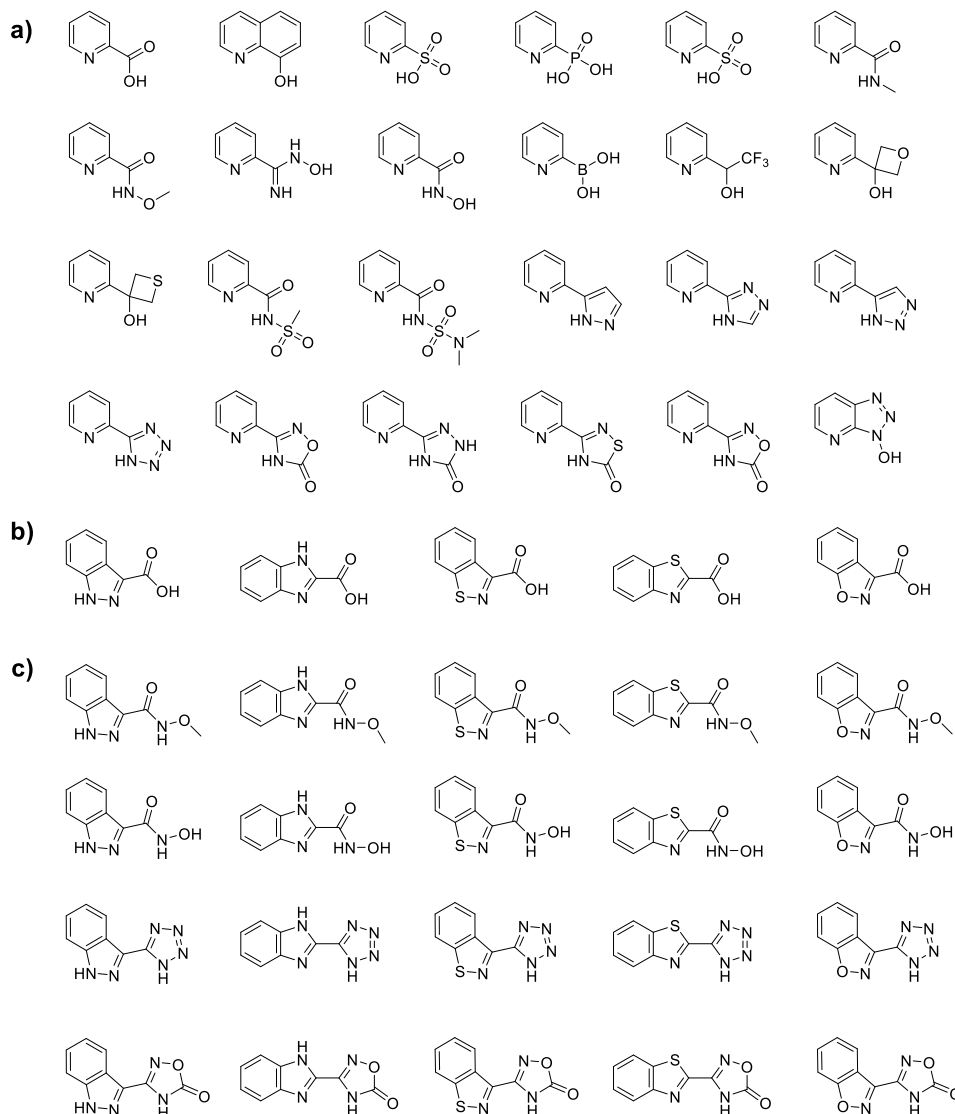
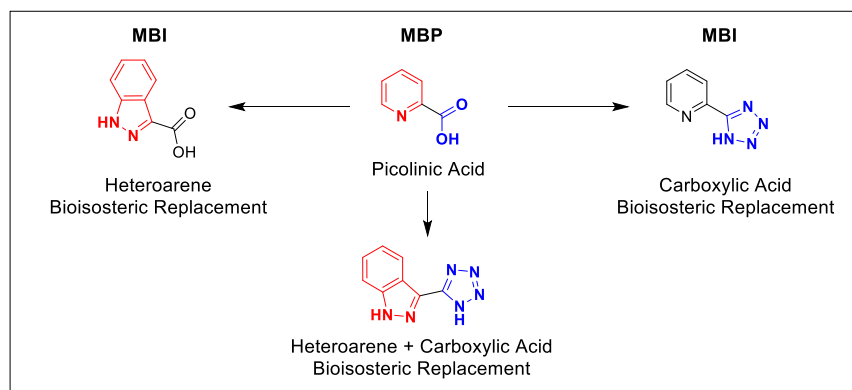


Figure 1.7. Isosteric replacement on picolinic acid has successfully developed into MBIs. Each coordinating group was replaced with a) carboxylic acid isosteres, b) heteroarene isosteres, and c) both carboxylic acid and heteroarene isosteres, respectively. These MBIs showed a broad range of physicochemical properties (i.e., pK_a and $\log P$) with decent metalloenzyme inhibitory activity.

1.5 Bioinorganic Model Complexes

In the study of metalloproteins, synthetic modeling approaches have been extensively used to understand structure, properties, function, and mechanism of metalloenzymes. Specifically, metal complexes designed to mimic metalloenzyme active sites undergo detailed characterization, providing comprehensive chemical insights into reactivity, coordination chemistry, electronic structures, and reaction mechanisms.⁶⁵⁻⁶⁷ This approach has benefits over direct studies of the enzymes themselves, including facile synthetic modification and characterization, and the ability to study intermediates that may be difficult to isolate in the biological system.⁶⁸ For all of these reasons, the use of model complexes have proven invaluable, from understanding the reversible oxygen binding by hemoglobin⁶⁹ to unraveling the mechanisms of oxidases⁷⁰ and nitrogenases.⁷¹

The core principle of bioinorganic model chemistry involves the design and synthesis of ligand systems to reproduce the first coordination sphere of metalloenzyme active sites.⁶⁸ Tris(pyrazolyl)borate complexes of zinc and its derivative complexes have been well established as versatile model system to mimic the active site of several metalloenzymes including carbonic anhydrase,⁷²⁻⁷³ matrix metalloproteinases (MMPs),⁷⁴⁻⁷⁶ and liver alcohol dehydrogenases.⁷⁷ For instance, previous work by Vahrenkamp and co-workers demonstrated that the tris(pyrazolyl)borate complexes of zinc (e.g., $[(\text{Tp}^{\text{t-Bu,Me}})\text{Zn}(\text{OH})]$ ($\text{Tp}^{\text{t-Bu,Me}}$ = hydrotris(5,3-methyl-*tert*-butylpyrazolyl) borate) could provide a structural and functional model of tris(histidine) active sites of hydrolytic Zn(II)-dependent metalloenzymes including carbonic anhydrases and MMPs.^{72, 74} The model complexes have tetrahedral coordination with three N-heterocycles and one OH ion as ligand, mimicking tris(histidine) active sites of the hydrolytic Zn(II)-dependent metalloenzymes (Figure 1.8).⁷² In one example, the $[(\text{Tp}^{\text{t-Bu,Me}})\text{Zn}(\text{OH})]$ complex was shown to perform the reversible uptake of CO₂ via an unstable bicarbonate complex,

which served as a functional analogy of carbonic anhydrase.⁷² This suggests that the model systems are suitable for elucidating metal-ligand interactions in metalloenzymes as well as providing basis for mechanistic studies.⁷⁸

In an ongoing research effort to model metal-ligand interactions in metalloenzymes, our laboratory have synthesized a series of $[(\text{Tp}^{\text{Ph,Me}})\text{Zn}(\text{OH})]$ ($\text{Tp}^{\text{Ph,Me}}$ = hydrotris(5,3-methylphenylpyrazolyl) borate) complexes as an adequate model for the MMP zinc active site (Figure 1.8).⁶⁸ In this work, the zinc complex $[(\text{Tp}^{\text{Ph,Me}})\text{Zn}(\text{OH})]$ combined with acetohydroxamic acid revealed a five-coordinate zinc center bound by the three nitrogen atoms of the $\text{Tp}^{\text{Ph,Me}}$ ligand and the two oxygen atoms of the hydroxamate. An overlay of the structure of the zinc center in $[(\text{Tp}^{\text{Ph,Me}})\text{Zn}(\text{acetohydroxamate})]$ indicates that the coordination geometry closely resembles that in enzyme-hydroxamate complexes of zinc-containing matrix metalloproteinases.⁶⁸

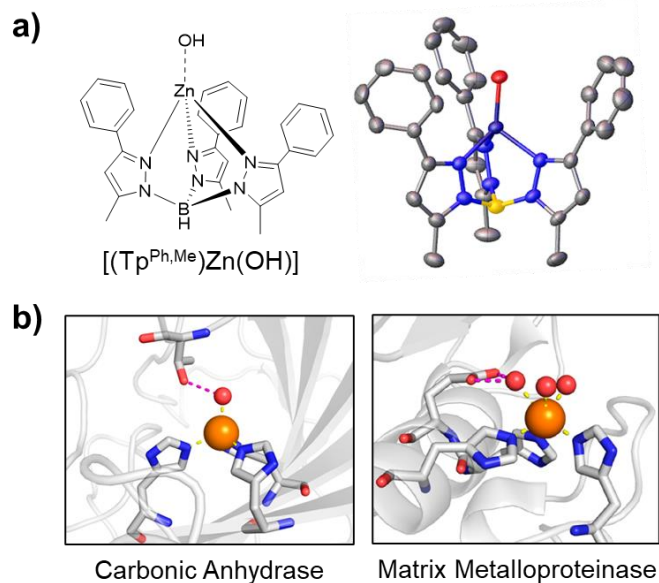


Figure 1.8. a) $[(\text{Tp}^{\text{Ph,Me}})\text{Zn}(\text{OH})]$ as a bioinorganic model system of hydrolytic Zn(II)-dependent metalloenzymes. Chemical structures (*Left*) and X-ray crystallographic (*Right*) structure of $[(\text{Tp}^{\text{Ph,Me}})\text{Zn}(\text{OH})]$. b) X-ray crystallographic structures of the active site of carbonic anhydrase (*Left*) (PDB: 1CA2) and MMP (*Right*) (PDB: 2OXU). The tetrahedral coordination geometry shown in the tris(pyrazolyl)borate complexes mimics three coordination sites occupied by protein residues such as tris-histidine shown in carbonic anhydrase and MMP. This bioinorganic model complexes provide insights into diverse coordination motifs and contribute to understanding metalloenzyme active sites.

Our laboratory has employed the $[(\text{Tp}^{\text{Ph,Me}})\text{Zn}(\text{OH})]$ model system to gain understanding about the metal-binding ability and coordination chemistry of MBPs and MBIs.^{68, 79-80} The model system readily forms complexes with monoanionic MBPs and MBIs, facilitating structural characterization by X-ray small molecule crystallography. Detailed structural information enables us to explore diverse binding modes of donor atoms, enriching our understanding of inhibitor-protein interactions. However, it is important to recognize the limitations of these models. Their simplicity, while advantageous for certain studies, may overlook the complexities of biological systems, such as second coordination sphere effects (hydrogen bonding, electrostatic interactions, hydrophobic effects, etc.). In addition, despite the broad use of the $[(\text{Tp}^{\text{Ph,Me}})\text{Zn}(\text{OH})]$ model system, few studies have looked at other spectator ligands (i.e., ligands other than $\text{Tp}^{\text{Ph,Me}}$) or metal ions beyond Zn(II) to examine metal-binding interactions and other characteristics of MBPs and MBIs.⁸¹ This highlights the need for developing alternative bioinorganic systems to broaden our understanding of MBPs and MBIs in metalloenzyme mimetics.

1.6 Scope of this Dissertation

This dissertation focuses on the comprehensive exploration and expansion of a fragment library to broaden the scope of MBPs/MBIs available for lead development. It introduces MBIs as a strategy to diversify the fragment library for metalloenzyme inhibition, utilizing isosteric replacements of 8-hydroxyquinoline to enhance the potency and selectivity of drug-target interactions. Additionally, bioinorganic model complexes are explored to study the structural and electronic characteristics of MBIs. The strategic design of thioamide, thiourea, and thiocarbamate MBPs is discussed to address the challenges of thiol-based MBPs, specifically against Zn(II)-dependent enzymes. The dissertation also underscores the identification and development of novel

small molecule inhibitors against Cu-only Superoxide Dismutase (SOD5), advancing antifungal agent discovery. Several tools and methods detailed facilitate the creation and screening of augmented fragment libraries, aiding in the identification of hit compounds and contributing to the broader landscape of metalloenzyme drug discovery.

Chapter 2 discusses the development of a new fragment library through the isosteric replacement of 8-hydroxyquinoline (8-HQ). The quinoline pharmacophore and its bioisosteres serve as important building blocks in the modulation of drug-target interactions. The study of 8-HQ and its MBIs ventures into uncharted biochemical space and may improve potency and selectivity in FBDD. A detailed examination of their coordination chemistry, physicochemical properties, and metalloenzyme inhibition activity is conducted, aiming to establish drug-like profiles.

Chapter 3 introduces an alternative bioinorganic model complex, $[M(\text{TPA})(\text{MBI})]^+$ ($M = \text{Ni(II)}$ and Co(II) , TPA = tris(2-pyridylmethyl)amine), designed to study structural and electronic characteristics of MBIs. Through meticulous characterization of picolinic acid and its known MBIs, the model complex provides a detailed understanding of the properties associated with each MBI, shedding light on both similarities and distinctions from the parent MBP. Furthermore, the introduction of a more conventional model complex, $[(\text{Tp}^{\text{Ph,Me}})\text{Co}(\text{MBI})]$ ($\text{Tp}^{\text{Ph,Me}} = \text{hydrotris}(3,5\text{-phenylmethylpyrazolyl})\text{borate}$) adds another layer of insight, leading to a thorough discussion on the limitations and merits of these two model systems.

Chapter 4 describes thioamide, thiourea, and thiocarbamate MBPs as potent warheads, strategically designed to mask the typical reactivity of conventional thiol MBPs. Thiol-based MBPs, renowned for their potency against Zn(II)-dependent metalloenzymes, present challenges related to metabolic liabilities and chemical reactivity. This chapter propose and demonstrates a

facile approach to introducing masked thiols, examining their reactivity, bioactivity, and structural studies. The findings reveal their potentials as ligands for Zn(II)-dependent metalloenzymes including human carbonic anhydrase II and matrix metalloproteinase-2.

Chapter 5 pursues the discovery of small molecule inhibitors targeting a novel antifungal target, SOD5. SOD5, a distinctive Cu-dependent enzyme crucial for fungal pathogenicity, stands out as a promising antifungal target. Screening ~400 fragments led to the identification of novel warheads for SOD5. From these hits, potential lead compounds are prepared, which were evaluated in biochemical assays against SOD5, and their bioactivity is analyzed to establish a preliminary structure-activity relationship (SAR). This chapter contributes to the ongoing quest for potential antifungal agents.

1.7 Acknowledgments

Chapter 1, in part, is a reprint of the material as it appears in “Evaluating Metal–Ligand Interactions of Metal-Binding Isosteres Using Model Complexes.” *Inorg. Chem.*, **2021**, 60, 22, 17161. The dissertation author was a primary author of this paper and gratefully acknowledges the contributions of coauthors Kathleen E. Prosser, Mark Kalaj, Johannes Karges, Benjamin Dick, and Seth M. Cohen.

1.8 References

1. Chen, A. Y.; Adamek, R. N.; Dick, B. L.; Credille, C. V.; Morrison, C. N.; Cohen, S. M., Targeting Metalloenzymes for Therapeutic Intervention. *Chem. Rev.* **2019**, *119* (2), 1323-1455.
2. Laity, J. H.; Lee, B. M.; Wright, P. E., Zinc finger proteins: new insights into structural and functional diversity. *Curr. Opin. Struct. Biol.* **2001**, *11* (1), 39-46.

3. Solomon, E. I.; Heppner, D. E.; Johnston, E. M.; Ginsbach, J. W.; Cirera, J.; Qayyum, M.; Kieber-Emmons, M. T.; Kjaergaard, C. H.; Hadt, R. G.; Tian, L., Copper Active Sites in Biology. *Chem. Rev.* **2014**, *114* (7), 3659-3853.
4. Laronha, H.; Caldeira, J., Structure and Function of Human Matrix Metalloproteinases. *Cells* **2020**, *9* (5), 1076.
5. Murphy, G., Riding the metalloproteinase roller coaster. *J. Biol. Chem.* **2017**, *292* (19), 7708-7717.
6. Lee, S.-L.; Chau, G.-Y.; Yao, C.-T.; Wu, C.-W.; Yin, S.-J., Functional Assessment of Human Alcohol Dehydrogenase Family in Ethanol Metabolism: Significance of First-Pass Metabolism. *Alcohol. Clin. Exp. Res.* **2006**, *30* (7), 1132-1142.
7. Sánchez-Ferrer, Á.; Neptuno Rodríguez-López, J.; García-Cánovas, F.; García-Carmona, F., Tyrosinase: a comprehensive review of its mechanism. *BBA-Protein. Struct. M.* **1995**, *1247* (1), 1-11.
8. Learmonth, D. A.; Kiss, L. E.; Soares-da-Silva, P., The Chemistry of Catechol-O-Methyltransferase Inhibitors. In *International Review of Neurobiology*, Nissinen, E., Ed. Academic Press: 2010; Vol. 95, pp 119-162.
9. Shen, M.; Pan, P.; Li, Y.; Li, D.; Yu, H.; Hou, T., Farnesyltransferase and geranylgeranyltransferase I: structures, mechanism, inhibitors and molecular modeling. *Drug Discov. Today* **2015**, *20* (2), 267-276.
10. Azadmanesh, J.; Borgstahl, G. E. O., A Review of the Catalytic Mechanism of Human Manganese Superoxide Dismutase. *Antioxidants* **2018**, *7* (2).
11. Yang, Y.; Hu, X.-Q.; Li, Q.-S.; Zhang, X.-X.; Ruan, B.-F.; Xu, J.; Liao, C., Metalloprotein Inhibitors for the Treatment of Human Diseases. *Curr. Top. Med. Chem.* **2016**, *16* (4), 384-396.

12. Solomon, E. I.; Sundaram, U. M.; Machonkin, T. E., Multicopper Oxidases and Oxygenases. *Chem. Rev.* **1996**, *96* (7), 2563-2606.
13. Andreini, C.; Bertini, I.; Cavallaro, G.; Holliday, G. L.; Thornton, J. M., Metal ions in biological catalysis: from enzyme databases to general principles. *J. Biol. Inorg. Chem.* **2008**, *13* (8), 1205-1218.
14. Waldron, K. J.; Rutherford, J. C.; Ford, D.; Robinson, N. J., Metalloproteins and metal sensing. *Nature* **2009**, *460* (7257), 823-830.
15. Cohen, S. M., A Bioinorganic Approach to Fragment-Based Drug Discovery Targeting Metalloenzymes. *Acc. Chem. Res.* **2017**, *50* (8), 2007-2016.
16. Lassalas, P.; Gay, B.; Lasfargeas, C.; James, M. J.; Tran, V.; Vijayendran, K. G.; Brunden, K. R.; Kozlowski, M. C.; Thomas, C. J.; Smith, A. B., 3rd; Huryn, D. M.; Ballatore, C., Structure Property Relationships of Carboxylic Acid Isosteres. *J. Med. Chem.* **2016**, *59* (7), 3183-3203.
17. Lassila, T.; Hokkanen, J.; Aatsinki, S. M.; Mattila, S.; Turpeinen, M.; Tolonen, A., Toxicity of Carboxylic Acid-Containing Drugs: The Role of Acyl Migration and CoA Conjugation Investigated. *Chem. Res. Toxicol.* **2015**, *28* (12), 2292-2303.
18. Sawamura, R.; Okudaira, N.; Watanabe, K.; Murai, T.; Kobayashi, Y.; Tachibana, M.; Ohnuki, T.; Masuda, K.; Honma, H.; Kurihara, A.; Okazaki, O., Predictability of Idiosyncratic Drug Toxicity Risk for Carboxylic Acid-containing Drugs Based on the Chemical Stability of Acyl Glucuronide. *Drug Metab. Dispos.* **2010**, *38* (10), 1857-1864.
19. Shen, S.; Kozikowski, A. P., Why Hydroxamates May Not Be the Best Histone Deacetylase Inhibitors--What Some May Have Forgotten or Would Rather Forget? *ChemMedChem* **2016**, *11* (1), 15-21.

20. Munday, R., Toxicity of Thiols and Disulphides: Involvement of Free-radical Species. *Free Radic. Biol. Med.* **1989**, 7 (6), 659-673.
21. Elliott, T. S.; Slowey, A.; Ye, Y.; Conway, S. J., The Use of Phosphate Bioisosteres in Medicinal Chemistry and Chemical Biology. *MedChemComm* **2012**, 3 (7), 735-751.
22. Kirsch, P.; Hartman, A. M.; Hirsch, A. K. H.; Empting, M., Concepts and Core Principles of Fragment-Based Drug Design. *Molecules* **2019**, 24 (23), 4309.
23. Erlanson, D. A.; Fesik, S. W.; Hubbard, R. E.; Jahnke, W.; Jhoti, H., Twenty years on: the impact of fragments on drug discovery. *Nat. Rev. Drug Discov.* **2016**, 15 (9), 605-619.
24. Lipinski, C. A.; Lombardo, F.; Dominy, B. W.; Feeney, P. J., Experimental And computational Approaches To Estimate Solubility And Permeability In Drug Discovery And Development Settings. *Adv. Drug Deliv. Rev.* **2001**, 46 (1), 3-26.
25. Köster, H.; Craan, T.; Brass, S.; Herhaus, C.; Zentgraf, M.; Neumann, L.; Heine, A.; Klebe, G., A Small Nonrule of 3 Compatible Fragment Library Provides High Hit Rate of Endothiapepsin Crystal Structures with Various Fragment Chemotypes. *J. Med. Chem.* **2011**, 54 (22), 7784-7796.
26. Hopkins, A. L.; Groom, C. R.; Alex, A., Ligand efficiency: a useful metric for lead selection. *Drug Discov. Today* **2004**, 9 (10), 430-431.
27. Murray, C. W.; Rees, D. C., The rise of fragment-based drug discovery. *Nat. Chem.* **2009**, 1 (3), 187-192.
28. Bon, M.; Bilsland, A.; Bower, J.; McAulay, K., Fragment-based drug discovery—the importance of high-quality molecule libraries. *Molecular Oncology* **2022**, 16 (21), 3761-3777.
29. Li, Q., Application of Fragment-Based Drug Discovery to Versatile Targets. *Front. Mol. Biosci.* **2020**, 7.

30. Ferenczy, G. G.; Keserű, G. M., How Are Fragments Optimized? A Retrospective Analysis of 145 Fragment Optimizations. *J. Med. Chem.* **2013**, *56* (6), 2478-2486.
31. Scott, D. E.; Coyne, A. G.; Hudson, S. A.; Abell, C., Fragment-Based Approaches in Drug Discovery and Chemical Biology. *Biochemistry* **2012**, *51* (25), 4990-5003.
32. Zhang, C.; Ibrahim, P. N.; Zhang, J.; Burton, E. A.; Habets, G.; Zhang, Y.; Powell, B.; West, B. L.; Matusow, B.; Tsang, G.; Shellooe, R.; Carias, H.; Nguyen, H.; Marimuthu, A.; Zhang, K. Y. J.; Oh, A.; Bremer, R.; Hurt, C. R.; Artis, D. R.; Wu, G.; Nespi, M.; Spevak, W.; Lin, P.; Nolop, K.; Hirth, P.; Tesch, G. H.; Bollag, G., Design and pharmacology of a highly specific dual FMS and KIT kinase inhibitor. *PNAS* **2013**, *110* (14), 5689-5694.
33. Tsai, J.; Lee, J. T.; Wang, W.; Zhang, J.; Cho, H.; Mamo, S.; Bremer, R.; Gillette, S.; Kong, J.; Haass, N. K.; Sproesser, K.; Li, L.; Smalley, K. S. M.; Fong, D.; Zhu, Y.-L.; Marimuthu, A.; Nguyen, H.; Lam, B.; Liu, J.; Cheung, I.; Rice, J.; Suzuki, Y.; Luu, C.; Settachatgul, C.; Shellooe, R.; Cantwell, J.; Kim, S.-H.; Schlessinger, J.; Zhang, K. Y. J.; West, B. L.; Powell, B.; Habets, G.; Zhang, C.; Ibrahim, P. N.; Hirth, P.; Artis, D. R.; Herlyn, M.; Bollag, G., Discovery of a selective inhibitor of oncogenic B-Raf kinase with potent antimelanoma activity. *PNAS* **2008**, *105* (8), 3041-3046.
34. Souers, A. J.; Levenson, J. D.; Boghaert, E. R.; Ackler, S. L.; Catron, N. D.; Chen, J.; Dayton, B. D.; Ding, H.; Enschede, S. H.; Fairbrother, W. J.; Huang, D. C. S.; Hymowitz, S. G.; Jin, S.; Khaw, S. L.; Kovar, P. J.; Lam, L. T.; Lee, J.; Maecker, H. L.; Marsh, K. C.; Mason, K. D.; Mitten, M. J.; Nimmer, P. M.; Oleksijew, A.; Park, C. H.; Park, C.-M.; Phillips, D. C.; Roberts, A. W.; Sampath, D.; Seymour, J. F.; Smith, M. L.; Sullivan, G. M.; Tahir, S. K.; Tse, C.; Wendt, M. D.; Xiao, Y.; Xue, J. C.; Zhang, H.; Humerickhouse, R. A.; Rosenberg, S. H.; Elmore, S. W.,

ABT-199, a potent and selective BCL-2 inhibitor, achieves antitumor activity while sparing platelets. *Nat. Med.* **2013**, *19* (2), 202-208.

35. Murray, C. W.; Newell, D. R.; Angibaud, P., A successful collaboration between academia, biotech and pharma led to discovery of erdafitinib, a selective FGFR inhibitor recently approved by the FDA. *Med. Chem. Commun.* **2019**, *10* (9), 1509-1511.

36. Wang, T.; Wu, M.-B.; Chen, Z.-J.; Chen, H.; Lin, J.-P.; Yang, L.-R., Fragment-Based Drug Discovery and Molecular Docking in Drug Design. *Curr. Pharm. Biotechno.* **2015**, *16* (1), 11-25.

37. Agrawal, A.; Johnson, S. L.; Jacobsen, J. A.; Miller, M. T.; Chen, L.-H.; Pellecchia, M.; Cohen, S. M., Chelator Fragment Libraries for Targeting Metalloproteinases. *ChemMedChem* **2010**, *5* (2), 195-199.

38. Jacobsen, J. A.; Fullagar, J. L.; Miller, M. T.; Cohen, S. M., Identifying Chelators for Metalloprotein Inhibitors Using a Fragment-Based Approach. *J. Med. Chem.* **2011**, *54* (2), 591-602.

39. Credille, C. V.; Chen, Y.; Cohen, S. M., Fragment-Based Identification of Influenza Endonuclease Inhibitors. *J. Med. Chem.* **2016**, *59* (13), 6444-6454.

40. Perez, C.; Barkley-Levenson, A. M.; Dick, B. L.; Glatt, P. F.; Martinez, Y.; Siegel, D.; Momper, J. D.; Palmer, A. A.; Cohen, S. M., Metal-Binding Pharmacophore Library Yields the Discovery of a Glyoxalase 1 Inhibitor. *J. Med. Chem.* **2019**, *62* (3), 1609-1625.

41. Perez, C.; Li, J.; Parlati, F.; Rouffet, M.; Ma, Y.; Mackinnon, A. L.; Chou, T.-F.; Deshaies, R. J.; Cohen, S. M., Discovery of an Inhibitor of the Proteasome Subunit Rpn11. *J. Med. Chem.* **2017**, *60* (4), 1343-1361.

42. Prosser, K. E.; Kohlbrand, A. J.; Seo, H.; Kalaj, M.; Cohen, S. M., 19F-Tagged metal binding pharmacophores for NMR screening of metalloenzymes. *Chem. Comm.* **2021**, *57* (40), 4934-4937.
43. Morrison, C. N.; Prosser, K. E.; Stokes, R. W.; Cordes, A.; Metzler-Nolte, N.; Cohen, S. M., Expanding Medicinal Chemistry Into 3D space: Metallofragments As 3D Scaffolds For Fragment-Based Drug Discovery. *Chem. Sci.* **2020**, *11* (5), 1216-1225.
44. Adamek, R. N.; Suire, C. N.; Stokes, R. W.; Brizuela, M. K.; Cohen, S. M.; Leissring, M. A., Hydroxypyridinethione Inhibitors of Human Insulin-Degrading Enzyme. *ChemMedChem* **2021**, *16* (11), 1776-1788.
45. Credille, C. V.; Morrison, C. N.; Stokes, R. W.; Dick, B. L.; Feng, Y.; Sun, J.; Chen, Y.; Cohen, S. M., SAR Exploration of Tight-Binding Inhibitors of Influenza Virus PA Endonuclease. *J. Med. Chem.* **2019**, *62* (21), 9438-9449.
46. Credille, C. V.; Dick, B. L.; Morrison, C. N.; Stokes, R. W.; Adamek, R. N.; Wu, N. C.; Wilson, I. A.; Cohen, S. M., Structure–Activity Relationships in Metal-Binding Pharmacophores for Influenza Endonuclease. *J. Med. Chem.* **2018**, *61* (22), 10206-10217.
47. Bauman, J. D.; Patel, D.; Baker, S. F.; Vijayan, R. S. K.; Xiang, A.; Parhi, A. K.; Martínez-Sobrido, L.; LaVoie, E. J.; Das, K.; Arnold, E., Crystallographic Fragment Screening and Structure-Based Optimization Yields a New Class of Influenza Endonuclease Inhibitors. *ACS Chem. Biol.* **2013**, *8* (11), 2501-2508.
48. Jones, J. C.; Marathe, B. M.; Lerner, C.; Kreis, L.; Gasser, R.; Pascua, P. N. Q.; Najera, I.; Govorkova, E. A., A Novel Endonuclease Inhibitor Exhibits Broad-Spectrum Anti-Influenza Virus Activity In Vitro. *Antimicrob. Agents Chemother.* **2016**, *60* (9), 5504-5514.

49. Miyagawa, M.; Akiyama, T.; Taoda, Y.; Takaya, K.; Takahashi-Kageyama, C.; Tomita, K.; Yasuo, K.; Hattori, K.; Shano, S.; Yoshida, R.; Shishido, T.; Yoshinaga, T.; Sato, A.; Kawai, M., Synthesis and SAR Study of Carbamoyl Pyridone Bicycle Derivatives as Potent Inhibitors of Influenza Cap-dependent Endonuclease. *J. Med. Chem.* **2019**, *62* (17), 8101-8114.
50. Ng, K. E., Xofluza (Baloxavir Marboxil) for the Treatment Of Acute Uncomplicated Influenza. *P. T.* **2019**, *44* (1), 9-11.
51. Lassila, T.; Hokkanen, J.; Aatsinki, S.-M.; Mattila, S.; Turpeinen, M.; Tolonen, A., Toxicity of Carboxylic Acid-Containing Drugs: The Role of Acyl Migration and CoA Conjugation Investigated. *Chem. Res. Toxicol.* **2015**, *28* (12), 2292-2303.
52. Pajouhesh, H.; Lenz, G. R., Medicinal chemical properties of successful central nervous system drugs. *NeuroRx* **2005**, *2* (4), 541-553.
53. Dick, B. L.; Cohen, S. M., Metal-Binding Isosteres as New Scaffolds for Metalloenzyme Inhibitors. *Inorg. Chem.* **2018**, *57* (15), 9538-9543.
54. Stokes, R. W.; Kohlbrand, A. J.; Seo, H.; Sankaran, B.; Karges, J.; Cohen, S. M., Carboxylic Acid Isostere Derivatives of Hydroxypyridinones as Core Scaffolds for Influenza Endonuclease Inhibitors. *ACS Med. Chem. Lett.* **2023**, *14* (1), 75-82.
55. Langmuir, I., ISOMORPHISM, ISOSTERISM AND COVALENCE. *J. Am. Chem. Soc.* **1919**, *41* (10), 1543-1559.
56. Patani, G. A.; LaVoie, E. J., Bioisosterism: A Rational Approach in Drug Design. *Chem. Rev.* **1996**, *96* (8), 3147-3176.
57. Dick, A.; Cocklin, S., Bioisosteric Replacement as a Tool in Anti-HIV Drug Design. *Pharmaceuticals* **2020**, *13* (3), 36.

58. Burger, A., Isosterism and Bioisosterism in Drug Design. *In Progress in Drug Research/Fortschritte der Arzneimittelforschung/Progrès des Recherches Pharmaceutique* **1991**, Birkhäuser: Basel, Switzerland.
59. Patani, G. A.; LaVoie, E. J., Bioisosterism: A Rational Approach in Drug Design. *Chem. Rev.* **1996**, *96* (8), 3147-3176.
60. Carini, D. J.; Duncia, J. V.; Aldrich, P. E.; Chiu, A. T.; Johnson, A. L.; Pierce, M. E.; Price, W. A.; Santella, J. B., 3rd; Wells, G. J.; Wexler, R. R., Nonpeptide angiotensin II receptor antagonists: the discovery of a series of N-(biphenylmethyl)imidazoles as potent, orally active antihypertensives. *J. Med. Chem.* **1991**, *34* (8), 2525-2547.
61. Ballatore, C.; Huryn, D. M.; Smith, A. B., Carboxylic acid (bio)isosteres in drug design. *ChemMedChem* **2013**, *8* (3), 385-395.
62. Meanwell, N. A., Synopsis of Some Recent Tactical Application of Bioisosteres in Drug Design. *J. Med. Chem.* **2011**, *54* (8), 2529-2591.
63. Adamek, R. N.; Credille, C. V.; Dick, B. L.; Cohen, S. M., Isosteres of hydroxypyridinethione as drug-like pharmacophores for metalloenzyme inhibition. *J. Biol. Inorg. Chem.* **2018**, *23* (7), 1129-1138.
64. Dick, B. L.; Patel, A.; Cohen, S. M., Effect of heterocycle content on metal binding isostere coordination. *Chem. Sci.* **2020**, *11* (26), 6907-6914.
65. Sun Cao, P.; Sommer, R. D.; Grice, K. A., Structural comparison of suberanihydroxamic acid (SAHA) and other zinc-enzyme inhibitors bound to a monomeric zinc species. *Polyhedron* **2016**, *114*, 344-350.
66. Tovmasyan, A.; Carballal, S.; Ghazaryan, R.; Melikyan, L.; Weitner, T.; Maia, C. G. C.; Reboucas, J. S.; Radi, R.; Spasojevic, I.; Benov, L.; Batinic-Haberle, I., Rational Design of

Superoxide Dismutase (SOD) Mimics: The Evaluation of the Therapeutic Potential of New Cationic Mn Porphyrins with Linear and Cyclic Substituents. *Inorg. Chem.* **2014**, *53* (21), 11467-11483.

67. Tekeste, T.; Vahrenkamp, H., Modeling Zinc Enzyme Inhibition with Functional Thiolate Ligands. *Inorg. Chem.* **2006**, *45* (26), 10799-10806.

68. Puerta, D. T.; Cohen, S. M., Elucidating drug-metalloprotein interactions with tris(pyrazolyl)borate model complexes. *Inorg. Chem.* **2002**, *41* (20), 5075-82.

69. Collman, J. P., Synthetic models for the oxygen-binding hemoproteins. *Acc. Chem. Res.* **1977**, *10* (7), 265-272.

70. Tshuva, E. Y.; Lee, D.; Bu, W.; Lippard, S. J., Catalytic Oxidation by a Carboxylate-Bridged Non-Heme Diiron Complex. *J. Am. Chem. Soc.* **2002**, *124* (11), 2416-2417.

71. Hauser, C.; Bill, E.; Holm, R. H., Single- and Double-Cubane Clusters in the Multiple Oxidation States $[\text{VFe}_3\text{S}_4]^{3+,2+,1+}$. *Inorg. Chem.* **2002**, *41* (6), 1615-1624.

72. Alsfasser, R.; Ruf, M.; Vahrenkamp, H., Ein L_3ZnOH -Komplex als funktionelles Modell des Enzyms Carboanhydrase. *Chem. Ber.* **1993**, *126* (3), 703-710.

73. Kimblin, C.; Parkin, G., Comparison of Zinc and Cadmium Coordination Environments in Synthetic Analogues of Carbonic Anhydrase: Synthesis and Structure of $\{[\text{Pim}^{\text{Pri,But}}]\text{Cd}(\text{OH}_2)(\text{OCIO}_3)\}(\text{ClO}_4)$. *Inorg. Chem.* **1996**, *35* (24), 6912-6913.

74. Ruf, M.; Weis, K.; Brasack, I.; Vahrenkamp, H., Modelling transition state analogues and enzyme-inhibitor complexes of zinc-containing class II aldolases and metalloproteases. *Inorg. Chim. Acta* **1996**, *250* (1), 271-281.

75. Puerta, D. T.; Lewis, J. A.; Cohen, S. M., New Beginnings for Matrix Metalloproteinase Inhibitors: Identification of High-Affinity Zinc-Binding Groups. *J. Am. Chem. Soc.* **2004**, *126* (27), 8388-8389.
76. Puerta, D. T.; Cohen, S. M., Examination of Novel Zinc-Binding Groups for Use in Matrix Metalloproteinase Inhibitors. *Inorg. Chem.* **2003**, *42* (11), 3423-3430.
77. Tesmer, M.; Shu, M.; Vahrenkamp, H., Sulfur-Rich Zinc Chemistry: New Tris(thioimidazolyl)hydroborate Ligands and Their Zinc Complex Chemistry Related to the Structure and Function of Alcohol Dehydrogenase. *Inorg. Chem.* **2001**, *40* (16), 4022-4029.
78. Vahrenkamp, H., Transitions, Transition States, Transition State Analogues: Zinc Pyrazolylborate Chemistry Related to Zinc Enzymes. *Acc. Chem. Res.* **1999**, *32* (7), 589-596.
79. Jacobsen, F. E.; Lewis, J. A.; Cohen, S. M., A New Role for Old Ligands: Discerning Chelators for Zinc Metalloproteinases. *J. Am. Chem. Soc.* **2006**, *128* (10), 3156-3157.
80. Puerta, D. T.; Lewis, J. A.; Cohen, S. M., New beginnings for matrix metalloproteinase inhibitors: identification of high-affinity zinc-binding groups. *J. Am. Chem. Soc.* **2004**, *126* (27), 8388-9.
81. Jacobsen, F. E.; Breece, R. M.; Myers, W. K.; Tierney, D. L.; Cohen, S. M., Model Complexes of Cobalt-Substituted Matrix Metalloproteinases: Tools for Inhibitor Design. *Inorg. Chem.* **2006**, *45* (18), 7306-7315.

Chapter 2: Developing Metal-binding Isoesters of 8-Hydroxyquinoline (8-HQ) as Metalloenzyme Inhibitor Scaffolds

2.1 Introduction

As discussed in Chapter 1, a diverse library of metal-binding pharmacophores (MBPs) has been developed in the Cohen laboratory to expand the available chemical space for targeting metalloenzymes, using a fragment-based drug discovery (FBDD) approach. Our previously reported MBP library, consisting of ~300 small molecule fragments, has been used to generate active and selective hits against a variety of metalloenzyme targets.¹ Metal-binding isosteres (MBIs) have been introduced as a new strategy to further expand the chemical space and address pharmacokinetic liabilities of MBPs.² For example, the application of isosteric replacement to the picolinic acid MBP resulted in ~50 picolinic acid MBIs.² These compounds maintain the metal coordination characteristics of the original picolinic acid MBP (based on structural characterization of bioinorganic model complexes), while altering physicochemical properties such as pK_a and $\log P$. Importantly, the MBIs exhibit inhibitory activity against several metalloenzymes that generally mirrors that of the parent picolinic acid MBP. These findings demonstrate that isosteric replacement of MBPs to produce MBIs is viable strategy to provide a novel source of metal binding functional groups and address pharmacokinetic liabilities for metalloenzyme inhibition.

Motivated by the potential of MBIs to open new avenues for exploring novel functional groups from known MBPs, Chapter 2 focuses on creating a new set of MBIs based on the 8-hydroxyquinoline (8-HQ) MBP. By extending this approach to 8-HQ, we seek to not only enrich our fragment library but also to provide a platform for uncovering new functional groups that can contribute to the rational design of metalloenzyme inhibitors. This effort reflects a strategic progression from our initial work with picolinic acid MBIs, aiming to fully exploit the capabilities of MBIs in the ongoing effort to target metalloenzymes more effectively.

8-HQ is a common scaffold found in bioactive small molecules and drugs, and has been used for iron-chelation for neuroprotection, anticancer activity, anti-HIV activity, and antifungal activity.³⁻⁴ Additionally, this motif has been applied as an MBP for metalloenzymes inhibitors including matrix metalloproteinases,⁵⁻⁶ 2-oxoglutarate (2OG)/Fe(II) dependent oxygenases,⁷⁻⁸ and aminopeptidase from *Aeromonas proteolytica* (AAP).⁹ For example, 5-carboxy-8-hydroxyquinoline was reported as a potent broad-spectrum inhibitor of the 2OG oxygenases including JmjC demethylases. However, like many MBPs, 5-carboxy-8-hydroxyquinoline suffers from low cell permeability.⁷ Furthermore, the propensity of underivatized 8-HQ to bind several different metalloenzymes can lead to undesirable off-target interactions. Indeed, various strategies, including functionalization of the molecule, molecule hybridization, and glycoconjugation have been performed to improve the selectivity and decrease toxicity of a broad range of 8-HQ-based drug candidates.¹⁰⁻¹² However, modifications of the core 8-HQ scaffold has not been widely studied in the context of metalloenzyme inhibitor development and it is unknown how changes to the molecular structure of 8-HQ will influence important parameters such as metal-binding ability and physicochemical properties.

In this chapter, a novel MBI library of 8-HQ was designed, synthesized, and characterized. In total, 30 MBIs of 8-HQ were prepared focusing on nitrogen heterocycle replacements with various ring systems. The 8-HQ MBIs described here can be categorized into four broad groups: 6,6-membered ring MBIs, 6,5-membered ring MBIs, sulfonamide MBIs, and 6,6,5-membered fused ring MBIs (Figure 2.1). Their physicochemical profiles (pK_a and $\log D_{7.4}$) were explored to gain insights about their electron donor ability and pharmacokinetic properties. The metal-binding of the MBIs was studied using a bioinorganic model system and compared to the parent 8-HQ

compound. Furthermore, the inhibition activity of MBIs against representative metalloenzymes was determined.

2.2 Library Design and 8-HQ MBI Synthesis

8-HQ binds to transition metal ions through its oxygen and nitrogen donor atoms.¹³ In the design of 8-HQ MBIs, the 5-membered chelate ring of the ligand bound to the metal was retained in the MBI design and selection. Two parts of the molecule, the quinoline ring and the hydroxyl group, were investigated for isosteric replacement (Figure 2.1). First, several different aromatic heterocyclic replacements were carried out on the quinoline ring by varying ring sizes and adding heteroatoms. The heterocyclic cores of the potential MBIs were evaluated using DrugBank¹⁴ to find drug-like fragments, which is a drug database that includes FDA-approved small-molecule drugs, as well as experimental drugs. Indole, purine, benzimidazole, and quinazoline were found as common substructures in the DrugBank database (>120 small molecules, Table 2.S1). These nitrogen heterocycles are widely used as scaffolds in drug discovery and are common motifs in FDA-approved drugs.¹⁵⁻¹⁶ Including these four scaffolds, 14 aromatic heterocycles were also considered for use as quinoline isosteres based on their structural similarity and synthetic accessibility (Table 2.S1). For the hydroxyl group replacements, sulfonamide, carbamate, carbamide, imidazole, and triazole groups were utilized. Combined, this produced a library consisting of 30 MBIs in total (Figure 2.1). Importantly, although some of these compounds, or substructures of these compounds have been reported to have biological activity,¹⁷⁻²² their use as a metal-binding scaffolds in metalloenzyme inhibitors have not been extensively investigated. Indeed, a search of the Cambridge Crystallographic Data Centre (CCDC) shows that even the fundamental coordination chemistry of most molecules described in this study have not been

described. For example, while >2300 structures containing 8-HQ bound to metals are available in the CCDC, few structures of 8-HQ MBIs have been described and at least 20 of the MBIs reported here have no entries of metal complexes in the CCDC (Table 2.S2).

MBIs **2.1**, **2.3**, **2.4**, **2.5**, **2.7**, **2.9**, **2.10**, **2.11**, **2.13**, **2.14**, **2.15**, and **2.17** were purchased from commercial vendors, while the remaining MBIs synthesized from widely available starting materials. MBIs **2.2**, **2.6**, **2.16**, and **2.25 – 2.30** were synthesized based on annulation reactions using commercially available starting materials. MBI **2.8** was prepared through methylation and deprotection of an *O*-benzyloxy-protected benzimidazole. MBI **2.12** was synthesized by deprotection of an *O*-benzyloxy-protected indole. MBIs **2.18 – 2.24** were prepared by the reaction of anilines with methyl sulfonyl chloride. The detailed synthetic procedures and the complete characterization of all synthesized MBIs can be found in the Appendix for Chapter 2.

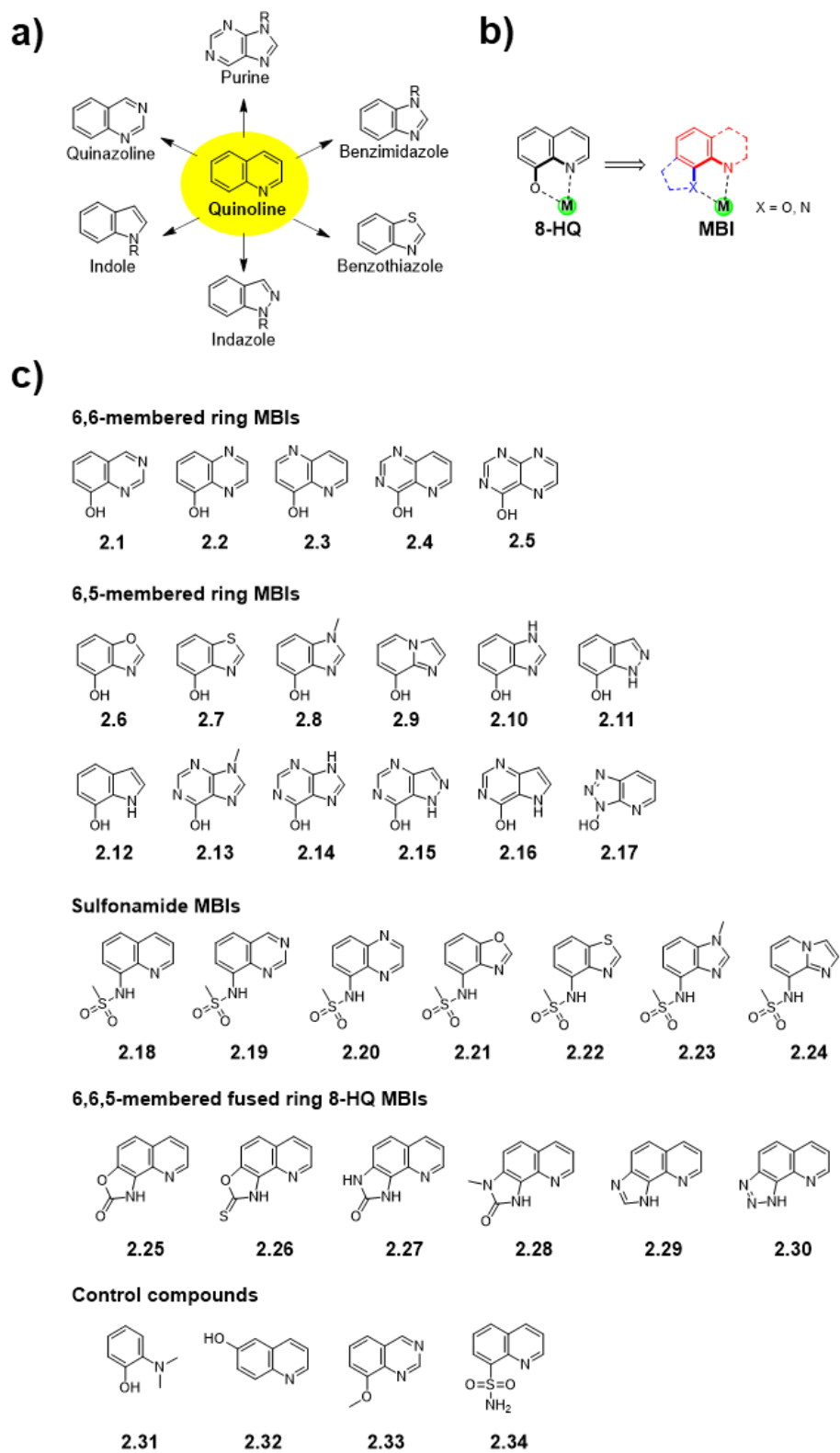


Figure 2.1. a) Quinoline and examples of its isosteres that are frequently used in drug discovery. b) The hydroxyl group (blue) and the quinoline ring scaffold (red) were replaced with various isosteres. c) Library of 8-HQ MBIs.

2.3 Physicochemical Properties Analysis

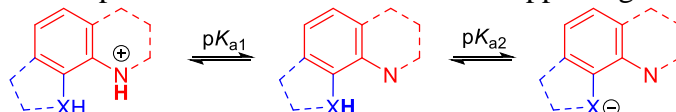
Physicochemical properties (pK_a and $\log P$) of MBIs were measured using UV-based or potentiometric methods using a SiriusT3 apparatus (Table 2.1).²³⁻²⁵ $\log D_{7.4}$ values were derived from measured pK_a and $\log P$ and $\log D_{7.4}$ values were used to gauge the lipophilicity of MBIs (Table 1). In general, for pK_a values of 8-HQ MBIs, there are two values in the range of pH 2.0 – 12.0. The first value (pK_{a1}) is related to the conjugated acid (protonated nitrogen) of the heteroaromatic ring system and the second value (pK_{a2}) corresponds to the hydroxyl group or its isosteric replacement (Table 2.1). Overall, a broad range of acidities ($pK_{a1} = 2.16 - 5.43$, $pK_{a2} = 3.34 - 11.75$) and lipophilicities ($\log D_{7.4} = -3.83 - 1.97$) were measured for the MBIs.

Physicochemical properties of 6,6-membered ring MBIs (MBIs **2.1 – 2.5**) were modulated by the presence of nitrogen atoms in the ring structure. This change was reflected in the acidity and the lipophilicity of the MBIs. Specifically, MBIs containing more nitrogen atoms had lower pK_a values indicating an increase in the acidity of the hydroxyl groups and a decrease in the basicity of the nitrogen atoms of the ring systems. In addition, significantly lower $\log D_{7.4}$ values were observed when more nitrogen atoms were added to the ring system. For example, MBI **5**, which contains the most nitrogen atoms in the ring system, showed the lowest pK_a and $\log D_{7.4}$ values in this group.

In the case of 6,5-membered ring MBIs (MBIs **2.6 – 2.17**), higher pK_{a1} values were observed for MBIs **2.8**, **2.9**, and **2.10**. These findings suggest that the heteroaromatic nitrogen atoms of MBIs **2.8**, **2.9**, and **2.10** are more basic compared to the other 6,5-membered rings. In general, the lipophilicity decreased as more heteroatoms are added to the ring system. Interestingly, this was not observed for MBI **2.7** containing the benzothiazole scaffold – the

lipophilicity of this MBI was almost identical to 8-HQ ($\log D_{7.4} = 1.84$ for MBI **2.7** vs 1.85 for 8-HQ).

Table 2.1. Measured and calculated pK_a and $\log P/D_{7.4}$ values of 8-HQ MBI library. pK_a values were measured in the range of pH 2.0 – 12.0. All pK_a and $\log P$ experiments yielded standard deviations <0.05 . Calculated pK_a and $\log P/D_{7.4}$ values were obtained using Marvin (ChemAxon) software package. Published pK_a values can be found in the Supporting Information (Table 2.S3).



MBI	Measured			Calculated		
	pK_a	$\log P$	$\log D_{7.4}$	pK_a	$\log P$	$\log D_{7.4}$
8-HQ	4.97, 9.62	1.86	1.85	4.83, 9.36	1.83	1.82
2.1	3.38, 8.55	-0.1	-0.13	1.66, 9.03	1.12	1.11
2.2	8.69	0.93	0.90	2.39, 8.31	1	0.95
2.3	3.04, 9.50	0.53	0.52	2.99, 13.57	1	0.99
2.4	2.44, 8.90	-0.52	-0.53	1.51, 11.44	0.88	0.88
2.5	7.64	-0.6	-0.80	10.65	-0.01	-0.01
2.6	8.40	1.22	1.18	7.85	1.02	0.89
2.7	8.74	1.86	1.84	1.61, 8.16	1.81	1.74
2.8	4.61, 9.30	0.71	0.70	4.82, 8.25	1.18	1.11
2.9	5.43, 9.29	-0.11	-0.12	5.48, 8.12	0.76	0.38
2.10	5.28, 8.88	0.68	0.67	5.19, 8.28	0.96	0.88
2.11	8.37	1.68	1.64	1.08, 8.21	0.99	0.99
2.12	9.43	1.56	1.56	9.61	1.77	1.77
2.13	9.17	-0.30	-0.31	2.79, 10.96	0.22	0.22
2.14	8.81	-1.4	-1.42	2.28, 9.41	-0.01	-0.01
2.16	2.88, 10.01	0.82	-2.46	0.07, 12.97	0.83	0.83
2.17	3.34	0.23	-3.83	4.98	-0.22	-2.32
2.18	3.17, 8.97	1.01	0.99	3.7, 7.25	0.5	0.18
2.19	8.25	0.23	0.17	1.96, 7.19	-0.2	-0.55
2.20	2.16, 8.11	0.49	0.41	2.35, 7.15	-0.33	-0.69
2.21	7.81	0.37	0.23	0.04, 6.97	-0.31	-0.76
2.22	8.18	1.23	1.16	2.09, 7.1	0.49	0.1
2.23	4.45, 8.67	0.69	0.67	5.26, 7.18	-0.14	-0.55
2.24	4.56, 8.34	-0.34	-0.39	5.97, 8.06	-0.87	-1.02
2.25	8.27	1.49	1.44	4.02, 8.93	1.49	1.48
2.26	6.45	1.21	0.22	2.41, 5.32	1.53	0.2
2.27	10.92	1.56	1.56	3.04, 12.09	1.3	1.3
2.29	4.92, 11.75	1.97	1.97	2.73, 12.01	1.42	1.41
2.30	7.27	1.59	1.23	1.41, 7.37	1.46	1.15

When the hydroxyl groups are replaced with sulfonamides (MBIs **2.18** – **2.24**), both pK_a values slightly decreased. However, similar trends shown in the above MBIs were observed for the sulfonamide MBIs. The nitrogen ring count in the aromatic system decreases the pK_a values (MBIs **2.18** – **2.20**) and certain scaffolds (MBIs **2.23** and **2.24**) show relatively high pK_{a1} values. The benzothiazole scaffold (MBI **2.22**) significantly increases lipophilicity and indicates the highest $\log D_{7.4}$ value in the sulfonamides MBIs ($\log D_{7.4} = 1.16$ for MBI **2.22**).

In 6,6,5-membered fused ring MBIs (MBIs **2.25** – **2.30**), MBI **2.29** have the highest pK_a values, which indicates that this MBI has the most basic nitrogen in this group. $\log D_{7.4}$ values of these MBIs ($\log D_{7.4} = 1.23$ to 1.97) were comparable to 8-HQ ($\log D_{7.4} = 1.85$). MBI **2.26** was an exception ($\log D_{7.4} = 0.22$), which can be explained with its stronger acidity ($pK_{a2} = 6.45$) compared to the other three-fused rings – at physiological pH a significant amount of MBI **2.26** is deprotonated, which decreases lipophilicity. The results demonstrate that important physicochemical properties can be optimized by isosteric replacements.

2.4 Structural Analysis

[Tp^{Ph,Me}Zn(MBI)] (Tp^{Ph,Me} = hydrotris(5,3-methylphenylpyrazolyl)borate) complexes were prepared as a model system to gain an understanding about the metal-binding ability and coordination chemistry of the MBIs. [Tp^{Ph,Me}Zn(OH)] complex and its derivatives have been broadly used to mimic the tris(histidine) Zn(II) active site of many metalloenzymes (e.g., carbonic anhydrase or matrix metalloproteinases).²⁶⁻²⁸ [Tp^{Ph,Me}Zn(MBI)] complexes of 6,6-membered ring MBIs (8-HQ and MBIs **2.1** – **2.5**) were prepared and analyzed by X-ray crystallography (Figure 2.2). These MBIs coordinate to the Zn(II) center in a bidentate fashion via the nitrogen atom of the aromatic ring system and the deprotonated hydroxyl group. All complexes generated trigonal

bipyramidal geometries with the structural parameter τ_5 in a similar range ($\tau_5 = 0.67 - 0.73$, $\tau_5 = 0$; square pyramidal geometry, $\tau_5 = 1$; trigonal pyramidal geometry). $[\text{Tp}^{\text{Ph,Me}}\text{Zn}(\mathbf{2.1})]$ containing quinazoline is most similar to $[\text{Tp}^{\text{Ph,Me}}\text{Zn}(8\text{-HQ})]$ based on their structural similarities (Table 2.2). Interestingly, while the Zn-O bond lengths were comparable for most MBIs, there was a significant difference in the bond lengths of MBI Zn-N distance depending on the ring scaffold. For example, MBI **2.5**, which has the highest nitrogen atom count, showed the largest increase in Zn-N bond length, with a Zn-N bond length 0.2 Å longer than the Zn-N bond in the 8-HQ complex (Table 2.2). This corresponds to the basicity of MBI **2.5** ($\text{p}K_{\text{a}1} < 2$) and 8-HQ ($\text{p}K_{\text{a}1} = 4.97$) and suggests that the donor ability of the nitrogen donor is reduced as the number of nitrogen atoms in the aromatic ring system increases.

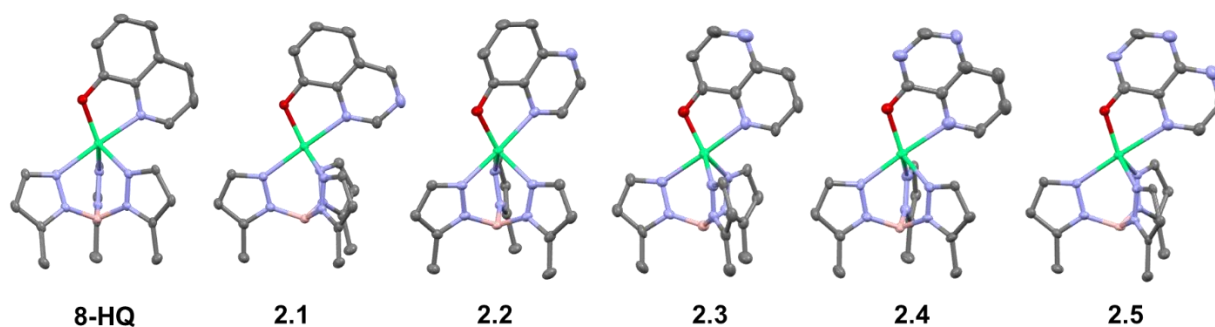


Figure 2.2. Crystal structure of $[\text{Tp}^{\text{Ph,Me}}\text{Zn}(\text{MBI})]$ complexes with 6,6-membered ring MBIs. (ORTEP, 50% probability ellipsoids). Hydrogen atoms and phenyl groups from the $\text{Tp}^{\text{Ph,Me}}$ ligand were removed for clarity. Color scheme: carbon = gray, nitrogen = blue, oxygen = red, boron = pink, and zinc = green.

Table 2.2. Selected bond lengths and angles of [Tp^{Ph,Me}Zn(MBI)] complexes with 6,6-membered ring MBIs.

MBI	Binding Mode	Zn-O (Å)	Zn-N (Å)	O-Zn-N (°)	Tau, τ ₅ (°)
8-HQ	Bidentate	1.9497(10)	2.1865(12)	80.68(5)	0.73
2.1	Bidentate	1.9590(13)	2.1893(16)	80.59(6)	0.72
		1.9552(13)	2.1938(16)	80.84(6)	0.71
2.2	Bidentate	1.947(3)	2.220(4)	79.77(12)	0.66
		1.944(3)	2.201(3)	79.65(13)	0.67
2.3	Bidentate	1.958(5)	2.239(6)	78.6(2)	0.73
		1.957(5)	2.217(6)	80.1(2)	0.74
2.4	Bidentate	1.971(6)	2.289(8)	76.5(3)	0.68
		1.960(6)	2.255(7)	78.5(2)	0.74
2.5	Bidentate	1.979(8)	2.363(10)	76.6(3)	0.71
		1.971(8)	2.407(10)	76.1(3)	0.68

Next, [Tp^{Ph,Me}Zn(MBI)] model complexes of 6,5-membered ring MBIs (MBIs **2.6**, **2.7**, **2.8**, **2.9**, **2.11**, **2.13**, and **2.16**) were studied (Figure 2.3). In general, these MBIs showed a larger variety of binding modes compared to the 6,6-membered ring MBIs. MBI **2.6** and **2.11** coordinate to the Zn(II) center in a monodentate fashion with the deprotonated hydroxyl group while MBI **2.7**, **2.8**, and **2.9** showed bidentate binding to the Zn(II) ion through the oxygen and nitrogen. This could be explained by stereo-electronic effects. For MBIs **2.6** and **2.11**, exchanging the 6-membered pyridine ring of 8-HQ for a 5-membered oxazole/pyrazole ring positions the oxygen and nitrogen donor atoms in a geometry that produces unfavorable bite-angles when bound to a metal. For example, MBIs **2.6** and **2.11** have the largest value in angle **a** (Figure 2.3), which is one of the angles that makes up the 5-membered chelate ring (~130° for MBIs **2.6** and **2.11** vs. ~116° for 8-HQ, Table 2.3). In addition, the NH group in the pyrazole ring of MBI **2.11** is predominantly located at N1 based on the X-ray structure, which would preclude a bidentate binding mode (Figure 2.3). In contrast, the thiazole ring in MBI **2.7** leads to a better geometry of the oxygen and nitrogen donor atoms for bidentate coordination. Due to the lack of hybridization of the sulfur atom, the thiazole ring is distorted, which “squeezes” the oxygen and nitrogen donor

atoms in a geometry more like 8-HQ, resulting in a bidentate binding mode (see angles designated **a** and **b** in Figure 2.3, Table 2.3). MBIs **2.8** and **2.9** have potentially better nitrogen donors based on their higher basicity ($pK_{a1} = 4.61$ and 5.43 , Table 2.1) compared to other 6,5-membered ring MBIs (pK_{a1} of MBI **2.6**, **2.7**, and **2.11** < 2 , Table 2.1), which could compensate for the unfavorable bite-angle and explain the bidentate binding modes. Another interesting set of MBIs was purine or pyrimidine-based scaffolds (MBI **2.13** – **2.16**). Figure 2.3 shows that MBI **2.13** and **2.16** provided monodentate coordination to the Zn(II) center through N1. This finding is explained by metal-binding patterns in the anionic form of purine or pyrimidine-based nucleobases such as guanine and thymine.²⁹⁻³⁰ Those nucleobases are known to be deprotonated at N1 and metal-bindings then take place through the deprotonated N1 site.³¹⁻³⁵

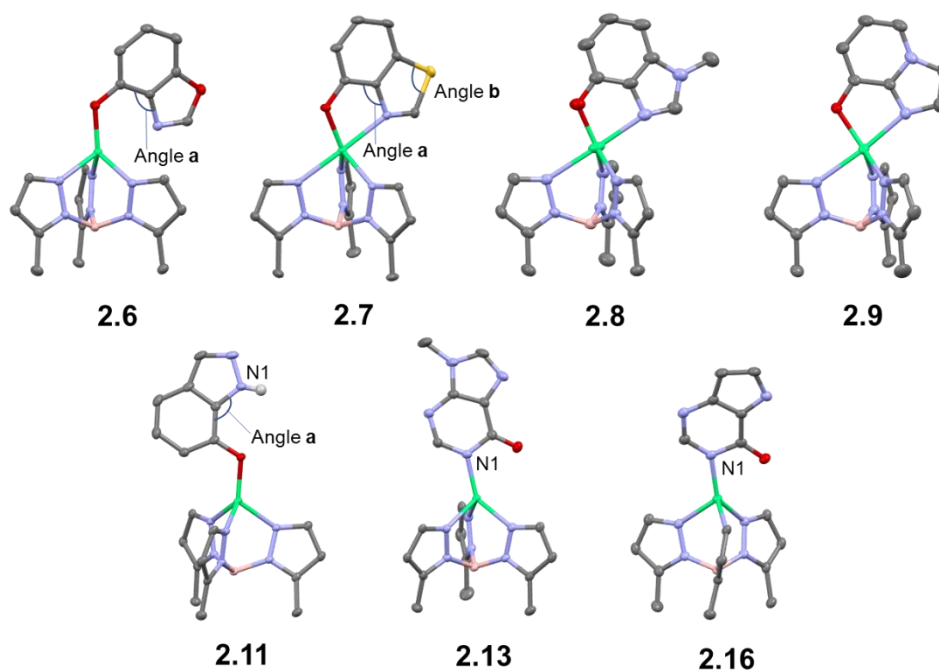


Figure 2.3. Crystal structure of $[\text{Tp}^{\text{Ph,Me}}\text{Zn}(\text{MBI})]$ complexes with 6,5-membered ring MBIs. (ORTEP, 50% probability ellipsoids). Angle **a** is defined between the 5- and 6-membered ligand rings and angles **a** and **b** together are used to describe overall internal ligand geometry on the binding modes of MBI **2.6**, **2.7**, and **2.11**. N1 is labeled to indicate the NH group on MBI **2.11** and the nitrogen atom providing monodentate coordination of MBI **2.13** and **2.16**. Hydrogen atoms and phenyl groups from the $\text{Tp}^{\text{Ph,Me}}$ ligand were removed for clarity. Color scheme: carbon = gray, nitrogen = blue, oxygen = red, sulfur = yellow, boron = pink, and zinc = green.

Table 2.3. Selected bond lengths and angles of [Tp^{Ph,Me}Zn(MBI)] complexes with 6,5-membered ring MBIs.

MBI	Binding Mode	Zn-O (Å)	Zn-N (Å)	O-Zn-N (°)	Angle a and b (°)	Tau (°)
8-HQ	Bidentate	1.9497(10)	2.1865(12)	80.68(5)	116.30(14), 122.19(15)	τ_5 , 0.73
2.6	Monodentate	1.8930(17)	-	-	129.29(19), 103.55(16)	τ_4 , 0.76
2.7	Bidentate	1.9417(11)	2.2792(13)	81.22(5)	120.48(13), 90.00(8)	τ_5 , 0.72
2.8	Bidentate	1.932(2)	2.292(3)	83.32(10)	124.3(3), 106.7(3)	τ_5 , 0.79
		1.918(2)	2.340(3)	82.30(10)	124.3(3), 107.1(3)	τ_5 , 0.72
2.9	Bidentate	1.9612(15)	2.1899(17)	83.40(6)	125.24(19), 105.9(2)	τ_5 , 0.54
2.11	Monodentate	1.8766(12)	-	-	130.28(17), 112.11(17)	τ_4 , 0.79

The [Tp^{Ph,Me}Zn(MBI)] complexes with sulfonamide series (MBI **2.18** – **2.24**) exhibited similar binding behavior as the hydroxyl series discussed above with a few exceptions (Figure 2.4). 6,6-Membered sulfonamide rings (MBIs **2.18** – **2.20**) coordinate to the Zn(II) ion in a bidentate fashion. Interestingly, MBIs **2.18** and **2.19** resulted in a complex where one pyrazole of the Tp^{Ph,Me} ligand was displaced from the metal center resulting in a tetrahedral geometry ($\tau_4 = 0.81 - 0.85$, $\tau_4 = 0$; square planar geometry, $\tau_4 = 1$; tetrahedral geometry, Table 2.S5). Pyrazole displacement in these model systems has been previously observed in rare cases,³⁶ but this remains a rare observation in these systems. In this case, this could indicate the ability of these MBIs to have a greater perturbation to the active site of a metalloenzyme upon binding. This may also be relevant to the use of 8-sulfonamidoquinoline and its derivatives as biological Zn(II) sensors, metal chelators, and ionophores.³⁷⁻⁴⁰ For 6,5-membered sulfonamide rings, monodentate (MBI **2.21**) and bidentate binding modes (MBIs **2.23** and **2.24**) were found with the [Tp^{Ph,Me}Zn(MBI)] system. Note that the nitrogen atoms of MBI **2.23** and **2.24** ($pK_{a1} = 4.45$ and 4.56 , Table 2.1) are more basic compared to MBI **2.21** ($pK_{a1} < 2$), which potentially translates to a stronger donor ability to

the metal center. The improved donor ability of benzoimidazole and imidazopyridine scaffolds was also observed for the 6,5-membered hydroxyl substituted MBIs (**2.8** and **2.9**, see above). All attempts to prepare $[\text{Tp}^{\text{Ph,Me}}\text{Zn}(\mathbf{2.22})]$ resulted in a neutral, homoleptic complex where two ligands coordinate to a single Zn(II) ion ($[\text{Zn}(\mathbf{2.22})_2]$, Figure 2.S1). This result was rather surprising, as prior studies have indicated it is extremely uncommon that an MBI will strip the Zn(II) ion from the $\text{Tp}^{\text{Ph,Me}}$ spectator ligand. Strong affinity toward Zn(II) or unanticipated reactivity with the $[\text{Tp}^{\text{Ph,Me}}\text{Zn}(\text{OH})]$ complex could explain the observed metal stripping phenomenon of MBI **2.22**. MBI **2.22** is a previously unreported compound and further studies will be required to elucidate its reactivity and affinity toward Zn(II) to explain the unusual behavior seen here. Overall, the results demonstrated that sulfonamide functionalization can be considered a good strategy for efficient metal-binding isosteric replacement of 8-HQ.

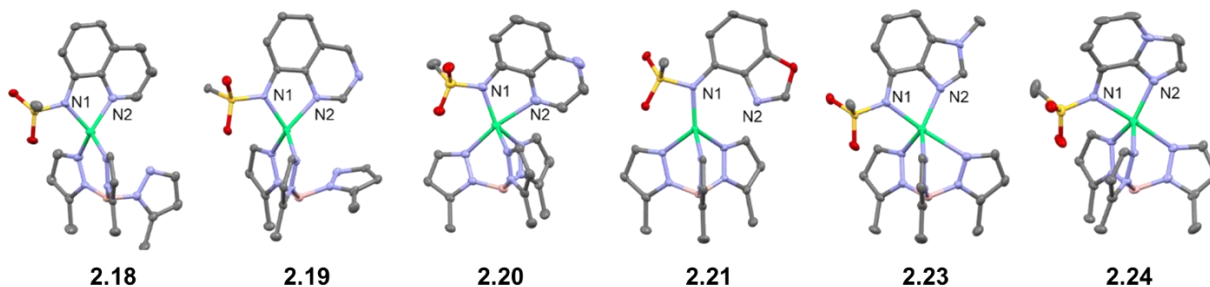


Figure 2.4. Crystal structure of $[\text{Tp}^{\text{Ph,Me}}\text{Zn}(\text{MBI})]$ complexes with sulfonamide MBIs. (ORTEP, 50% probability ellipsoids). N1 and N2 are labeled to identify nitrogen atoms that are position to participate in bidentate coordination to Zn(II) center. Hydrogen atoms and phenyl groups from the $\text{Tp}^{\text{Ph,Me}}$ ligand were removed for clarity. Color scheme: carbon = gray, nitrogen = blue, oxygen = red, sulfur = yellow, boron = pink, and zinc = green.

Lastly, $[\text{Tp}^{\text{Ph,Me}}\text{Zn}(\text{MBI})]$ model complexes of the 6,6,5-membered fused ring MBIs were prepared, and their binding behavior was investigated (Figure 2.5). Surprisingly, except for MBI **2.29**, all MBIs bound the metal in a monodentate binding mode. This indicates that the rigid backbone of these MBIs pre-arranges the donor atoms in a geometry that would result in unfavorable bite angles. For example, angle **a** of the 6,6,5-membered fused ring MBIs was at least

10° greater (~127 – 130°, Figure 5, Table 4) than the corresponding angle of the 8-HQ (~116°). Consequently, monodentate binding is favored and few bidentate binding modes are observed for these compounds. MBIs **2.25**, **2.27**, **2.28**, and **2.30** bind to the Zn(II) center via the deprotonated nitrogen atoms (labeled N1, Figure 2.5) of the carbamate, carbamide, and tetrazole. MBI **2.25** was specifically designed to try to enforce bidentate binding by the arrangement and substitution of the heteroatoms in the 5-membered ring; indeed, these complexes, although possessing 4-coordinate Zn(II) centers show a strongly distorted geometry with Zn-N2 distances of 2.62 (Table 2.4). MBI **2.26** binds to the metal center with a negatively charged sulfur atom formed by deprotonation of the thiocarbamate moiety. A possible explanation for the metal-binding behavior could be that sterically restrained 6,6,5-fused rings decreases its coordination ability and iminothiolate could act as a dominant metal-binder as a result of tautomerization of the thiocarbamate upon deprotonation.⁴¹ As mentioned previously, MBI **2.29** was the only compound exhibiting bidentate coordination. This may be explained by the increased donor ability of the imidazole nitrogen atom found in MBI **2.29**, which is reflected in the relatively high p*K*_a values compared to other MBIs in this subgroup (p*K*_{a1} and p*K*_{a2} of MBI **2.29** = 4.92 and 11.75, Table 2.1). As described above, a correlation between metal-binding behavior and basicity is observed for many of the other 8-HQ MBIs. Presumably, the increased donor ability compensates for the unfavorable bite-angle caused by steric constraints, resulting in a bidentate binding mode. In summary, the comprehensive structural analysis on 8-HQ MBIs in the [Tp^{Ph,Me}Zn(MBI)] model complex not only shed light on the effect of different isosteric replacements on the coordination chemistry of each MBI (i.e., ligand basicity, bond angle/orientation, donor atom identity, and tautomerization), but also presented potentially useful MBIs with various metal-binding modes.

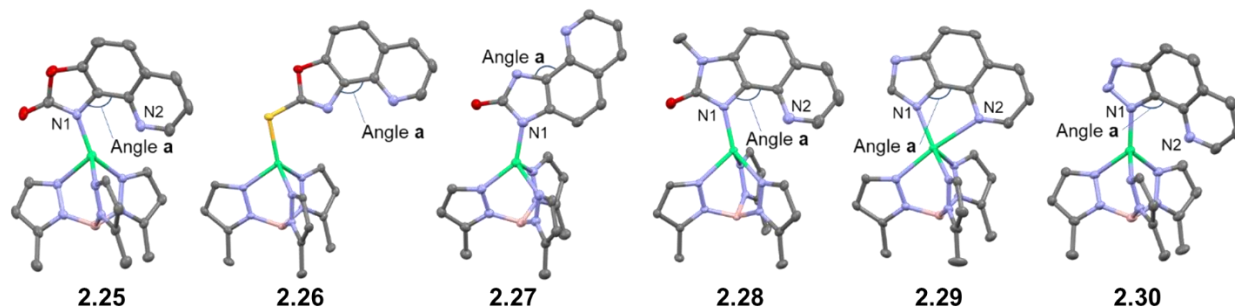


Figure 2.5. Crystal structure of $[\text{Tp}^{\text{Ph,Me}}\text{Zn}(\text{MBI})]$ complexes with 6,6,5-membered ring MBIs. (ORTEP, 50% probability ellipsoids). Angle **a** is defined between the 5- and 6-membered ligand rings and is used to describe overall internal ligand geometry on the binding modes of the MBIs. N1 and N2 are labeled to identify nitrogen atoms that are positioned to participate in bidentate coordination to Zn(II) center. Hydrogen atoms and phenyl groups from the $\text{Tp}^{\text{Ph,Me}}$ ligand were removed for clarity. Color scheme: carbon = gray, nitrogen = blue, oxygen = red, sulfur = yellow, boron = pink, and zinc = green.

Table 2.4. Selected bond lengths and angles of $\text{Tp}^{\text{Ph,Me}}\text{Zn}(\text{MBI})$ complexes with 6,6,5-membered fused ring MBIs. ^aZn-S bond distance. ^bZn-external nitrogen bond distance. ^cNot bound to the Zn(II) center, measured values based on X-ray crystallographic data.

MBI	Binding Mode	Zn-N1 (Å)	Zn-N2 (Å)	N1-Zn-N2 (°)	Angle a (°)	Tau (°)
2.25	Monodentate	1.9438(18)	2.621 ^c	75.73 ^c	127.1(2)	τ_4 , 0.72
2.26	Monodentate	2.2505(6) ^a	-	-	131.8(2)	τ_4 , 0.76
2.27	Monodentate	1.910(3) ^b	-	-	131.4(3)	τ_4 , 0.72
2.28	Monodentate	1.9486(14)	2.811 ^c	72.584 ^c	128.42(15)	τ_4 , 0.72
2.29	Bidentate	1.9779(14)	2.4413(14)	79.68(5)	126.55(15)	τ_5 , 0.54
2.30	Monodentate	1.934(2)	2.933 ^c	71.21 ^c	129.9(2)	τ_4 , 0.74

2.5 Metal-binding Isosteres Screening

To evaluate 8-HQ MBIs as potential fragment scaffolds for metalloenzyme inhibitors, the inhibitory activity of these MBIs against three Zn(II)-based metalloenzymes was measured. Matrix metalloproteinase-2 (MMP-2) and human glyoxalase 1 (GLO1) were selected as these enzymes are known to be inhibited by 8-HQ.^{5-6, 42} Human carbonic anhydrase II (hCAII) is another Zn(II)-based metalloenzyme that was tested in this study. There is no significant inhibitory activity reported for 8-HQ against hCAII and thus selectivity of the 8-HQ MBI library was evaluated with this enzyme. Both MMP-2 and hCAII contain a catalytic Zn(II) ion coordinated by three histidine residues and a water molecule in a tetrahedral geometry.⁴³⁻⁴⁴ In GLO1, the Zn(II) ion is coordinated to Gln33, Glu99, His126, and Glu172 in an octahedral coordination geometry with two open coordination sites occupied by exchangeable water molecules.⁴⁵ It has been reported that the nitrogen and the hydroxyl oxygen donor atoms of 8-HQ bind to the catalytic Zn(II) ion in MMP-2 and GLO1 resulting in inhibition.^{5-6, 42} To validate this hypothesis, the inhibition activity of compounds **2.31** and **2.32**, as well as 8-HQ were measured against MMP-2 and GLO1 at a concentration of 200 mM (Table 2.5). Compound **2.31** replaces the pyridine nitrogen donor atom with a poor dimethylamino ligand. Compound **2.32** moves the hydroxyl group to the 6-position of the quinoline scaffold resulting in an inability to produce bidentate binding. Unsurprisingly, the inhibition activity of **2.31** and **2.32** against MMP-2 and GLO1 was reduced by >50% compared to 8-HQ, suggesting the importance of metal binding to inhibit these enzymes (Table 2.5). All the 8-HQ MBIs were screened at a fragment concentration of 200 mM. The percent inhibition activity of each MBI is shown in Table 2.5.

Table 2.5. Percent inhibition values of 8-HQ MBIs (200 μ M) against MMP-2, GLO1, and hCAII. Standard deviations from triplicate measurements are given in parentheses. Cells are color-coded by percent inhibition: white (<20%), yellow (20–50%), and red (>50%). Black cells were compounds that interfered with the assay due to the poor solubility under the assay condition.

MBI	MMP-2	GLO1	hCAII
8-HQ	57 (3)	95 (6)	<5
2.1	32 (3)	95 (7)	<5
2.2	34 (2)	37 (5)	<5
2.3	39 (3)	<5	<5
2.4		6 (4)	<5
2.5	34 (5)	10 (5)	<5
2.6	7 (5)	22 (4)	37 (4)
2.7	<5	27 (4)	<5
2.8	7 (5)	23 (7)	44 (8)
2.9	6 (9)	41 (4)	<5
2.10	<5	44 (7)	<5
2.11	<5	77 (1)	<5
2.12	17 (7)	30 (5)	89 (2)
2.13		36 (7)	<5
2.14		7 (9)	<5
2.15	6 (6)	<5	<5
2.16	<5	13 (5)	18 (5)
2.17	20 (3)	<5	<5
2.18	59 (2)	95 (1)	<5
2.19	13 (5)	87 (4)	51 (6)
2.20	12 (5)	63 (8)	9 (6)
2.21	<5	<5	<5
2.22	<5	<5	<5
2.23	<5	<5	<5
2.24	<5	60 (9)	11 (9)
2.25	7 (5)	<5	
2.26	41 (3)	50 (13)	6 (8)
2.27	9 (5)	31 (10)	<5
2.28	6 (4)	<5	63 (2)
2.29	<5	65 (9)	<5
2.30	<5	<5	
2.31	<5	36 (3)	<5
2.32	26 (7)	<5	N/A
2.33	6 (11)	78 (5)	N/A
2.34	9 (5)	<5	<5

The screening result show that MMP-2 is more effectively inhibited by the 6,6-membered ring MBIs. While the 6,6-membered ring MBIs **2.1 – 2.3** and **2.5** showed moderate inhibition (30 – 40% at 200 μ M), the 5,6-membered ring MBIs **2.6 – 2.16** were nearly inactive. These results confirm previous studies on the development of MMP-2 inhibitors based on 8-sulfonamido quinoline derivatives and its 5,6-membered heterocycle isosteres.⁴⁶⁻⁴⁷ MBIs **2.1 – 2.3** and **2.5**, which have more nitrogen atoms in the ring system, showed a poorer IC₅₀ value than 8-HQ (Figure 2.S2), suggesting that adding nitrogen atoms to the core scaffold does not enhance interaction with the binding pocket. On the other hand, sulfonamide MBI **2.18** showed modest improvements in inhibition activity compared to 8-HQ (IC₅₀ of MBI **2.18** = 153.6 \pm 9.8 μ M, IC₅₀ of 8-HQ = 165.7 \pm 12.4 μ M, Figure 2.S2). Placing nitrogen atoms on the core scaffold (MBIs **2.19** and **2.20**) did not improve inhibition activity as observed in MBIs **2.1 – 2.3** and **2.5**. Interestingly, MBI **2.26** showed much higher inhibition activity compared to the other 6,6,5-membered fused ring MBIs, presumably due to the high affinity of sulfur for zinc. The moderate inhibition activity of MBI **2.26** was confirmed by measuring its IC₅₀ value (Figure 2.S2). Compounds **2.33** and **2.34** were additionally screened to validate the metal binding interaction of MBIs **2.1** and **2.18** with MMP-2. Compound **2.33** has a methyl group on the hydroxyl oxygen atom when compared to MBI **2.1**, and compound **2.34** contains a reverse sulfonamide group when compared to MBI **2.19**. Not surprisingly, both compounds **2.33** and **2.34** are not effective inhibitors of MMP-2.

More than half of the 8-HQ MBIs showed significant inhibition activity against GLO1 at a fragment concentration of 200 μ M. In general, 6,6-membered ring MBIs **2.1**, **2.2**, **2.18**, **2.19**, and **2.20** showed inhibition (>37% at 200 μ M) and maintained activity at a lower fragment concentration (>21% at 50 μ M, Table 2.S6). Importantly, many 6,5-membered MBIs (MBIs **2.6 – 2.13** and **2.24**), which did not show significant inhibition of MMP-2, showed moderate inhibition

against GLO1. Based on the X-ray data obtained for the model complexes, replacing 6,6-membered rings with 6,5-membered ring MBIs produced a greater variety in metal-binding modes and orientations. It is possible that the active site of GLO1 is less susceptible to those changes in metal-binding. Note that indazole-based MBI **2.11** showed the highest inhibition activity (77% at 200 mM) among the 6,5-membered ring MBIs, and MBIs **2.9** and **2.24** containing imidazopyridine core exhibited potent inhibition of GLO1 (41% and 60% at 200 mM, respectively). These findings suggest that these 8-HQ MBIs could be applied as selective fragments for the development of GLO1 inhibitors. In addition, the inhibition activity of compounds **2.33** and **2.34** were compared with MBI **2.1** and **2.18**, which showed the highest percent inhibition (>95% at 200 mM). Compound **2.33** showed a modest decrease in inhibition activity while compound **2.34** exhibited a complete loss of inhibition. Finally, as an orthogonal method to evaluate MBI binding with GLO1, thermal shift assays (TSAs) were carried out on five select compounds (8-HQ, **2.1**, **2.18**, **2.19**, and **2.20**, Table 2.S7). The TSA data was reported as ΔT_M (in °C), which refers to the difference in melting temperature of MBI-bound GLO1 compared to native, unbound GLO1. Significant ΔT_M values (>3 °C) were observed for all test compounds, providing independent validation of a binding interaction between these select MBIs and GLO1.

In contrast to MMP-2 and GLO1, only few MBIs showed inhibition activity against hCAII. MBI **2.12** showed the greatest inhibition of hCAII (89% at 200 mM). TSA data verified binding of **2.12** with hCAII, showing a significant ΔT_M value ($\Delta T_M = 7.28 \pm 0.18$ °C, Table 2.S7). Why MBI **2.12** is an effective inhibitor of hCAII is not obvious; a possible explanation could be that the indole group interacts with the zinc-coordinated water molecule, which was suggested by molecular docking studies of indole-containing compounds in hCAII.⁴⁸ Moreover, a series of benzenesulfonamide derivatives including the indole moiety have been reported with an effective

inhibitory activity against hCAII.⁴⁹ Interestingly, compound **2.34** did not show any inhibition activity against hCAII, which is surprising because sulfonamides are privileged scaffolds for hCAII inhibition.⁵⁰⁻⁵¹ The lack of hCAII inhibition by compound **2.34** may be due to the narrow and deep shape of the hCAII active site.⁴⁴

2.6 Conclusions

In Chapter 2, we designed and prepared 30 MBIs derived from 8-HQ that covered a wide range of physiochemical properties. The correlation between electron donor ability of the MBI and ligand basicity was observed based on the pK_a measurement and X-ray crystallography of an $[(Tp^{Ph,Me})Zn(MBI)]$ model system. In addition, we confirmed that other factors such as ring scaffold geometry, donor atom identity, bond angle/orientation, and ligand tautomerization can have a pronounced effect on their coordination ability and metal-binding modes. This in-depth analysis allows us to gain better understanding of structural and electronic features of the MBIs and establish a rudimentary rule for future MBI development. Furthermore, bioactivity of the MBIs was monitored by measuring enzymatic activity against several metalloenzymes. The results indicated that the MBIs have comparable potency and in some cases improved selectivity, which demonstrates the potential use of 8-HQ MBIs as starting points for the discovery of novel lead candidates in developing metalloenzyme inhibitors.

2.7 Acknowledgements

Chapter 2 is a reprint of the material as it appears in “Developing Metal-binding Isosteres of 8-Hydroxyquinoline as Metalloenzyme Inhibitor Scaffolds.” *Inorg. Chem.*, **2022**, 61, 19, 7631. The dissertation author was a primary author of this paper and gratefully acknowledges the contributions of coauthors Moritz K. Jackl, Mark Kalaj, and Seth M. Cohen.

2.8 Appendix: Supporting Information

General Experimental Details

All reagents and solvents were obtained from commercial sources (Sigma Aldrich, Alfa Aesar, TCI, Combi-Blocks etc.) and used without further purification. 8-HQ, MBIs **2.1**, **2.3**, **2.4**, **2.5**, **2.7**, **2.9**, **2.10**, **2.11**, **2.13**, **2.14**, **2.15**, **2.17**, compounds **2.32** and **2.34** were purchased from commercial vendors, and the remaining were synthesized from widely available starting materials. To obtain an X-ray structure of [(Tp^{Ph,Me})Zn(MBI)], [(Tp^{Ph,Me})K] and [(Tp^{Ph,Me})ZnOH] was prepared according to literature methods.⁵² Column chromatography was performed using a CombiFlash Rf automated system from Teledyne Isco using prepacked silica cartridges. ¹H and ¹³C NMR spectra were recorded at ambient temperature on 300 MHz Bruker, 400 MHz Jeol NMR instrument, or 500 MHz Varian NMR instrument in the Department of Chemistry and Biochemistry at the University of California, San Diego. Processing of the NMR data was performed using the MestReNova 14.2 program. High resolution mass spectrometry (HRMS) analysis was performed using an Agilent 6230 accurate-mass liquid chromatography time-of-flight mass spectrometry LC–TOFMS at the Molecular Mass Spectrometry Facility (MMSF) in the Department of Chemistry and Biochemistry at the University of California, San Diego.

Synthesis and Crystallization of Model Complexes

To obtain an X-ray structure of $[(\text{Tp}^{\text{Ph,Me}})\text{Zn}(\text{MBI})]$, $[(\text{Tp}^{\text{Ph,Me}})\text{K}]$ and $[(\text{Tp}^{\text{Ph,Me}})\text{ZnOH}]$ was prepared according to literature methods.⁵² $[(\text{Tp}^{\text{Ph,Me}})\text{ZnOH}]$ (50 mg, 0.09 mmol) was dissolved in 15 mL of CH_2Cl_2 in a 50 mL round-bottom flask. The MBI (0.09 mmol, 1 equiv) in 10 mL of MeOH was added, and the reaction mixture was stirred overnight under a nitrogen atmosphere. The resulting mixture was evaporated to dryness and subsequently dissolved in a minimal amount (~1 mL) of benzene. The solution was filtered using a syringe filter to remove any undissolved solids. The resulting complex in benzene was recrystallized using vapor diffusion with pentane. Crystals typically formed within a few days.

Physicochemical Properties Analysis

Physicochemical properties were determined using a Sirius T3 instrument.^{24, 53-54} All titrations, both $\text{p}K_a$ and $\log P$, were performed in 0.15 M KCl with 0.5 M HCl and KOH. The $\text{p}K_a$ of a compound was determined by analysing each MBI sample in triplicate using potentiometric titrations. Experiments were typically performed over a pH range of 2.0 – 12.0. Standard deviations were derived from fitting all three replicate experiments. For water insoluble compounds methanol was added and the obtained apparent $\text{p}K_a$ (p_sK_a) was extrapolated to the aqueous $\text{p}K_a$ by the Yasuda–Shedlovsky procedure.⁵⁵ $\log P$ was determined via potentiometric titrations in the presence of varying ratios of octanol and water. The presence of octanol shifts the $\text{p}K_a$ of ionizable species, and based on the shifts, a $\log P$ can be determined. Measurements for $\log P$ determination were typically performed over a pH range of 2.0 – 12.0. Three experiments with varying ratios of water:octanol was performed, allowing for a standard deviation to be

determined from the fitting of all measurements. MBI sample sizes were ~0.5 mg for both pK_a and logP measurements.

MMP-2 Assay

Human recombinant MMP-2 catalytic domain was purchased from ENZO Life Sciences (catalog # BML-SE237-0010). Assays were carried out in clear Costar 96-well, half-area, flat-bottom assay plates (catalog # 80-2404). Each well contained a total volume of 100 μ L including buffer (50 mM MES, 10 mM CaCl_2 , 0.05% Brij-35, pH 7.5), MMP-2 (1.16 U), and the fragment solution (200 μ M final concentration). After a 30 min incubation period at 37 °C, the reaction was initiated by the addition of 10 μ L of fluorogenic MMP-2 substrate (4 μ M final concentration, Mca-Pro-Leu-Gly-Leu-Dpa-Ala-Arg-NH₂·AcOH, ENZO Life Sciences, catalog # BML-P126-0001). Fluorescence was monitored at $E_x/E_m=328/420$ nm using BioTek Synergy H4 plate reader, and measurements were recorded every minute for 10 min. The rate of fluorescence increase was compared for samples versus negative controls (no inhibitor, arbitrarily set as 100% activity). A positive control (NNGH as inhibitor, 50 μ M final concentration) showed complete inhibition under the assay conditions described above. Dose-response curves were generated, analyzed, and fitted to obtain IC_{50} values of MBIs using a concentration range of between 10 μ M and 1000 or 1500 μ M depending on compound solubility (Figure S2). 8-HQ gave an IC_{50} value of 165.7 ± 12.4 μ M, which is comparable to the literature reported value (130 ± 28 μ M).⁵

GLO1 Assay

Recombinant human glyoxalase I (GLO1) was purchased from R&D Systems (catalog #4959-GL). Assays were carried out in 0.1 M sodium phosphate, pH 7.0 buffer, utilizing 96-well

clear UV plates (Corning UV Transparent Microplates, catalog #3635). A fresh solution of GSH (100 mM) and methylglyoxal (MG) (100 mM) was prepared in Millipore grade water. The substrate for the assay was prepared by adding 0.43 mL of GSH and 0.43 mL of MG to 15.14 mL of buffer. The substrate mixture was vortexed vigorously for 45 s and then allowed to sit at room temperature for 15 min. The initial well volume was 50 μ L containing GLO1 (40 ng) and inhibitor. This protein and inhibitor mixture was incubated for 15–20 min prior to addition of the substrate. The substrate (150 μ L) was then added to the wells yielding a maximum amount of 5% DMSO per well. The enzyme activity was measured utilizing a Biotek Synergy HT plate reader by measuring absorbance at 240 nm every 1 min for a duration of 8 min. The rate of absorbance increase was compared for samples versus controls containing no inhibitor (set at 100% activity). The absorbance reading for background wells containing DMSO, buffer, and substrate (no enzyme or inhibitor) was subtracted from the experimental wells. A positive control (Chugai-3d inhibitor, 50 μ M final concentration) showed complete inhibition under the assay conditions described above.⁵⁶

hCAII Assay

The plasmid for recombinant expression of hCAII with a T7 RNA polymerase promoter and ampicillin resistance gene (pACA) was a gift from Thomas R. Ward (U. Basel, Switzerland). The protein for activity assays was expressed in BL21 Escherichia coli cells and purified as reported previously.⁵⁷ The Zn(II) content of expressed hCAII was measured by inductively coupled plasma-mass spectrometry (ICP-MS). The metal-to-protein (Zn:protein) molar ratio was determined to be 0.951 ± 0.006 , indicating the holo enzyme (fully metalated) is was isolated (data not shown). Assays were carried out in clear-bottom Costar 96-well plates (catalog # 07-200-706)

with a total volume of 100 μ L per well. The assay buffer was comprised of 50 mM HEPES pH 8.0 and 100 mM NaSO₄. MBIs were added from a 50 mM DMSO stock to a final concentration of 200 μ M and incubated with hCAII (40 nM final concentration) for 15 min at room temperature. *p*-Nitrophenyl acetate was used as the substrate (500 μ M final concentration), and the absorbance at 405 nM was monitored for 20 min at 1 min intervals using BioTek Synergy H4 plate reader. Percent inhibition was determined by comparing the activity of wells. A positive control (acetazolamide inhibitor, 50 μ M final concentration) showed complete inhibition under the assay conditions described above.

Compound Synthesis

Quinoxalin-5-ol (2.2). The compound was synthesized by using a modified literature procedure.⁵⁸ To a stirred solution of sodium acetate (5 mL, 4 M aq.) and acetic acid (8 mL, 2 M aq.), 2,3-diaminophenol (500 mg, 1 eq, 4.03 mmol) was added and then heated at 60 °C. In a second flask, a solution of sodium glyoxal bisulfite (1.13 g, 1.05 eq, 4.23 mmol) in H₂O (30 mL) was heated at 60 °C. The 2,3-diaminophenol solution was then transferred into the sodium glyoxal bisulfite solution and stirred for 1 h at 60 °C. After cooling, 1N NaOH aq. was used to adjust the pH to ~8. The resulting solution was then extracted with EtOAc (50 mL). The organic layer was separated, washed with water (2 \times 20 mL) and brin (20 mL), dried over MgSO₄ and concentrated in vacuo. The crude product was purified via flash column chromatography (hexane:EtOAc 0-50%) to give the product as a beige solid. Yield: 355 mg (2.43 mmol, 60%). ¹H NMR (400 MHz, MeOH-*d*₄): δ 8.82 (dd, *J* = 15.3, 1.9 Hz, 2H), 7.69 (dd, *J* = 8.5, 7.8 Hz, 1H), 7.55 (dd, *J* = 8.5, 1.2 Hz, 1H), 7.18 (dd, *J* = 7.7, 1.2 Hz, 1H). ¹³C NMR (101 MHz, MeOH-*d*₄): δ 154.91, 146.51, 144.53, 144.21,

135.22, 132.36, 119.84, 113.18. HR-MS (ESI) (m/z): $[M+H]^+$ calcd. for $[C_8H_7N_2O]^+$, 147.0553; found, 147.0555.

Benzo[d]oxazol-4-ol (2.6). The compound was synthesized by using a modified literature procedure.⁵⁹ To a stirred solution of 2-aminobenzene-1,3-diol (500 mg, 1 eq, 4.00 mmol) and triethoxymethane (711 mg, 798 μ L, 1.2 eq, 4.80 mmol) in EtOH (30 mL), catalytic amount of concentrated sulfuric acid (392 mg, 1 mL, 1 eq, 4.00 mmol) was added. The mixture was heated at 80 °C for 1.5 h under microwave reaction. After cooling, the resulting solution was diluted with ethyl acetate (50 mL) and water (30 mL). The organic layer was separated, washed with water (3 \times 20 mL), dried over MgSO₄ and concentrated in vacuo. The crude product was purified via flash column chromatography (DCM:MeOH 0-5%) to give the product as an off-white solid. Yield: 220 mg (1.63 mmol, 41%). ¹H NMR (400 MHz, CDCl₃): δ 8.17 (s, 1H), 7.33 (t, J = 8.2 Hz, 1H), 7.16 (dd, J = 8.2, 0.8 Hz, 1H), 6.94 (dd, J = 8.1, 0.9 Hz, 1H), 6.42 (s, 1H). ¹³C NMR (101 MHz, CDCl₃): δ 151.72, 151.43, 148.80, 127.75, 127.34, 111.27, 102.82. HR-MS (ESI) (m/z): $[M+H]^+$ calcd. for $[C_7H_6NO_2]^+$, 136.0393; found, 136.0393.

1-Methyl-1H-benzo[d]imidazol-4-ol (2.8). To a solution of 4-(benzyloxy)-1H-benzo[d]imidazole (120 mg, 1 eq, 535 μ mol) in 5 mL of DMF, potassium hydroxide (60.0 mg, 2 eq, 1.07 mmol) was added. The mixture was stirred for 15 min at room temperature, and iodomethane (83.5 mg, 36.6 μ L, 1.1 eq, 589 μ mol) was added dropwise under vigorous stirring. After the overnight reaction at room temperature, the mixture was diluted with water (10 mL) and extracted with dichloromethane (3 \times 20 mL). The combined organic layers were washed with brine (20 ml), dried over MgSO₄, and concentrated in vacuo. The resulting product was brown viscous liquid, which was directly used for the subsequent reaction without any further separation or purification. To a solution of the crude 4-(benzyloxy)-1-methyl-1H-benzo[d]imidazole in EtOH

(5 mL), Pd/C (27.9 mg, 10% Wt, 0.05 eq, 26.2 μ mol) was added. The reaction proceeded with H₂ at room temperature overnight. The resulting solution was filtered, concentrated in vacuo, and purified via flash column chromatography (DCM:MeOH 0-5%) to give the product. Yield: 20 mg (0.13 mmol, 26%). ¹H NMR (400 MHz, DMSO-*d*₆): δ 9.73 (s, 1H), 8.02 (s, 1H), 7.04 (t, *J* = 7.9 Hz, 1H), 6.94 (dd, *J* = 8.1, 1.0 Hz, 1H), 6.55 (dd, *J* = 7.7, 1.0 Hz, 1H), 3.77 (s, 3H). ¹³C NMR (101 MHz, DMSO-*d*₆): δ 149.22, 142.56, 136.49, 132.98, 123.16, 106.43, 100.88, 30.76. HR-MS (ESI) (*m/z*): [M+H]⁺ calcd. for [C₈H₉N₂O]⁺, 149.0709; found, 149.0707.

1H-Indol-7-ol (2.12). To a solution of 7-(benzyloxy)-1H-indole (200 mg, 1 eq, 896 μ mol) in EtOH (5 mL), Pd/C (20 mg, 10% Wt, 1 eq, 896 μ mol) was added. The reaction proceeded with H₂ at room temperature for 6 h. The resulting solution was filtered and concentrated in vacuo to give the product as pale purple solids. Yield: 77 mg (0.58 mmol, 65%). ¹H NMR (400 MHz, DMSO-*d*₆): δ 10.87 (s, 1H), 9.50 (s, 1H), 7.19 (q, *J* = 2.4 Hz, 1H), 6.99 – 6.95 (m, 1H), 6.76 (td, *J* = 7.7, 1.9 Hz, 1H), 6.48 (dd, *J* = 7.3, 1.9 Hz, 1H), 6.33 (q, *J* = 2.2 Hz, 1H). ¹³C NMR (101 MHz, DMSO-*d*₆): δ 143.62, 129.60, 126.02, 124.58, 119.45, 111.14, 105.16, 101.33. HR-MS (ESI) (*m/z*): [M+H]⁺ calcd. for [C₈H₈NO]⁺, 134.0600; found, 134.0599.

3,5-Dihydro-4H-pyrrolo[3,2-d]pyrimidin-4-one (2.16). The compound was synthesized by using a modified literature procedure.⁶⁰ To a solution of ethyl 3-amino-1H-pyrrole-2-carboxylate (500 mg, 1 eq, 3.24 mmol) in EtOH (30 mL), formamidine acetate (506 mg, 1.5 eq, 4.86 mmol) was added and then heated under reflux for 16 h at 100 – 105 °C. After cooling, the solid formed was filtered and washed with EtOH. The precipitate was then dried in vacuo to give the product as grey solids. Yield: 304 mg (2.25 mmol, 69%). ¹H NMR (400 MHz, DMSO-*d*₆): δ 12.09 (s, 1H), 11.87 (s, 1H), 7.79 (s, 1H), 7.37 (t, *J* = 2.8 Hz, 1H), 6.37 (dd, *J* = 2.9, 1.7 Hz, 1H). ¹³C NMR

(101 MHz, DMSO-*d*₆): δ 153.77, 144.71, 141.58, 127.44, 117.85, 103.02. HR-MS (ESI) (*m/z*): [M+H]⁺ calcd. for [C₆H₆N₃O]⁺, 136.0505; found, 136.0506.

N-(Quinolin-8-yl)methanesulfonamide (2.18). The compound was synthesized by using a modified literature procedure.⁶¹ To a solution of quinolin-8-amine (200 mg, 1 eq, 1.39 mmol) and pyridine (143 mg, 145 μ L, 1.3 eq, 1.80 mmol) in DCM (5 mL), methanesulfonyl chloride (318 mg, 215 μ L, 2 eq, 2.77 mmol) was added. The mixture was stirred at room temperature overnight. After stirring, H₂O (10 mL) was added to the reaction mixture and the solution was extracted with EtOAc (3 \times 20 mL). The combined organic layers were dried over MgSO₄, filtered, and concentrated in vacuo. The crude product was purified via flash column chromatography (hexane:EtOAc 0-80%) to give the product as an off-white solid. Yield: 100mg (1.4 mmol, 32%). ¹H NMR (500 MHz, CDCl₃): δ 8.93 (s, 1H), 8.83 (dd, *J* = 4.2, 1.7 Hz, 1H), 8.20 (dd, *J* = 8.3, 1.7 Hz, 1H), 7.86 (dd, *J* = 7.3, 1.5 Hz, 1H), 7.61 – 7.47 (m, 3H), 3.03 (s, 3H). ¹³C NMR (126 MHz, CDCl₃): δ 149.13, 138.77, 136.54, 134.25, 128.53, 127.20, 122.64, 122.36, 115.26, 39.33. HR-MS (ESI) (*m/z*): [M+H]⁺ calcd. for [C₁₀H₁₁N₂O₂S]⁺, 223.0536; found, 223.0534.

N-(Quinazolin-8-yl)methanesulfonamide (2.19). To a solution of quinazolin-8-amine (53 mg, 1 eq, 0.37 mmol) in pyridine (2 mL), methanesulfonyl chloride (84 mg, 57 μ L, 2 eq, 0.73 mmol) was added. The clear orange solution was heated at 140 °C for 1 hr under microwave reaction creating a dark brown solution. After stirring, H₂O (10 mL) was added to the reaction mixture and the solution was extracted with EtOAc (3 \times 20 mL). The combined organic layers were washed with brin, dried over MgSO₄, filtered, and concentrated in vacuo. The crude product was purified via flash column chromatography (hexane:EtOAc 0-80%) to give the product. Yield: 25 mg (0.11 mmol, 31%). ¹H NMR (300 MHz, CDCl₃): δ 9.45 (s, 1H), 9.30 (s, 1H), 8.59 (s, 1H), 8.08 (dd, *J* = 6.5, 2.5 Hz, 1H), 7.75 – 7.63 (m, 2H), 3.08 (s, 3H). ¹³C NMR (101 MHz, DMSO-*d*₆): δ 161.42,

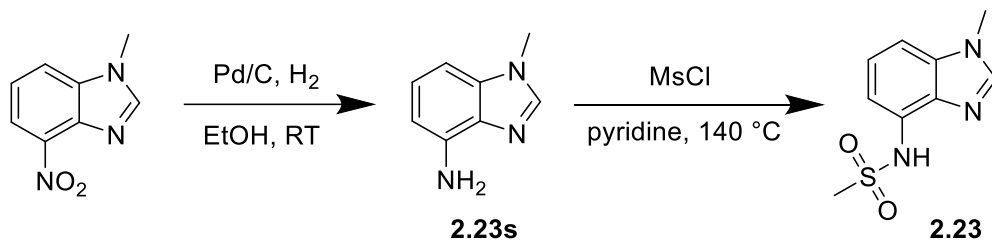
154.87, 142.16, 134.45, 128.94, 125.56, 123.46, 123.23, 43.66. HR-MS (ESI) (m/z): $[M+H]^+$ calcd. for $[C_9H_{10}N_3O_2S]^+$, 224.0488; found, 224.0490.

N-(Quinoxalin-5-yl)methanesulfonamide (2.20). To a solution of quinoxalin-5-amine (240 mg, 1 eq, 1.65 mmol) and pyridine (170 mg, 173 μ L, 1.3 eq, 2.15 mmol) in DCM (5 mL), methanesulfonyl chloride (379 mg, 256 μ L, 2 eq, 3.31 mmol) was added. The mixture was stirred at room temperature overnight. After stirring, H₂O (10 mL) was added to the reaction mixture and the solution was extracted with EtOAc (3 \times 20 mL). The combined organic layers were dried over MgSO₄, filtered, and concentrated in vacuo. The crude product was purified via flash column chromatography (hexane:EtOAc 0-80%) to give the product. Yield: 174mg (0.8 mmol, 47%). ¹H NMR (500 MHz, CDCl₃): δ 8.96 (d, J = 1.8 Hz, 1H), 8.78 (d, J = 1.8 Hz, 1H), 8.63 (s, 1H), 7.94 – 7.84 (m, 2H), 7.78 (dd, J = 8.5, 7.6 Hz, 1H), 3.08 (s, 3H). ¹³C NMR (126 MHz, CDCl₃): δ 146.08, 143.37, 143.32, 134.31, 133.61, 130.82, 124.26, 115.58, 39.67. HR-MS (ESI) (m/z): $[M+H]^+$ calcd. for $[C_9H_{10}N_3O_2S]^+$, 224.0488; found, 224.0490.

N-(Benzo[d]oxazol-4-yl)methanesulfonamide (2.21). To a solution of benzo[d]oxazol-4-amine (120 mg, 1 eq, 895 μ mol) in pyridine (2 mL), methanesulfonyl chloride (205 mg, 138 μ L, 2 eq, 1.79 mmol) was added. The solution was heated at 150 °C for 20 min under microwave reaction. After stirring, H₂O (10 mL) was added to the reaction mixture and the solution was extracted with EtOAc (3 \times 20 mL). The combined organic layers were washed with brin, dried over MgSO₄, filtered, and concentrated in vacuo. The crude product was purified via flash column chromatography (DCM:MeOH 0-5%) to give the product. Yield: 180mg (0.9mmol, 95%). ¹H NMR (400 MHz, CDCl₃): δ 8.18 (s, 1H), 7.92 (s, 1H), 7.53 (dd, J = 5.8, 3.2 Hz, 1H), 7.45 – 7.35 (m, 2H), 3.09 (s, 3H). ¹³C NMR (101 MHz, CDCl₃): δ 152.78, 150.76, 131.48, 129.44, 126.85,

114.45, 107.44, 40.01. HR-MS (ESI) (m/z): $[M+H]^+$ calcd. for $[C_8H_9N_2O_3S]^+$, 213.0328; found, 213.0328.

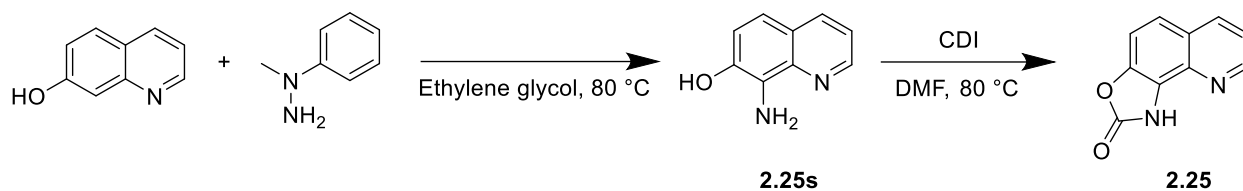
N-(Benzo[d]thiazol-4-yl)methanesulfonamide (2.22). To a solution of benzo[d]thiazol-4-amine (100 mg, 1 eq, 666 μ mol) in pyridine (3 mL), methanesulfonyl chloride (76.3 mg, 1 eq, 666 μ mol) was added. The solution was heated at 140 °C for 1 hr under microwave reaction. After stirring, H₂O (10 mL) was added to the reaction mixture and the solution was extracted with EtOAc (3 \times 20 mL). The combined organic layers were washed with brin, dried over MgSO₄, filtered, and concentrated in vacuo. The crude product was purified via flash column chromatography (hexane:EtOAc 0-80%) to give the product. Yield: 30 mg (0.13 mmol, 20%). ¹H NMR (300 MHz, CDCl₃): δ 8.95 (s, 1H), 7.90 (s, 1H), 7.76 – 7.64 (m, 2H), 7.46 (t, J = 8.0 Hz, 1H), 3.07 (s, 3H). ¹³C NMR (101 MHz, CDCl₃): δ 154.05, 144.23, 134.59, 131.88, 126.88, 117.55, 114.49, 39.74. HR-MS (ESI) (m/z): $[M+H]^+$ calcd. for $[C_8H_9N_2O_2S_2]^+$, 229.0100; found, 229.0102.



1-Methyl-1H-benzo[d]imidazol-4-amine (2.23s). To a solution of 1-methyl-4-nitro-1H-benzo[d]imidazole (200 mg, 1 eq, 1.13 mmol) in EtOH (10 mL), Pd/C (60.1 mg, 10% Wt, 0.05 eq, 56.4 μ mol) was added. The reaction proceeded with H₂ at room temperature overnight. The resulting solution was filtered and concentrated in vacuo to give the product as a beige solid, which was directly used for the subsequent reaction without any further separation or purification. Yield: 140 mg (0.96 mmol, 84.3%). ¹H NMR (300 MHz, CDCl₃): δ 7.75 (s, 1H), 7.14 (t, J = 7.9 Hz, 1H), 6.80 (d, J = 8.1 Hz, 1H), 6.57 (d, J = 7.6 Hz, 1H), 4.39 (s, 2H), 3.82 (s, 3H).

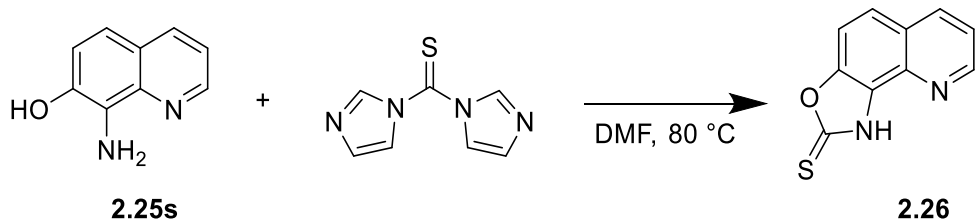
N-(1-methyl-1H-benzo[d]imidazol-4-yl)methanesulfonamide (2.23). To the solution of 1-methyl-1H-benzo[d]imidazol-4-amine (120 mg, 1 eq, 815 μ mol) in pyridine (2 mL), methanesulfonyl chloride (187 mg, 126 μ L, 2 eq, 1.63 mmol) was added. The solution was heated at 150 °C for 20 min under microwave reaction. After stirring, H₂O (5 mL) was added to the reaction mixture and the solution was extracted with EtOAc (3 \times 20 mL). The combined organic layers were washed with brine, dried over MgSO₄, filtered, and concentrated in vacuo. The resulting solution was purified via flash column chromatography (DCM:MeOH 0-5%). Yield: 86 mg (0.38 mmol, 47%). ¹H NMR (300 MHz, DMSO-*d*₆): δ 9.54 (s, 1H), 8.20 (s, 1H), 7.38 (dd, *J* = 8.1, 1.1 Hz, 1H), 7.22 (t, *J* = 7.9 Hz, 1H), 7.11 (dd, *J* = 7.7, 1.0 Hz, 1H), 3.84 (s, 3H), 3.17 (s, 3H). ¹³C NMR (101 MHz, DMSO-*d*₆): δ 144.10, 136.84, 135.59, 128.76, 122.70, 115.05, 107.12, 40.85, 30.95. HR-MS (ESI) (*m/z*): [M+H]⁺ calcd. for [C₉H₁₂N₃O₂S]⁺, 226.0645; found, 226.0646.

N-(1-Methyl-1H-benzo[d]imidazol-4-yl)methanesulfonamide (2.24). To a solution of 1-methyl-1H-benzo[d]imidazol-4-amine (120 mg, 1 eq, 815 μ mol) in pyridine (2 mL), methanesulfonyl chloride (206 mg, 139 μ L, 2 eq, 1.80 mmol) was added. The solution was heated at 150 °C for 20 min under microwave reaction. After stirring, H₂O (10 mL) was added to the reaction mixture and the solution was extracted with EtOAc (3 \times 20 mL). The combined organic layers were washed with brin, dried over MgSO₄, filtered, and concentrated in vacuo. The crude product was purified via flash column chromatography (DCM:MeOH 0-5%) to give the product. Yield: 100 mg (0.47 mmol, 53%). ¹H NMR (400 MHz, CDCl₃): δ 7.95 (dd, *J* = 6.8, 1.0 Hz, 1H), 7.66 – 7.60 (m, 2H), 7.37 (dd, *J* = 7.5, 1.0 Hz, 1H), 6.84 (t, *J* = 7.1 Hz, 1H), 3.10 (s, 3H). ¹³C NMR (101 MHz, CDCl₃): δ 139.30, 132.15, 126.95, 121.68, 114.23, 113.21, 111.51, 39.99. HR-MS (ESI) (*m/z*): [M+H]⁺ calcd. for [C₈H₁₀N₃O₂S]⁺, 212.0488; found, 212.0488.

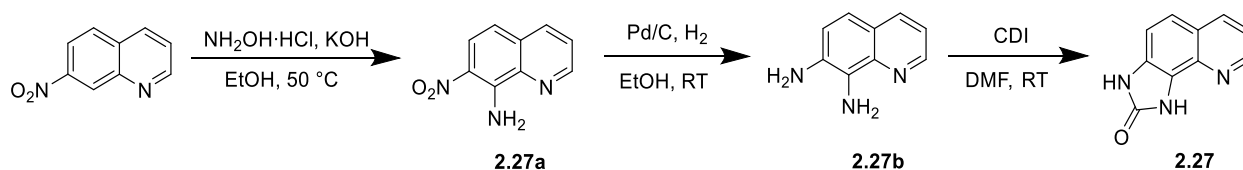


8-Aminoquinolin-7-ol (2.25s). The compound was synthesized by using a modified literature procedure.⁴⁷ To a mixture of quinolin-7-ol (308 mg, 1 eq, 2.12 mmol) in ethylene glycol (2.5 mL), 1-methyl-1-phenylhydrazine (518 mg, 498 μ L, 2 eq, 4.24 mmol) was added under an argon atmosphere. The mixture was stirred at 80 °C overnight. After cooling, H₂O (10 mL) was added to the reaction mixture and the solution was extracted with EtOAc (3 \times 20 mL). The combined organic layers were washed with brine, dried over MgSO₄, filtered, and concentrated in vacuo. The crude product was purified via flash column chromatography (hexane:EtOAc 0-50%) to give the product. Yield: 260mg (1.62 mmol, 77%). ¹H NMR (300 MHz, DMSO-*d*₆): δ 8.67 (dd, *J* = 4.2, 1.7 Hz, 1H), 8.11 (dd, *J* = 8.3, 1.7 Hz, 1H), 7.26 (dd, *J* = 8.2, 4.2 Hz, 1H), 7.16 (d, *J* = 8.6 Hz, 1H), 7.07 (d, *J* = 8.7 Hz, 1H), 5.05 (s, 2H).

Oxazolo[5,4-*h*]quinolin-2(1H)-one (2.25). To a solution of 8-aminoquinolin-7-ol (250 mg, 1 eq, 1.56 mmol) in DMF (4 mL), di(1H-imidazol-1-yl)methanone (506 mg, 2 eq, 3.12 mmol) was added under an argon atmosphere. The mixture was stirred at 80 °C overnight. After cooling, H₂O (10 mL) was added to the reaction mixture and the solution was extracted with EtOAc (3 \times 20 mL). The combined organic layers were purified via flash column chromatography (hexane:EtOAc 0-100%). Yield: 130 mg (0.70 mmol, 45%). ¹H NMR (300 MHz, DMSO-*d*₆): δ 12.62 (s, 1H), 8.92 (dd, *J* = 4.2, 1.7 Hz, 1H), 8.45 (dd, *J* = 8.5, 1.7 Hz, 1H), 7.80 – 7.65 (m, 2H), 7.54 (dd, *J* = 8.4, 4.2 Hz, 1H). ¹³C NMR (101 MHz, DMSO-*d*₆): δ 154.91, 150.58, 142.23, 137.10, 134.34, 125.67, 124.99, 121.76, 120.68, 111.34. HR-MS (ESI) (*m/z*): [M+H]⁺ calcd. for [C₁₀H₇N₂O₂]⁺, 187.0502; found, 187.0504.



Oxazolo[5,4-h]quinoline-2(1H)-thione (2.26). To a solution of 8-aminoquinolin-7-ol (90.0 mg, 1 eq, 562 μmol) in DMF (2 mL), di(1H-imidazol-1-yl)methanethione (200 mg, 2 eq, 1.12 mmol) was added under an argon atmosphere. The mixture was stirred at 80 $^\circ\text{C}$ overnight. After cooling, H₂O (10 mL) was added to the reaction mixture and the solution was extracted with EtOAc (3 \times 20 mL). The combined organic layers were purified via flash column chromatography (hexane:EtOAc 0-100%). Yield: 100 mg (494 μmol , 88%). ¹H NMR (400 MHz, DMSO-*d*₆): δ 8.99 (dd, *J* = 4.3, 1.6 Hz, 1H), 8.53 (dd, *J* = 8.4, 1.7 Hz, 1H), 7.92 (d, *J* = 8.9 Hz, 1H), 7.86 (d, *J* = 8.9 Hz, 1H), 7.63 (dd, *J* = 8.4, 4.3 Hz, 1H). ¹³C NMR (101 MHz, DMSO-*d*₆): δ 180.22, 151.08, 147.88, 137.18, 134.33, 125.70, 124.13, 121.42, 111.23. HR-MS (ESI) (*m/z*): [M+H]⁺ calcd. for [C₁₀H₇N₂OS]⁺, 203.0274; found, 203.0275.



7-Nitroquinolin-8-amine (2.27a). The compound was synthesized by using a modified literature procedure.⁶² To a solution of 7-nitroquinoline (5.0 g, 1 eq, 29 mmol) and hydroxylamine hydrochloride (10 g, 5 eq, 0.14 mol) in EtOH (100 mL), a solution of potassium hydroxide (9.7 g, 4.6 mL, 6 eq, 0.17 mol) in absolute EtOH (100 mL) was added dropwise. The mixture was stirred at 50 $^\circ\text{C}$ for 1 h. After cooling, the reaction mixture was poured into iced water (20 mL) and left overnight. The yellow precipitates were filtered and washed with water to give a product. Yield: 5.27 g (27.9 mmol, 97%). ¹H NMR (300 MHz, DMSO-*d*₆): δ 8.91 (dd, *J* = 4.3, 1.7 Hz, 1H), 8.42

(s, 2H), 8.35 (dd, $J = 8.2, 1.7$ Hz, 1H), 8.04 (d, $J = 9.5$ Hz, 1H), 7.77 (dd, $J = 8.2, 4.3$ Hz, 1H), 7.10 (d, $J = 9.4$ Hz, 1H).

Quinoline-7,8-diamine (2.27b). To a solution of 7-nitroquinolin-8-amine (500 mg, 1 eq, 2.64 mmol) in EtOH (40 mL), Pd/C (141 mg, 10% Wt, 0.05 eq, 132 μ mol) was added. The reaction proceeded with H₂ 50 °C overnight. The reaction is continued until the yellow color of the mixture disappears. After cooling, the resulting solution was filtered and concentrated in vacuo to give the product as a brown solid, which was directly used for the subsequent reaction without any further separation or purification. Yield: 385 mg (2.42 mmol, 91.5%). ¹H NMR (300 MHz, DMSO-*d*₆): δ 8.59 (dd, $J = 4.2, 1.8$ Hz, 1H), 8.00 (dd, $J = 8.1, 1.8$ Hz, 1H), 7.16 – 6.97 (m, 3H), 5.02 (d, $J = 6.7$ Hz, 4H).

1,3-Dihydro-2H-imidazo[4,5-h]quinolin-2-one (2.27). To a solution of quinoline-7,8-diamine (200 mg, 1 eq, 1.26 mmol) in DMF (5 mL), di(1H-imidazol-1-yl)methanone (224 mg, 1.1 eq, 1.38 mmol) was added under an argon atmosphere. The mixture was stirred at room temperature overnight. After stirring, H₂O (10 mL) was added to the reaction mixture and the solution was extracted with EtOAc (3 \times 20 mL). After removal of the DMF in vacuo, the resulting white solid was washed with H₂O and dried on high vacuum to give the product as a white solid. Yield: 140 mg (756 μ mol, 60%). ¹H NMR (300 MHz, DMSO-*d*₆): δ 11.56 (s, 1H), 11.01 (s, 1H), 8.81 (dd, $J = 4.2, 1.7$ Hz, 1H), 8.33 (dd, $J = 8.4, 1.7$ Hz, 1H), 7.58 (d, $J = 8.5$ Hz, 1H), 7.43 – 7.33 (m, 2H). ¹³C NMR (101 MHz, DMSO-*d*₆): δ 155.27, 149.52, 136.78, 134.37, 128.27, 123.78, 123.22, 120.41, 119.00, 111.30. HR-MS (ESI) (m/z): [M+H]⁺ calcd. for [C₁₀H₈N₃O]⁺, 186.0662; found, 186.0661.

3-Methyl-1,3-dihydro-2H-imidazo[4,5-h]quinolin-2-one (2.28). To a solution of sodium hydride (19.4 mg, 60% Wt, 0.9 eq, 486 μ mol) in DMF (3 mL), 1,3-dihydro-2H-imidazo[4,5-

h]quinolin-2-one (100 mg, 1 eq, 540 μmol) in 2 mL DMF was added and stirred for 30 min. A solution of iodomethane (84.3 mg, 37.0 μL , 1.1 eq, 594 μmol) in 2 mL of DMF was added at once to the mixture under an ice bath. The mixture was stirred at room temperature overnight. After the overnight reaction, H_2O (10 mL) was added to the reaction mixture and the solution was extracted with EtOAc (3 \times 20 mL). The combined organic layers were washed with brine, dried over MgSO_4 , filtered, and concentrated in vacuo. The crude product was purified via flash column chromatography (hexane:EtOAc 10-70%) to give the product. Yield: 50 mg (0.25 mmol, 46 %). ^1H NMR (400 MHz, $\text{DMSO-}d_6$): δ 11.81 (s, 1H), 8.83 (dd, $J = 4.2, 1.7$ Hz, 1H), 8.36 (dd, $J = 8.3, 1.7$ Hz, 1H), 7.67 (d, $J = 8.6$ Hz, 1H), 7.58 (d, $J = 8.6$ Hz, 1H), 7.41 (dd, $J = 8.3, 4.2$ Hz, 1H), 3.42 (s, 3H). ^{13}C NMR (101 MHz, $\text{DMSO-}d_6$): δ 154.52, 149.72, 136.85, 134.23, 129.50, 123.47, 122.43, 120.45, 119.16, 110.35, 26.90. HR-MS (ESI) (m/z): $[\text{M}+\text{H}]^+$ calcd. for $[\text{C}_{11}\text{H}_{10}\text{N}_3\text{O}]^+$, 200.0818; found, 200.0817.

1H-Imidazo[4,5-h]quinoline (2.29). The compound was synthesized by using a modified literature procedure.⁶³ Quinoline-7,8-diamine (29b) (180 mg, 1 eq, 1.13 mmol), N,N-dimethylformamide (579 mg, 613 μL , 7 eq, 7.92 mmol) and hydrogen chloride (7 mL, 37% Wt, 9e+1 eq, 0.1 mol) was introduced into a microwave reaction vessel (10 mL) with a magnetic stirrer. The reaction vessel was sealed, and the reaction mixture was stirred at room temperature for 1 min. The reaction mixture was heated at 150 $^\circ\text{C}$ for 2 min under microwave reaction. After cooling, water (10 mL) was added. Then, the reaction mixture was neutralized by solid Na_2CO_3 till slightly basic pH (8–9) to get the precipitate. The solid was filtered, washed repeatedly with water, dried, and recrystallized using ethanol to afford the product. Yield: 107 mg (632 μmol , 56%). ^1H NMR (300 MHz, $\text{DMSO-}d_6$): δ 8.92 (dd, $J = 4.4, 1.7$ Hz, 1H), 8.47 (dd, $J = 8.2, 1.7$ Hz, 1H), 8.34 (s, 1H), 7.88 (d, $J = 8.7$ Hz, 1H), 7.72 (d, $J = 8.7$ Hz, 1H), 7.54 (dd, $J = 8.2, 4.3$ Hz, 1H). ^{13}C NMR

(101 MHz, DMSO-*d*₆): δ 148.88, 142.78, 141.36, 137.74, 136.60, 128.86, 124.67, 121.55, 120.50, 120.03. HR-MS (ESI) (*m/z*): [M+H]⁺ calcd. for [C₁₀H₈N₃]⁺, 170.0713; found, 170.0712.

1H-[1,2,3]Triazolo[4,5-h]quinoline (2.30). To quinoline-7,8-diamine (240 mg, 1 eq, 1.51 mmol) in water (2 mL) and AcOH (1 mL), sodium nitrite (156 mg, 1.5 eq, 2.26 mmol) in water (2 mL) was added drop-wise. The mixture was stirred at room temperature overnight. The resulting brown solid was filtered, washed with water, and dried under a high vacuum. Yield: 140 mg (0.823 mmol, 55%). ¹H NMR (300 MHz, DMSO-*d*₆): δ 9.03 (dd, *J* = 4.5, 1.7 Hz, 1H), 8.57 (d, *J* = 8.2 Hz, 1H), 8.10 (s, 1H), 7.88 (s, 1H), 7.72 (dd, *J* = 8.3, 4.5 Hz, 1H). ¹³C NMR (101 MHz, DMSO-*d*₆): δ 149.89, 144.48, 136.95, 131.02, 127.02, 124.63, 122.58, 118.30, 111.86. HR-MS (ESI) (*m/z*): [M+H]⁺ calcd. for [C₉H₇N₄]⁺, 171.0665; found, 171.0665.

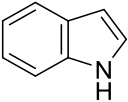
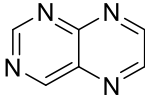
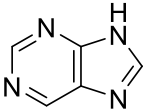
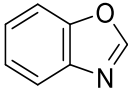
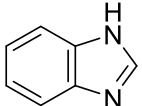
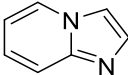
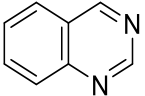
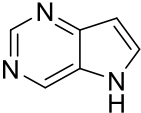
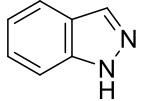
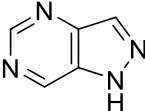
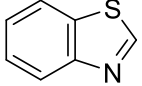
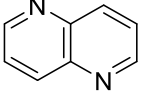
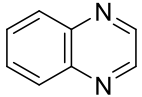
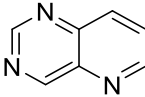
2-(Dimethylamino)phenol (2.31). To a solution of 2-aminophenol (900 mg, 1 eq, 8.25 mmol) in MeOH (30 mL), 37% formaldehyde (1.67 g, 1.54 mL, 37% Wt, 2.5 eq, 20.6 mmol) was added under argon. After stirring for 30 minutes at room temperature, Pd/C (439 mg, 10% Wt, 0.05 eq, 412 μ mol) was added. The reaction proceeded with H₂ at room temperature for 4.5 h. The resulting solution was filtered, concentrated in vacuo, and purified via flash column chromatography (hexane:EtOAc 0-50%) to give the product as white solids. Yield: 811 mg (5.91 mmol, 72%). ¹H NMR (300 MHz, CDCl₃): δ 7.17 (dd, *J* = 7.8, 1.6 Hz, 1H), 7.05 (td, *J* = 7.7, 1.6 Hz, 1H), 6.93 (dd, *J* = 8.0, 1.5 Hz, 1H), 6.86 (td, *J* = 7.6, 1.6 Hz, 1H), 2.65 (s, 7H). ¹³C NMR (101 MHz, CDCl₃): δ 151.53, 140.34, 126.30, 120.80, 120.10, 114.25, 45.29. HR-MS (ESI) (*m/z*): [M+H]⁺ calcd. for [C₈H₁₂NO]⁺, 138.0913; found, 138.0913.

8-Methoxyquinazoline (2.33). To a solution of quinazolin-8-ol (100 mg, 1 Eq, 684 μ mol) in THF (5 mL), potassium tert-butoxide (422 mg, 473 μ L, 20% Wt, 1.1 Eq, 753 μ mol) was added under argon. The reaction was carried out for 1 h under reflux at 60 °C. Subsequently, a solution of

iodomethane (97.1 mg, 42.6 μ L, 1 Eq, 684 μ mol) was added at room temperature. The reaction was carried out at room temperature overnight. After the overnight reaction, H₂O (10 mL) was added to the reaction mixture and the solution was extracted with EtOAc (3 \times 20 mL). The combined organic layers were washed with brine, dried over MgSO₄, filtered, and concentrated in vacuo. The crude product was purified via flash column chromatography (hexane:EtOAc 10-70%) to give the product. Yield: 62 mg (0.39 mmol, 57 %). ¹H NMR (400 MHz, CDCl₃): δ 9.43 (s, 1H), 9.38 (s, 1H), 7.63 (t, *J* = 8.0 Hz, 1H), 7.54 (dd, *J* = 8.2, 1.2 Hz, 1H), 7.30 (d, *J* = 1.2 Hz, 1H), 4.13 (s, 3H). ¹³C NMR (101 MHz, CDCl₃): δ 159.87, 154.81, 154.25, 142.23, 128.50, 125.98, 118.64, 112.09, 56.31. HR-MS (ESI) (*m/z*): [M+H]⁺ calcd. for [C₉H₉N₂O]⁺, 161.0709; found, 161.0710.

Quinoline and its Isoesters in DrugBank Database

Table 2.S1. Aromatic heterocycles used to replace quinoline in the design of 8-HQ MBIs. The frequency of occurrence as a substructure in DrugBank database is listed. The listed number of FDA-approved drugs also includes drugs classified as nutraceuticals, illicit, withdrawn, investigational, and experimental.

Scaffolds	Frequency as substructure in FDA-approved drugs	Scaffolds	Frequency as substructure in FDA-approved drugs
 1H-indole	464	 pteridine	39
 9H-purine	447	 benzo[d]oxazole	28
 1H-benzo[d]imidazole	192	 imidazo[1,2-a]pyridine	21
 quinazoline	132	 5H-pyrrolo[3,2-d]pyrimidine	17
 1H-indazole	71	 1H-pyrazolo[4,3-d]pyrimidine	12
 benzo[d]thiazole	50	 1,5-naphthyridine	4
 quinoxaline	39	 pyrido[3,2-d]pyrimidine	3

8-Hydroxyquinoline (8-HQ) and its MBIs bound to metals in CCDC Database

Table 2.S2. Crystal structures containing 8-HQ and its MBIs bound to metals in Cambridge Crystallographic Data Centre (CCDC) database. The number of structures and refcodes (entry ID) are listed. Maximum five refcodes are shown when the number of result structures are over 10. No result was obtained for MBIs that are not reported below.

MBIs	Number of HITs	Refcodes (Entry ID)	MBIs	Number of HITs	Refcodes (Entry ID)
8-HQ	> 2300	CATXON (Zn) QOVFOZ (Re) XOPSIH (Ni) FORQIM01 (Ru) ELIT0J01 (Fe)	17	4	JIDTAU (Zn) LAQWIK (Zr) PUXZAK (Co) QUXWUC (Co)
19	54	ADAZIP (Zn) AKEXUJ (Cu) CEZCAL (Co) COGJUE (Au) SANNAX (Ni)	7	3	SIYQOG (Zn) BIYPOP (Cu) BIYPUV (Cu)
5	23	RURVIL (Zn) DICXAR (Cu) GIPMOH (Co) LERROR (Ni) NIKFAO (Fe)	2	2	GILLIZ (Ru) EYABEM (Ir)
3	20	FOXPOA (Gd) LUTNUL (Pt) VEYTIE (Nd) XOXMAZ (Al) ZOGJOX (Ir)	21	1	FAZXEL (Zn)
13	19	DAZTED (Zn) CINCUX (Fe) EGMPPT (Pt) GOXCAX (Au) IMPACU (Cu)	29	1	ACAWEJ (Ir)

Published pK_a and $\log P/D_{7.4}$ Values

Table 2.S3. Published pK_a values.

MBI	Published pK_a
8-HQ	4.92, 9.7 ⁶⁴
1	3.41, 8.65 ⁶⁵
2	0.90, 8.65 ⁶⁵
3	2.85, 10.01 ⁶⁵
4	2.00, 8.95 ⁶⁶
5	-0.17, 7.89 ⁶⁶⁻⁶⁷
10	5.3, 9.5 ⁶⁸
11	8.6 ⁶⁹
13	8.9 ⁷⁰

Single Crystal X-ray Diffraction

Suitable crystals of $[(\text{Tp}^{\text{Ph,Me}})\text{Zn}(\text{MBI})]$ ($\text{Tp}^{\text{Ph,Me}}$ = hydrotris(3,5-phenylmethylpyrazolyl)borate) were selected and data was collected at 100 K on a Bruker APEX-II Ultra diffractometer with a Mo-K α Microfocus Rotating Anode and a APEX-II CCD area detector or a Bruker Kappa diffractometer equipped with a Bruker X8 APEX II Mo sealed tube and a Bruker APEX-II CCD. The data were integrated using the Bruker SAINT Software program and scaled using the SADABS software program. The structure was solved with the ShelXT⁷¹ structure solution program using direct methods and refined with the XL⁷² refinement package using least squares minimization using Olex2.⁷³ The crystal data files were deposited into the Cambridge Crystallographic Data Centre (CCDC). Crystallographic data collection and refinement information is listed in Table S1. Disordered solvent was treated with the PLATON SQUEEZE⁷⁴ function in $[(\text{Tp}^{\text{Ph,Me}})\text{Zn}(\mathbf{2.8})]$, $[(\text{Tp}^{\text{Ph,Me}})\text{Zn}(\mathbf{2.9})]$, $[(\text{Tp}^{\text{Ph,Me}})\text{Zn}(\mathbf{2.13})]$, $[(\text{Tp}^{\text{Ph,Me}})\text{Zn}(\mathbf{2.20})]$, $[(\text{Tp}^{\text{Ph,Me}})\text{Zn}(\mathbf{2.24})]$, $[(\text{Tp}^{\text{Ph,Me}})\text{Zn}(\mathbf{2.26})]$, and $[(\text{Tp}^{\text{Ph,Me}})\text{Zn}(\mathbf{2.29})]$. Crystallographic data for $[(\text{Tp}^{\text{Ph,Me}})\text{Zn}(\mathbf{8-HQ})]$ has been previously reported under different crystallization conditions using heptane vapor diffused into a toluene solution of $[(\text{Tp}^{\text{Ph,Me}})\text{Zn}(\mathbf{8-HQ})]$.⁷⁵ Here, single crystals of $[(\text{Tp}^{\text{Ph,Me}})\text{Zn}(\mathbf{8-HQ})]$ were obtained by diffusion of pentane vapor into a benzene solution of $[(\text{Tp}^{\text{Ph,Me}})\text{Zn}(\mathbf{8-HQ})]$, which resulted in the complex crystallizing in a different space group; however, the structural parameters, including bond angles and bond distances, are similar for both reported structures.

Table 2.S4. Crystal data and structure refinement for [(Tp^{Ph,Me})Zn(MBI)] complexes.

Compound	[(Tp ^{Ph,Me})Zn(2.1)]	[(Tp ^{Ph,Me})Zn(2.2)]	[(Tp ^{Ph,Me})Zn(2.3)]
Identification code	2123145	2123148	2123152
Empirical formula	C ₃₈ H ₃₃ BN ₈ OZn	C _{43.5} H ₄₂ BN ₈ OZn	C ₇₂ H ₆₈ B ₂ ClN ₁₄ O ₂ Zn ₂
Formula weight	693.9	769.03	1349.21
Temperature/K	100	100	100
Crystal system	monoclinic	triclinic	orthorhombic
Space group	<i>P</i> 2 ₁ / <i>c</i>	<i>P</i> -1	<i>P</i> 2 ₁ 2 ₁ 2 ₁
<i>a</i> /Å	17.4900(6)	11.1106(9)	15.6701(15)
<i>b</i> /Å	22.4889(8)	17.6328(14)	19.8460(19)
<i>c</i> /Å	17.1032(6)	20.1966(18)	42.050(3)
α /°	90	97.248(3)	90
β /°	90.310(2)	91.365(3)	90
γ /°	90	100.322(3)	90
Volume/Å ³	6727.1(4)	3857.2(6)	13077(2)
<i>Z</i>	8	4	8
ρ_{calc} /cm ³	1.37	1.324	1.371
μ /mm ⁻¹	1.363	0.683	0.833
F(000)	2880	1608	5608
Crystal size/mm ³	0.1 × 0.1 × 0.1	0.1 × 0.1 × 0.1	0.1 × 0.1 × 0.1
Radiation	CuK α (λ = 1.54178)	MoK α (λ = 0.71073)	MoK α (λ = 0.71073)
2 θ range for data collection/°	3.928 to 140.324	4.58 to 52.128	3.836 to 50.71
Index ranges	-21 ≤ <i>h</i> ≤ 21, -27 ≤ <i>k</i> ≤ 27, -19 ≤ <i>l</i> ≤ 20	-13 ≤ <i>h</i> ≤ 13, -21 ≤ <i>k</i> ≤ 21, -24 ≤ <i>l</i> ≤ 24	-18 ≤ <i>h</i> ≤ 18, -23 ≤ <i>k</i> ≤ 23, -50 ≤ <i>l</i> ≤ 50
Reflections collected	127039	95437	119143
Independent reflections	12761 [<i>R</i> _{int} = 0.0361, <i>R</i> _{sigma} = 0.0180]	15206 [<i>R</i> _{int} = 0.0832, <i>R</i> _{sigma} = 0.0524]	23900 [<i>R</i> _{int} = 0.0764, <i>R</i> _{sigma} = 0.0636]
Data/restraints/parameters	12761/0/890	15206/0/990	23900/0/1692
Goodness-of-fit on F ²	1.015	1.035	0.562
Final <i>R</i> indexes [<i>I</i> ≥ 2 σ (<i>I</i>)]	<i>R</i> ₁ = 0.0294, <i>wR</i> ₂ = 0.0744	<i>R</i> ₁ = 0.0464, <i>wR</i> ₂ = 0.1077	<i>R</i> ₁ = 0.0466, <i>wR</i> ₂ = 0.1227
Final <i>R</i> indexes [all data]	<i>R</i> ₁ = 0.0325, <i>wR</i> ₂ = 0.0772	<i>R</i> ₁ = 0.0609, <i>wR</i> ₂ = 0.1149	<i>R</i> ₁ = 0.0639, <i>wR</i> ₂ = 0.1453
Largest diff. peak/hole / e Å ⁻³	0.27/-0.46	1.24/-0.87	0.80/-0.60

Table 2.S4 (continued). Crystal data and structure refinement for [(Tp^{Ph,Me})Zn(MBI)] complexes.

Compound	[(Tp ^{Ph,Me})Zn(2.4)]	[(Tp ^{Ph,Me})Zn(2.5)]	[(Tp ^{Ph,Me})Zn(2.6)]
Identification code	2123159	2123149	2123147
Empirical formula	C ₇₄ H ₆₈ B ₂ N ₁₈ O ₄ Zn ₂	C ₃₆ H ₃₃ BN ₁₀ O ₂ Zn	C ₃₇ H _{32.9} BN ₇ O _{2.4} Zn
Formula weight	1425.82	713.9	69.07
Temperature/K	100	100	100
Crystal system	orthorhombic	orthorhombic	monoclinic
Space group	<i>Pca</i> 2 ₁	<i>Pca</i> 2 ₁	<i>P</i> 2 ₁ / <i>c</i>
<i>a</i> /Å	11.8855(5)	11.894	11.589(8)
<i>b</i> /Å	23.2048(10)	23.196	18.006(13)
<i>c</i> /Å	24.3520(11)	24.379	15.803(11)
<i>α</i> /°	90	90	90
<i>β</i> /°	90	90	101.320(8)
<i>γ</i> /°	90	90	90
Volume/Å ³	6716.3(5)	6726	3233(4)
<i>Z</i>	4	8	40
ρ_{calc} /cm ³	1.41	1.41	1.419
μ /mm ⁻¹	0.781	0.781	0.808
F(000)	2960	2960	1433
Crystal size/mm ³	0.1 × 0.1 × 0.1	0.1 × 0.1 × 0.1	0.1 × 0.1 × 0.1
Radiation	MoK α (λ = 0.71073)	MoK α (λ = 0.71073)	MoK α (λ = 0.71073)
2 θ range for data collection/°	4.85 to 52.792	4.906 to 51.958	3.468 to 51.362
Index ranges	-14 ≤ <i>h</i> ≤ 14, -29 ≤ <i>k</i> ≤ 29, -30 ≤ <i>l</i> ≤ 30	-14 ≤ <i>h</i> ≤ 14, -28 ≤ <i>k</i> ≤ 28, -30 ≤ <i>l</i> ≤ 30	-14 ≤ <i>h</i> ≤ 14, -21 ≤ <i>k</i> ≤ 21, -19 ≤ <i>l</i> ≤ 19
Reflections collected	160351	70994	36816
Independent reflections	13749 [<i>R</i> _{int} = 0.1161, <i>R</i> _{sigma} = 0.0485]	13129 [<i>R</i> _{int} = 0.0924, <i>R</i> _{sigma} = 0.0638]	6136 [<i>R</i> _{int} = 0.0671, <i>R</i> _{sigma} = 0.0451]
Data/restraints/parameters	13749/1/914	13129/1/918	6136/0/449
Goodness-of-fit on F ²	1.052	1.031	0.91
Final <i>R</i> indexes [<i>I</i> ≥ 2 σ (<i>I</i>)]	<i>R</i> ₁ = 0.0657, <i>wR</i> ₂ = 0.1627	<i>R</i> ₁ = 0.0404, <i>wR</i> ₂ = 0.0850	<i>R</i> ₁ = 0.0318, <i>wR</i> ₂ = 0.0731
Final <i>R</i> indexes [all data]	<i>R</i> ₁ = 0.0831, <i>wR</i> ₂ = 0.1784	<i>R</i> ₁ = 0.0503, <i>wR</i> ₂ = 0.0894	<i>R</i> ₁ = 0.0460, <i>wR</i> ₂ = 0.0813
Largest diff. peak/hole / e Å ⁻³	3.51/-0.80	0.51/-0.34	0.29/-0.35

Table 2.S4 (continued). Crystal data and structure refinement for [(Tp^{Ph,Me})Zn(MBI)] complexes.

Compound	[(Tp ^{Ph,Me})Zn(2.7)]	[(Tp ^{Ph,Me})Zn(2.8)]	[(Tp ^{Ph,Me})Zn(2.9)]
Identification code	2123146	2123162	2123153
Empirical formula	C ₃₇ H ₃₂ BN ₇ OSZn	C ₃₈ H ₃₅ BN ₈ OZn	C ₃₇ H ₃₃ BN ₈ OZn
Formula weight	698.93	695.92	681.89
Temperature/K	100	100	100
Crystal system	monoclinic	monoclinic	monoclinic
Space group	<i>P</i> 2 ₁ / <i>n</i>	<i>P</i> 2 ₁ / <i>n</i>	<i>C</i> 2/ <i>c</i>
<i>a</i> /Å	9.3276(2)	9.8607(3)	28.6891(6)
<i>b</i> /Å	17.1077(3)	19.0082(7)	13.4206(3)
<i>c</i> /Å	21.3101(4)	41.1646(14)	19.8403(4)
α /°	90	90	90
β /°	97.9870(10)	94.0070(10)	109.1820(10)
γ /°	90	90	90
Volume/Å ³	3367.55(11)	7696.8(5)	7214.9(3)
<i>Z</i>	4	8	8
ρ_{calc} /cm ³	1.379	1.201	1.256
μ /mm ⁻¹	0.833	0.677	0.721
F(000)	1448	2896	2832
Crystal size/mm ³	0.348 × 0.234 × 0.204	0.1 × 0.1 × 0.1	0.1 × 0.1 × 0.1
Radiation	MoK α (λ = 0.71073)	MoK α (λ = 0.71073)	MoK α (λ = 0.71073)
2 θ range for data collection/°	3.064 to 61.156	4.662 to 52.142	3.006 to 54.264
Index ranges	-12 ≤ <i>h</i> ≤ 13, -23 ≤ <i>k</i> ≤ 18, -30 ≤ <i>l</i> ≤ 30	-12 ≤ <i>h</i> ≤ 12, -23 ≤ <i>k</i> ≤ 23, -50 ≤ <i>l</i> ≤ 50	-36 ≤ <i>h</i> ≤ 34, -17 ≤ <i>k</i> ≤ 17, -15 ≤ <i>l</i> ≤ 25
Reflections collected	20133	205654	29635
Independent reflections	9802 [<i>R</i> _{int} = 0.0469, <i>R</i> _{sigma} = 0.0687]	15220 [<i>R</i> _{int} = 0.1724, <i>R</i> _{sigma} = 0.0601]	7982 [<i>R</i> _{int} = 0.0679, <i>R</i> _{sigma} = 0.0635]
Data/restraints/parameters	9802/0/436	15220/0/891	7982/0/436
Goodness-of-fit on F ²	0.879	1.012	1.02
Final <i>R</i> indexes [<i>I</i> ≥ 2 σ (<i>I</i>)]	<i>R</i> ₁ = 0.0398, <i>wR</i> ₂ = 0.1191	<i>R</i> ₁ = 0.0474, <i>wR</i> ₂ = 0.1119	<i>R</i> ₁ = 0.0402, <i>wR</i> ₂ = 0.0901
Final <i>R</i> indexes [all data]	<i>R</i> ₁ = 0.0520, <i>wR</i> ₂ = 0.1318	<i>R</i> ₁ = 0.0869, <i>wR</i> ₂ = 0.1365	<i>R</i> ₁ = 0.0652, <i>wR</i> ₂ = 0.1009
Largest diff. peak/hole / e Å ⁻³	0.57/-0.37	0.37/-0.57	0.27/-0.49

Table 2.S4 (continued). Crystal data and structure refinement for [(Tp^{Ph,Me})Zn(MBI)] complexes.

Compound	[(Tp ^{Ph,Me})Zn(2.11)]	[(Tp ^{Ph,Me})Zn(2.13)]	[(Tp ^{Ph,Me})Zn(2.16)]
Identification code	2123151	2123154	2123155
Empirical formula	C ₄₆ H ₄₂ BN ₈ OZn	C ₃₆ H ₃₃ BN ₁₀ OZn	C ₃₆ H ₃₂ BN ₉ OZn
Formula weight	799.05	73.46	682.88
Temperature/K	100	100	100
Crystal system	triclinic	triclinic	triclinic
Space group	<i>P</i> -1	<i>P</i> -1	<i>P</i> -1
<i>a</i> /Å	11.4407(7)	11.6433(16)	11.8190(17)
<i>b</i> /Å	12.0685(7)	13.3913(18)	12.708(2)
<i>c</i> /Å	16.9672(10)	13.8012(19)	13.3860(15)
α /°	95.132(2)	65.2980(10)	113.708(5)
β /°	101.591(2)	84.570(2)	92.837(7)
γ /°	116.401(2)	69.1220(10)	116.693(6)
Volume/Å ³	2012.4(2)	1822.9(4)	1578.3(4)
<i>Z</i>	2	19	2
ρ_{calc} /cm ³	1.319	1.272	1.437
μ /mm ⁻¹	0.657	0.716	0.825
F(000)	834	724	708
Crystal size/mm ³	0.4 × 0.2 × 0.2	0.28 × 0.155 × 0.095	0.1 × 0.1 × 0.1
Radiation	MoK α (λ = 0.71073)	MoK α (λ = 0.71073)	MoK α (λ = 0.71073)
2 θ range for data collection/°	2.502 to 52.162	3.254 to 52.336	3.898 to 52.894
Index ranges	-14 ≤ <i>h</i> ≤ 14, -10 ≤ <i>k</i> ≤ 14, -20 ≤ <i>l</i> ≤ 20	-14 ≤ <i>h</i> ≤ 14, -16 ≤ <i>k</i> ≤ 16, -17 ≤ <i>l</i> ≤ 17	-14 ≤ <i>h</i> ≤ 14, -15 ≤ <i>k</i> ≤ 15, -16 ≤ <i>l</i> ≤ 16
Reflections collected	17398	37417	40271
Independent reflections	7964 [<i>R</i> _{int} = 0.0287, <i>R</i> _{sigma} = 0.0394]	7288 [<i>R</i> _{int} = 0.0358, <i>R</i> _{sigma} = 0.0246]	6480 [<i>R</i> _{int} = 0.1225, <i>R</i> _{sigma} = 0.0627]
Data/restraints/parameters	7964/0/521	7288/0/446	6480/0/440
Goodness-of-fit on F ²	1	0.673	1.055
Final <i>R</i> indexes [<i>I</i> ≥ 2 σ (<i>I</i>)]	<i>R</i> ₁ = 0.0336, <i>wR</i> ₂ = 0.0830	<i>R</i> ₁ = 0.0289, <i>wR</i> ₂ = 0.0751	<i>R</i> ₁ = 0.0377, <i>wR</i> ₂ = 0.0893
Final <i>R</i> indexes [all data]	<i>R</i> ₁ = 0.0423, <i>wR</i> ₂ = 0.0876	<i>R</i> ₁ = 0.0330, <i>wR</i> ₂ = 0.0792	<i>R</i> ₁ = 0.0568, <i>wR</i> ₂ = 0.1002
Largest diff. peak/hole / e Å ⁻³	0.37/-0.24	0.39/-0.26	0.44/-1.00

Table 2.S4 (continued). Crystal data and structure refinement for [(Tp^{Ph,Me})Zn(MBI)] complexes.

Compound	[(Tp ^{Ph,Me})Zn(2.18)]	[(Tp ^{Ph,Me})Zn(2.19)]	[(Tp ^{Ph,Me})Zn(2.20)]
Identification code	2123165	2123161	2123156
Empirical formula	C ₄₀ H _{37.3} BN ₈ O _{2.1} SZn	C ₃₉ H _{36.5} BN ₉ O ₂ SZn	C ₃₉ H ₃₆ BN ₉ O ₂ SZn
Formula weight	1544.59	771.51	771.01
Temperature/K	100	100	100
Crystal system	monoclinic	triclinic	triclinic
Space group	<i>P</i> 2 ₁ / <i>c</i>	<i>P</i> -1	<i>P</i> -1
<i>a</i> /Å	20.5637(14)	11.7779(9)	11.3435(8)
<i>b</i> /Å	19.3962(11)	17.0987(12)	12.3237(8)
<i>c</i> /Å	18.8559(13)	18.0504(13)	16.1326(10)
<i>α</i> /°	90	90.599(3)	74.745(2)
<i>β</i> /°	90.307(3)	96.178(3)	76.050(2)
<i>γ</i> /°	90	91.210(3)	80.318(2)
Volume/Å ³	7520.7(8)	3612.9(5)	2098.3(2)
<i>Z</i>	4	4	2
$\rho_{\text{calc}}/\text{cm}^3$	1.364	1.418	1.22
μ/mm^{-1}	0.756	0.787	0.678
F(000)	3209	1602	800
Crystal size/mm ³	0.1 × 0.1 × 0.065	0.1 × 0.1 × 0.1	0.1 × 0.1 × 0.1
Radiation	MoK α ($\lambda = 0.71073$)	MoK α ($\lambda = 0.71073$)	MoK α ($\lambda = 0.71073$)
2 θ range for data collection/°	4.484 to 50.08	3.944 to 52.286	4.65 to 51.02
Index ranges	-24 ≤ <i>h</i> ≤ 24, -23 ≤ <i>k</i> ≤ 23, -22 ≤ <i>l</i> ≤ 22	-14 ≤ <i>h</i> ≤ 14, -21 ≤ <i>k</i> ≤ 21, -22 ≤ <i>l</i> ≤ 21	-13 ≤ <i>h</i> ≤ 13, -14 ≤ <i>k</i> ≤ 14, -19 ≤ <i>l</i> ≤ 19
Reflections collected	120948	96046	49430
Independent reflections	13285 [<i>R</i> _{int} = 0.1662, <i>R</i> _{sigma} = 0.0720]	14343 [<i>R</i> _{int} = 0.1321, <i>R</i> _{sigma} = 0.0757]	7759 [<i>R</i> _{int} = 0.1353, <i>R</i> _{sigma} = 0.0861]
Data/restraints/parameters	13285/105/1015	14343/0/963	7759/0/482
Goodness-of-fit on F ²	1.017	1.134	1.028
Final <i>R</i> indexes [<i>I</i> ≥ 2 σ (<i>I</i>)]	<i>R</i> ₁ = 0.0487, <i>wR</i> ₂ = 0.0844	<i>R</i> ₁ = 0.0769, <i>wR</i> ₂ = 0.1977	<i>R</i> ₁ = 0.0431, <i>wR</i> ₂ = 0.0996
Final <i>R</i> indexes [all data]	<i>R</i> ₁ = 0.0925, <i>wR</i> ₂ = 0.1039	<i>R</i> ₁ = 0.0921, <i>wR</i> ₂ = 0.2059	<i>R</i> ₁ = 0.0666, <i>wR</i> ₂ = 0.1090
Largest diff. peak/hole / e Å ⁻³	0.43/-0.48	2.57/-1.21	0.47/-0.54

Table 2.S4 (continued). Crystal data and structure refinement for [(Tp^{Ph,Me})Zn(MBI)] complexes.

Compound	[(Tp ^{Ph,Me})Zn(2.21)]	[(Tp ^{Ph,Me})Zn(2.22)]	[(Tp ^{Ph,Me})Zn(2.23)]
Identification code	2123163	2123157	2123158
Empirical formula	C ₄₃ H ₄₇ BN ₈ O ₃ SZn	C ₁₆ H ₁₄ N ₄ O ₄ S ₄ Zn	C ₄₅ H ₄₄ BN ₉ O ₂ SZn
Formula weight	832.12	519.92	851.13
Temperature/K	100	273.15	100
Crystal system	triclinic	monoclinic	triclinic
Space group	<i>P</i> -1	<i>Cc</i>	<i>P</i> -1
<i>a</i> /Å	12.0675(5)	9.643(3)	11.1900(8)
<i>b</i> /Å	12.7548(6)	16.676(3)	13.2817(13)
<i>c</i> /Å	14.0666(5)	11.899(3)	15.4341(13)
<i>α</i> /°	87.0630(10)	90	106.336(3)
<i>β</i> /°	69.5130(10)	90.065(13)	100.568(3)
<i>γ</i> /°	79.740(2)	90	101.639(3)
Volume/Å ³	1995.60(14)	1913.6(8)	2084.4(3)
<i>Z</i>	2	4	2
ρ_{calc} /cm ³	1.385	1.805	1.356
μ /mm ⁻¹	0.719	1.754	0.689
F(000)	872	1056	888
Crystal size/mm ³	0.1 × 0.1 × 0.1	0.1 × 0.1 × 0.1	0.1 × 0.1 × 0.1
Radiation	MoK α (λ = 0.71073)	MoK α (λ = 0.71073)	MoK α (λ = 0.71073)
2 θ range for data collection/°	4.67 to 52.158	4.88 to 52.164	5.136 to 52.882
Index ranges	-14 ≤ <i>h</i> ≤ 14, -15 ≤ <i>k</i> ≤ 15, -17 ≤ <i>l</i> ≤ 17	-11 ≤ <i>h</i> ≤ 9, -20 ≤ <i>k</i> ≤ 17, -14 ≤ <i>l</i> ≤ 13	-13 ≤ <i>h</i> ≤ 13, -15 ≤ <i>k</i> ≤ 16, -19 ≤ <i>l</i> ≤ 19
Reflections collected	51739	5016	27051
Independent reflections	7895 [<i>R</i> _{int} = 0.0716, <i>R</i> _{sigma} = 0.0399]	2774 [<i>R</i> _{int} = 0.0706, <i>R</i> _{sigma} = 0.1060]	8479 [<i>R</i> _{int} = 0.0661, <i>R</i> _{sigma} = 0.0634]
Data/restraints/parameters	7895/0/520	2774/2/264	8479/0/537
Goodness-of-fit on F ²	0.777	1.068	0.881
Final <i>R</i> indexes [<i>I</i> ≥ 2 σ (<i>I</i>)]	<i>R</i> ₁ = 0.0387, <i>wR</i> ₂ = 0.1023	<i>R</i> ₁ = 0.0527, <i>wR</i> ₂ = 0.1152	<i>R</i> ₁ = 0.0403, <i>wR</i> ₂ = 0.1164
Final <i>R</i> indexes [all data]	<i>R</i> ₁ = 0.0478, <i>wR</i> ₂ = 0.1108	<i>R</i> ₁ = 0.0674, <i>wR</i> ₂ = 0.1261	<i>R</i> ₁ = 0.0522, <i>wR</i> ₂ = 0.1330
Largest diff. peak/hole / e Å ⁻³	1.33/-0.58	0.43/-0.66	0.32/-0.41

Table 2.S4 (continued). Crystal data and structure refinement for [(Tp^{Ph,Me})Zn(MBI)] complexes.

Compound	[(Tp ^{Ph,Me})Zn(2.24)]	[(Tp ^{Ph,Me})Zn(2.25)]	[(Tp ^{Ph,Me})Zn(2.26)]
Identification code	2123160	2123167	2123166
Empirical formula	C ₃₈ H ₃₆ BN ₉ O ₂ SZn	C ₄₀ H ₃₃ BN ₈ O ₂ Zn	C ₄₀ H ₃₃ BN ₈ OSZn
Formula weight	759	733.92	749.98
Temperature/K	100	100	100
Crystal system	triclinic	monoclinic	triclinic
Space group	<i>P</i> -1	<i>P</i> 2 ₁ /n	<i>P</i> -1
<i>a</i> /Å	12.3705(5)	11.3172(4)	9.9046(4)
<i>b</i> /Å	12.4122(6)	23.4823(9)	11.0598(4)
<i>c</i> /Å	16.0318(7)	13.3187(5)	17.8804(8)
α /°	82.815(2)	90	98.590(2)
β /°	88.208(2)	94.0950(10)	98.145(2)
γ /°	68.325(2)	90	90.004(2)
Volume/Å ³	2269.29(18)	3530.5(2)	1916.71(14)
<i>Z</i>	2	4	2
ρ_{calc} /cm ³	1.111	1.381	1.299
μ /mm ⁻¹	0.626	0.744	0.738
F(000)	788	1520	776
Crystal size/mm ³	0.1 × 0.1 × 0.1	0.1 × 0.1 × 0.1	0.1 × 0.1 × 0.1
Radiation	MoK α (λ = 0.71073)	MoK α (λ = 0.71073)	MoK α (λ = 0.71073)
2 θ range for data collection/°	4.406 to 52.168	5.198 to 50.816	4.682 to 50.92
Index ranges	-15 ≤ <i>h</i> ≤ 15, -15 ≤ <i>k</i> ≤ 15, -19 ≤ <i>l</i> ≤ 19	-13 ≤ <i>h</i> ≤ 13, -28 ≤ <i>k</i> ≤ 28, -16 ≤ <i>l</i> ≤ 16	-11 ≤ <i>h</i> ≤ 11, -13 ≤ <i>k</i> ≤ 13, -21 ≤ <i>l</i> ≤ 21
Reflections collected	45143	86779	33004
Independent reflections	8985 [<i>R</i> _{int} = 0.0705, <i>R</i> _{sigma} = 0.0491]	6487 [<i>R</i> _{int} = 0.1023, <i>R</i> _{sigma} = 0.0363]	7022 [<i>R</i> _{int} = 0.0626, <i>R</i> _{sigma} = 0.0433]
Data/restraints/parameters	8985/0/473	6487/0/472	7022/0/472
Goodness-of-fit on F ²	1.022	1.033	1.041
Final <i>R</i> indexes [<i>I</i> ≥ 2 σ (<i>I</i>)]	<i>R</i> ₁ = 0.0366, <i>wR</i> ₂ = 0.0847	<i>R</i> ₁ = 0.0340, <i>wR</i> ₂ = 0.0804	<i>R</i> ₁ = 0.0343, <i>wR</i> ₂ = 0.0799
Final <i>R</i> indexes [all data]	<i>R</i> ₁ = 0.0503, <i>wR</i> ₂ = 0.0909	<i>R</i> ₁ = 0.0450, <i>wR</i> ₂ = 0.0891	<i>R</i> ₁ = 0.0391, <i>wR</i> ₂ = 0.0833
Largest diff. peak/hole / e Å ⁻³	0.30/-0.40	0.28/-0.44	0.69/-0.26

Table 2.S4 (continued). Crystal data and structure refinement for [(Tp^{Ph,Me})Zn(MBI)] complexes.

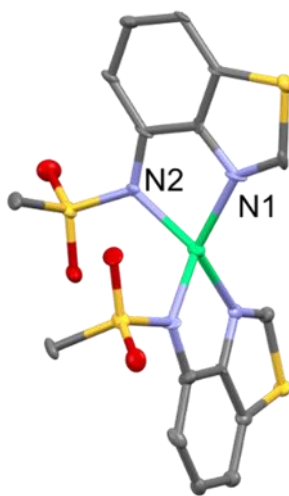
Compound	[(Tp ^{Ph,Me})Zn(2.27)]	[(Tp ^{Ph,Me})Zn(2.28)]	[(Tp ^{Ph,Me})Zn(2.29)]
Identification code	2123170	2123164	2123169
Empirical formula	C ₄₀ H ₃₄ BN ₉ OZn	C ₄₁ H ₃₆ BN ₉ OZn	C ₄₀ H ₃₄ BN ₉ Zn
Formula weight	732.94	746.97	716.94
Temperature/K	100	100	100
Crystal system	monoclinic	triclinic	monoclinic
Space group	<i>P</i> 2 ₁ / <i>n</i>	<i>P</i> -1	<i>P</i> 2 ₁ / <i>n</i>
<i>a</i> /Å	15.9881(14)	12.0443(13)	14.5521(5)
<i>b</i> /Å	12.4420(11)	12.2326(13)	13.3030(5)
<i>c</i> /Å	17.6052(13)	13.1255(14)	18.2540(6)
<i>α</i> /°	90	66.813(2)	90
<i>β</i> /°	102.735(3)	88.069(2)	96.1800(10)
<i>γ</i> /°	90	82.365(2)	90
Volume/Å ³	3415.9(5)	1761.5(3)	3513.2(2)
<i>Z</i>	4	2	4
$\rho_{\text{calc}}/\text{cm}^3$	1.425	1.408	1.355
μ/mm^{-1}	0.768	0.746	0.743
F(000)	1520	776	1488
Crystal size/mm ³	0.1 × 0.1 × 0.1	0.2 × 0.2 × 0.2	0.1 × 0.1 × 0.1
Radiation	MoK α (λ = 0.71073)	MoK α (λ = 0.71073)	MoK α (λ = 0.71073)
2 θ range for data collection/°	4.042 to 50.81	3.376 to 54.502	5.434 to 52.83
Index ranges	-19 ≤ <i>h</i> ≤ 19, -14 ≤ <i>k</i> ≤ 15, -21 ≤ <i>l</i> ≤ 21	-15 ≤ <i>h</i> ≤ 15, -15 ≤ <i>k</i> ≤ 15, -16 ≤ <i>l</i> ≤ 16	-18 ≤ <i>h</i> ≤ 18, -16 ≤ <i>k</i> ≤ 16, -22 ≤ <i>l</i> ≤ 22
Reflections collected	100956	27009	67084
Independent reflections	6271 [<i>R</i> _{int} = 0.1776, <i>R</i> _{sigma} = 0.0578]	7882 [<i>R</i> _{int} = 0.0638, <i>R</i> _{sigma} = 0.0540]	7196 [<i>R</i> _{int} = 0.0539, <i>R</i> _{sigma} = 0.0253]
Data/restraints/parameters	6271/0/472	7882/0/482	7196/0/463
Goodness-of-fit on F ²	1.001	1.037	1.047
Final <i>R</i> indexes [<i>I</i> ≥ 2 σ (<i>I</i>)]	<i>R</i> ₁ = 0.0491, <i>wR</i> ₂ = 0.1282	<i>R</i> ₁ = 0.0380, <i>wR</i> ₂ = 0.0999	<i>R</i> ₁ = 0.0300, <i>wR</i> ₂ = 0.0792
Final <i>R</i> indexes [all data]	<i>R</i> ₁ = 0.0740, <i>wR</i> ₂ = 0.1520	<i>R</i> ₁ = 0.0400, <i>wR</i> ₂ = 0.1018	<i>R</i> ₁ = 0.0356, <i>wR</i> ₂ = 0.0833
Largest diff. peak/hole / e Å ⁻³	0.34/-0.89	0.78/-0.30	0.34/-0.33

Table 2.S4 (continued). Crystal data and structure refinement for [(Tp^{Ph,Me})Zn(MBI)] complexes.

Compound	[(Tp ^{Ph,Me})Zn(2.30)]	[(Tp ^{Ph,Me})Zn(8-HQ)]
Identification code	2123168	2123150
Empirical formula	C ₃₉ H ₃₃ BN ₁₀ Zn	C ₃₉ H ₃₄ BN ₇ OZn
Formula weight	717.93	692.91
Temperature/K	273.15	100
Crystal system	monoclinic	monoclinic
Space group	<i>P</i> 2 ₁ / <i>n</i>	<i>P</i> 2 ₁ / <i>c</i>
<i>a</i> /Å	11.2475(5)	11.6025(3)
<i>b</i> /Å	26.2048(11)	13.9396(3)
<i>c</i> /Å	11.7941(7)	21.5613(4)
<i>α</i> /°	90	90
<i>β</i> /°	94.200(2)	100.3530(10)
<i>γ</i> /°	90	90
Volume/Å ³	3466.8(3)	3430.42(13)
<i>Z</i>	4	4
$\rho_{\text{calc}}/\text{cm}^3$	1.375	1.342
μ/mm^{-1}	0.754	0.759
F(000)	1488	1440
Crystal size/mm ³	0.1 × 0.1 × 0.1	0.5 × 0.4 × 0.4
Radiation	MoK α ($\lambda = 0.71073$)	MoK α ($\lambda = 0.71073$)
2 θ range for data collection/°	3.796 to 50.764	3.496 to 52.086
Index ranges	-13 ≤ <i>h</i> ≤ 13, -28 ≤ <i>k</i> ≤ 31, -14 ≤ <i>l</i> ≤ 14	-14 ≤ <i>h</i> ≤ 14, -17 ≤ <i>k</i> ≤ 17, -26 ≤ <i>l</i> ≤ 21
Reflections collected	36476	20690
Independent reflections	6366 [<i>R</i> _{int} = 0.0763, <i>R</i> _{sigma} = 0.0487]	6756 [<i>R</i> _{int} = 0.0737, <i>R</i> _{sigma} = 0.0517]
Data/restraints/parameters	6366/0/463	6756/0/445
Goodness-of-fit on F ²	1.039	1.068
Final <i>R</i> indexes [<i>I</i> ≥ 2 σ (<i>I</i>)]	<i>R</i> ₁ = 0.0400, <i>wR</i> ₂ = 0.1020	<i>R</i> ₁ = 0.0337, <i>wR</i> ₂ = 0.0926
Final <i>R</i> indexes [all data]	<i>R</i> ₁ = 0.0571, <i>wR</i> ₂ = 0.1145	<i>R</i> ₁ = 0.0393, <i>wR</i> ₂ = 0.0952
Largest diff. peak/hole / e Å ⁻³	0.28/-0.60	0.46/-0.56

Table 2.S5. Selected bond lengths and angles of [Tp^{Ph,Me}Zn(MBI)] complexes with sulfonamide MBIs.

MBI	Binding Mode	Zn-N2 (Å)	Zn-N1 (Å)	N1-Zn-N2 (°)	Tau (°)
2.18	Bidentate	1.969(3)	2.058(3)	82.18(12)	τ_4 , 0.83
		1.970(3)	2.031(3)	81.99(12)	τ_4 , 0.85
2.19	Bidentate	1.984(4)	2.069(5)	81.62(19)	τ_4 , 0.85
		1.976(5)	2.062(5)	81.41(19)	τ_4 , 0.81
2.20	Bidentate	2.013(2)	2.295(2)	75.97(9)	τ_5 , 0.39
2.21	Monodentate	1.9555(18)	-	-	τ_4 , 0.76
2.23	Bidentate	2.1212(19)	2.0664(18)	81.63(7)	τ_5 , 0.61
2.24	Bidentate	2.1839(17)	2.0116(17)	81.04(7)	τ_5 , 0.60



2.22

Figure 2.S1. Crystal structure of [Zn(**2.22**)₂] complex. (ORTEP, 50% probability ellipsoids). Hydrogen atoms were removed for clarity. Color scheme: carbon = gray, nitrogen = blue, oxygen = red, sulfur = yellow, and zinc = green.

IC₅₀ Curves of 8-HQ and MBIs

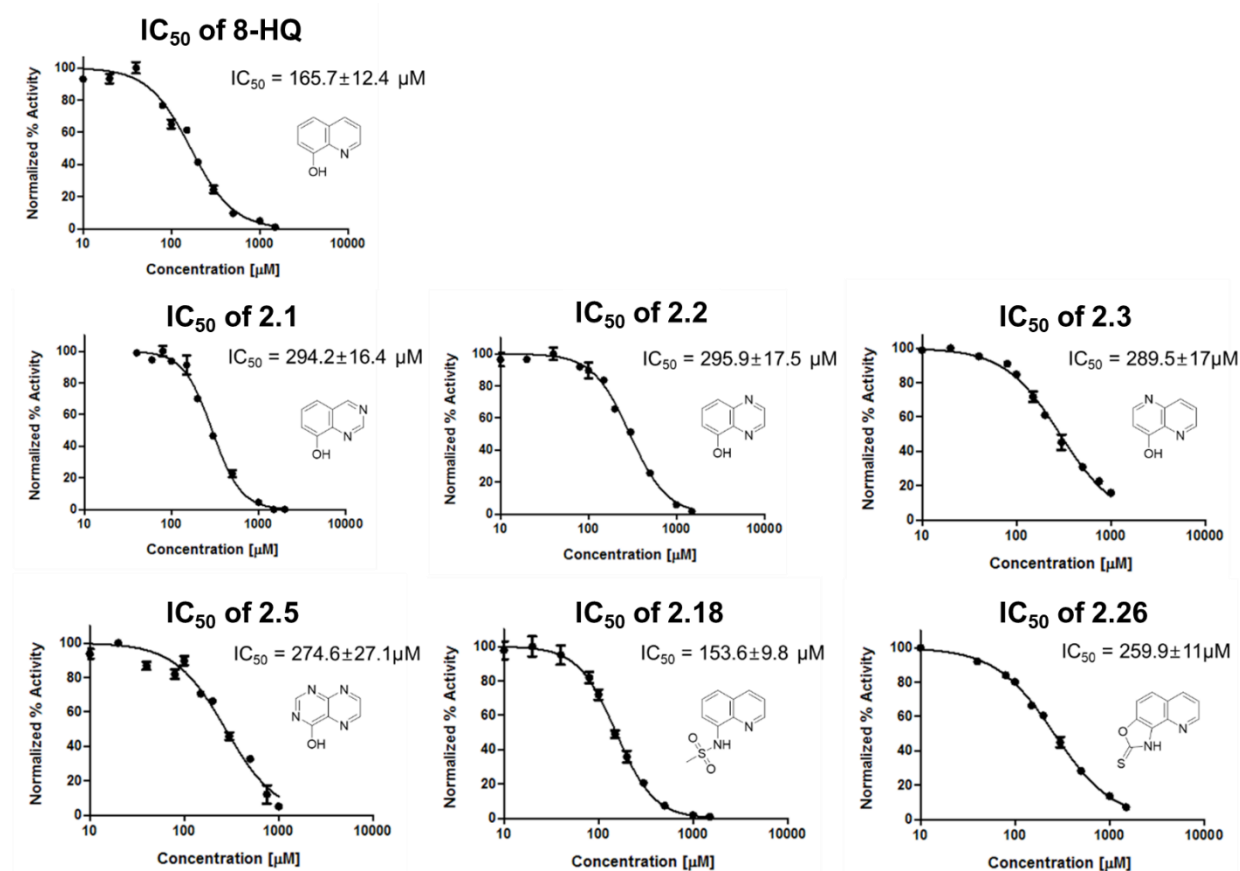


Figure 2.S2. IC₅₀ curves of 8-HQ, MBI 2.1, 2.2, 2.3, 2.5, 2.18, and 2.26 against MMP-2. The assay conditions used to obtain IC₅₀ values are the same as the conditions used to measure percent inhibition values. The range of concentration of the MBIs is between 10 µM and 1000 or 1500 µM depending on compound solubility. 8-HQ gave an IC₅₀ value of 165.7±12.4 µM, which is comparable to the value reported in the original literature report (130±28 µM).⁵ IC₅₀ values reported in µM with the 95% confidence interval indicated.

Percent Inhibition Values of 8-HQ MBIs against GLO1

Table 2.S6. Percent inhibition values of 8-HQ MBIs against GLO1. Whole library of 8-HQ MBIs was screened at 50 μ M final concentration against GLO1. The MBIs having less than 5% inhibition activity were omitted in this table. Standard deviations are given in parentheses. Cells are color-coded by percent inhibition: white (<20%), yellow (20–50%), and red (>50%).

MBI	GLO1
8-HQ	46 (3)
2.1	35 (3)
2.2	21 (7)
2.11	18 (2)
2.12	6 (4)
2.18	58 (4)
2.19	63 (3)
2.20	27 (5)
2.24	20 (3)

Protein Thermal Shift Assays (GLO1 and hCAII)

The same thermal shift assay (TSA) was employed for GLO1 and hCAII. The buffer utilized for GLO1 was 10 mM Tris chloride at pH 8. The buffer utilized for hCAII was 50 mM Tris sulfate at pH 8. To each well of a 96-well 0.2 mL optical MicroAmp (ThermoFisher) thermocycler plate was added 9.5 μ l buffer, 4 μ l of protein solution, 4 μ l MBIs in buffer, and 2.5 μ l of 20x sypro orange Thermal Shift[®] dye (ThermoFisher) in buffer. This gave a final well volume of 20 μ L containing 1 μ g protein, 200 μ M MBIs or 50 μ M reference compound, and 1x dye in buffer with a final concentration DMSO of 0.2%. The wells were sealed then heated in a thermocycler from 25 $^{\circ}$ C to 99 $^{\circ}$ C at a ramp rate of 0.1 $^{\circ}$ C per second. Fluorescence was read using the ROX filter channel ($E_x/E_m=580/623$ nm) and the fluorescence signal was fitted to a first derivative curve to identify T_M . In our experiments, native GLO1 unfolded at \sim 68 $^{\circ}$ C, native hCAII unfolded at \sim 46 $^{\circ}$ C.

Table 2.S7. Inhibition and binding data on select 8-HQ MBIs against GLO1 and hCAII. Select MBIs (200 μ M final concentration) and reference compounds (50 μ M final concentration) were prepared for enzymatic assay and thermal shift assay. *Chugai-3d and acetazolamide were used as reference compounds as they are known inhibitors for GLO1 and hCAII respectively.

Metalloenzyme	MBIs	Inhibition (%)	ΔT_M ($^{\circ}$ C)
GLO1	8-HQ	95 \pm 6	11.84 \pm 0.08
	2.1	95 \pm 7	5.22 \pm 0.07
	2.18	95 \pm 1	12.34 \pm 0.07
	2.19	87 \pm 4	4.81 \pm 0.03
	2.20	63 \pm 8	3.14 \pm 0.12
	*Chugai-3d	100 \pm 3	10.19 \pm 0.10
hCAII	2.12	89 \pm 2	7.28 \pm 0.18
	*Acetazolamide	100 \pm 1	12.74 \pm 0.12

2.9 References

1. Chen, A. Y.; Adamek, R. N.; Dick, B. L.; Credille, C. V.; Morrison, C. N.; Cohen, S. M., Targeting Metalloenzymes for Therapeutic Intervention. *Chem. Rev.* **2019**, *119* (2), 1323-1455.
2. Dick, B. L.; Cohen, S. M., Metal-Binding Isosteres as New Scaffolds for Metalloenzyme Inhibitors. *Inorg. Chem.* **2018**, *57* (15), 9538-9543.
3. Song, Y. n.; Xu, H.; Chen, W.; Zhan, P.; Liu, X., 8-Hydroxyquinoline: a privileged structure with a broad-ranging pharmacological potential. *Med. Chem. Commun.* **2015**, *6* (1), 61-74.
4. Gupta, R.; Luxami, V.; Paul, K., Insights of 8-hydroxyquinolines: A novel target in medicinal chemistry. *Bioorg. Chem.* **2021**, *108*, 104633.
5. Jacobsen, J. A.; Fullagar, J. L.; Miller, M. T.; Cohen, S. M., Identifying Chelators for Metalloprotein Inhibitors Using a Fragment-Based Approach. *J. Med. Chem.* **2011**, *54* (2), 591-602.
6. Chen, C.; Yang, X.; Fang, H.; Hou, X., Design, synthesis and preliminary bioactivity evaluations of 8-hydroxyquinoline derivatives as matrix metalloproteinase (MMP) inhibitors. *Eur. J. Med. Chem.* **2019**, *181*, 111563.
7. Hopkinson, R. J.; Tumber, A.; Yapp, C.; Chowdhury, R.; Aik, W.; Che, K. H.; Li, X. S.; Kristensen, J. B. L.; King, O. N. F.; Chan, M. C.; Yeoh, K. K.; Choi, H.; Walport, L. J.; Thines, C. C.; Bush, J. T.; Lejeune, C.; Rydzik, A. M.; Rose, N. R.; Bagg, E. A.; McDonough, M. A.; Krojer, T. J.; Yue, W. W.; Ng, S. S.; Olsen, L.; Brennan, P. E.; Oppermann, U.; Müller, S.; Klose, R. J.; Ratcliffe, P. J.; Schofield, C. J.; Kawamura, A., 5-Carboxy-8-hydroxyquinoline is a broad spectrum 2-oxoglutarate oxygenase inhibitor which causes iron translocation. *Chem. Sci.* **2013**, *4* (8), 3110-3117.

8. King, O. N. F.; Li, X. S.; Sakurai, M.; Kawamura, A.; Rose, N. R.; Ng, S. S.; Quinn, A. M.; Rai, G.; Mott, B. T.; Beswick, P.; Klose, R. J.; Oppermann, U.; Jadhav, A.; Heightman, T. D.; Maloney, D. J.; Schofield, C. J.; Simeonov, A., Quantitative High-Throughput Screening Identifies 8-Hydroxyquinolines as Cell-Active Histone Demethylase Inhibitors. *PLOS ONE* **2010**, *5* (11), e15535.
9. Hanaya, K.; Suetsugu, M.; Saijo, S.; Yamato, I.; Aoki, S., Potent inhibition of dinuclear zinc(II) peptidase, an aminopeptidase from *Aeromonas proteolytica*, by 8-quinolinol derivatives: inhibitor design based on Zn²⁺ fluorophores, kinetic, and X-ray crystallographic study. *J. Biol. Inorg. Chem.* **2012**, *17* (4), 517-529.
10. Gupta, R.; Luxami, V.; Paul, K., Insights of 8-hydroxyquinolines: A novel target in medicinal chemistry. *Bioorg. Chem.* **2021**, *108*, 104633.
11. Krawczyk, M.; Pastuch-Gawolek, G.; Mrozek-Wilczkiewicz, A.; Kuczak, M.; Skonieczna, M.; Musiol, R., Synthesis of 8-hydroxyquinoline glycoconjugates and preliminary assay of their β 1,4-GalT inhibitory and anti-cancer properties. *Bioorg. Chem.* **2019**, *84*, 326-338.
12. Lawung, R.; Cherdtrakulkiat, R.; Nabu, S.; Prachayasittikul, S.; Isarankura-Na-Ayudhya, C.; Prachayasittikul, V., Repositioning of 8-hydroxyquinoline derivatives as a new promising candidate for combating multidrug resistant *Neisseria gonorrhoeae*. *Excli j.* **2018**, *17*, 840-846.
13. Prachayasittikul, V.; Prachayasittikul, V.; Prachayasittikul, S.; Ruchirawat, S., 8-Hydroxyquinolines: a review of their metal chelating properties and medicinal applications. *DDDT* **2013**, 1157.
14. Wishart, D. S.; Knox, C.; Guo, A. C.; Shrivastava, S.; Hassanali, M.; Stothanrd, P.; Chang, Z.; Woolsey, J., DrugBank: a comprehensive resource for in silico drug discovery and exploration. *Nucleic Acids Res.* **2006**, *34* (90001), D668-D672.

15. Welsch, M. E.; Snyder, S. A.; Stockwell, B. R., Privileged scaffolds for library design and drug discovery. *Current Opinion in Chemical Biology* **2010**, *14* (3), 347-361.
16. Vitaku, E.; Smith, D. T.; Njardarson, J. T., Analysis of the Structural Diversity, Substitution Patterns, and Frequency of Nitrogen Heterocycles among U.S. FDA Approved Pharmaceuticals: Miniperspective. *J. Med. Chem.* **2014**, *57* (24), 10257-10274.
17. Liang, S. H.; Southon, A. G.; Fraser, B. H.; Krause-Heuer, A. M.; Zhang, B.; Shoup, T. M.; Lewis, R.; Volitakis, I.; Han, Y.; Greguric, I.; Bush, A. I.; Vasdev, N., Novel Fluorinated 8-Hydroxyquinoline Based Metal Ionophores for Exploring the Metal Hypothesis of Alzheimer's Disease. *ACS Med. Chem. Lett.* **2015**, *6* (9), 1025-1029.
18. Jin, G. H.; Li, H.; An, S.; Ryu, J.-H.; Jeon, R., Design, synthesis and activity of benzothiazole-based inhibitors of NO production in LPS-activated macrophages. *Bioorganic Med. Chem. Lett.* **2010**, *20* (21), 6199-6202.
19. Cottyn, B.; Acher, F.; Ramassamy, B.; Alvey, L.; Lepoivre, M.; Frapart, Y.; Stuehr, D.; Mansuy, D.; Boucher, J.-L.; Vichard, D., Inhibitory effects of a series of 7-substituted-indazoles toward nitric oxide synthases: Particular potency of 1H-indazole-7-carbonitrile. *Bioorg. Med. Chem.* **2008**, *16* (11), 5962-5973.
20. Keough, D. T.; Skinner-Adams, T.; Jones, M. K.; Ng, A.-L.; Brereton, I. M.; Guddat, L. W.; de Jersey, J., Lead Compounds for Antimalarial Chemotherapy: Purine Base Analogs Discriminate between Human and *P. Falciparum* 6-Oxopurine Phosphoribosyltransferases. *J. Med. Chem.* **2006**, *49* (25), 7479-7486.
21. McGuigan, C.; Harris, S. A.; Daluge, S. M.; Gudmundsson, K. S.; McLean, E. W.; Burnette, T. C.; Marr, H.; Hazen, R.; Condreay, L. D.; Johnson, L.; De Clercq, E.; Balzarini, J.,

Application of Phosphoramidate Pronucleotide Technology to Abacavir Leads to a Significant Enhancement of Antiviral Potency. *J. Med. Chem.* **2005**, *48* (10), 3504-3515.

22. Munk, S. A.; Harcourt, D. A.; Arasasingham, P. N.; Burke, J. A.; Kharlamb, A. B.; Manlapaz, C. A.; Padillo, E. U.; Roberts, D.; Runde, E.; Williams, L.; Wheeler, L. A.; Garst, M. E., Synthesis and Evaluation of 2-(Arylamino)imidazoles as α 2-Adrenergic Agonists. *J. Med. Chem.* **1997**, *40* (1), 18-23.

23. Schönherr, D.; Wollatz, U.; Haznar-Garbacz, D.; Hanke, U.; Box, K. J.; Taylor, R.; Ruiz, R.; Beato, S.; Becker, D.; Weitschies, W., Characterisation of selected active agents regarding pKa values, solubility concentrations and pH profiles by SiriusT3. *Eur. J. Pharm. Biopharm.* **2015**, *92*, 155-170.

24. Tam, K. Y.; Takács-Novák, K., Multi-wavelength spectrophotometric determination of acid dissociation constants: a validation study. *Anal. Chim. Acta* **2001**, *434* (1), 157-167.

25. Slater, B.; McCormack, A.; Avdeef, A.; Comer, J. E., pH-metric log *P*. 4. Comparison of partition coefficients determined by HPLC and potentiometric methods to literature values. *J. Pharm. Sci.* **1994**, *83* (9), 1280-1283 .

26. Kimblin, C.; Parkin, G., Comparison of Zinc and Cadmium Coordination Environments in Synthetic Analogues of Carbonic Anhydrase: Synthesis and Structure of $\{[\text{Pim}^{\text{Pr}^i, \text{Bu}^t}]\text{Cd}(\text{OH}_2)(\text{OCIO}_3)\}(\text{ClO}_4)$. *Inorg. Chem.* **1996**, *35* (24), 6912-6913.

27. Puerta, D. T.; Cohen, S. M., Examination of Novel Zinc-Binding Groups for Use in Matrix Metalloproteinase Inhibitors. *Inorg. Chem.* **2003**, *42* (11), 3423-3430.

28. Puerta, D. T.; Lewis, J. A.; Cohen, S. M., New Beginnings for Matrix Metalloproteinase Inhibitors: Identification of High-Affinity Zinc-Binding Groups. *J. Am. Chem. Soc.* **2004**, *126* (27), 8388-8389.

29. Verdolino, V.; Cammi, R.; Munk, B. H.; Schlegel, H. B., Calculation of pKa Values of Nucleobases and the Guanine Oxidation Products Guanidinohydantoin and Spiroiminodihydantoin using Density Functional Theory and a Polarizable Continuum Model. *J. Phys. Chem. B* **2008**, *112* (51), 16860-16873.
30. Lippert, B., Multiplicity of metal ion binding patterns to nucleobases. *Coord. Chem. Rev* **2000**, 200-202, 487-516.
31. Kosturko, L. D.; Folzer, C.; Stewart, R. F., Crystal and molecular structure of a 2:1 complex of 1-methylthymine-mercury(II). *Biochemistry* **1974**, *13* (19), 3949-3952.
32. Grehl, M.; Krebs, B., Reaction of Model Nucleobases with the Diaqua(bis(N-methylimidazol-2-yl) ketone)platinum(II) Dication. Synthesis and Structure of the Head-to-Tail Isomers of Bis(9-methylguanine-N7)(bis(N-methylimidazol-2-yl) ketone)platinum(II) Perchlorate, Bis(1-methylcytosine-N3)(bis(N-methylimidazol-2-yl) ketone)platinum(II) Perchlorate, Bis(μ -1-methylthyminato-N3,O4)bis[(bis(N-methylimidazol-2-yl) ketone)platinum(II)] Perchlorate, and Bis(μ -1-methyluracilato-N3,O4)bis[(bis(N-methylimidazol-2-yl) ketone)platinum(II)] Nitrate. *Inorg. Chem.* **1994**, *33* (18), 3877-3885.
33. Chen, H.; Olmstead, M. M.; Maestre, M. F.; Fish, R. H., Bioorganometallic Chemistry. 7. A Novel, Linear, Two-Coordinate Rh(I) Anionic Amide Complex Formed by the Reaction of the Nucleobase, 1-Methylthymine, with the [(Cp*Rh)₂(μ -OH)₃]⁺ Cation at pH 10: Molecular Recognition and Electrostatic Interaction within an Organometallic Hydrophobic Cavity. *J. Am. Chem. Soc.* **1995**, *117* (35), 9097-9098.
34. Faggiani, R.; Howard-Lock, H. E.; Lock, C. J. L.; Turner, M. A., The reaction of chloro(triphenylphosphine)gold(I) with 1-methylthymine. *Can. J. Chem.* **1987**, *65* (7), 1568-1575

35. Frommer, G.; Mutikainen, I.; Pesch, F. J.; Hillgeris, E. C.; Preut, H.; Lippert, B., Platinum(II) coordination to N1 and N7,N1 of guanine: cis-DDP model cross-links in the interior and simultaneous cross-links at the periphery and the interior of DNA. *Inorg. Chem.* **1992**, *31* (12), 2429-2434.
36. Rombach, M.; Gelinsky, M.; Vahrenkamp, H., Coordination modes of aminoacids to zinc. *Inorganica Chim. Acta* **2002**, *334*, 25-33.
37. Fahrni, C. J.; O'Halloran, T. V., Aqueous Coordination Chemistry of Quinoline-Based Fluorescence Probes for the Biological Chemistry of Zinc. *J. Am. Chem. Soc.* **1999**, *121* (49), 11448-11458.
38. Carter, K. P.; Young, A. M.; Palmer, A. E., Fluorescent Sensors for Measuring Metal Ions in Living Systems. *Chem. Rev.* **2014**, *114* (8), 4564-4601.
39. McRae, R.; Bagchi, P.; Sumalekshmy, S.; Fahrni, C. J., In Situ Imaging of Metals in Cells and Tissues. *Chem. Rev.* **2009**, *109* (10), 4780-4827.
40. McGowan, J. E.; Harper, A. D.; Davison, E. K.; Jeong, J. Y.; Mros, S.; Harbison-Price, N.; Van Zuylen, E. M.; Knottenbelt, M. K.; Heikal, A.; Ferguson, S. A.; McConnell, M. A.; Cook, G. M.; Krittaphol, W.; Walker, G. F.; Brimble, M. A.; Rennison, D., Substituted sulfonamide bioisosteres of 8-hydroxyquinoline as zinc-dependent antibacterial compounds. *Bioorg. Med. Chem. Lett.* **2020**, *30* (11), 127110.
41. Okamoto, K.; Kuwabara, J.; Kanbara, T., *Chemistry of Thioamides*; Murai, T., Ed.; Springer: Singapore, 2019; pp 157-191.
42. Al-Oudat, B. A.; Jaradat, H. M.; Al-Balas, Q. A.; Al-Shar'i, N. A.; Bryant-Friedrich, A.; Bedi, M. F., Design, synthesis and biological evaluation of novel glyoxalase I inhibitors possessing

diazenylbenzenesulfonamide moiety as potential anticancer agents. *Bioorg. Med. Chem.* **2020**, *28* (16), 115608.

43. Lovejoy, B.; Welch, A. R.; Carr, S.; Luong, C.; Broka, C.; Hendricks, R. T.; Campbell, J. A.; Walker, K. A.; Martin, R.; Van Wart, H.; Browner, M. F., Crystal structures of MMP-1 and -13 reveal the structural basis for selectivity of collagenase inhibitors. *Nat. Struct. Biol.* **1999**, *6* (3), 217-21.

44. Eriksson, A. E.; Jones, T. A.; Liljas, A., Refined structure of human carbonic anhydrase II at 2.0 Å resolution. *Proteins* **1988**, *4* (4), 274-282.

45. Sellin, S.; Eriksson, L. E.; Aronsson, A. C.; Mannervik, B., Octahedral metal coordination in the active site of glyoxalase I as evidenced by the properties of Co(II)-glyoxalase I. *J. Biol. Chem.* **1983**, *258* (4), 2091-2093.

46. Rouffet, M.; de Oliveira, C. A. F.; Udi, Y.; Agrawal, A.; Sagi, I.; McCammon, J. A.; Cohen, S. M., From Sensors to Silencers: Quinoline- and Benzimidazole-Sulfonamides as Inhibitors for Zinc Proteases. *J. Am. Chem. Soc.* **2010**, *132* (24), 8232-8233.

47. Tanakit, A.; Rouffet, M.; Martin, D. P.; Cohen, S. M., Investigating chelating sulfonamides and their use in metalloproteinase inhibitors. *Dalton Trans.* **2012**, *41* (21), 6507-6515.

48. Ekinci, D.; Çavdar, H.; Durdagi, S.; Talaz, O.; Şentürk, M.; Supuran, C. T., Structure–activity relationships for the interaction of 5,10-dihydroindeno[1,2-b]indole derivatives with human and bovine carbonic anhydrase isoforms I, II, III, IV and VI. *Eur. J. Med. Chem.* **2012**, *49*, 68-73.

49. Awadallah, F. M.; Bua, S.; Mahmoud, W. R.; Nada, H. H.; Nocentini, A.; Supuran, C. T., Inhibition studies on a panel of human carbonic anhydrases with N1-substituted secondary

sulfonamides incorporating thiazolinone or imidazolone-indole tails. *J. Enzyme Inhib. Med. Chem.* **2018**, *33* (1), 629-638.

50. Bonardi, A.; Nocentini, A.; Bua, S.; Combs, J.; Lomelino, C.; Andring, J.; Lucarini, L.; Sgambellone, S.; Masini, E.; McKenna, R.; Gratteri, P.; Supuran, C. T., Sulfonamide Inhibitors of Human Carbonic Anhydrases Designed through a Three-Tails Approach: Improving Ligand/Isoform Matching and Selectivity of Action. *J. Med. Chem.* **2020**, *63* (13), 7422-7444.

51. Carta, F.; Di Cesare Mannelli, L.; Pinard, M.; Ghelardini, C.; Scozzafava, A.; McKenna, R.; Supuran, C. T., A class of sulfonamide carbonic anhydrase inhibitors with neuropathic pain modulating effects. *Bioorg. Med. Chem.* **2015**, *23* (8), 1828-1840.

52. Puerta, D. T.; Cohen, S. M., Elucidating Drug-Metalloprotein Interactions with Tris(pyrazolyl)borate Model Complexes. *Inorg. Chem.* **2002**, *41* (20), 5075-5082.

53. Schönherr, D.; Wollatz, U.; Haznar-Garbacz, D.; Hanke, U.; Box, K. J.; Taylor, R.; Ruiz, R.; Beato, S.; Becker, D.; Weitschies, W., Characterisation of selected active agents regarding pK_a values, solubility concentrations and pH profiles by SiriusT3. *Eur. J. of Pharm. Biopharm.* **2015**, *92*, 155-170.

54. Slater, B.; McCormack, A.; Avdeef, A.; Comer, J. E. A., PH-Metric logP.4. Comparison of Partition Coefficients Determined by HPLC and Potentiometric Methods to Literature Values. *J. Pharm. Sci.* **1994**, *83* (9), 1280-1283.

55. Avdeef, A.; Box, K. J.; Comer, J. E.; Gilges, M.; Hadley, M.; Hibbert, C.; Patterson, W.; Tam, K. Y., PH-metric log P 11. pK_a determination of water-insoluble drugs in organic solvent-water mixtures. *J. Pharm. Biomed. Anal.* **1999**, *20* (4), 631-41.

56. Chiba, T.; Ohwada, J.; Sakamoto, H.; Kobayashi, T.; Fukami, T. A.; Irie, M.; Miura, T.; Ohara, K.; Koyano, H., Design and evaluation of azaindole-substituted N-hydroxypyridones as glyoxalase I inhibitors. *Bioorganic Med. Chem. Lett.* **2012**, *22* (24), 7486-7489.
57. Monnard, F. W.; Nogueira, E. S.; Heinisch, T.; Schirmer, T.; Ward, T. R., Human carbonic anhydrase II as host protein for the creation of artificial metalloenzymes: the asymmetric transfer hydrogenation of imines. *Chem. Sci.* **2013**, *4* (8), 3269-3274.
58. Thinnes, C. C.; Tumber, A.; Yapp, C.; Scozzafava, G.; Yeh, T.; Chan, M. C.; Tran, T. A.; Hsu, K.; Tarhonskaya, H.; Walport, L. J.; Wilkins, S. E.; Martinez, E. D.; Müller, S.; Pugh, C. W.; Ratcliffe, P. J.; Brennan, P. E.; Kawamura, A.; Schofield, C. J., Betti reaction enables efficient synthesis of 8-hydroxyquinoline inhibitors of 2-oxoglutarate oxygenases. *Chem. Commun.* **2015**, *51* (84), 15458-15461.
59. Cui, G.; Jin, J.; Chen, H.; Cao, R.; Chen, X.; Xu, B., Synthesis and biological evaluation of pyrimidine derivatives as novel human Pin1 inhibitors. *Bioorg. Med. Chem.* **2018**, *26* (8), 2186-2197.
60. Furneaux, R. H.; Tyler, P. C., Improved Syntheses of 3H,5H-Pyrrolo[3,2-d]pyrimidines. *J. Org. Chem.* **1999**, *64* (22), 8411-8412.
61. Perez, C.; Barkley-Levenson, A. M.; Dick, B. L.; Glatt, P. F.; Martinez, Y.; Siegel, D.; Momper, J. D.; Palmer, A. A.; Cohen, S. M., Metal-Binding Pharmacophore Library Yields the Discovery of a Glyoxalase 1 Inhibitor. *J. Med. Chem.* **2019**, *62* (3), 1609-1625.
62. Villa, S.; Cignarella, G.; Barlocco, D.; Gervasoni, M.; Carcassola, G.; Giannino, L.; Mantegazza, P., Congo red analogues as potential anti-prion agents. *Il Farmaco* **2003**, *58* (9), 929-937.

63. Kattimani, P. P.; Kamble, R. R.; Meti, G. Y., Expedient synthesis of benzimidazoles using amides. *RSC Advances* **2015**, *5* (37), 29447-29455.
64. Phillips, J. P.; Merritt, L. L., Ionization Constants of Some Substituted 8-Hydroxyquinolines. *J. Am. Chem. Soc.* **1948**, *70* (1), 410-411.
65. Albert, A.; Phillips, J. N., 264. Ionization constants of heterocyclic substances. Part II. Hydroxy-derivatives of nitrogenous six-membered ring-compounds. *J. Chem. Soc.* **1956**, (0), 1294-1304.
66. Albert, A.; Hampton, A., Analogues of 8-hydroxyquinoline having additional cyclic nitrogen atoms. Part II. Further preparations, and some physico-chemical properties. *J. Chem. Soc.* **1954**, (0), 505-513.
67. Mason, S. F., 131. The tautomerism of N-heteroaromatic hydroxy-compounds. Part III. Ionisation constants. *J. Chem. Soc.* **1958**, (0), 674-685.
68. Bruice, T. C.; Schmir, G. L., Imidazole Catalysis. II. The Reaction of Substituted Imidazoles with Phenyl Acetates in Aqueous Solution. *J. Am. Chem. Soc.* **1958**, *80* (1), 148-156.
69. Catalan, J.; Elguero, J., In *Advances in Heterocyclic Chemistry*; Katritzky, A. R., Ed.; Academic Press: Cambridge, MA, 1987; Vol. 41, pp 187-274.
70. Ogston, A. G.; Syed, I. Z.; Wheeler, T. S., Notes. *J. Chem. Soc.* **1936**, (0), 1713-1714.
71. Sheldrick, G. M., SHELXT - integrated space-group and crystal-structure determination. *Acta Cryst. A* **2015**, *71* (1), 3-8.
72. Sheldrick, G. M., A short history of SHELX. *Acta Cryst. A* **2008**, *64* (1), 112-122.
73. Dolomanov, O. V.; Bourhis, L. J.; Gildea, R. J.; Howard, J. A. K.; Puschmann, H., OLEX2: a complete structure solution, refinement and analysis program. *J. Appl. Crystallogr.* **2009**, *42* (2), 339-341.

74. Spek, A., PLATON SQUEEZE: a tool for the calculation of the disordered solvent contribution to the calculated structure factors. *Acta Cryst. C* **2015**, *71* (1), 9-18.
75. Sun Cao, P.; Sommer, R. D.; Grice, K. A., Structural comparison of suberanolhydroxamic acid (SAHA) and other zinc-enzyme inhibitors bound to a monomeric zinc species. *Polyhedron* **2016**, *114*, 344-350.

Chapter 3: Evaluating Metal-Ligand Interactions of Metal-Binding Isoosteres (MBIs) Using Model Complexes

3.1 Introduction

Chapter 2 was focused on broadening the chemical diversity of our fragment library, specifically through the development of 30 metal-binding isosteres (MBIs) derived from 8-hydroxyquinoline (8-HQ).¹ This work not only expanded the range of physicochemical properties of our library but also offered valuable insights into the relationships between the structural and electronic properties of MBIs and their metal-binding capabilities. Through detailed investigations including pK_a measurements and X-ray crystallography, preliminary guidelines were established for the design of future MBIs and demonstrated their potential in enhancing potency and selectivity against metalloenzymes, showcasing progress in the development of novel metalloenzyme inhibitors.

While previous studies highlighted the potential of MBIs for targeting metalloenzymes, these efforts mainly focused on assessing the metal-binding ability of MBIs with the Zn(II) ion, utilizing the bioinorganic model complex $[(\text{Tp}^{\text{Ph,Me}})\text{Zn}(\mathbf{L})]$ ($\text{Tp}^{\text{Ph,Me}}$ = hydrotris(5,3-methylphenylpyrazolyl)borate, \mathbf{L} = metal-binding ligand).¹⁻³ Despite the broad use of the $[(\text{Tp}^{\text{Ph,Me}})\text{Zn}(\mathbf{L})]$ model system, few studies have looked at alternative spectator ligands (i.e., ligands other than $\text{Tp}^{\text{Ph,Me}}$) to examine binding of MBPs or MBIs to metals beyond Zn(II).⁴ The lack of a comprehensive study on the structural, electronic, and spectroscopic behaviors of MBIs in different model systems leaves a gap in understanding the potential similarities or differences between MBIs and the parent MBPs. Exploring different bioinorganic model complexes could thus significantly enhance our understanding of both the structural and electronic characteristics of MBIs, offering a broader perspective on their utility in targeting metalloenzymes.

In Chapter 3, the model complex, $[\text{M}(\text{TPA})(\text{MBI})]$ ($\text{M} = \text{Ni}^{2+}$ and Co^{2+} , TPA = tris(2-pyridylmethyl)amine) has been employed to investigate the coordination chemistry and

spectroscopic characteristics of MBIs (Figure 3.1). TPA has been used as a tetradentate ligand for biologically relevant first-row transition metal ions, while providing flexible structural modification via the pyridine moieties.⁵⁻¹⁴ TPA complexes of Ni(II) have been used to study Ni(II)-dependent metalloenzymes such as acireductone dioxygenase,¹⁴ urease,¹¹ and glyoxalase I.¹³ In this chapter, Ni(II) and Co(II) complexes were used to enable structural and spectroscopic study of MBI-metal interactions. Picolinic acid (pic), several picolinic acid MBIs, and 2,2'-bipyridine (bpy) were examined (Figure 3.1). Bipyridine was included as an additional comparative ligand because it can also be regarded as an isostere of the heterocyclic MBIs studied here. The $[M(\text{TPA})(\text{MBI})]$ complexes were prepared, and their reactivity, structural features, and spectroscopic properties were investigated by X-ray crystallography, NMR, IR, UV-Vis, and magnetic moment analysis. In addition, $[(\text{Tp}^{\text{Ph,Me}})\text{Co}(\text{MBI})]$ complexes were similarly investigated as spectroscopically active analogues of the previously reported $[(\text{Tp}^{\text{Ph,Me}})\text{Zn}(\text{MBI})]$ complexes.

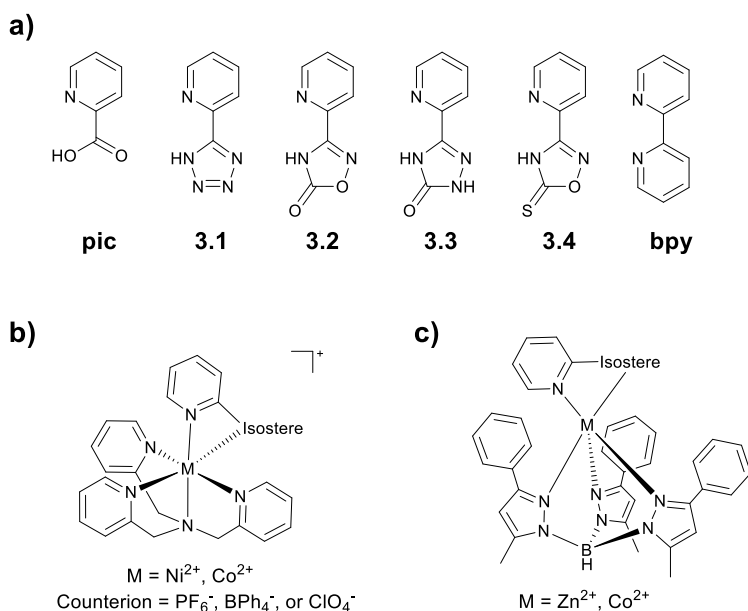


Figure 3.1. a) Picolinic acid (pic), MBIs of picolinic acid, and 2,2'-bipyridine (bpy). b) Chemical structure of the $[M(\text{TPA})(\text{MBI})]^+$ model system (TPA = tris(2-pyridylmethyl)amine). c) Chemical structure of the $[(\text{Tp}^{\text{Ph,Me}})\text{Zn}(\text{MBI})]$ model system ($\text{Tp}^{\text{Ph,Me}}$ = hydrotris(5,3-methylphenylpyrazolyl)borate).

3.2 Preparation of MBIs and Model Complexes

Pic, bpy, and four MBIs were examined in this study (Figure 3.1). The four heterocyclic carboxylic acid isosteres studied were 2-(1*H*-tetrazol-5-yl)pyridine (MBI **3.1**), 3-(pyridin-2-yl)-1,2,4-oxadiazol-5(4*H*)-one (MBI **3.2**), 5-(pyridin-2-yl)-2,4-dihydro-3*H*-1,2,4-triazol-3-one (MBI **3.3**), and 3-(pyridin-2-yl)-1,2,4-oxadiazole-5(4*H*)-thione (MBI **3.4**) (Figure 3.1). These heterocycles have been used as carboxylic acid isosteres in drug design to modulate key parameters, such as acidity, geometry (i.e., planarity), charge distribution, and lipophilicity.¹⁵ Bpy was added as an alternative isostere of these heterocycles as it shares general structure of the other ring scaffolds, but is aprotic (neutral donor). Pic and bpy were purchased from commercial sources, while the MBIs were synthesized according to published procedures (see Appendix to Chapter 3 for details).^{3, 16-17}

Each of the [Ni(TPA)(MBI)](PF₆) complexes including [Ni(TPA)(pic)](PF₆) were synthesized in a one-pot reaction. For complexes with pic, **3.1**, **3.2**, and **3.4**, an equimolar solution of Ni(CH₃CO₂)₂·4H₂O, TPA, and the respective MBI was prepared in MeOH and then NaPF₆ was added to the mixture. The resulting purple precipitates were collected by filtration and washed with MeOH. To prepare [Ni(TPA)(**3.3**)](PF₆), the reaction was carried out in *i*PrOH to promote precipitation of the desired complex and NBu₄PF₆ was used as a counter ion source based on the solubility of the product in *i*PrOH. Different synthetic conditions were required to make [Ni(TPA)(bpy)](PF₆)₂, as under either of the aforementioned conditions bpy formed [Ni(bpy)₃]²⁺ as the major product. [Ni(TPA)(bpy)](PF₆)₂ was obtained by first isolating the intermediate, [Ni(TPA)(CH₃CO₂)(H₂O)]PF₆, followed by the addition of a MeOH solution of one equivalent of bpy and NaPF₆ with stirring in an ice bath for 2 h to generate a purple precipitate. All Ni(II)

complexes were isolated as purple solids in yields between 22-54% and vapor diffusion of Et₂O into CH₃CN solutions of the complexes gave crystals suitable for X-ray diffraction.

The synthesis and crystallization of Co(II) complexes was slightly different from the Ni(II) complexes, depending on the MBIs. [Co(TPA)(pic)](PF₆), [Co(TPA)(**3.1**)](PF₆), and [Co(TPA)(**2**)](PF₆) were prepared in a one-pot reaction similar to the Ni(II) complexes. Equimolar amounts of Co(CH₃CO₂)₂·4H₂O, TPA, and the respective MBI were mixed in a 1:1 mixture of iPrOH and MeOH, and then NBu₄PF₆ was added to the solution. Pink solids were isolated in yields between 59-70% and vapor diffusion of Et₂O into CH₃CN yielded X-ray quality crystals. To make [Co(TPA)(**3.3**)](BPh₄) and [Co(TPA)(**3.4**)](BPh₄), it was necessary to first prepare an intermediate, [Co(TPA)(CH₃CO₂)]BPh₄.¹⁰ This intermediate was then combined with one equivalent of **3.3** or **3.4** in THF. [Co(TPA)(**3.3**)](BPh₄) was crystallized from cyclohexane diffusion into a CH₂Cl₂ solution of the complex, while [Co(II)(TPA)(**3.4**)](BPh₄) was directly obtained by slow evaporation from THF in yields of 56% and 51%, respectively. The use of the [Co(TPA)(CH₃CO₂)]BPh₄ intermediate allowed formation of the desired product and prevented formation of insoluble byproducts, including homoleptic complexes (i.e., [Co(MBI)₃]). Note that while the Co(II) complexes for pic and MBIs were readily synthesized, it was challenging to obtain [Co(TPA)(bpy)]²⁺ under any circumstance. Attempts to prepare [Co(TPA)(bpy)]²⁺ always produced [Co(bpy)₃]²⁺ as the major product. This result shows that the reactivity of bpy in these TPA model systems is significantly different from pic and the MBIs.

[(Tp^{Ph,Me})Co(MBI)] was applied as an alternative model system with two objectives. The first objective was to compare the coordination geometry of [(Tp^{Ph,Me})Co(pic)] and [(Tp^{Ph,Me})Co(MBI)] complexes to each other and with those of the corresponding [(Tp^{Ph,Me})Zn(MBI)] complexes.³ The second goal was to examine the spectroscopic properties of

$[(\text{Tp}^{\text{Ph,Me}})\text{Co}(\mathbf{MBI})]$ with those of $[(\text{Tp}^{\text{Ph,Me}})\text{Co}(\text{pic})]$ and $[(\text{Tp}^{\text{Ph,Me}})\text{Co}(\text{bpy})]^+$, the latter of which could not be prepared using the TPA model system. $[(\text{Tp}^{\text{Ph,Me}})\text{Co}(\mathbf{MBI})]$ complexes were prepared via a $[(\text{Tp}^{\text{Ph,Me}})\text{Co}(\text{Cl})]$ intermediate,^{4, 18} where 1 equiv. of each ligand in MeOH was added to the solution of $[(\text{Tp}^{\text{Ph,Me}})\text{Co}(\text{Cl})]$ in CH_2Cl_2 . To prepare $\text{Tp}^{\text{Ph,Me}}$ complexes coordinated with pic and its MBIs, excess triethylamine (TEA) was required to prevent acid-promoted decomposition of the $[(\text{Tp}^{\text{Ph,Me}})\text{Co}(\text{Cl})]$. NaPF_6 was added as a counterion to produce $[(\text{Tp}^{\text{Ph,Me}})\text{Co}(\text{bpy})]\text{PF}_6$. Pinkish-purple solids were isolated for $[(\text{Tp}^{\text{Ph,Me}})\text{Co}(\text{pic})]$, $[(\text{Tp}^{\text{Ph,Me}})\text{Co}(\mathbf{3.1})]$ and $[(\text{Tp}^{\text{Ph,Me}})\text{Co}(\mathbf{3.2})]$, while $[(\text{Tp}^{\text{Ph,Me}})\text{Co}(\text{bpy})]\text{PF}_6$ gave brownish-orange colored solid in good yields. The complexes were recrystallized by diffusing pentane into a solution of the complex in benzene. MBIs **3.3** and **3.4** generated $[\text{Co}(\text{pz}^{\text{Ph,Me}})_2(\mathbf{MBI})_2]$ ($\text{pz}^{\text{Ph,Me}} = 5,3\text{-methylphenylpyrazole}$) as a major product (confirmed by X-ray crystallography, data not shown). This result is tentatively attributed to both the intrinsic instability of the starting material, $[(\text{Tp}^{\text{Ph,Me}})\text{Co}(\text{Cl})]$,^{4, 19} and different metal-binding properties of MBI **3.3** and **3.4**, as observed in $[(\text{Tp}^{\text{Ph,Me}})\text{Zn}(\mathbf{MBI})]$ system.³

3.3 Structural Analysis

$[(\text{Tp}^{\text{Ph,Me}})\text{Zn}(\mathbf{MBI})]$ complexes of pic, **3.1**, **3.2**, **3.3**, and **3.4** have been previously reported and show bidentate binding to the Zn(II) ion in all cases.^{3, 20} In addition, the $\text{Tp}^{\text{Ph,Me}}$ spectator ligand in $[(\text{Tp}^{\text{Ph,Me}})\text{Zn}(\mathbf{MBI})]$ complexes of pic, **3.1**, and **3.2** show the expected tridentate binding, while with **3.3** and **3.4**, an unexpected coordination mode where a water molecule displaces one of the pyrazole arms of the $\text{Tp}^{\text{Ph,Me}}$ ligand was reported.³ Herein, the structural features of $[\text{M}(\text{TPA})(\text{pic})]^+$, $[\text{M}(\text{TPA})(\mathbf{MBI})]^+$ and $[\text{M}(\text{TPA})(\text{bpy})]^{2+}$ complexes were examined in the context of the previously reported $[(\text{Tp}^{\text{Ph,Me}})\text{Zn}(\mathbf{MBI})]$ complexes.

MBIs bound to the TPA complexes showed a bidentate mode of coordination, generating metal ion centers with distorted octahedral geometries (Figures 3.2 and 3.3). The bite angles of MBI ligands (N5-M-N6) decreased compared to that of the parent pic complexes (N5-M-O1) (Tables 3.1 and 3.2). This trend was expected because of the rigidity of the heterocyclic isosteres. [M(TPA)(**3.1**)]⁺ showed the most significant decrease in bite angle by $\sim 2.1^\circ$ and $\sim 3.8^\circ$ for the Ni(II) and Co(II) complexes, respectively (Tables 3.1 and 2.2). All MBIs showed slightly longer bond distances ($>0.1 \text{ \AA}$) compared to the parent pic complexes. For all TPA complexes, the bond lengths between the metal ions and the tertiary nitrogen donor atom of TPA were similar ($<0.1 \text{ \AA}$) (Table S5 and S6) and were consistent with previously reported values.^{14, 21-24}

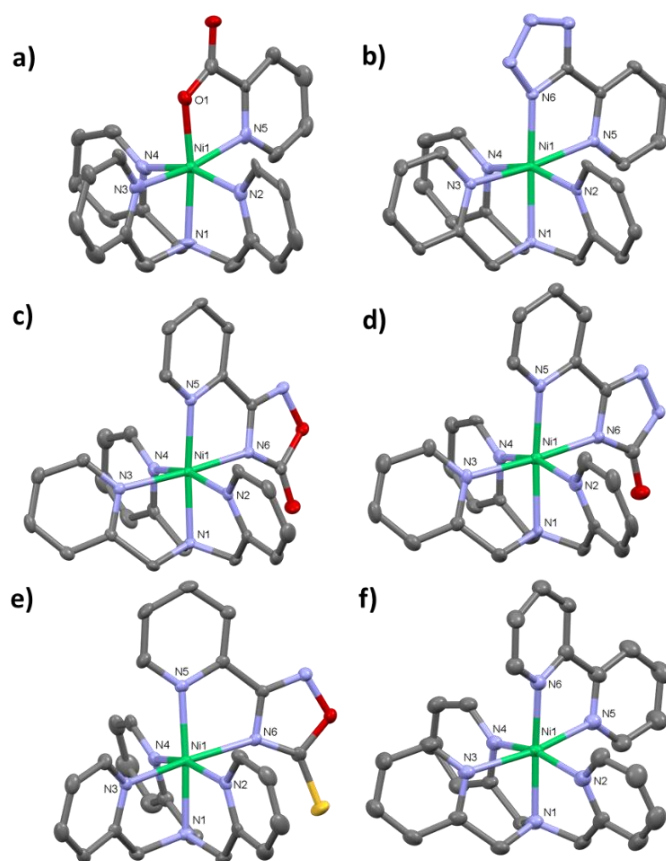


Figure 3.2. Crystal structures of [Ni(TPA)(L)] complexes (ORTEP, 50% probability ellipsoids). a) [Ni(TPA)(pic)]⁺, b) [Ni(TPA)(**3.1**)]⁺, c) [Ni(TPA)(**3.2**)]⁺, d) [Ni(TPA)(**3.3**)]⁺, e) [Ni(TPA)(**3.4**)]⁺, f) [Ni(TPA)(bpy)]²⁺. Solvent molecules, counter ions, and hydrogen atoms have been omitted for clarity. Donor atoms are alphanumerically labelled. Color scheme: carbon = gray, oxygen = red, nitrogen = blue, nickel = green, and sulfur = yellow.

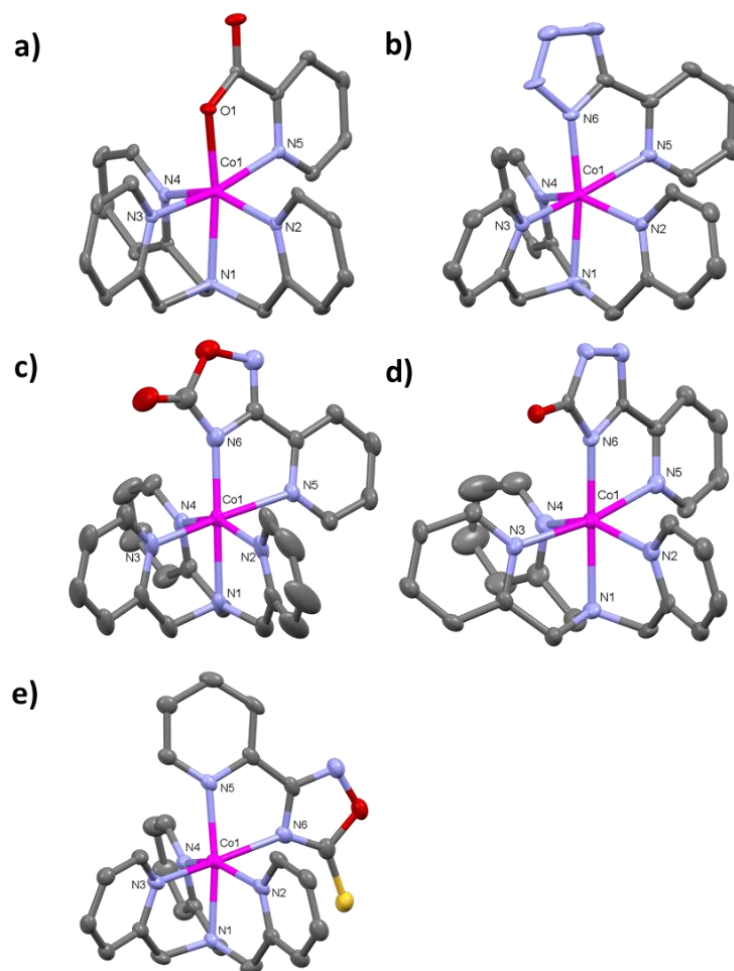


Figure 3.3. Crystal structures of $[\text{Co}(\text{TPA})(\text{L})]$ complexes (ORTEP, 50% probability ellipsoids). a) $[\text{Co}(\text{TPA})(\text{pic})]^+$, b) $[\text{Co}(\text{TPA})(\mathbf{3.1})]^+$, c) $[\text{Co}(\text{TPA})(\mathbf{3.2})]^+$, d) $[\text{Co}(\text{TPA})(\mathbf{3.3})]^+$, e) $[\text{Co}(\text{TPA})(\mathbf{3.4})]^+$. Solvent molecules, counter ions, and hydrogen atoms have been omitted for clarity. Donor atoms are alphanumerically labelled. Color scheme: carbon = gray, oxygen = red, nitrogen = blue, cobalt = pink, and sulfur = yellow.

Table 3.1. Selected bond lengths and angles for [Ni(TPA)(L)]⁺²⁺. Structures with more than one complex in the asymmetric unit are marked with an asterisk.

Ligand	Ni-N5 (Å)	Ni-O1/N6 (Å)	Bite angle (°)	Sigma, Theta (Σ, Θ) (°)
Pic*	2.126(9)	1.984(8)	80.1(3)	89, 287
	2.129(9)	2.003(8)	80.0(3)	89, 294
3.1	2.231(4)	2.039(3)	77.99(15)	83, 258
3.2	2.111(2)	2.110(2)	79.70(9)	98, 257
3.3*	2.128(4)	2.123(4)	79.31(14)	100, 274
	2.116(4)	2.114(4)	79.52(14)	94, 240
	2.093(4)	2.104(4)	80.14(14)	99, 250
3.4	2.072(3)	2.155(3)	79.59(9)	101, 288
bpy	2.148(3)	2.054(3)	78.51(12)	104, 302

Table 3.2. Selected bond lengths and angles for [Co(TPA)(L)]⁺. Structures with more than one complex in the asymmetric unit are marked with an asterisk.

Ligand	Co-N5 (Å)	Co-O1/N6 (Å)	Bite angle (°)	Sigma, Theta (Σ, Θ) (°)
pic	2.178(3)	2.012(2)	78.87(9)	113, 360
3.1*	2.317(5)	2.058(5)	75.2(2)	141, 490
	2.307(6)	2.058(6)	75.5(2)	132, 424
	2.320(6)	2.057(6)	75.3(2)	129, 416
	2.357(6)	2.062(5)	74.5(2)	142, 458
3.2	2.2743(18)	2.073(2)	77.22(7)	111, 302
3.3	2.267(3)	2.060(3)	76.94(12)	130, 386
3.4	2.130(3)	2.181(3)	77.48(11)	121, 401
	2.204(3)	2.161(3)	76.74(11)	122, 359

Some differences in metal binding orientation between Ni(II) and Co(II) complexes were observed. Pic, **3.1** and **3.4** showed the same binding orientation regardless of the metal ion, with [M(TPA)(pic)]⁺ and [M(TPA)(**3.1**)]⁺ positioning the pyridine ring nitrogen atom (N5) of the MBI cis to the bridgehead nitrogen (N1) of TPA while [M(TPA)(**3.4**)]⁺ had the N5 of the MBI trans to N1 of TPA. [Ni(TPA)(**3.2**)]⁺ and [Ni(TPA)(**3.3**)]⁺ bound such that N5 were trans to N1 of TPA while the corresponding Co(II) complexes showed the opposite (i.e., cis) orientation. The results suggest that subtle differences in metal ion coordination preferences influence how these MBIs bind to metals. Another observation is that the bite angles of the Co(II) complexes were smaller

than the Ni(II) complexes (Tables 3.1 and 3.2). In addition, the Co(II) complexes are much more distorted than the Ni(II) complexes based on angular distortion parameter Σ and Θ (Tables 3.1 and 3.2).²⁵⁻²⁶ The higher degree of distortion observed in the Co(II) complexes can be explained by a subtle change in electronics and energetics of each complex including Jahn-Teller distortion which are commonly found in six-coordinate Co(II) complexes.²⁷⁻²⁸ Overall, all MBIs showed slightly different, but not particularly notable, structural features when compared to the parent pic complex. The structure features of the [Ni(TPA)(**MBI**)]⁺ complexes were also generally similar to those found with [Ni(TPA)(bpy)]²⁺ (Figure 3.2, Table 3.1).

To have a better understanding of how the MBIs studied here are similar to pic or bpy, the structural features of [(Tp^{Ph,Me})Co(**3.1**)] and [(Tp^{Ph,Me})Co(**3.2**)] were compared with those of [(Tp^{Ph,Me})Co(pic)] and [(Tp^{Ph,Me})Co(bpy)]⁺ (Figure 3.4). In all cases, pic, **3.1**, **3.2**, and bpy showed bidentate coordination to the Co(II) center, as found for [(Tp^{Ph,Me})Zn(**MBI**)] complexes as well (Figure S1).³ [(Tp^{Ph,Me})Co(pic)] resulted in trigonal bipyramidal geometry ($\tau = 0.71$), which is isomorphous with [(Tp^{Ph,Me})Zn(pic)] ($\tau = 0.72$). By contrast, [(Tp^{Ph,Me})Co(**3.1**)] and [(Tp^{Ph,Me})Co(**3.2**)] showed distorted square pyramidal geometries ($\tau = 0.32$ and 0.41 , respectively) when compared to the analogous Zn(II) complexes ($\tau = 0.52$ and 0.55 , respectively). Bpy formed a more square pyramidal geometry with both Co(II) and Zn(II) complexes ($\tau = 0.01$ and 0.11 , respectively). This pattern of Co(II) complexes trending toward square pyramidal geometry was expected, as the trigonal bipyramidal geometry is less likely to be preferred relative to square pyramidal in 5-coordinate d⁷ complexes due to ligand field stabilization energy.^{4,29} The structural features of MBI **3.3** and **3.4** could not be compared as they could not be prepared under the same synthetic conditions used with pic, MBI **3.1** and **3.2**. Interestingly, MBIs **3.3** and **3.4** showed different coordination behavior from pic, **3.1**, and **3.2** in [(Tp^{Ph,Me})Zn(**MBI**)] system,³ which

suggests that MBIs **3.3** and **3.4** might also have different metal-binding behavior in $[(\text{Tp}^{\text{Ph,Me}})\text{Co}(\text{MBI})]$ system.

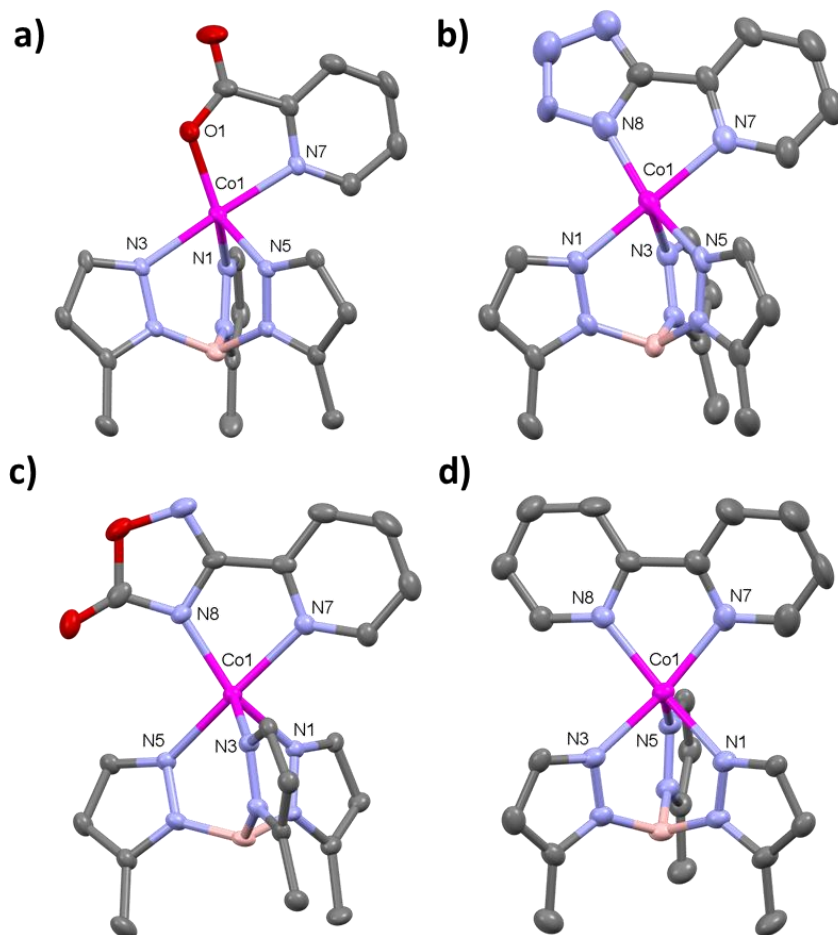


Figure 3.4. Crystal structures of $[(\text{Tp}^{\text{Ph,Me}})\text{Co}(\text{L})]$ complexes (ORTEP, 50% probability ellipsoids). a) $[(\text{Tp}^{\text{Ph,Me}})\text{Co}(\text{pic})]$, b) $[(\text{Tp}^{\text{Ph,Me}})\text{Co}(\mathbf{3.1})]$, c) $[(\text{Tp}^{\text{Ph,Me}})\text{Co}(\mathbf{3.2})]$, d) $[(\text{Tp}^{\text{Ph,Me}})\text{Co}(\text{bpy})]$. Phenyl groups of $\text{Tp}^{\text{Ph,Me}}$ have been omitted for clarity. Donor atoms are alphanumerically labelled. Color scheme: carbon = gray, oxygen = red, nitrogen = blue, cobalt = pink, and boron = pink.

Table 3.3. Selected bond lengths and angles for $[(\text{Tp}^{\text{Ph,Me}})\text{Co}(\text{L})]^{0/+}$.

Ligand	Co-N7 (Å)	Co-O1/N8 (Å)	Bite angle (°)	Tau, τ (°)
pic	2.135(3)	1.965(2)	79.97(9)	0.71
3.1	2.145(4)	1.963(4)	78.48(17)	0.32
3.2	2.167(4)	2.023(4)	78.17(16)	0.41
bpy	2.080(3)	2.069(3)	78.09(13)	0.01

3.4 Computational Analysis

In order to understand the energetics and in particular the crystallographic findings of the MBIs in the model complexes, density functional theory (DFT) calculations for MBIs **3.1** – **3.4** in the TPA model system complexes were performed. All calculations were carried out at the wB97x-D/LanL2DZ level of theory. The computations were performed under standard conditions (1 atm, 298 K) in the gas phase to exclude any solvent or crystal packing effects which might have been observed under experimental conditions.

The bond lengths and angles of the computationally optimized structures (Table 3.S7) were compared with the crystallographically determined ones (Tables 3.1 and 3.2). The biggest difference in bond length (0.027 Å) and bite angle (1.1°) was observed for [Ni(TPA)(**3.1**)]⁺. Overall, a very good agreement between the experimentally determined and theoretically calculated structures was observed with the same trends as described between the MBIs and the corresponding metals. This indicates that the calculated structures accurately reproduce the experimentally characterized complexes.

To investigate the difference in binding orientation of the N5 of MBIs either cis or trans to the N1 of TPA, the difference in energy between these isomers was calculated. The crystallographically described binding orientation of the MBIs (Figure 3.2 and 2.3) were also found to possess the lowest calculated energy, confirming that the structures correspond to the inherent preferred orientation of the MBI (Figure 3.5). The direct comparison between coordination orientation isomers indicates that there are energy differences of between 2.3 - 4.2 kcal/mol. The biggest difference in energy was observed for MBI **3.1** ($\Delta G = 3.6 - 4.4$ kcal/mol) and MBI **3.4** ($\Delta G = 3.8 - 4.2$ kcal/mol), which showed the same orientation of the MBI pyridine N5 to N1 of TPA in the corresponding Ni(II) and Co(II) complexes.

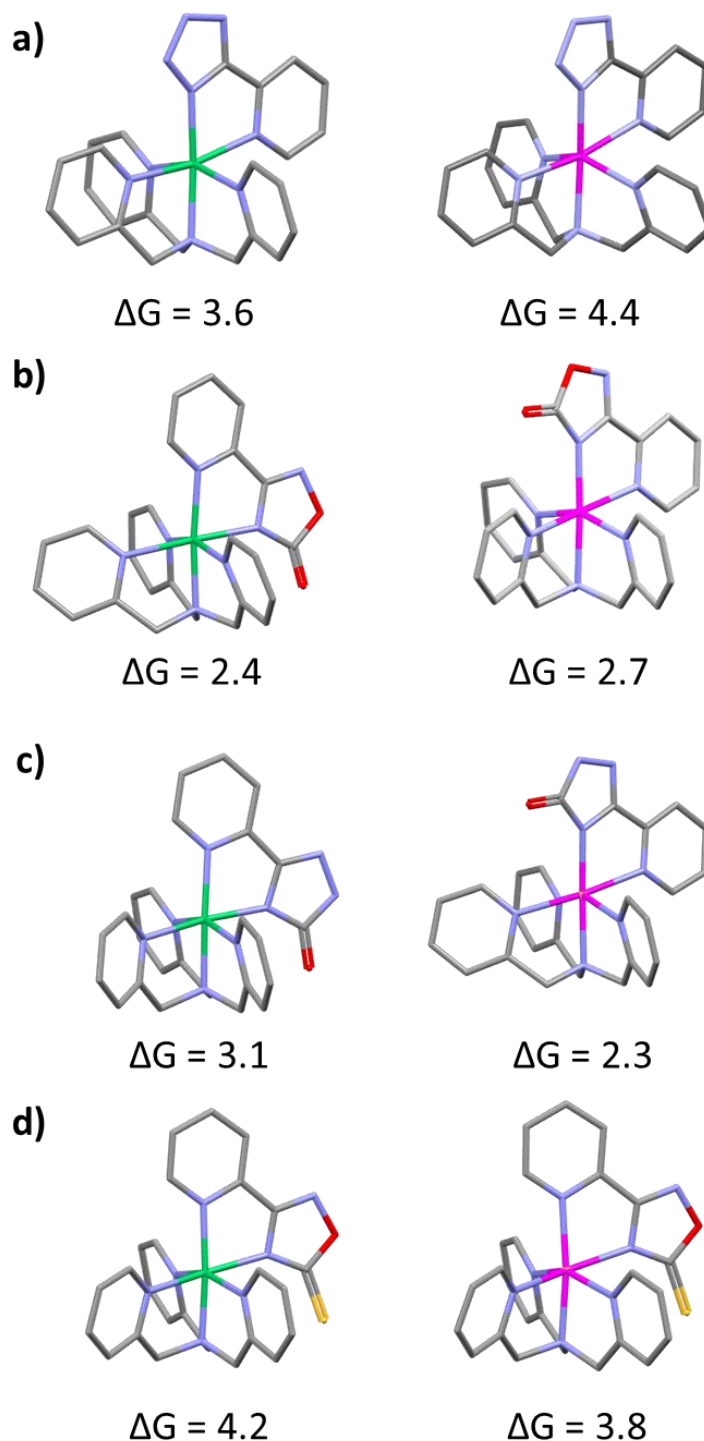


Figure 3.5. Computationally optimized structures and relative free Gibbs energy differences of the binding orientation isomers of the MBI **3.1** – **3.4** coordinated to Ni(II) (*left*) or Co(II) (*right*) TPA complexes at the wB97x-D/LanL2DZ level of theory. a) [Ni(TPA)(**3.1**)]⁺ and [Co(TPA)(**3.1**)]⁺, b) [Ni(TPA)(**3.2**)]⁺ and [Co(TPA)(**3.2**)]⁺, c) [Ni(TPA)(**3.3**)]⁺ and [Co(TPA)(**3.3**)]⁺, d) [Ni(TPA)(**3.4**)]⁺ and [Co(TPA)(**3.4**)]⁺. Color scheme: carbon = gray, oxygen = red, nitrogen = blue, nickel = green, cobalt = pink, and sulfur = yellow.

This result suggests that MBI **3.1** and **3.4** favors a specific coordination orientation independent from the central metal ion. By contrast, a somewhat smaller energy difference ($\Delta G = 2.3 - 3.1$ kcal/mol) was observed for MBI **3.2** and **3.3**, which show different binding orientations in the crystallographically characterized metal complexes. While the Ni(II) complexes of these MBIs favor a trans coordination of the N5 to the N1, a cis binding coordination preferred in the analogous Co(II) complexes. Note that the energy differences between these two different conformations is still quite small (<5.0 kcal/mol), suggesting that the binding orientation of the MBIs could be readily perturbed by the metalloenzyme active site.

3.5 Spectroscopic Analysis

A distinct feature of both Ni(II) and Co(II) is that they are paramagnetic and have unpaired electrons – 2 for Ni(II) and either 3 or 1 for Co(II)) depending on the spin state. While the typical ^1H NMR spectra fall between 0 and 14 ppm, the ^1H resonances of Ni(II) and Co(II) complexes can often be found from -30 to 160 ppm. Paramagnetic ^1H NMR has been a useful tool for characterizing active site structural features of Co(II)-substituted Zn(II)-dependant enzymes including liver alcohol dehydrogenase³⁰ as well as monitoring model reactions relevant to Ni(II)-containing metalloenzyme such as acireductone dioxygenase.^{14, 31} To evaluate the coordination complexes formed herein the ^1H NMR spectra of all complexes were obtained (Figures 3.S2 and 3.S3). The paramagnetically shifted resonances of the TPA complexes were observed, which was used for to confirm the stability and solution characteristics of the complexes. For the Ni(II) complexes, broad peaks between 30 - 70 ppm were assigned as the β -protons of TPA pyridyl rings based on ^1H NMR resonances of structurally related Ni(II) complexes (Figure 3.S2).¹⁴ It is interesting to note that all of the Ni(II) complexes, except $[\text{Ni}(\text{TPA})(\text{bpy})]^{2+}$, showed more than

two peaks in the range of 30 – 70 ppm, suggesting that the asymmetric scaffold of the MBIs in solution might cause magnetically inequivalence in the β -protons of the TPA spectator ligand. Paramagnetic ^1H NMR resonances of the Co(II) complexes showed sharper peaks compared to the Ni(II) complexes (Figure 3.S3). Note that the ^1H NMR resonances of $[\text{Co}(\text{TPA})(\mathbf{3.4})]^+$ showed a distinct spectrum, having only one sharp peak between 35 and 75 ppm while the other complexes showed more than two peaks in this same region of the spectra. Typically, in this region, β -protons of TPA pyridyl rings are found in structurally related Co(II) complexes.^{11, 31} Interestingly, $[\text{Co}(\text{TPA})(\mathbf{3.4})]^+$ is the only compound that showed a different binding orientation in the solid state, where the N5 was trans to the N1 of TPA (in all the other $[\text{Co}(\text{TPA})(\mathbf{MBI})]^+$ complexes a cis orientation was observed). This suggests that MBI **3.4** could have distinct binding characteristics both in solution and in the solid state when bound to Co(II) TPA complexes.

The magnetic properties of the Ni(II) and Co(II) complexes were examined to confirm the oxidation and spin state of each TPA complex. This measurement was especially meaningful for Co(II) complexes as they can adopt either high spin or low spin states while Ni(II) complexes should display two unpaired electrons in all cases.³² The solution magnetic moment of all complexes were determined by the Evans method in $\text{DMSO-}d_6$ (Table 3.4).³³ The Ni(II) complexes were found to exhibit magnetic moments between 3.09 – 3.34 μ_{B} , which is higher than the spin-only magnetic moment for Ni(II) (2.8 μ_{B}) due to spin-orbit coupling.³⁴ These values confirm that Ni(II) complexes have two unpaired electrons and are well within the range predicted for high spin six-coordinate Ni(II).³⁴ Similarly, the Co(II) complexes had magnetic moments from 4.56 – 4.76 μ_{B} , which are higher than the spin-only value for Co(II) (3.9 μ_{B}).³⁴ These magnetic moments correspond to three unpaired electrons per Co(II) ion and are in good agreement with those observed for most high-spin octahedral Co(II) complexes.³⁵⁻³⁶ This result is consistent with

the distortion of the TPA Co(II) system observed in solid-state X-ray structural data. The ground state of an octahedral high spin d^7 complex is ${}^4T_{1g}$ that is Jahn-Teller active.^{28, 37}

Table 3.4. UV-visible and magnetic moment data for $[M(\text{TPA})(\text{L})]^{+2+}$.

Ligand	$[\text{Ni}(\text{TPA})(\text{L})]^{n+}$		$[\text{Co}(\text{TPA})(\text{L})]^{n+}$	
	$\mu_{\text{eff.}}$, B.M.	λ_{max} , nm (ϵ , $\text{M}^{-1} \text{cm}^{-1}$)	$\mu_{\text{eff.}}$, B.M.	λ_{max} , nm (ϵ , $\text{M}^{-1} \text{cm}^{-1}$)
pic	3.16	531 (21)	4.60	493 (103)
3.1	3.12	534 (23)	4.76	485 (117)
3.2	3.33	548 (21)	4.56	486 (64)
3.3	3.32	552 (19)	4.74	484 (88)
3.4	3.34	555 (16)	4.62	483 (76)
bpy	3.09	576 (21)	-	-

The UV-vis spectra of the TPA complexes were also measured, and all spectra showed a strong absorption at <400 nm. For the Ni(II) TPA complexes, all compounds had a single absorption in the region 400-700 nm, which was found in structurally related octahedral Ni(II) complexes (Table 3.4 and Figure 3.S4).³⁸ The absorption maximum for $[\text{Ni}(\text{TPA})(\mathbf{3.1})(\text{PF}_6)]$ (531 nm) was similar to that for $[\text{Ni}(\text{TPA})(\text{pic})(\text{PF}_6)]$ (534 nm) while the other MBI complexes were clustered around 550 nm. This difference in absorption maxima is likely related to a combination of factors including the different binding orientations between MBI **3.1** versus **3.2**, **3.3**, and **3.4**. Note that the absorption maxima of $[\text{Ni}(\text{TPA})(\text{MBI})]^+$ complexes were more similar to that generated with pic than bpy in the Ni(II) systems. The UV-vis spectra of the Co(II) complexes showed one major absorption band in the range of 400 - 700 nm consistent with previously reported high-spin octahedral Co(II) complexes (Table 3.4 and Figure 3.S5).³⁹ All the $[\text{Co}(\text{TPA})(\text{MBI})]^+$ complexes showed a similar range of absorption wavelength maxima (483 - 486 nm), which was slightly shifted from the value for $[\text{Co}(\text{TPA})(\text{pic})]^+$ (493 nm).

Finally, spectroscopic characterization of the $[(\text{Tp}^{\text{Ph,Me}})\text{Co}(\text{MBI})]$ complexes was carried out to further understand the electronic difference between MBIs, pic, and bpy in the model

systems. Regarding magnetic moments, pic, **3.1**, and **3.2** showed a similar range of magnetic moments around 4.84 μ_B for each complex while bpy had a value of 4.66 μ_B . These values are in the range of those observed for other 5-coordinate, high-spin Co(II) complexes.³⁶ UV-vis data showed that there are three main absorption bands in the visible range. Interestingly, [(Tp^{Ph,Me})Co(pic)], [(Tp^{Ph,Me})Co(**3.1**)], and [(Tp^{Ph,Me})Co(**3.2**)] showed similar UV-vis spectra, while the spectrum of [(Tp^{Ph,Me})Co(bpy)] was clearly different from the others (Table 5 and Figure S6). These results suggest that MBIs **3.1** and **3.2** are electronically more similar to pic than bpy in these model systems.

Table 3.5. UV-visible and magnetic moment data for [(Tp^{Ph,Me})Co(L)]^{0/+}.

Ligand	[(Tp ^{Ph,Me})Co(L)] ⁿ⁺	
	$\mu_{\text{eff.}}$, B.M.	λ_{max} , nm (ϵ , M ⁻¹ cm ⁻¹)
pic	4.84	452 (41), 538 (49), 561 (51)
3.1	4.84	456 (37), 540 (49), 563 (47)
3.2	4.85	448 (47), 542 (44), 562 (42)
bpy	4.66	417 (333), 520 (76), 676 (34)

3.6 Conclusion

A TPA model system was used to provide structural and electronic information on picolinic acid and its MBIs. Their coordination modes were determined from X-ray crystallography and their energetic differences in binding conformations were evaluated using DFT calculations. From these data it was determined that all four heterocyclic MBIs retain bidentate coordination to the metal centers and small energetic disparities in binding geometries can explain differences in MBI binding orientation. NMR, UV-vis, and magnetic moment analysis indicate that each MBI displays slightly different electronic characteristics while retaining overall similarities in oxidation states and spin states. In addition, the comparison of MBIs to picolinic acid and 2,2'-bipyridine indicate that these MBIs are better described as isosteres of picolinic acid than 2,2'-bipyridine. Furthermore, the investigation of [(Tp^{Ph,Me})Co(MBI)] as a secondary model complex underlines

the need to use different model systems to best implement isosteric replacement for metalloenzyme inhibition. This work demonstrates that the binding of MBIs can be influenced by several factors including structural and electronic nature of MBIs, the active site metal ion, the spectator ligand (TPA vs $\text{Tp}^{\text{Ph,Me}}$), and by analogy the metalloenzyme active site environment. When using model complexes, we must consider other factors when translating these findings to the biological targets, such as steric constraints presented by the metalloenzyme, polar/nonpolar pockets, the presence or absence of H-bond acceptors/donors, and potential competition from biological anions. Making broader use of model systems provides a better understanding of MBIs, and the results studied here will prove useful when optimizing important factors in the rational design of metalloenzyme inhibitors.

3.7 Acknowledgements

Chapter 3 is a reprint of the material as it appears in “Evaluating Metal–Ligand Interactions of Metal-Binding Isosteres Using Model Complexes.” *Inorg. Chem.*, **2021**, 60, 22, 17161. The dissertation author was a primary author of this paper and gratefully acknowledges the contributions of coauthors Kathleen E. Prosser, Mark Kalaj, Johannes Karges, Benjamin L. Dick, and Seth M. Cohen.

3.8 Appendix: Supporting Information

General Experimental Details

All reagents and solvents were obtained from commercial sources (Sigma Aldrich, Alfa Aesar, TCI, Combi-Blocks etc.) and used without further purification. Tris((2-pyridylmethyl)amine) (TPA) was synthesized using a modified literature procedure.⁴⁰

$[(\text{Tp}^{\text{Ph,Me}})\text{K}]$ ($\text{Tp}^{\text{Ph,Me}}$ = hydrotris(5,3-methylphenylpyrazolyl)borate) was prepared as previously reported.⁴¹ Picolinic acid and 2,2'-bipyridine were purchased from commercial suppliers. MBIs **3.1**, **3.2**, **3.3**, and **3.4** have been previously reported and were prepared according to literature procedures.³ $[\text{Ni}(\text{TPA})(\text{OAc})(\text{H}_2\text{O})]\text{PF}_6$ and $[\text{Co}(\text{TPA})(\text{OAc})]\text{BPh}_4$ were prepared using a modified literature procedure.^{10, 40} To obtain an X-ray structure of $[\text{Co}(\text{TPA})(\text{pic})]^+$, it was necessary to use an alternative counterion, ClO_4^- , because of its higher crystal quality and non-hygroscopic nature. $[(\text{Tp}^{\text{Ph,Me}})\text{ZnOH}]$ and $[(\text{Tp}^{\text{Ph,Me}})\text{CoCl}]$ was prepared according to literature methods,¹⁸ and $[(\text{Tp}^{\text{Ph,Me}})\text{Co}(\text{MBI})]$ and $[(\text{Tp}^{\text{Ph,Me}})\text{Zn}(\text{bpy})]$ were prepared by a modification of the literature procedure.³⁻⁴ Column chromatography was performed using a CombiFlash Rf automated system from Teledyne Isco using prepacked silica cartridges. All the solution-state characterization was carried out in DMSO to prevent any solubility issues. ^1H NMR spectra were recorded at ambient temperature on 300 MHz Bruker instrument and ^{13}C NMR spectra were collected using 500 MHz Varian NMR instrument. Magnetic measurements were performed by solution ^1H NMR using the Evans' method³³ on a 300 MHz Bruker NMR spectrometer for all complexes performed at room temperature in an open-air system. The measurements were performed in a standard 5 mm NMR tube containing the paramagnetic sample of 20 mM dissolved in 400 - 500 μL of $\text{DMSO}-d_6$ against a co-axial reference tube filled with the same solvent. Processing of the NMR data was performed using the MestReNova 14.2 program. UV-visible spectra were recorded with the samples of 5 mM dissolved in DMSO using a Perkin-Elmer Lambda 25 spectrophotometer. Absorbance maxima are given as λ_{max} (nm) with extinction coefficients reported (ϵ , $\text{M}^{-1} \text{cm}^{-1}$). Infrared spectra were collected on a Bruker Alpha FT-IR instrument. Mass spectra were obtained at the Molecular Mass Spectrometry Facility (MMSF) in the Department of Chemistry and Biochemistry at the University of California, San Diego.

Compound Synthesis

2-(1*H*-tetrazol-5-yl)pyridine (3.1). The compound was made following a previously reported procedure.³ Picolinonitrile (2.00 g, 19.2 mmol) was dissolved in 20 mL of DMF. Sodium azide (1.87 g, 28.8 mmol) and ammonium chloride (1.54 g, 28.8 mmol) were added to the DMF solution and the mixture was stirred under nitrogen at 110 °C for 3 h. The reaction mixture was concentrated down almost to dryness on a rotary evaporator. Water was added to the residue and the solution was acidified to pH 2.0 using 6 M HCl. The product precipitated as a solid and was collected by filtration. The collected white solid was washed with water and dried. Yield: 2.0 g (13.6 mmol, 71%). ¹H NMR (300 MHz, DMSO-*d*₆): δ 8.81 (ddd, *J*₁ = 4.8, *J*₂ = 1.7, *J*₃ = 0.9 Hz, 1H), 8.24 (dt, *J*₁ = 7.9, *J*₂ = 1.1 Hz, 1H), 8.09 (td, *J*₁ = 7.7, *J*₂ = 1.7 Hz, 1H), 7.64 (ddd, *J*₁ = 7.6, *J*₂ = 4.8, *J*₃ = 1.2 Hz, 1H). ESI-MS (*m/z*): [M+H]⁺ calcd. for C₆H₆N₅, 148.06; found, 148.11. ATR-FTIR (neat, cm⁻¹): 1606, 1620, 1637.

3-(pyridin-2-yl)-1,2,4-oxadiazol-5(4H)-one (3.2). The compound was made following a previously reported procedure.¹⁶ *N*-Hydroxypicolinimidamide (1.37 g, 10.0 mmol) was dissolved in 20 mL of dry pyridine. Ethyl chloroformate was added to the pyridine solution and the mixture was stirred under nitrogen for 6 h at reflux. The reaction mixture was concentrated and diluted with water and a precipitate formed. The precipitate was washed with water and recrystallized from water producing beige needles, which were collected by filtration. Yield: 0.89 g (5.5 mmol, 55%). ¹H NMR (300 MHz, DMSO-*d*₆): δ 13.16 (s, 1H), 8.77 (ddd, *J*₁ = 4.8, *J*₂ = 1.6, *J*₃ = 1.0 Hz, 1H), 8.09 - 8.02 (m, 1H), 8.00 (dt, *J*₁ = 7.9, *J*₂ = 1.4 Hz, 1H), 7.67 (ddd, *J*₁ = 7.3, *J*₂ = 4.8, *J*₃ = 1.5 Hz, 1H). ESI-MS (*m/z*): [M+H]⁺ calcd. for C₇H₆N₃O₂, 164.05; found, 164.12. ATR-FTIR (neat, cm⁻¹): 1565, 1582, 1779.

5-(pyridin-2-yl)-2,4-dihydro-3H-1,2,4-triazol-3-one (3.3). The compound was made following a previously reported procedure.¹⁷ Methyl picolinimidate (0.80 g, 5.9 mmol) and ethyl carbazate (0.61 g, 5.9 mmol) were melted together at 200 °C and stirred for 10 min. The resulting solid was recrystallized from EtOH to yield a white solid. Yield: 0.36 g (2.2 mmol, 37%). ¹H NMR (300 MHz, DMSO-*d*₆): δ 12.07 (s, 1H), 11.81 (s, 1H), 8.63 (dt, *J*₁ = 4.9, *J*₂ = 1.3 Hz, 1H), 7.93 (t, *J*₁ = 1.5 Hz, 1H), 7.92 (d, *J*₁ = 1.3 Hz, 1H), 7.52 – 7.42 (m, 1H). ESI-MS (*m/z*): [M+H]⁺ calcd. for C₇H₇N₄O, 163.06; found, 163.22. ATR-FTIR (neat, cm⁻¹): 1600, 1713.

3-(pyridin-2-yl)-1,2,4-oxadiazole-5(4H)-thione (3.4). The compound was made following a previously reported procedure.³ *N*-Hydroxypicolinimidamide (1.0 g, 7.3 mmol) was dissolved in 60 mL of acetonitrile. 1,1'-Thiocarbonyldiimidazole (1.94 g, 10.9 mmol) and 1,8-diazabicyclo[5.4.0]undec-7-ene (4.4 mL, 29 mmol) were added to the acetonitrile solution and the mixture was stirred under nitrogen at room temperature overnight. The reaction mixture was diluted with water and acidified with 6 M HCl until a yellow precipitate formed. The precipitate was collected by filtration, washed with water, and dried resulting in a yellow solid. Yield: 0.93 g (5.2 mmol, 71%). ¹H NMR (300 MHz, DMSO-*d*₆): δ 8.80 (d, *J*₁ = 4.7 Hz, 1H), 8.13 - 8.02 (m, 2H), 7.70 (ddd, *J*₁ = 6.8, *J*₂ = 4.8, *J*₃ = 2.1 Hz, 1H). ESI-MS (*m/z*): [M+H]⁺ calcd. for C₇H₆N₃OS, 180.02; found, 180.11. ATR-FTIR (neat, cm⁻¹): 1565, 1589.

(tris(2-pyridylmethyl)amine) (TPA). TPA was synthesized using a modified literature procedure.⁴⁰ In a 100 ml round bottom flask 2-(bromomethyl)pyridine hydrobromide (0.6 g, 2 mmol) and potassium carbonate (0.8 g, 6 mmol) were added to acetonitrile (30 mL), bis(pyridin-2-ylmethyl)amine (0.4 g, 0.4 mL, 2 mmol) was then added and the reaction was stirred overnight at room temperature. The reaction mixture was then filtered, and the filtrate was dried down and loaded onto silica. The product was purified via column chromatography using a CH₂Cl₂ : MeOH

gradient of 0-10% ($R_f = 0.30$, 7% MeOH in CH_2Cl_2). The fraction containing the product was dried down yielding a light brown to white solid. Yield: 0.31 g (2 mmol, 50%). $^1\text{H NMR}$ (300 MHz, $\text{DMSO-}d_6$): δ 8.49 (d, $J_1 = 4.4$ Hz, 1H), 7.77 (td, $J_1 = 7.7$, $J_2 = 1.9$ Hz, 1H), 7.59 (d, $J_1 = 7.8$ Hz, 1H), 7.25 (ddd, $J_1 = 7.5$, $J_2 = 4.8$, $J_3 = 1.2$ Hz, 1H), 3.77 (s, 2H). ESI-MS (m/z): $[\text{M}+\text{H}]^+$ calcd. for $\text{C}_{18}\text{H}_{18}\text{N}_4$, 291.15; found, 291.26. ATR-FTIR (neat, cm^{-1}): 1588, 1568, 1473, 1436, 1366, 1311.

[Ni(TPA)(pic)]PF₆. Nickel(II) acetate tetrahydrate (85.7 mg, 344 μmol) and TPA (100 mg, 344 μmol) were dissolved in MeOH (5 mL) and stirred for 10 min at room temperature. Picolinic acid (42 mg, 344 μmol) was then added to the reaction vessel and stirred for another 10 min. Sodium hexafluorophosphate(V) (58 mg, 344 μmol) was then added and stirred overnight at room temperature. A light purple solid precipitate resulted, which was collected by filtration. The resulting solid was washed with MeOH and dried. Vapor diffusion of Et_2O into a CH_3CN solution of the complex gave crystals suitable for X-ray diffraction. Yield: 39%. ATR-FTIR (neat, cm^{-1}): 557, 834 (PF_6^-), 1603, 1018, 1051, 1646, 1363. UV-vis: 531(21). ESI-MS (m/z): $[\text{M}-\text{PF}_6]^+$ calcd. for $\text{C}_{24}\text{H}_{22}\text{N}_5\text{NiO}_2$, 470.11; found, 470.17. HR-MS (m/z): $[\text{M}-\text{PF}_6]^+$ calcd. for $\text{C}_{24}\text{H}_{22}\text{N}_5\text{NiO}_2$, 470.1121; found, 470.1125.

[Ni(TPA)(3.1)]PF₆. The same procedure was used as in the synthesis of $[\text{Ni}(\text{TPA})(\text{pic})]\text{PF}_6$. The product was isolated as a purple solid. Vapor diffusion of Et_2O into a CH_3CN solution of the complex gave purple crystals suitable for X-ray diffraction. Yield: 38%. ATR-FTIR (neat, cm^{-1}): 557, 833 (PF_6^-), 1608, 1020, 1054. UV-vis: 534 (23). ESI-MS (m/z): $[\text{M}-\text{PF}_6]^+$ calcd. for $\text{C}_{24}\text{H}_{22}\text{N}_9\text{Ni}$, 494.14; found, 494.14. HR-MS (m/z): $[\text{M}-\text{PF}_6]^+$ calcd. for $\text{C}_{24}\text{H}_{22}\text{N}_9\text{Ni}$, 494.1346; found, 494.1343.

[Ni(TPA)(3.2)]PF₆. The same procedure was used as in the synthesis of [Ni(TPA)(pic)]PF₆. The product was isolated as a purple solid. Vapor diffusion of Et₂O into a CH₃CN solution of the complex gave purple crystals suitable for X-ray diffraction. Yield: 37%. ATR-FTIR (neat, cm⁻¹): 557, 833 (PF₆⁻), 1608, 1020, 1051, 1696, 1398. UV-vis: 548 (21). ESI-MS (*m/z*): [M-PF₆]⁺ calcd. for C₂₅H₂₂N₇NiO₂, 510.12; found, 510.14. HR-MS (*m/z*): [M-PF₆]⁺ calcd. for C₂₅H₂₂N₇NiO₂, 510.1183; found, 510.1181.

[Ni(TPA)(3.3)]PF₆. Nickel(II) acetate tetrahydrate (86 mg, 344 μmol) and TPA (100 mg, 344 μmol) were dissolved in iPrOH (5 mL) and stirred for 10 min at room temperature. 5-(Pyridin-2-yl)-2,4-dihydro-3H-1,2,4-triazol-3-one (**3**, 56 mg, 344 μmol) was then added to the reaction vessel and stirred for another 10 min. Tetrabutylammonium hexafluorophosphate(V) (133 mg, 344 μmol) was then added and stirred overnight. A light purple solid precipitate resulted, which was collected by filtration. The resulting solid was washed with iPrOH and dried. Vapor diffusion of Et₂O into a CH₃CN solution of the complex gave purple crystals suitable for X-ray diffraction. Yield: 41%. ATR-FTIR (neat, cm⁻¹): 557, 834 (PF₆⁻), 1606, 1023, 1052, 1625. UV-vis: 552 (19). ESI-MS (*m/z*): [M-PF₆]⁺ calcd. for C₂₅H₂₃N₈NiO, 509.14; found, 509.14. HR-MS (*m/z*): [M-PF₆]⁺ calcd. for C₂₅H₂₃N₈NiO, 509.1343; found, 509.1345.

[Ni(TPA)(3.4)]PF₆. The same procedure was used as in the synthesis of [Ni(TPA)(pic)]PF₆. The product was a purple solid. Vapor diffusion of Et₂O into a CH₃CN solution of the complex gave purple crystals suitable for X-ray diffraction. Yield: 54%. ATR-FTIR (neat, cm⁻¹): 557, 834 (PF₆⁻), 1607, 1021, 1054, 1344. UV-vis: 555 (16). ESI-MS (*m/z*): [M-PF₆]⁺ calcd. for C₂₅H₂₂N₇NiO₂, 526.10; found, 526.14. HR-MS (*m/z*): [M-PF₆]⁺ calcd. for C₂₅H₂₂N₇NiO₂, 526.0955; found, 526.0950.

[Ni(TPA)(bpy)](PF₆)₂. To a solution of [Ni(TPA)(OAc)(H₂O)]PF₆ (100 mg, 175 μmol) dissolved in MeOH (5 mL) was added 2,2'-bipyridine (27 mg, 175 μmol) and NaPF₆ (35 mg, 210 μmol). The reaction was stirred under ice bath for 2 h. The purple precipitates were collected by filtration and dried. Vapor diffusion of Et₂O into a CH₃CN solution of the complex gave purple crystals suitable for X-ray diffraction. Yield: 22%. ATR-FTIR (neat, cm⁻¹): 557, 827 (BPh₄⁻), 1607, 1021, 1054. UV-vis: 557 (12). ESI-MS (*m/z*): [M-PF₆]²⁺ calcd. for C₂₈H₂₆N₆Ni, 252.08; found, 252.16.

[Co(TPA)(pic)]PF₆. Cobalt(II) acetate tetrahydrate (85.8 mg, 344 μmol) was dissolved in a mixture of MeOH (3 mL) and iPrOH (2 mL). TPA (100 mg, 344 μmol) was then dissolved to the solution, sonicated and stirred for 10 min until all pink cobalt solution was transformed into a bright green color. Picolinic acid (42 mg, 344 μmol) was added to the solution and stirred for 10 min giving brown color. Tetrabutylammonium hexafluorophosphate(V) (133 mg, 344 μmol) was added and stirred overnight. The pink precipitates were washed with a mixture of iPrOH and Ether. Vapor diffusion of Et₂O into a CH₃CN solution of the complex gave pink crystals suitable for X-ray diffraction. Yield: 70%. ATR-FTIR: 557, 834 (PF₆⁻), 1646, 1603, 1024, 1059. UV-vis: 493 (103). ESI-MS (*m/z*): [M-PF₆]⁺ calcd. for C₂₄H₂₂CoN₅O₂, 471.11; found, 471.11. HR-MS (*m/z*): [M-PF₆]⁺ calcd. for C₂₄H₂₂CoN₅O₂, 471.1100; found, 471.1089.

[Co(TPA)(3.1)]PF₆. The same procedure was used as in the synthesis of [Co(TPA)(pic)]PF₆. The product was a pink solid. Vapor diffusion of Et₂O into a CH₃CN solution of the complex gave pink crystals suitable for X-ray diffraction. Yield: 59%. ATR-FTIR (neat, cm⁻¹): 557, 833 (PF₆⁻), 1606, 1020, 1052. UV-vis: 485 (117). ESI-MS (*m/z*): [M-PF₆]⁺ calcd. for C₂₄H₂₂CoN₉, 495.13; found, 495.09. HR-MS (*m/z*): [M-PF₆]⁺ calcd. for C₂₄H₂₂CoN₉, 495.1325; found, 495.1328.

[Co(TPA)(3.2)]PF₆. The same procedure was used as in the synthesis of [Co(TPA)(pic)]PF₆. The product was a pink solid. Vapor diffusion of Et₂O into a CH₃CN solution of the complex gave pink crystals suitable for X-ray diffraction. Yield: 61%. ATR-FTIR (neat, cm⁻¹): 557, 833 (PF₆⁻), 1606, 1023, 1052, 1713, 1731, 1398. UV-vis: 486 (64). ESI-MS (*m/z*): [M-PF₆]⁺ calcd. for C₂₅H₂₂CoN₇O₂, 511.12; found, 511.09.

[Co(TPA)(3.3)]BPh₄. 5-(Pyridin-2-yl)-2,4-dihydro-3*H*-1,2,4-triazol-3-one (**3**, 8.7 mg, 54 μmol) was added into THF (5 mL) of [Co(TPA)(OAc)]BPh₄ (40 mg, 54 μmol). The solution changed color from green to brown. The solution was left to stir overnight at room temperature, resulting in pink precipitates, which were collected by filtration and dried. Vapor diffusion of cyclohexane into a CH₂Cl₂ solution of the complex gave pink crystals suitable for X-ray diffraction. Yield: 51%. ATR-FTIR (neat, cm⁻¹): 704, 732 (BPh₄⁻), 1602, 1021, 1058, 1633. UV-vis: 484 (88). ESI-MS (*m/z*): [M-PF₆]⁺ calcd. for C₂₅H₂₃CoN₈O, 510.13; found, 510.19.

[Co(TPA)(3.4)]BPh₄. 3-(Pyridin-2-yl)-1,2,4-oxadiazole-5(4*H*)-thione (**4**, 9.7 mg, 54 μmol) was added into THF (5 mL) of [Co(TPA)(OAc)]BPh₄ (40 mg, 54 μmol). The solution changed color from green to brown. Pink crystals suitable for X-ray diffraction were grown by slow evaporation of the complex from THF. Yield: 56%. ATR-FTIR (neat, cm⁻¹): 704, 732 (BPh₄⁻), 1605, 1021, 1055, 1346. UV-vis: 483 (76). ESI-MS (*m/z*): [M-PF₆]⁺ calcd. for C₂₅H₂₂CoN₇OS, 527.09; found, 527.09.

[(Tp^{Ph,Me})Co(pic)]. To a solution of [(Tp^{Ph,Me})CoCl] (50 mg, 87 μmol) dissolved in CH₂Cl₂ (10 ml) was added 2-3 drops of triethylamine. 1 equiv of picolinic acid (11 mg, 87 μmol) dissolved in 2 mL of MeOH to this solution, resulting in a pink-colored solution. The mixture was stirred at room temperature overnight under a nitrogen atmosphere. After stirring, the solution was evaporated to dryness to give a purple solid. The resulting precipitates was purified via silica gel

chromatography eluting a gradient of 0-3% MeOH in CH₂Cl₂ ($R_f = 0.23$, 5% MeOH in CH₂Cl₂). Pinkish-purple crystals suitable for X-ray diffraction were grown from a solution of the purified precipitates in benzene diffused with pentane. Yield: 63%. ATR-FTIR (neat, cm⁻¹): 1057, 1164, 1333, 1434, 1540, 1600, 1657, 1667, 2532 (B-H). UV-vis: 452 (41), 538 (49), 561 (51). ESI-MS (m/z): [M+Na]⁺ calcd. for C₃₆H₃₂BCoN₇O₂, 687.20; found, 687.28.

[(Tp^{Ph,Me})Co(3.1)]. The same procedure was used as in the synthesis of [(Tp^{Ph,Me})Co(pic)]. The product was a purple solid. ($R_f = 0.18$, 5% MeOH in CH₂Cl₂). Pinkish-purple crystals suitable for X-ray diffraction were grown from a solution of the purified precipitates in benzene diffused with pentane. Yield: 70%. ATR-FTIR (neat, cm⁻¹): 1061, 1169, 1341, 1434, 1538, 1613, 2537 (B-H). UV-vis: 456 (37), 540 (49), 563 (47). ESI-MS (m/z): [M+Na]⁺ calcd. for C₃₆H₃₂BCoN₁₁, 711.23; found, 711.33. HR-MS (m/z): [M+H]⁺ calcd. for C₃₆H₃₂BCoN₁₁, 689.2346; found, 689.2339.

[(Tp^{Ph,Me})Co(3.2)]. The same procedure was used as in the synthesis of [(Tp^{Ph,Me})Co(pic)]. The product was a purple solid. ($R_f = 0.30$, 5% MeOH in CH₂Cl₂). Pinkish-purple crystals suitable for X-ray diffraction were grown from a solution of the purified precipitates in benzene diffused with pentane. Yield: 89%. ATR-FTIR (neat, cm⁻¹): 1060, 1173, 1342, 1436, 1541, 1610, 1732, 1752, 2541 (B-H). UV-vis: 448 (47), 542 (44), 562 (42). ESI-MS (m/z): [M+Na]⁺ calcd. for C₃₆H₃₀BCoN₉O₂, 727.21; found, 727.25.

[(Tp^{Ph,Me})Co(bpy)]PF₆. To a solution of [(Tp^{Ph,Me})CoCl] (50 mg, 87 μmol) dissolved in 10 mL CH₂Cl₂ was added 1 equiv of 2,2'-bipyridine (14 mg, 87 μmol) dissolved in 2 mL of MeOH. The mixture was stirred for 10 min. 2,2'-bipyridine was added and stirred at room temperature overnight under a nitrogen atmosphere. After stirring, the solution was evaporated to give a brownish orange solid. Brownish-orange crystals suitable for X-ray diffraction were grown from

a solution of the precipitates in benzene diffused with pentane. Yield: 83%. ATR-FTIR (neat, cm^{-1}): 1060, 1175, 1340, 1435, 1541, 1603, 2552 (B-H). UV-vis: 417 (333), 520 (76), 676 (34). ESI-MS (m/z): $[\text{M-PF}_6]^+$ calcd. for $\text{C}_{40}\text{H}_{36}\text{BCoN}_8$, 698.25; found, 698.21. HR-MS (m/z): $[\text{M-PF}_6]^+$ calcd. for $\text{C}_{40}\text{H}_{36}\text{BCoN}_8$, 698.2489; found, 698.2484.

$[(\text{Tp}^{\text{Ph,Me}})\text{Zn}(\text{bpy})]\text{ClO}_4$. $[(\text{Tp}^{\text{Ph,Me}})\text{ZnOH}]$ (40 mg, 71 μmol) was dissolved in 15 mL of CH_2Cl_2 . 2,2'-bipyridine (11 mg, 71 μmol) and sodium perchlorate (9mg, 71 μmol) in 10 mL of MeOH was added to the solution, and the reaction mixture was stirred at room temperature overnight under a nitrogen atmosphere. The resulting solution was evaporated to give white solid. Colorless crystals suitable for X-ray diffraction were grown from a solution of the precipitates in benzene diffused with pentane. The crystals were characterized by X-ray crystallography. Yield: 80%. HR-MS (m/z): $[\text{M-ClO}_4]^+$ calcd. for $\text{C}_{40}\text{H}_{36}\text{BZnN}_8$, 703.2449; found, 703.2443. *Caution:* Perchlorate salts of metal complexes with organic ligands are potentially explosive. Only small amounts of these materials should be prepared, and they should be handled with great care.

Single Crystal X-ray Diffraction

Suitable crystals of $[\text{M}(\text{TPA})(\text{L})]$ ($\text{M} = \text{Ni}^{2+}$ and Co^{2+} , TPA = tris(2-pyridylmethyl)amine), $[(\text{Tp}^{\text{Ph,Me}})\text{Co}(\text{L})]$ ($\text{Tp}^{\text{Ph,Me}} = \text{hydrotris}(3,5\text{-phenylmethylpyrazolyl})\text{borate}$, and $[(\text{Tp}^{\text{Ph,Me}})\text{Zn}(\text{bpy})]$ were selected and data was collected at 100 K on a Bruker APEX-II Ultra diffractometer with a Mo- $\text{K}\alpha$ Microfocus Rotating Anode and a APEX-II CCD area detector or a Bruker Kappa diffractometer equipped with a Bruker X8 APEX II Mo sealed tube and a Bruker APEX-II CCD. The data was integrated and merged within the APEXIII software suite (Bruker, 2017). The structure was refined with the XL refinement package using least squares minimization using Olex2.⁴² The crystal data files were deposited into the Cambridge Crystallographic Data Centre (CCDC). Crystallographic data collection and refinement information is listed in Table S1-S4.

Disordered solvent was treated with the PLATON SQUEEZE⁴³ function in [Co(TPA)(2)]PF₆.

[Ni(TPA)(pic)]PF₆ was solved as a non-merohedral twin.

Table 3.S1. Crystal data and structure refinement for [Ni(TPA)(L)] complexes.

Compound	[Ni(TPA)(pic)]PF ₆	[Ni(TPA)(3.1)]PF ₆	[Ni(TPA)(3.2)]PF ₆
Identification code	2081982	2081990	2081980
Empirical formula	C ₂₄ H ₂₂ F ₆ N ₅ NiO ₂ P	C ₂₈ H ₂₈ F ₆ N ₁₁ NiP	C ₂₅ H ₂₂ F ₆ N ₇ NiO ₂ P
Formula weight	616.14	722.29	656.17
Temperature/K	100	293(2)	100
Crystal system	triclinic	monoclinic	monoclinic
Space group	P1	P2 ₁ /n	P2 ₁ /n
a/Å	9.725(2)	13.23(3)	11.5160(13)
b/Å	9.781(2)	15.59(4)	14.7537(13)
c/Å	14.724(3)	15.43(3)	16.0607(16)
α/°	108.293(2)	90	90
β/°	101.816(2)	104.59(2)	90.579(4)
γ/°	101.938(2)	90	90
Volume/Å ³	1244.9(5)	3083(12)	2728.6(5)
Z	2	4	4
ρ _{calc} /cm ³	1.644	1.556	1.597
μ/mm ⁻¹	0.922	0.758	0.849
F(000)	628	1480	1336
Crystal size/mm ³	0.1 × 0.1 × 0.1	0.2 × 0.1 × 0.1	0.3 × 0.3 × 0.17
Radiation	MoKα (λ = 0.71073)	MoKα (λ = 0.71073)	MoKα (λ = 0.71073)
2θ range for data collection/°	3.044 to 51.36	4.472 to 51.486	3.748 to 51.378
Index ranges	-11 ≤ h ≤ 11, -11 ≤ k ≤ 11, -17 ≤ l ≤ 17	-16 ≤ h ≤ 16, -19 ≤ k ≤ 19, -18 ≤ l ≤ 18	-14 ≤ h ≤ 13, -17 ≤ k ≤ 17, -19 ≤ l ≤ 19
Reflections collected	9404	38392	33019
Independent reflections	9404 [R _{int} = ?, R _{sigma} = 0.0691]	5864 [R _{int} = 0.0483, R _{sigma} = 0.0298]	5162 [R _{int} = 0.0503, R _{sigma} = 0.0356]
Data/restraints/parameters	9404/3/704	5864/0/426	5162/0/379
Goodness-of-fit on F ²	1.057	1.073	1.037
Final R indexes [I ≥ 2σ (I)]	R ₁ = 0.0531, wR ₂ = 0.1134	R ₁ = 0.0327, wR ₂ = 0.0697	R ₁ = 0.0425, wR ₂ = 0.1019
Final R indexes [all data]	R ₁ = 0.0641, wR ₂ = 0.1198	R ₁ = 0.0385, wR ₂ = 0.0719	R ₁ = 0.0558, wR ₂ = 0.1094
Largest diff. peak/hole / e Å ⁻³	0.66/-0.74	0.47/-0.44	1.01/-0.70

Table 3.S1 (continued). Crystal data and structure refinement for [Ni(TPA)(L)] complexes.

Compound	[Ni(TPA)(3.3)]PF ₆	[Ni(TPA)(3.4)]PF ₆	[Ni(TPA)(bpy)](PF ₆) ₂
Identification code	2081979	2081981	2081987
Empirical formula	C ₇₇ H ₇₂ F ₁₈ N ₂₅ Ni ₃ O ₃ P ₃	C ₂₅ H ₂₂ F ₆ N ₇ NiOPS	C ₂₈ H ₂₆ F ₁₂ N ₆ NiP ₂
Formula weight	2006.63	672.23	795.2
Temperature/K	100	100	100
Crystal system	monoclinic	monoclinic	monoclinic
Space group	P2 ₁ /c	P2 ₁ /n	P2 ₁ /n
a/Å	17.9743(12)	11.489(4)	12.7867(9)
b/Å	34.133(2)	15.004(4)	18.2178(13)
c/Å	16.5741(11)	16.121(8)	13.6783(10)
α/°	90	90	90
β/°	116.111(2)	91.771(16)	100.355(2)
γ/°	90	90	90
Volume/Å ³	9130.7(11)	2777.6(19)	3134.4(4)
Z	4	4	4
ρ _{calc} /cm ³	1.46	1.608	1.685
μ/mm ⁻¹	0.762	0.906	0.825
F(000)	4096	1368	1608
Crystal size/mm ³	0.7 × 0.18 × 0.03	0.3 × 0.28 × 0.28	0.359 × 0.21 × 0.206
Radiation	MoKα (λ = 0.71073)	MoKα (λ = 0.71073)	MoKα (λ = 0.71073)
2θ range for data collection/°	2.792 to 50.842	3.71 to 51.982	3.764 to 52.93
Index ranges	-21 ≤ h ≤ 18, -41 ≤ k ≤ 28, -19 ≤ l ≤ 19	-14 ≤ h ≤ 14, -17 ≤ k ≤ 15, -19 ≤ l ≤ 19	-15 ≤ h ≤ 16, -22 ≤ k ≤ 22, -17 ≤ l ≤ 17
Reflections collected	49843	16724	39821
Independent reflections	16742 [R _{int} = 0.0743, R _{sigma} = 0.0965]	5177 [R _{int} = 0.0674, R _{sigma} = 0.0585]	6446 [R _{int} = 0.0693, R _{sigma} = 0.0492]
Data/restraints/parameters	16742/0/1163	5177/0/379	6446/0/442
Goodness-of-fit on F ²	1.018	1.057	1.19
Final R indexes [I ≥ 2σ (I)]	R ₁ = 0.0648, wR ₂ = 0.1457	R ₁ = 0.0467, wR ₂ = 0.1178	R ₁ = 0.0553, wR ₂ = 0.1577
Final R indexes [all data]	R ₁ = 0.1027, wR ₂ = 0.1603	R ₁ = 0.0573, wR ₂ = 0.1236	R ₁ = 0.0878, wR ₂ = 0.1766
Largest diff. peak/hole / e Å ⁻³	1.58/-0.68	1.49/-0.99	1.02/-0.63

Table 3.S2. Crystal data and structure refinement for [Co(TPA)(L)] complexes.

Compound	[Co(TPA)(pic)]ClO ₄	[Co(TPA)(3.1)]PF ₆	[Co(TPA)(3.2)]PF ₆
Identification code	2081983	2081977	2081988
Empirical formula	C ₂₄ H ₂₂ ClCoN ₅ O ₆	C ₁₀₄ H ₁₀₀ Co ₄ F ₂₄ N ₄₀ P ₄	C ₂₅ H ₂₂ CoF ₆ N ₇ O ₂ P
Formula weight	570.84	2725.83	656.39
Temperature/K	100	100.15	100
Crystal system	monoclinic	monoclinic	monoclinic
Space group	P2 ₁	P2 ₁	P2 ₁ /n
a/Å	8.4639(8)	14.4887(5)	11.3705(5)
b/Å	15.2766(15)	12.1410(5)	17.8558(9)
c/Å	9.6760(9)	33.0277(12)	14.7664(7)
α/°	90	90	90
β/°	98.636(3)	90.021(2)	102.5210(10)
γ/°	90	90	90
Volume/Å ³	1236.9(2)	5809.8(4)	2926.7(2)
Z	2	2	4
ρ _{calc} /cm ³	1.533	1.558	1.49
μ/mm ⁻¹	0.852	0.721	0.715
F(000)	586	2776	1332
Crystal size/mm ³	0.4 × 0.3 × 0.3	0.2 × 0.1 × 0.1	0.1 × 0.03 × 0.03
Radiation	MoKα (λ = 0.71073)	MoKα (λ = 0.71073)	MoKα (λ = 0.71073)
2θ range for data collection/°	4.868 to 52.202	2.466 to 52.298	3.632 to 52.784
Index ranges	-10 ≤ h ≤ 10, -18 ≤ k ≤ 18, -11 ≤ l ≤ 11	-17 ≤ h ≤ 16, -14 ≤ k ≤ 15, -40 ≤ l ≤ 40	-14 ≤ h ≤ 14, -22 ≤ k ≤ 22, -16 ≤ l ≤ 18
Reflections collected	17400	51175	25409
Independent reflections	4883 [R _{int} = 0.0383, R _{sigma} = 0.0422]	21766 [R _{int} = 0.0498, R _{sigma} = 0.0695]	5991 [R _{int} = 0.0408, R _{sigma} = 0.0296]
Data/restraints/parameters	4883/1/336	21766/1/1590	5991/212/437
Goodness-of-fit on F ²	1.031	1.019	1.027
Final R indexes [I >= 2σ (I)]	R ₁ = 0.0271, wR ₂ = 0.0547	R ₁ = 0.0422, wR ₂ = 0.0915	R ₁ = 0.0438, wR ₂ = 0.1107
Final R indexes [all data]	R ₁ = 0.0313, wR ₂ = 0.0564	R ₁ = 0.0483, wR ₂ = 0.0950	R ₁ = 0.0489, wR ₂ = 0.1149
Largest diff. peak/hole / e Å ⁻³	0.20/-0.28	0.41/-0.36	1.84/-0.49

Table 3.S2 (continued). Crystal data and structure refinement for [Co(TPA)(L)] complexes.

Compound	[Co(TPA)(3.3)]BPh ₄	[Co(TPA)(3.4)]BPh ₄
Identification code	2081976	2081978
Empirical formula	C ₄₉ H ₄₃ BCoN ₈ O	C ₅₃ H _{49.5} BCoN ₇ O ₂ S
Formula weight	829.65	918.29
Temperature/K	100	100
Crystal system	triclinic	monoclinic
Space group	P-1	P2 ₁ /c
a/Å	11.0760(11)	9.2064(12)
b/Å	11.0794(11)	20.633(3)
c/Å	18.375(2)	49.933(6)
α/°	91.635(4)	90
β/°	92.023(3)	94.383(2)
γ/°	101.488(3)	90
Volume/Å ³	2206.9(4)	9457(2)
Z	2	8
ρ _{calc} /cm ³	1.249	1.29
μ/mm ⁻¹	0.435	0.456
F(000)	866	3844
Crystal size/mm ³	0.2 × 0.1 × 0.02	0.2 × 0.1 × 0.1
Radiation	MoKα (λ = 0.71073)	MoKα (λ = 0.71073)
2θ range for data collection/°	3.754 to 50.75	3.272 to 52.24
Index ranges	-13 ≤ h ≤ 13, -12 ≤ k ≤ 13, -22 ≤ l ≤ 22	-10 ≤ h ≤ 11, -25 ≤ k ≤ 25, -61 ≤ l ≤ 45
Reflections collected	18222	58101
Independent reflections	7976 [R _{int} = 0.0985, R _{sigma} = 0.1638]	18808 [R _{int} = 0.0881, R _{sigma} = 0.1064]
Data/restraints/parameters	7976/0/541	18808/0/1171
Goodness-of-fit on F ²	0.993	1.02
Final R indexes [I >= 2σ (I)]	R ₁ = 0.0587, wR ₂ = 0.1148	R ₁ = 0.0657, wR ₂ = 0.1275
Final R indexes [all data]	R ₁ = 0.1289, wR ₂ = 0.1365	R ₁ = 0.1167, wR ₂ = 0.1459
Largest diff. peak/hole / e Å ⁻³	0.41/-0.47	0.56/-0.62

Table 3.S3. Crystal data and structure refinement for [(Tp^{Ph,Me})Co(L)]complexes.

Compound	[(Tp ^{Ph,Me})Co(pic)]	[(Tp ^{Ph,Me})Co(3.1)]
Identification code	2081986	2081985
Empirical formula	C ₃₆ H ₃₂ BCoN ₇ O ₂	C ₃₆ H ₃₂ BCoN ₁₁
Formula weight	664.42	688.46
Temperature/K	100	100
Crystal system	triclinic	triclinic
Space group	P-1	P-1
a/Å	11.6721(17)	11.701(2)
b/Å	11.7119(16)	11.819(2)
c/Å	11.7812(18)	11.840(2)
α/°	92.294(4)	87.693(6)
β/°	98.143(4)	81.811(6)
γ/°	90.633(4)	89.297(6)
Volume/Å ³	1592.8(4)	1619.3(5)
Z	2	2
ρ _{calc} /cm ³	1.385	1.412
μ/mm ⁻¹	0.584	0.576
F(000)	690	714
Crystal size/mm ³	0.1 × 0.1 × 0.1	0.1 × 0.1 × 0.1
Radiation	MoKα (λ = 0.71073)	MoKα (λ = 0.71073)
2θ range for data collection/°	3.48 to 52.526	3.448 to 50.908
Index ranges	-14 ≤ h ≤ 14, -14 ≤ k ≤ 14, -14 ≤ l ≤ 14	-13 ≤ h ≤ 14, -14 ≤ k ≤ 14, -14 ≤ l ≤ 14
Reflections collected	22783	13851
Independent reflections	6428 [R _{int} = 0.0929, R _{sigma} = 0.1002]	5966 [R _{int} = 0.0831, R _{sigma} = 0.1499]
Data/restraints/parameters	6428/0/431	5966/0/445
Goodness-of-fit on F ²	0.869	1.018
Final R indexes [I ≥ 2σ (I)]	R ₁ = 0.0498, wR ₂ = 0.1235	R ₁ = 0.0680, wR ₂ = 0.1280
Final R indexes [all data]	R ₁ = 0.0962, wR ₂ = 0.1508	R ₁ = 0.1439, wR ₂ = 0.1557
Largest diff. peak/hole / e Å ⁻³	0.20/-0.28	0.41/-0.36

Table 3.S3 (continued). Crystal data and structure refinement for [(Tp^{Ph,Me})Co(L)]complexes.

Compound	[(Tp ^{Ph,Me})Co(3.2)]	[(Tp ^{Ph,Me})Co(bpy)]PF ₆
Identification code	2081984	2081989
Empirical formula	C ₃₇ H ₃₂ BCoN ₉ O ₂	C ₄₀ H ₃₆ BCoF ₆ N ₈ P
Formula weight	704.45	843.48
Temperature/K	100	100
Crystal system	orthorhombic	tetragonal
Space group	P2 ₁ 2 ₁ 2 ₁	P4/ncc
a/Å	11.3095(4)	30.038(2)
b/Å	17.2601(6)	30.038(2)
c/Å	17.4135(8)	17.0629(16)
α/°	90	90
β/°	90	90
γ/°	90	90
Volume/Å ³	3399.2(2)	15395(3)
Z	4	16
ρ _{calc} /cm ³	1.377	1.456
μ/mm l	0.553	0.559
F(000)	1460	6928
Crystal size/mm ³	0.1 × 0.1 × 0.1	0.2 × 0.2 × 0.2
Radiation	MoKα (λ = 0.71073)	MoKα (λ = 0.71073)
2θ range for data collection/°	3.322 to 52.824	2.712 to 48.342
Index ranges	-13 ≤ h ≤ 14, -21 ≤ k ≤ 21, -21 ≤ l ≤ 18	-34 ≤ h ≤ 33, -14 ≤ k ≤ 34, -19 ≤ l ≤ 19
Reflections collected	23790	83296
Independent reflections	6856 [R _{int} = 0.0791, R _{sigma} = 0.0883]	6158 [R _{int} = 0.1314, R _{sigma} = 0.0646]
Data/restraints/parameters	6856/0/454	6158/0/522
Goodness-of-fit on F ²	0.813	1.029
Final R indexes [I ≥ 2σ (I)]	R ₁ = 0.0450, wR ₂ = 0.1128	R ₁ = 0.0512, wR ₂ = 0.1066
Final R indexes [all data]	R ₁ = 0.0653, wR ₂ = 0.1321	R ₁ = 0.0974, wR ₂ = 0.1279
Largest diff. peak/hole / e Å ⁻³	1.84/-0.49	0.39/-0.64

Table 3.S4. Crystal data and structure refinement for [(Tp^{Ph,Me})Zn(bpy)]complex.

Compound	[(Tp ^{Ph,Me})Zn(bpy)]ClO ₄
Identification code	2085664
Empirical formula	C ₄₇ H ₄₆ BClN ₈ O ₅ Zn
Formula weight	914.55
Temperature/K	100
Crystal system	monoclinic
Space group	P2 ₁ /c
a/Å	15.2609(7)
b/Å	15.0743(6)
c/Å	19.8118(8)
α/°	90
β/°	102.4780(10)
γ/°	90
Volume/Å ³	4450.0(3)
Z	4
ρ _{calc} /g/cm ³	1.365
μ/mm ⁻¹	0.668
F(000)	1904
Crystal size/mm ³	0.1 × 0.1 × 0.1
Radiation	MoKα (λ = 0.71073)
2θ range for data collection/°	2.734 to 52.228
Index ranges	-18 ≤ h ≤ 18, -18 ≤ k ≤ 18, -24 ≤ l ≤ 21
Reflections collected	54952
Independent reflections	8829 [R _{int} = 0.0343, R _{sigma} = 0.0219]
Data/restraints/parameters	8829/0/573
Goodness-of-fit on F ²	1.021
Final R indexes [I >= 2σ (I)]	R ₁ = 0.0278, wR ₂ = 0.0680
Final R indexes [all data]	R ₁ = 0.0334, wR ₂ = 0.0710
Largest diff. peak/hole / e Å ⁻³	0.35/-0.34

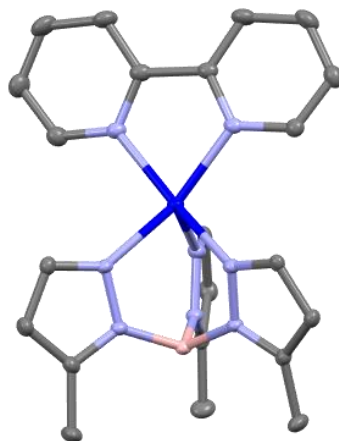


Figure 3.S1. Crystal structure of $[(\text{Tp}^{\text{Ph,Me}})\text{Zn}(\text{bpy})]$ (ORTEP, 50% probability ellipsoids). Color scheme: carbon = gray, oxygen = red, nitrogen = blue, zinc = navy, and boron = pink.

Table 3.S5. Selected bond lengths for $[\text{Ni}(\text{TPA})(\text{L})]$ (N1: amine nitrogen of TPA, N2-4: pyridyl nitrogen of TPA). Structures with more than one complex in the asymmetric unit are marked with an asterisk.

Compound	Ni-N1 (Å)	Ni-N2 (Å)	Ni-N3 (Å)	Ni-N4 (Å)
pic*	2.130(9)	2.095(9)	2.070(10)	2.100(10)
	2.141(9)	2.096(9)	2.072(10)	2.072(9)
3.1	2.119(3)	2.074(4)	2.070(4)	2.080(4)
3.2	2.090(2)	2.087(2)	2.138(2)	2.099(2)
3.3*	2.107(4)	2.087(4)	2.153(4)	2.087(4)
	2.097(4)	2.105(4)	2.149(4)	2.104(4)
	2.094(4)	2.083(4)	2.183(4)	2.080(4)
3.4	2.058(3)	2.064(3)	2.141(3)	2.087(3)
bpy	2.101(3)	2.074(3)	2.196(3)	2.053(3)

Table 3.S6. Selected bond lengths for $[\text{Co}(\text{TPA})(\text{L})]$ (N1: amine nitrogen of TPA, N2-4: pyridyl nitrogen of TPA). Structures with more than one complex in the asymmetric unit are marked with an asterisk.

Compound	Co-N1 (Å)	Co-N2 (Å)	Co-N3 (Å)	Co-N4 (Å)
pic	2.210(3)	2.131(3)	2.113(2)	2.128(3)
3.1*	2.217(5)	2.071(6)	2.121(6)	2.120(6)
	2.233(5)	2.109(6)	2.147(6)	2.061(6)
	2.216(5)	2.110(6)	2.130(6)	2.077(6)
	2.240(5)	2.076(6)	2.133(6)	2.101(6)
3.2	2.207(2)	2.107(2)	2.144(2)	2.1258(19)
3.3	2.233(3)	2.109(3)	2.160(3)	2.123(3)
3.4	2.157(3)	2.107(3)	2.131(3)	2.117(3)
	2.168(3)	2.141(3)	2.149(3)	2.134(3)

Computations

Computational experiments were performed using density-functional theory (DFT) calculations with the Gaussian 09 software package.⁴⁴ All computations were carried out at the wB97x-D/LanL2DZ level of theory in the gas phase at standard conditions at 1 atm and 298 K. The structures of all calculated molecules correspond to minima on the ground state potential energy surfaces with no imaginary frequencies present.

Table 3.S7. Bonds lengths and angles for Ni(II) and Co(II) coordinated TPA complexes with the MBIs **3.2 – 3.4** using DFT calculations at the wB97x-D/LanL2DZ level of theory. a = N5 cis to the N1 of TPA, b = N5 trans to the N1 of TPA, * = crystallographically observed conformation.

Compound	M-N5 (Å)	M-N6 (Å)	Bite angle (°)
Ni-3.1a*	2.258	2.062	76.88
Ni-3.1b	2.266	2.068	76.63
Ni-3.2a	2.109	2.111	79.68
Ni-3.2b*	2.112	2.101	79.84
Ni-3.3a	2.111	2.117	79.21
Ni-3.3b*	2.113	2.115	79.43
Ni-3.4a	2.075	2.156	79.37
Ni-3.4b*	2.073	2.154	79.48
Co-3.1a*	2.343	2.083	74.39
Co-3.1b	2.359	2.092	76.43
Co-3.2a*	2.280	2.082	77.18
Co-3.2b	2.274	2.090	76.64
Co-3.3a*	2.266	2.061	76.96
Co-3.3b	2.263	2.068	76.39
Co-3.4a	2.165	2.177	76.74
Co-3.4b*	2.166	2.172	76.89

¹H NMR Spectra

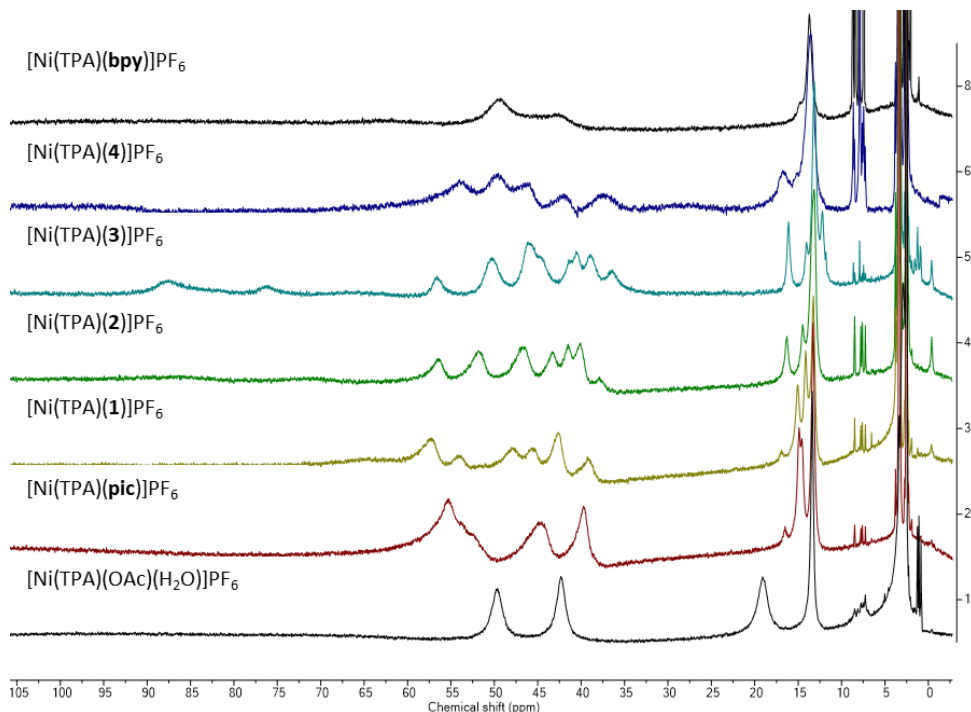


Figure 3.S2. ¹H NMR spectra of [Ni(TPA)(L)] system in DMSO. [Ni(TPA)(OAc)(H₂O)]PF₆ complex (*bottom*) was characterized to guide the interpretation of the other complexes.

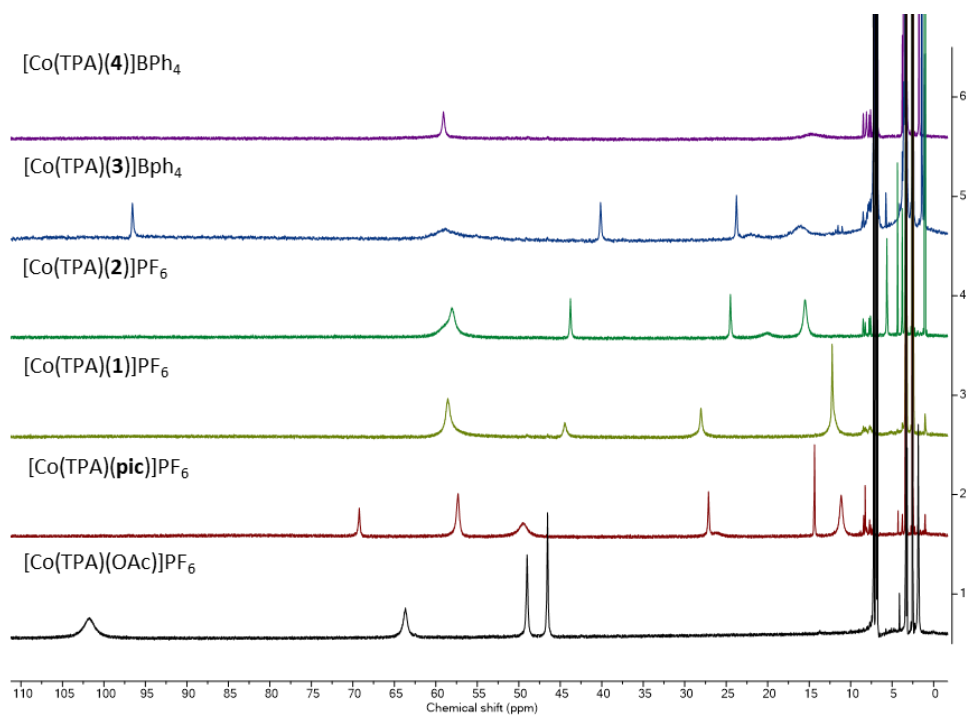


Figure 3.S3. ¹H NMR spectra of [Co(TPA)(L)] system in DMSO. [Co(TPA)(OAc)]PF₆ complex (*bottom*) was characterized to guide the interpretation of the other complexes.

UV-visible Spectra

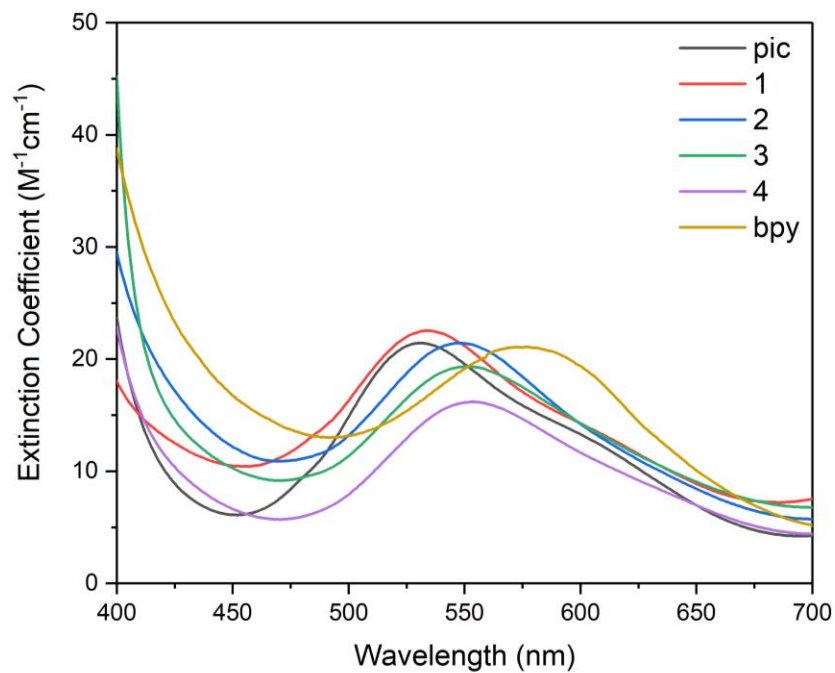


Figure 3.S4. UV-visible spectra of [Ni(TPA)(L)] complexes (5 mM) in DMSO.

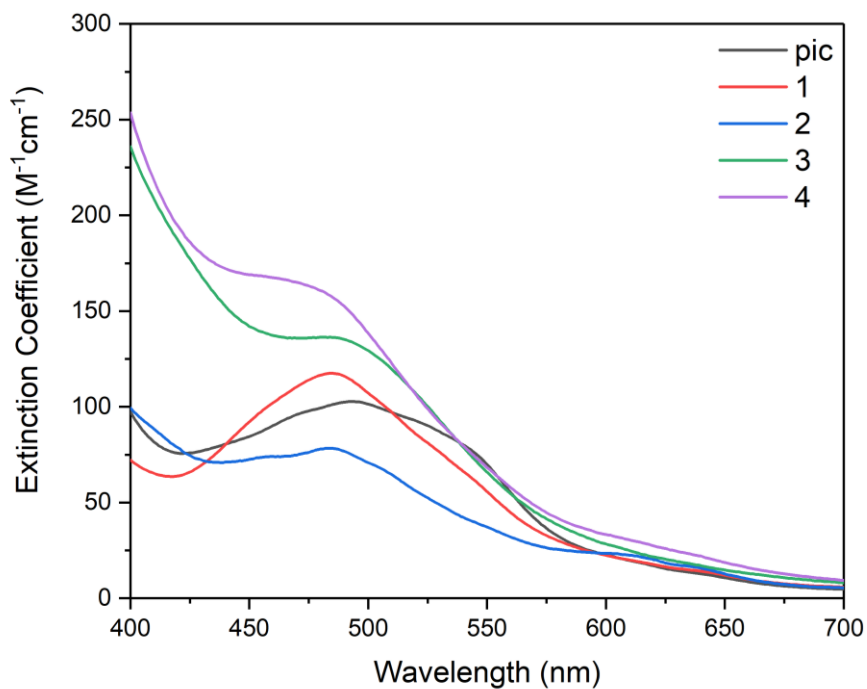


Figure 3.S5. UV-visible spectra of [Co(TPA)(L)] complexes (5 mM) in DMSO.

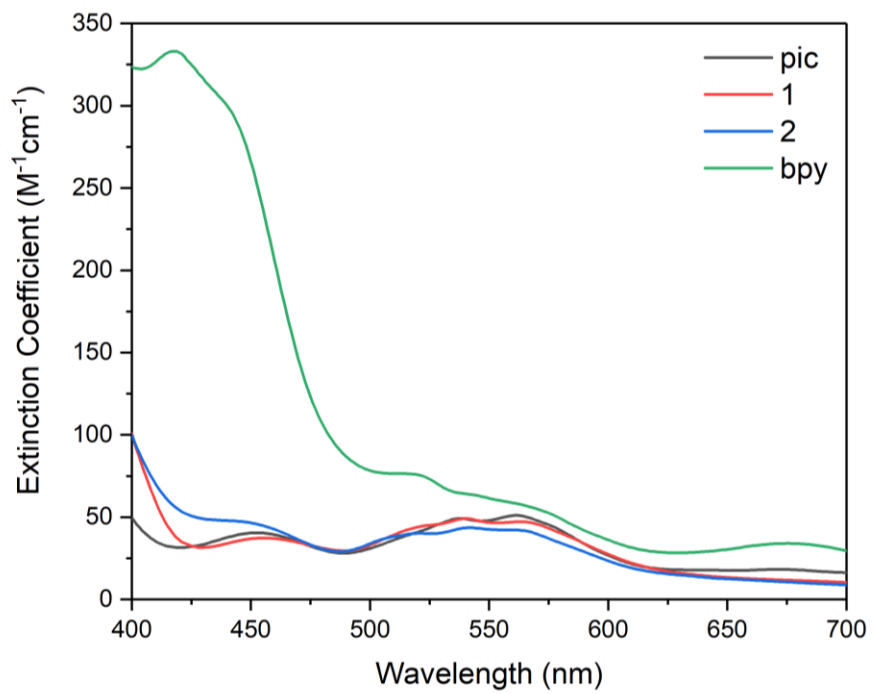


Figure 3.S6. UV-visible spectra of $[(Tp^{Ph,Me})Co(L)]$ complexes (5 mM) in DMSO.

IR Spectra

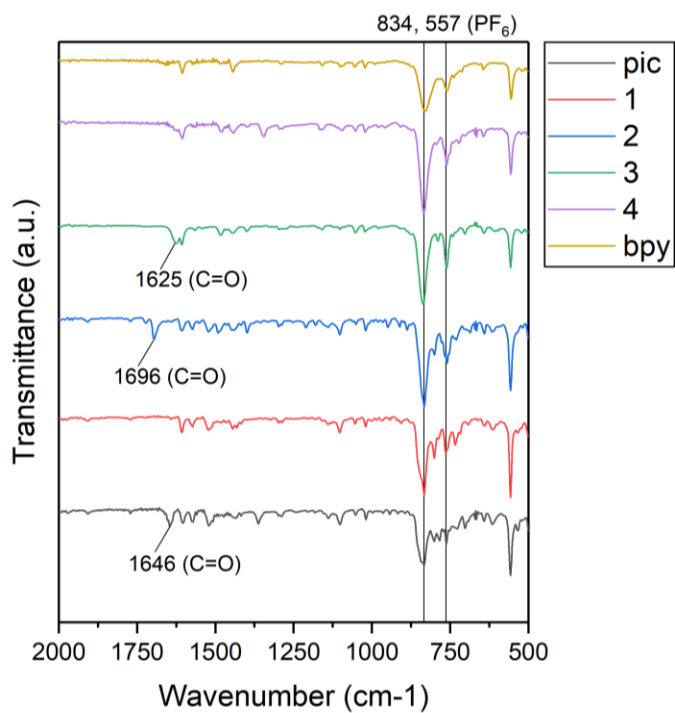


Figure 3.S7. IR spectra of [Ni(TPA)(L)] complexes.

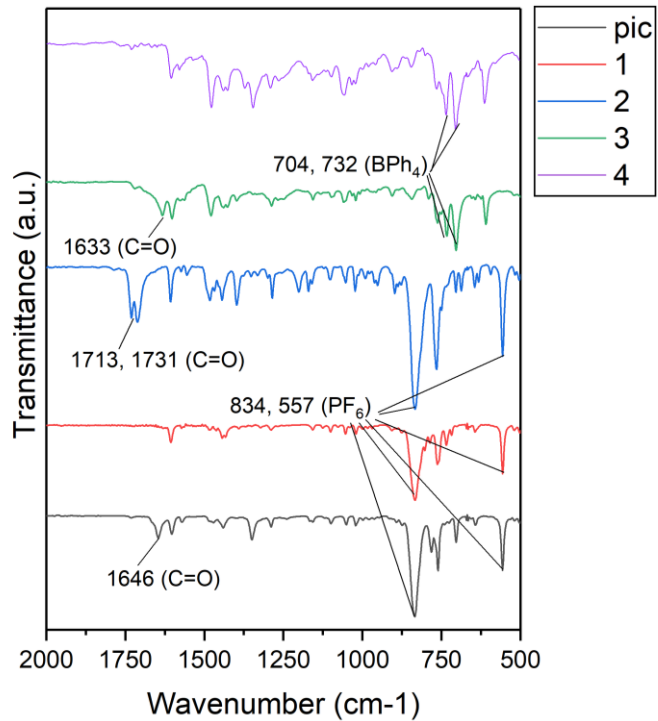


Figure 3.S8. IR spectra of [Co(TPA)(L)] complexes.

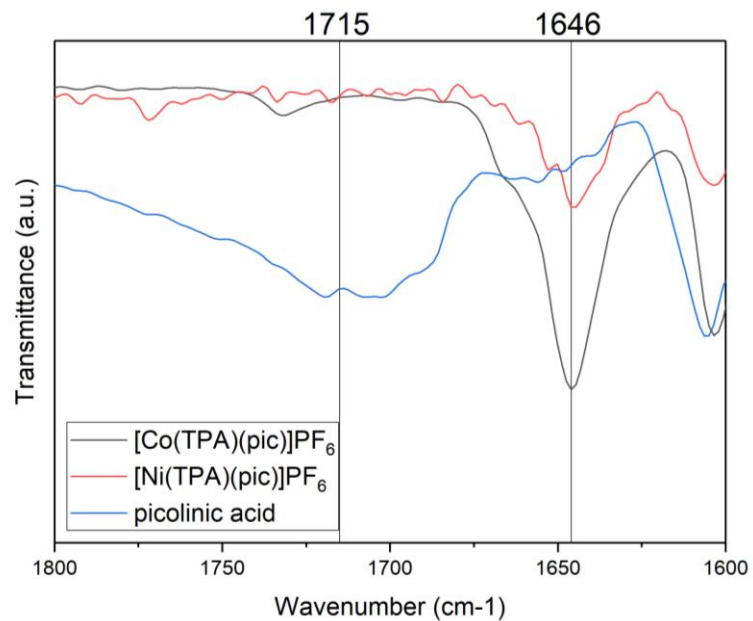


Figure 3.S9. IR spectra showing C=O stretching peaks of picolinic acid, [Ni(TPA)(L)], and [Co(TPA)(L)] complexes. The carbonyl band of picolinic acid was shifted to a lower wavenumber when bound to the TPA complex.

3.9 References

1. Seo, H.; Jackl, M. K.; Kalaj, M.; Cohen, S. M., Developing Metal-binding Isosteres of 8-Hydroxyquinoline as Metalloenzyme Inhibitor Scaffolds. *Inorg. Chem.* **2022**, *61* (19), 7631-7641.
2. Jackl, M. K.; Seo, H.; Karges, J.; Kalaj, M.; Cohen, S. M., Salicylate Metal-Binding Isosteres as Fragments for Metalloenzyme Inhibition. *Chem. Sci.* **2022**, *13* (7), 2128-2136.
3. Dick, B. L.; Cohen, S. M., Metal-Binding Isosteres as New Scaffolds for Metalloenzyme Inhibitors. *Inorg. Chem.* **2018**, *57* (15), 9538-9543.
4. Jacobsen, F. E.; Breece, R. M.; Myers, W. K.; Tierney, D. L.; Cohen, S. M., Model Complexes of Cobalt-Substituted Matrix Metalloproteinases: Tools for Inhibitor Design. *Inorg. Chem.* **2006**, *45* (18), 7306-7315.
5. Wang, H.-Y.; Mijangos, E.; Ott, S.; Thapper, A., Water Oxidation Catalyzed by a Dinuclear Cobalt–Polypyridine Complex. *Angew. Chem. Int. Ed.* **2014**, *53* (52), 14499-14502.
6. Bonnitcha, P. D.; Kim, B. J.; Hocking, R. K.; Clegg, J. K.; Turner, P.; Neville, S. M.; Hambley, T. W., Cobalt complexes with tripodal ligands: implications for the design of drug chaperones. *Dalton Trans.* **2012**, *41* (37), 11293.
7. Culpitt, T.; Guzei, I. A.; Spencer, L. C.; Simonson, A.; Miller, J. S.; Wimmer, M. R.; Nelson, K. J., Synthesis, crystal structures, and characterization of 4,5-diaza-9-[4,5-bis(methylthio)-1,3-dithiol-2-ylidene]-fluorene (L) metal complexes [(TPyA)M^{II}(L)](SbF₆)₂ (M^{II} = Mn, Fe, Co; TPyA=tris(2-pyridylmethyl)amine). *Inorg. Chim. Acta* **2015**, *427*, 162-167.
8. Massoud, S. S.; Perkins, R. S.; Louka, F. R.; Xu, W.; Roux, A. L.; Dutercq, Q.; Fischer, R. C.; Mautner, F. A.; Handa, M.; Hiraoka, Y.; Kreft, G. L.; Bortolotto, T.; Terenzi, H., Efficient hydrolytic cleavage of plasmid DNA by chloro-cobalt(II) complexes based on sterically hindered

pyridyl tripod tetraamine ligands: synthesis, crystal structure and DNA cleavage. *Dalton Trans.* **2014**, 43 (26), 10086-10103.

9. Melchior, A.; Tolazzi, M., Co(II) complexes with tripodal N-donor ligands: Thermodynamics of formation in anaerobic conditions and oxygen binding. *Inorg. Chim. Acta* **2011**, 367 (1), 120-126.

10. Nagataki, T.; Tachi, Y.; Itoh, S., NiII(TPA) as an efficient catalyst for alkane hydroxylation with m-CPBA. *Chem. Commun.* **2006**, (38), 4016-4018.

11. Rudzka, K.; Arif, A. M.; Berreau, L. M., Chemistry of a Ni(II) Acetohydroxamic Acid Complex: Formation, Reactivity with Water, and Attempted Preparation of Zinc and Cobalt Analogues. *Inorg. Chem.* **2005**, 44 (20), 7234-7242.

12. Chan, S. L.-F.; Lam, T. L.; Yang, C.; Lai, J.; Cao, B.; Zhou, Z.; Zhu, Q., Cobalt(II) tris(2-pyridylmethyl)amine complexes [Co(TPA)X]⁺ bearing coordinating anion (X=Cl⁻, Br⁻, I⁻ and NCS⁻): synthesis and application for carbon dioxide reduction. *Polyhedron* **2017**, 125, 156-163.

13. Rudzka, K.; Arif, A. M.; Berreau, L. M., Glyoxalase I-type Hemithioacetal Isomerization Reactivity of a Mononuclear Ni(II) Deprotonated Amide Complex. *J. Am. Chem. Soc.* **2006**, 128 (51), 17018-17023.

14. Szajna, E.; Dobrowolski, P.; Fuller, A. L.; Arif, A. M.; Berreau, L. M., NMR Studies of Mononuclear Octahedral Ni(II) Complexes Supported by Tris((2-pyridyl)methyl)amine-Type Ligands. *Inorg. Chem.* **2004**, 43 (13), 3988-3997.

15. Ballatore, C.; Huryn, D. M.; Smith, A. B., Carboxylic Acid (Bio)Isosteres in Drug Design. *ChemMedChem* **2013**, 8 (3), 385-395.

16. Gobis, K.; Foks, H.; Kędzia, A.; Wierzbowska, M.; Zwolska, Z., Synthesis and antibacterial activity of novel pyridine and pyrazine derivatives obtained from amidoximes. *J. Heterocycl. Chem.* **2009**, *46* (6), 1271-1279.
17. Dowell, R. I.; Hales, N. H.; Tucker, H., Novel inhibitors of prolyl 4-hydroxylase. Part 4 pyridine-2-carboxylic acid analogues with alternative 2-substituents. *Eur. J. Med. Chem.* **1993**, *28* (6), 513-516.
18. Uehara, K.; Hikichi, S.; Akita, M. Highly labile cationic tris-acetonitrile complexes, [Tp^RM(NCMe)₃]OTf (M = Ni, Co; Tp^R: hydrotrispyrazolylborato, R = Ph, Me and iPr₂): versatile precursors for Tp^R-containing nickel and cobalt complexes. *J. Chem. Soc., Dalton Trans.* **2002**, (18), 3529-3538.
19. Hammes, B. S.; Luo, X.; Chohan, B. S.; Carrano, M. W.; Carrano, C. J., Metal complexes of 3-carboxyethyl substituted trispyrazolylborates: interactions with the ester carbonyl oxygens. *J. Chem. Soc., Dalton Trans.* **2002**, (17), 3374-3380.
20. Jacobsen, F. E.; Lewis, J. A.; Cohen, S. M., A New Role for Old Ligands: Discerning Chelators for Zinc Metalloproteinases. *J. Am. Chem. Soc.* **2006**, *128* (10), 3156-3157.
21. Woods, T. J.; Stout, H. D.; Dolinar, B. S.; Vignesh, K. R.; Ballesteros-Rivas, M. F.; Achim, C.; Dunbar, K. R., Strong Ferromagnetic Exchange Coupling Mediated by a Bridging Tetrazine Radical in a Dinuclear Nickel Complex. *Inorg. Chem.* **2017**, *56* (20), 12094-12097.
22. van der Meer, M.; Rechkemmer, Y.; Frank, U.; Breitgoff, F. D.; Hohloch, S.; Su, C.-Y.; Neugebauer, P.; Marx, R.; Dörfel, M.; van Slageren, J.; Sarkar, B., A Dicobalt Complex with an Unsymmetrical Quinonoid Bridge Isolated in Three Units of Charge: A Combined Structural, (Spectro)electrochemical, Magnetic and Spectroscopic Study. *Chem. Eur. J.* **2016**, *22* (39), 13884-13893.

23. Areas, E. S.; de Assunção Paiva, J. L.; Ribeiro, F. V.; Pereira, T. M.; Kummerle, A. E.; Silva, H.; Guedes, G. P.; Cellis do Nascimento, A. C.; da Silva Miranda, F.; Neves, A. P., Redox-Activated Drug Delivery Properties and Cytotoxicity of Cobalt Complexes Based on a Fluorescent Coumarin- β -Keto Ester Hybrid. *Eur. J. Inorg. Chem.* **2019**, 2019 (37), 4031-4039.
24. Cho, J.; Furutachi, H.; Fujinami, S.; Suzuki, M., A Bis(μ -alkylperoxo)dinickel(II) Complex as a Reaction Intermediate for the Oxidation of the Methyl Groups of the Me₂-tpa Ligand to Carboxylate and Alkoxide Ligands. *Angew. Chem. Int. Ed.* **2004**, 43 (25), 3300-3303.
25. McCusker, J. K.; Rheingold, A. L.; Hendrickson, D. N. Variable-Temperature Studies of Laser-Initiated $^5T_2 \rightarrow ^1A_1$ Intersystem Crossing in Spin-Crossover Complexes: Empirical Correlations between Activation Parameters and Ligand Structure in a Series of Polypyridyl Ferrous Complexes. *Inorg. Chem.* **1996**, 35 (7), 2100-2112.
26. Marchivie, M.; Guionneau, P.; Létard, J.-F.; Chasseau, D., Photo-induced spin-transition: the role of the iron(II) environment distortion. *Acta Crystallogr. Sect. B: Struct. Sci.* **2005**, 61 (1), 25-28.
27. Bunker, P. R. J., Per Molecular Symmetry and Spectroscopy. *NRC Research Press, Ottawa* **1998**.
28. Schmiedekamp, A. M.; Ryan, M. D.; Deeth, R. J., Six-Coordinate Co²⁺ with H₂O and NH₃ Ligands: Which Spin State Is More Stable? *Inorg. Chem.* **2002**, 41 (22), 5733-5743.
29. Rossi, A. R.; Hoffmann, R., Transition metal pentacoordination. *Inorg. Chem.* **1975**, 14 (2), 365-374.
30. Bertini, I.; Luchinat, C., High spin cobalt(II) as a probe for the investigation of metalloproteins. *Adv. Inorg. Biochem.* **1984**, 6, 71-111.

31. Tubbs, K. J.; Szajna, E.; Bennett, B.; Halfen, J. A.; Watkins, R. W.; Arif, A. M.; Berreau, L. M., Mononuclear nitrogen/sulfur-ligated cobalt(ii) methoxide complexes: Structural, EPR, paramagnetic ^1H NMR, and electrochemical investigations. *Dalton Trans.* **2004**, (16), 2398.
32. Jolly, W. L., *The synthesis and characterization of inorganic compounds*. Prentice Hall: Hoboken, 1970.
33. Evans, D. F., 400. The determination of the paramagnetic susceptibility of substances in solution by nuclear magnetic resonance. *J. Chem. Soc.* **1959**, (0), 2003-2005.
34. Barefield, E. K.; Busch, D. H.; Nelson, S. M., Iron, cobalt, and nickel complexes having anomalous magnetic moments. *Q. Rev. Chem. Soc.* **1968**, 22 (4), 457.
35. Lewis, B. N. F. J., In *Progress in Inorganic Chemistry*; 1 ed.; Cotton, F. A., Ed.; Wiley: Hoboken, **1964**; Chapter 2, Vol. 6, pp 37-239.
36. Banci, L.; Bencini, A.; Benelli, C.; Gatteschi, D.; Zanchini, C., In *Structures versus Special Properties*; 1 ed.; Springer Berlin, **1982**; Vol. 52, pp 37-86.
37. Farrukh, M. A., *Advanced Aspects of Spectroscopy*. IntechOpen: London, **2012**.
38. Makowska-Grzyska, M. M.; Szajna, E.; Shipley, C.; Arif, A. M.; Mitchell, M. H.; Halfen, J. A.; Berreau, L. M., First Row Divalent Transition Metal Complexes of Aryl-Appended Tris((pyridyl)methyl)amine Ligands: Syntheses, Structures, Electrochemistry, and Hydroxamate Binding Properties. *Inorg. Chem.* **2003**, 42 (23), 7472-7488.
39. Basu Baul, T. S.; Nongsiej, K.; Rocha, B. G. M.; Guedes da Silva, M. F. C., Cobalt(II) complexes with pyridine and 5-[(E)-2-(aryl)-1-diazenyl]-quinolin-8-olates: synthesis, electrochemistry and X-ray structural characterization. *J. Coord. Chem.* **2018**, 71 (16-18), 2856-2874.

40. Gransbury, G. K.; Livesay, B. N.; Janetzki, J. T.; Hay, M. A.; Gable, R. W.; Shores, M. P.; Starikova, A.; Boskovic, C., Understanding the Origin of One- or Two-Step Valence Tautomeric Transitions in Bis(dioxolene)-Bridged Dinuclear Cobalt Complexes. *J. Am. Chem. Soc.* **2020**, *142* (24), 10692-10704.
41. Puerta, D. T.; Cohen, S. M., Elucidating Drug-Metalloprotein Interactions with Tris(pyrazolyl)borate Model Complexes. *Inorg. Chem.* **2002**, *41* (20), 5075-5082.
42. Sheldrick G., A short history of SHELX. *Acta Crystallogr. Sect. A: Found. Crystallogr.*, **2008**, *64*, 112-122.
43. Spek, A., *PLATON SQUEEZE*: a tool for the calculation of the disordered solvent contribution to the calculated structure factors. *Acta Crystallogr. Sect. C: Cryst. Struct. Commun.*, **2015**, *71*, 9-18.
44. Frisch M. J.; Trucks G. W.; Schlegel H. B.; Scuseria G. E.; Robb M. A.; Cheeseman J. R.; Scalmani G.; Barone V.; Mennucci B.; Petersson G. A.; Nakatsuji H.; Caricato M.; Li X.; Hratchian H. P.; Izmaylov A. F.; Bloino J.; Zheng G.; Sonnenberg J. L.; Hada M.; Ehara M.; Toyota K.; Fukuda R.; Hasegawa J.; Ishida M.; Nakajima T.; Honda Y.; Kitao O.; Nakai H.; Vreven T.; Montgomery J. A.; Jr.; Peralta J. E.; Ogliaro F.; Bearpark M.; Heyd J. J.; Brothers E.; Kudin K. N.; Staroverov V. N.; Kobayashi R.; Normand J.; Raghavachari K.; Rendell A.; Burant J. C.; Iyengar S. S.; Tomasi J.; Cossi M.; Rega N.; Millam J. M.; Klene M.; Knox J. E.; Cross J. B.; Bakken V.; Adamo C.; Jaramillo J.; Gomperts R.; Stratmann R. E.; Yazyev O.; Austin A. J.; Cammi R.; Pomelli C.; Ochterski J. W.; Martin R. L.; Morokuma K.; Zakrzewski V. G.; Voth G. A.; Salvador P.; Dannenberg J. J.; Dapprich S.; Daniels A. D.; Farkas Ö.; Foresman J. B.; Ortiz J. V.; Cioslowski J.; Fox D. J., *Gaussian 09*, Gaussian, Inc., Wallingford, CT, **2009**.

Chapter 4: Masking Thiol Reactivity with Thioamide, Thiourea, and Thiocarbamate-based Metal-Binding Pharmacophores (MBPs)

4.1 Introduction

In Chapter 3, we presented an analysis of the interactions between metal-binding isosteres (MBIs) and metal ions using bioinorganic model complexes.¹ Chapter 3 described the structural and electronic characteristics of picolinic acid MBIs bound to two different bioinorganic models. These studies elucidated the specific coordination modes and binding energy differences of these MBIs, as well as demonstrated the importance of using a variety of model systems to effectively study and understand MBIs. Our findings revealed that the picolinic MBIs closely resemble the parent MBP, suggesting a preferable isosteric relationship over alternatives like 2,2'-bipyridine. This foundational work underscored the concept of MBIs as a crucial tool for modifying and enhancing the function of existing metal-binding pharmacophores (MBPs).

Building upon these findings, Chapter 4 turns to another crucial aspect of constructing a robust fragment library, which involves enhancing the stability and addressing the reactivity of selected fragments. Given that chemically unstable and highly reactive compounds can undermine the effectiveness of a fragment library, this chapter is dedicated to creating a stable and reliable fragment library for metalloenzyme inhibition. The goal of Chapter 4 is to introduce a strategically designed fragment sublibrary, with a particular focus on thiol-based MBPs, aiming to harness the potential of thiol-based MBPs while mitigating their associated reactivity issues.

Among the metal-binding pharmacophores (MBPs) explored, thiol-based MBPs have been suggested as a useful class of fragments, especially for Zn(II)-dependent metalloenzymes.²⁻³ Captopril is an FDA-approved inhibitor with a thiol ligand serving as an MBP for the Zn(II)-dependent angiotensin-converting enzyme (ACE).⁴ The X-ray crystal structure of captopril bound to ACE reveals monodentate binding of the thiol functional group to the Zn(II) ion, which is further ligated by the protein residues His283, His387, and Glu411.⁵ Unfortunately, captopril has adverse

effects that are attributed to the thiol MBP, including rash and disruption of taste.⁶⁻⁷ Furthermore, the thiol moiety presents challenges for drug candidates more broadly because of the chemical reactivity and metabolic liability.⁸⁻⁹ Free thiols can be oxidized or form covalent adducts with biologically relevant thiol species such as cysteine residues or glutathione (GSH).⁸⁻⁹ This indiscriminate reactivity causes promiscuous biological activity that results in undesirable side effects.

To overcome some of these limitations, thioamides, thioureas, and thiocarbamates can serve as a thiol-like MBP with reduced liabilities. Thioamides, thioureas, and thiocarbamates are increasingly used as organosulfur ligands in coordination chemistry and are more stable when compared to other thiocarbonyls such as thioketones and thioaldehydes. Thioamides, thioureas, and thiocarbamates already plays a significant role in drug discovery. For example, propylthiouracil and methimazole are among the most important hyperthyroidism drugs used in the United States.¹⁰ These drugs contain a thiocarbamide group that is essential for their hyperthyroidism activity.

In Chapter 4, thioamides, thioureas, and thiocarbamates compounds are proposed as MBPs for inhibiting Zn(II)-dependent metalloenzymes. The reactivity of these compounds with DTNB (5,5'-dithiobis(2-nitrobenzoic acid)) and cysteine derivatives was studied using UV-visible and NMR spectroscopy, as well as by HPLC as a proxy for their biostability. The biological activity of these novel MBPs was evaluated by performing inhibition assays against two Zn(II)-dependent metalloenzymes, human carbonic anhydrase II (hCAII) and matrix metalloproteinase-2 (MMP-2). In addition, their binding in a Zn(II) model complex was elucidated utilizing single crystal X-ray diffraction. Finally, the binding modes of these MBPs in the active site of hCAII were investigated using protein crystallography. The results show that these ligands are effective MBPs that can

serve as useful fragments in future metalloenzyme fragment-based drug discovery (mFBDD) campaigns.

4.2 Library Design and Preparation

Eight (**4.1** – **8**, Figure 4.1) were investigated as MBPs in this study. Compounds **4.1**, **4.4**, and **4.7** are thiocarbamates, compounds **4.2**, **4.3**, and **4.6** are thioureas, and compounds **4.5** and **4.8** are thioamides. Compounds **4.1** – **4.8** have been reported as bioactive compounds, but not widely explored as metalloenzyme inhibitors. Among them, **4.1** (benzo[d]oxazole-2-(3H)-thione) was reported as hCA inhibitor.¹¹ The metal-binding mode of **4.1** to the hCA active site was elucidated by protein crystallography and its activity against different hCA isoforms suggested the possibility of developing selective hCA inhibitors. Compounds **4.9** and **4.10** were also studied here, as they have been reported as thione-based MBPs for metalloenzyme inhibitors.¹² Lastly, **4.11** – **4.13** were studied as representative thiol-containing compounds.¹

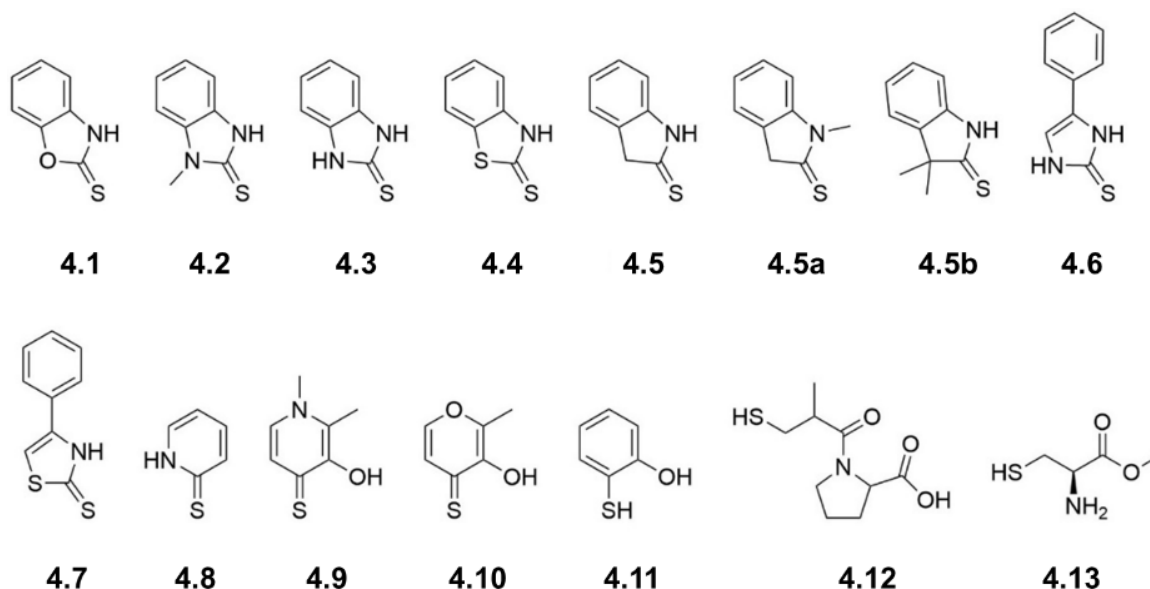


Figure 4.1. Thioamide, thiourea, and thiocarbamate MBPs were proposed for use in Zn(II)-dependent metalloenzymes. Compounds **4.9** and **4.10** were utilized as known thione-based MBPs and 2-mercaptophenol (**4.11**), captopril (**4.12**), and L-cysteine methyl ester (**4.13**) were used as representative thiol-based compounds in this paper.

4.3 Reactivity Evaluation

The reactivity of the compounds in Figure 4.1 with DTNB (5,5'-dithio-bis-(2-nitrobenzoic acid)), also known as Ellman's reagent, was monitored spectroscopically (Figure 4.2). DTNB reacts with sulfhydryl groups to produce a yellow-colored product, which can be quantified by its strong absorbance at 412 nm. Reactivity with DTNB was used as a surrogate for the propensity of the compounds to undergo disulfide exchange reactions with thiol-containing biomolecules and to qualitatively reflect the equilibrium of the tautomeric states between thione and thiol forms of each compound. Absorbance measurements were quantified against a standard calibration curve composed of known concentrations of L-cysteine methyl ester (**4.13**, Figure 4.S1). An excess of different DTNB ratios (1:2, 1:5, and 1:10) were used and the compounds and DTNB were incubated for 90 min prior to measuring the solution absorbance (Table 4.S1).

Thiol compounds **4.11** and **4.12** showed essentially quantitative conversion with DTNB, as expected. Compound **4.9** showed ~50% conversion, while **4.10** was more variable (between 50 and 75% with different DTNB ratios). The variability with **4.10** is tentatively attributed to the instability of the disulfide adduct between **4.10** and DTNB. Compounds **4.1** – **4**, **6**, and **8** showed essentially no reaction with DTNB after 90 min. Compounds **4.5** and **4.7** showed ~35% and ~20% conversion, respectively, which is significantly less than compounds **4.9** – **4.12**. The findings demonstrate that thioamide, thiourea, and thiocarbamate compounds are much less reactive with DTNB when compared with simple thiols. It also supports previous studies reporting that **4.1** – **4.8** predominantly exist as the thione tautomer,¹³⁻¹⁹ which is important for bioactivity. The stability of the thione tautomer may prevent these compounds from being oxidized spontaneously to their corresponding disulfides.

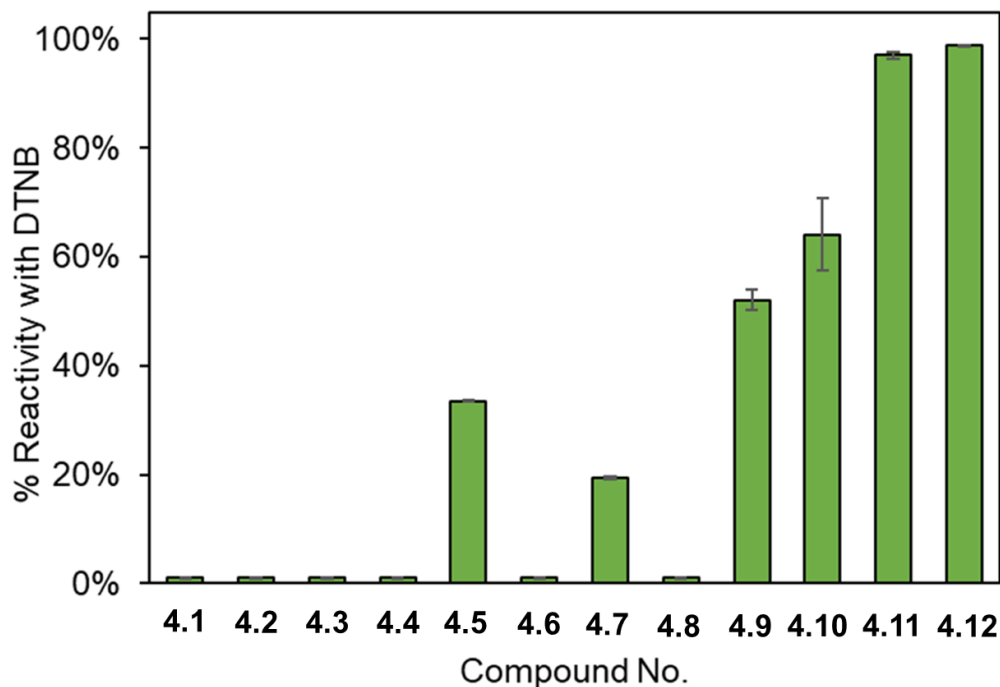


Figure 4.2. Percent reactivity of compounds **4.1** – **4.12** with DTNB. The molar ratio of compounds tested to DTNB was 1:10 with an incubation time of 90 min. 2-Mercaptophenol (**4.11**) and captopril (**4.12**) were used as representative thiol-based compounds that showed essential quantitative disulfide formation with DTNB.

As a secondary assay for biological stability, the reaction of compounds with L-cysteine methyl ester (**4.13**) was examined using HPLC (Figure 4.3). For this analysis, compounds were incubated with equimolar amounts of **4.13** for 24 h in 10% acetonitrile and 90% water at pH 7.4 (final concentration 1.25 mM). Compounds **4.1** – **4.7**, **4.9**, and **4.10** showed no reactivity with **4.13** under these conditions. By contrast, compounds **4.8** and **4.11** were found to generate disulfide products with **4.13** as revealed by the emergence of a new peak in the HPLC chromatogram. For **4.11**, several reaction products are observed, which are likely a combination of 2-mercapophenol-cysteine residues and products from the intrinsic oxidation of **4.11**. The findings observed in the HPLC analysis were confirmed by NMR analysis (Figure 4.S2).

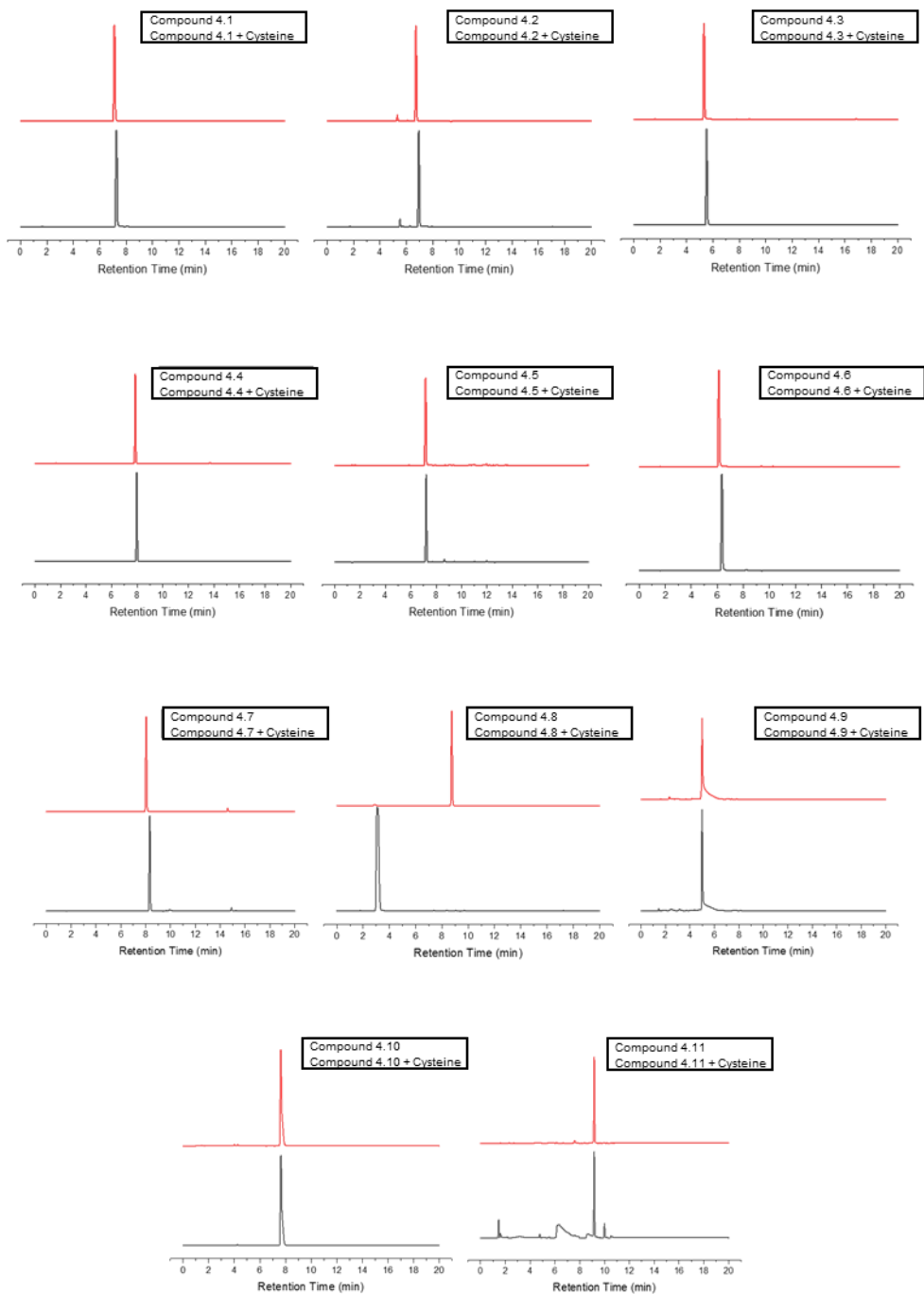


Figure 4.3. HPLC traces of the thioamide, thiourea, and thiocarbamate compounds (*red*), and 1:1 molar mixture of the compounds and L-cysteine methyl ester after 24 h incubation (*black*).

Taken together, **4.1**, **4.2**, **4.3**, **4.4**, and **4.6** were found to be the most stable compounds in both the disulfide exchange reaction with DTNB and the disulfide formation reaction with a cysteine residue. The result implies that they can be considered stable fragments for inhibitor development. In addition, **4.5** and **4.7** are also promising as MBPs, as they have lower reactivity with DTNB and are stable in the presence of **4.13**.

4.4 Structural Analysis

The coordination chemistry of thioamides, thioureas, and thiocarbamates show monodentate, bidentate, and bridging modes. To elucidate the structural features of these MBPs, $[\text{Tp}^{\text{Ph,Me}}\text{Zn}(\text{MBP})]$ ($\text{Tp}^{\text{Ph,Me}}$ = hydrotris(5,3-methylphenylpyrazolyl)-borate) complexes were prepared as a bioinorganic model system. The $[\text{Tp}^{\text{Ph,Me}}\text{Zn}(\text{OH})]$ complex and its derivatives have been broadly used to mimic the tris(histidine) Zn(II) active site of many metalloenzymes (e.g., hCA or MMPs).²⁰⁻²¹ The structures of the $[\text{Tp}^{\text{Ph,Me}}\text{Zn}(\text{MBP})]$ complexes of **4.1**, **4.2**, **4.3**, **4.4**, **4.5**, and **4.7** are shown in Figure 4.4. Compounds **4.1**, **4.2**, **4.4**, **4.5**, and **4.7** coordinate to the Zn(II) center in a monodentate fashion via the sulfur atom while compound **4.3** coordinates to the Zn(II) center via the nitrogen atom. The C-S bond lengths of compounds **4.1**, **4.2**, **4.4**, and **4.7** in the $[\text{Tp}^{\text{Ph,Me}}\text{Zn}(\text{MBP})]$ complexes are in the range of 1.72 - 1.73 Å, which are typical bond lengths of C-S partial double bonds (Table 4.S2). The coordination behavior suggests the propensity of the electrons to delocalize toward the sulfur atom upon deprotonation when in proximity to the Zn(II) center. Notably, compound **4.5** has the longest C-S bond length (1.77 Å), which is almost identical to **4.11**, which contains a C-S single bond (Figure 4.5, Table 4.S2). Interestingly, deprotonation of **4.5** at the C3-position was observed in the $[\text{Tp}^{\text{Ph,Me}}\text{Zn}(\text{4.5})]$ with concomitant C-C bond shortening.

To confirm this unusual coordination mode, this deprotonation was confirmed with **4.5** bound to another Zn(II) model complex, [Zn(TPA)(**4.5**)] (TPA = tris(2-pyridylmethyl)amine) (Figure 4.6).¹ This finding indicates that the proton at the C3-position in **4.5** has a lower pK_a when compared to the amine proton in this ligand. Previous reports indicate **4.5** is in an equilibrium between the 2-indolinethione and the 2-mercapto-indole, with the 2-indoleinethione predominant in solution.¹⁸ The observations with the two different model complexes here not only confirmed the dominant equilibrium state of **4.5** but also reveal its coordination behavior at these biomimetic Zn(II) centers.

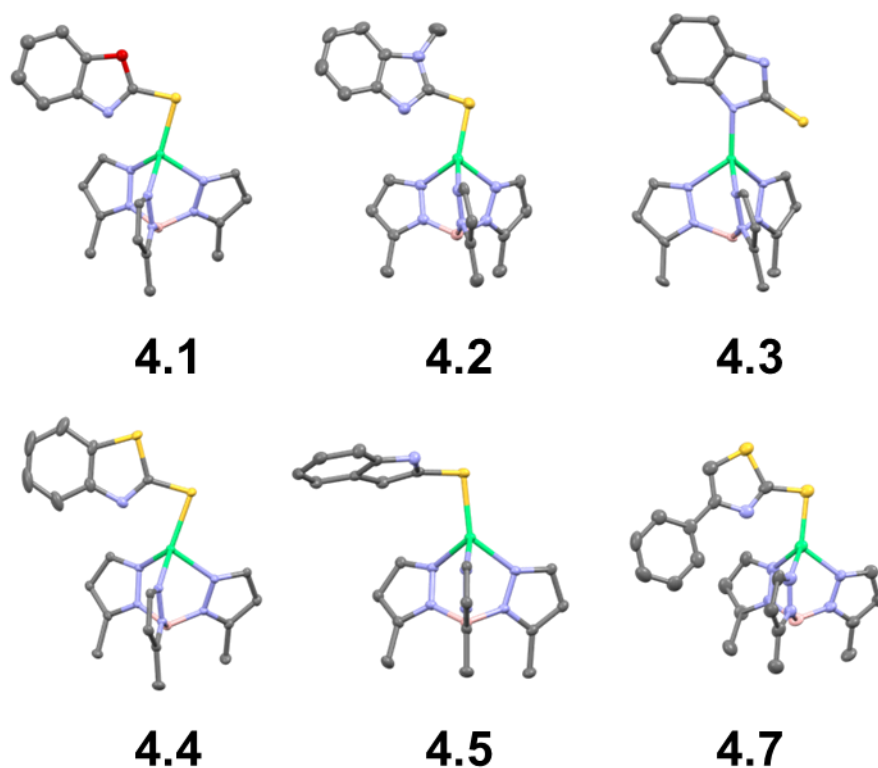


Figure 4.4. Crystal structure of [Tp^{Ph,Me}Zn(MBP)] complexes (ORTEP, 50% probability ellipsoids). Hydrogen atoms and phenyl groups from the Tp^{Ph,Me} ligand were removed for clarity. Color scheme: carbon = gray, nitrogen = blue, oxygen = red, sulfur = yellow, boron = pink, and zinc = green.

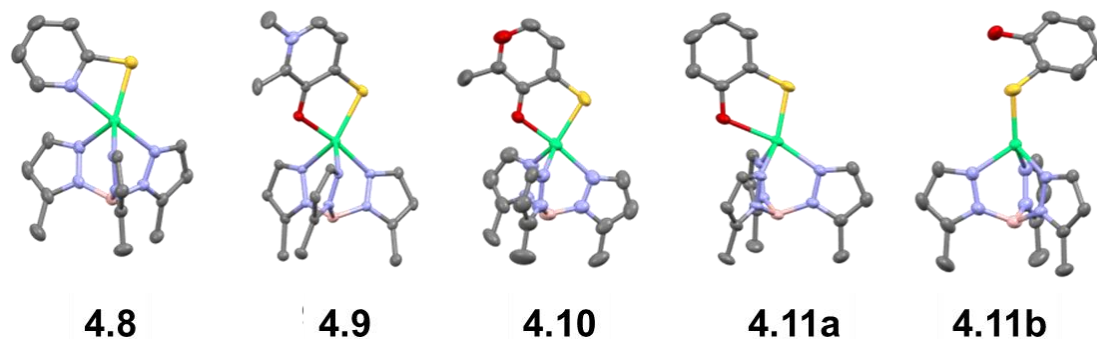


Figure 4.5. Reported crystal structure of $[\text{Tp}^{\text{Ph,Me}}\text{Zn}(\text{MBP})]$ complexes (ORTEP, 50% probability ellipsoids). Hydrogen atoms and phenyl groups from the $\text{Tp}^{\text{Ph,Me}}$ ligand were removed for clarity. Color scheme: carbon = gray, nitrogen = blue, oxygen = red, sulfur = yellow, boron = pink, and zinc = green.

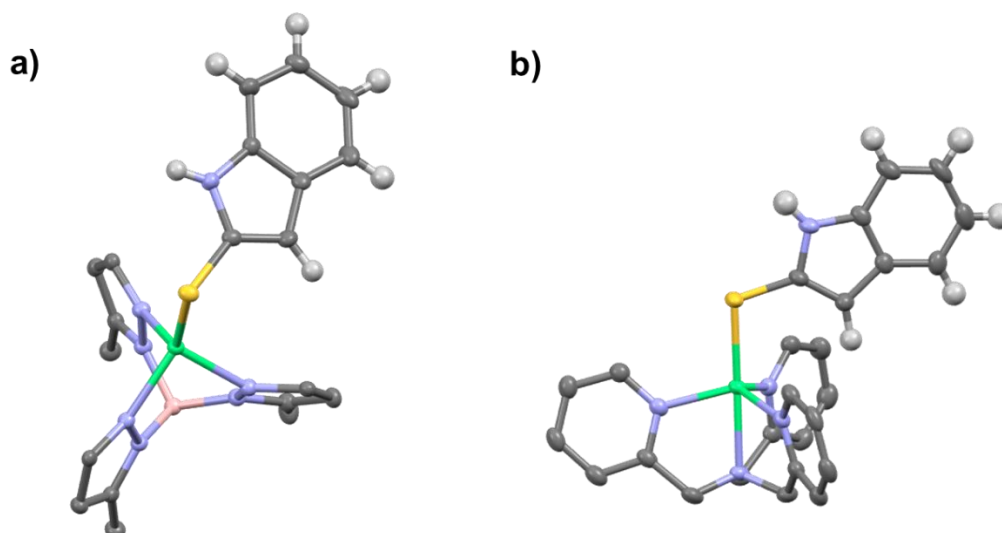


Figure 4.6. Crystal structure of a) $[(\text{Tp}^{\text{Ph,Me}})\text{Zn}(\mathbf{4.5})]$ b) $[\text{Zn}(\text{TPA})(\mathbf{4.5})]\text{BPh}_4$ complexes (ORTEP, 50% probability ellipsoids). Hydrogen atoms and phenyl groups from the $\text{Tp}^{\text{Ph,Me}}$ ligand were removed for clarity. Color scheme: carbon = gray, nitrogen = blue, sulfur = yellow, boron = pink, and zinc = green.

4.5 Biochemical Evaluation

To evaluate these MBPs as potential fragments for Zn(II) dependent metalloenzyme inhibitors, hCAII and MMP-2 were selected as representative Zn-dependent metalloenzymes (Table 4.1, Figures 4.7 and 4.8). Both MMP-2 and hCAII contain a catalytic Zn(II) ion coordinated by three histidine residues and a water molecule in a tetrahedral geometry.²²⁻²³ Compounds **4.1** ($K_i = 0.97 \mu\text{M}$)¹¹ and **4.11** ($K_i = 0.63 \mu\text{M}$)² are reported inhibitors of hCAII. Compounds **4.9** and **4.10** are reported inhibitors for MMP-2 ($\text{IC}_{50} = 60$ and $140 \mu\text{M}$, respectively).¹²

The screening results show that **4.4** and **4.5** have significant inhibition against both hCAII and MMP-2. It was interesting that **4.7**, which shares the same thiazole scaffold as **4.4** but contains a phenyl group, showed 15-fold better activity against hCAII compared to **4.4** but poorer performance against MMP-2. Compound **4.5**, which showed the best IC_{50} value for both enzymes, was further investigated. *N*-Methylated (**4.5a**) and *C*-dimethylated (at C3-position, **4.5b**) derivatives of **4.5** were prepared to see the effect of thione/thiol tautomerism on the inhibition activity. Both compounds exhibited a decrease in the inhibition activity, with **4.5b** showing a more significant loss of inhibitory activity. This result confirms the importance of C3-deprotonation for metal ion coordination by these ligands. It is worth noting that despite the previous report of **4.1** as a hCAII inhibitor,¹¹ compound **4.1** was not active under the assay conditions used in the present study (which are not the same as the prior report).

Table 4.1. IC₅₀ values of the proposed compounds against hCAII and MMP-2. IC₅₀ values reported in μM with the 95% confidence interval indicated. IC₅₀ titration curves can be found in Figures 4.7 and 4.8.

Compound	IC ₅₀ (μM)	
	hCAII	MMP-2
4.1	>200	>200
4.2	>200	>200
4.3	>200	>200
4.4	68.27 ± 10.69	102.2 ± 12.7
4.5	3.42 ± 0.34	76.64 ± 4.26
4.5a	20.34 ± 2.09	103.4 ± 10.6
4.5b	>200	>200
4.6	>200	>200
4.7	4.56 ± 0.62	>200
4.8	>200	>200
4.9	>200	25.85 ± 1.08
4.10	>200	44.52 ± 3.01
4.11	19.40 ± 5.15	>200

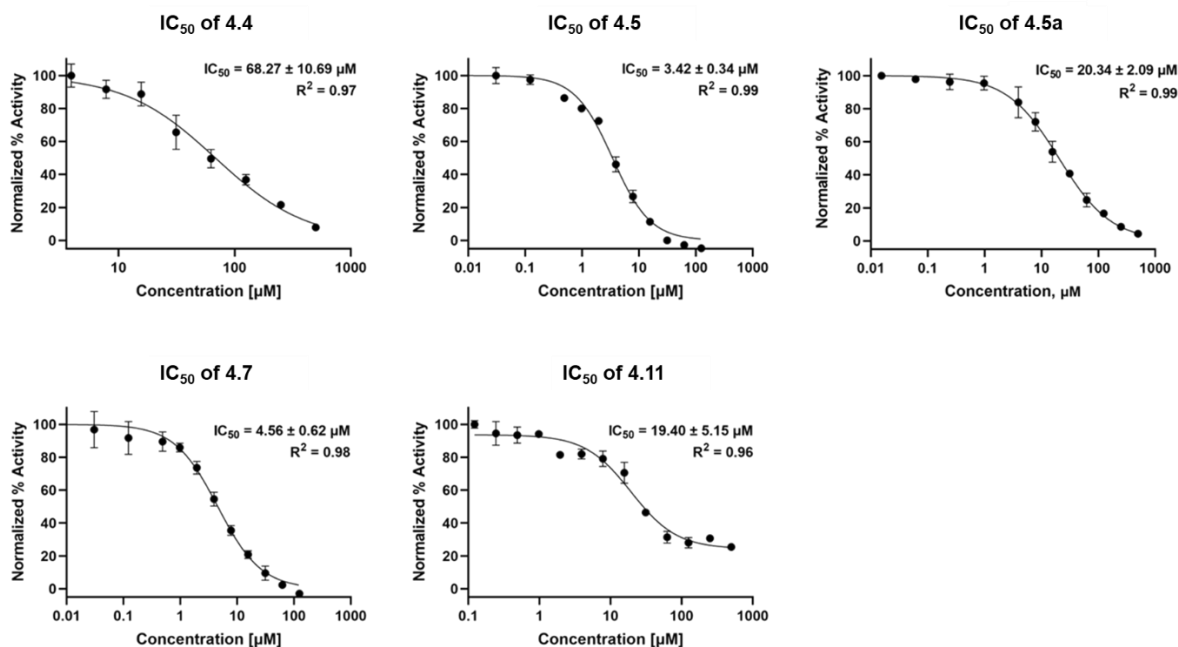


Figure 4.7. IC₅₀ curves of compounds 4.4, 4.5, 4.5a, 4.7, and 4.11 against hCAII. The range of concentration of the compounds is between 0.01 and 1000 μM. IC₅₀ values reported in μM with the 95% confidence interval indicated.

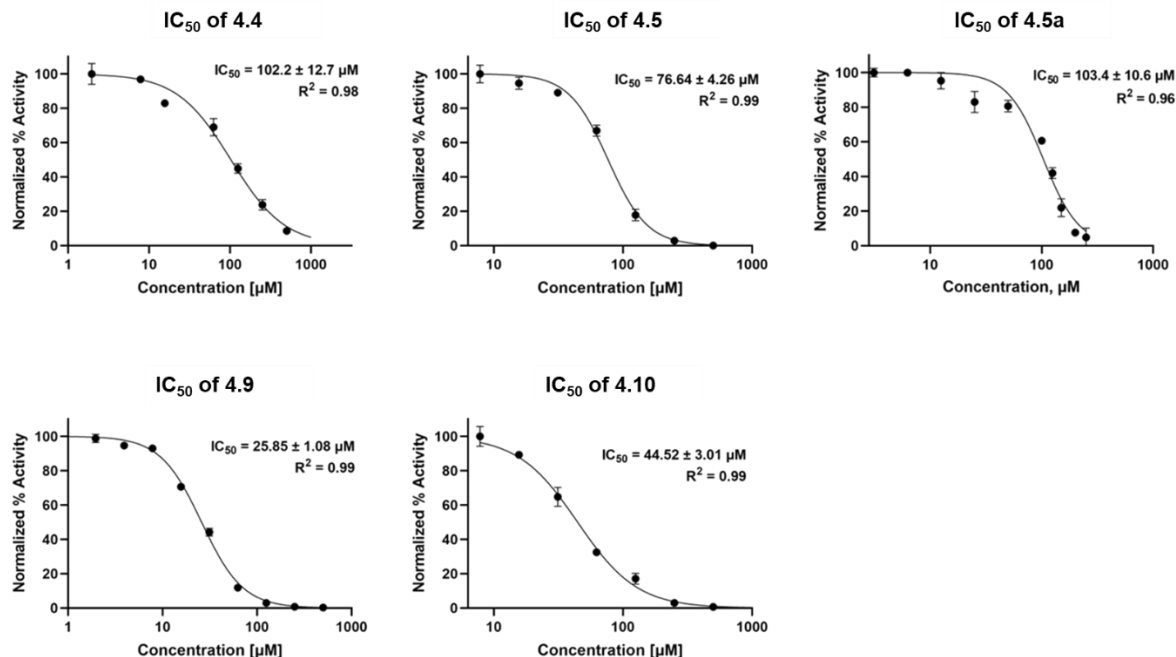


Figure 4.8. IC₅₀ curves of compounds **4.4**, **4.5**, **4.5a**, **4.9**, and **4.10** against MMP-2. The range of concentration of the compounds is between 1 and 1000 µM. IC₅₀ values reported in µM with the 95% confidence interval indicated.

4.6 Protein X-ray Crystallography

To elucidate the binding mode of the hit compounds, the structure of the adducts formed between **4.4** and **4.7** with hCAII was determined by X-ray crystallography. Crystals of the protein complexes were obtained by soaking crystals of ~50-150 microns in diameter in 8 mM solutions of the compounds for 2-3 days (see ESI for details, Table 4.S4).

The structure of **4.4** bound to hCAII shows a monodentate coordination through the exocyclic sulfur atom (Figure 4.9a, Figure 4.S3). A water molecule is also bound to the Zn(II) center, changing the coordination geometry from tetrahedral to a distorted trigonal bipyramidal (Figure 4.9a). The same distorted trigonal bipyramidal coordination geometry was observed in the structure of **4.1** bound to hCAII (PDB:6YQU).¹¹ Both structures engage in hydrogen bonding with the Zn-coordinated water molecule through an oxygen atom for **4.1** and a nitrogen atom for **4.4**. The Zn-S distance of **4.4** is 2.63 Å, which is a shorter than the reported corresponding distance of

4.1 (2.75 Å),¹¹ and both are within the range of pentacoordinate Zn(II) complexes with different sulfur donor ligands (2.25 to 2.93 Å).²⁴⁻²⁵

Compound **4.7** binds via monodentate coordination through the exocyclic sulfur atom to the Zn(II) center in tetrahedral geometry (Figure 4.9b, Figure 4.S3). Unlike **1** and **4**, no Zn-bound water molecule is observed in the structure of **4.7**. However, a water-mediated hydrogen bond interaction was observed through the water molecule positioned between the nitrogen atom of **4.7** and Thr200. The thiazole moieties both of **4.4** and **4.7** have the same binding orientation but the phenyl group is rotated in **4.7**, showing flexibility to occupy the active site (Figure 4.S3). The phenyl ring of **4.7** could be derivatized to establish further interactions with additional regions of the hCAII active site. Note that the Zn-S distance of **4.7** (2.30 Å) is shorter than that observed for compounds **4.1** and **4.4** (2.75 Å and 2.63 Å, respectively), suggesting strong metal-ligand interactions.

The binding modes of compounds **4.4** and **4.7** were compared with the known thiol-based inhibitor **4.11** (PDB: 2OSM) bound to hCAII (Figure 4.10). When comparing the binding conformations, **4.7** has a binding geometry that more closely resembles **4.11** than **4.4**. The thiazole ring of **4.7** and the phenol ring of **4.11** are well aligned in the same plane and display angles and distances in a similar range. Furthermore, there is a clear difference in the binding conformation of these compounds when compared to a canonical benzenesulfonamide inhibitor of hCAII (PDB: 2WEJ, Figure 4.10c). While the binding angle and distance of the nitrogen in benzenesulfonamide to the Zn center is 1.95 Å and 120°, sulfur-containing inhibitors **4.4** and **4.7** have longer distances (2.30-2.63 Å) and more shallow angles (102-105°).

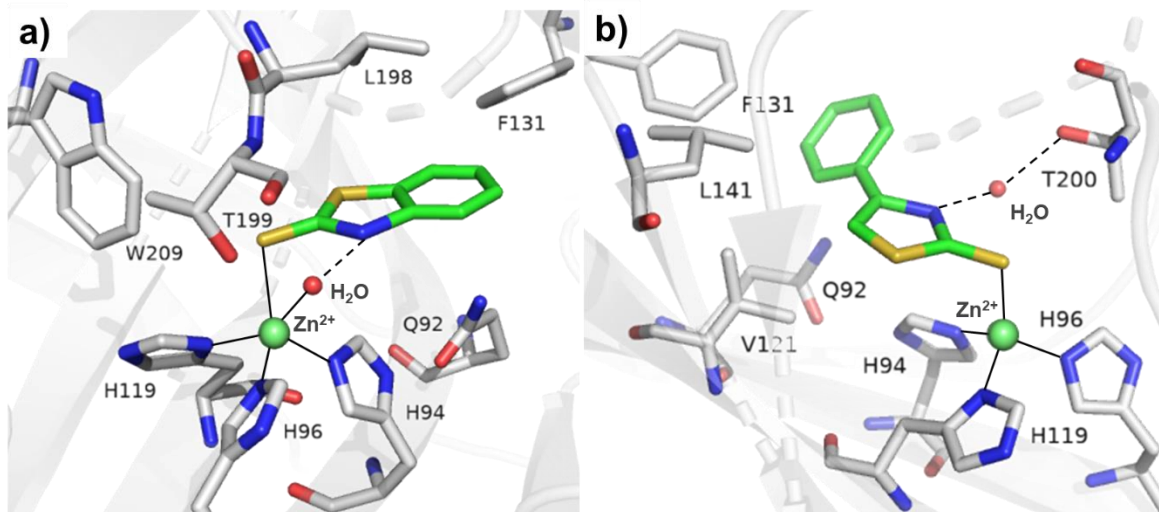


Figure 4.9. Structure of a) **4.4** (PDB: 8FAL) and b) **4.7** (PDB: 8FAU) bound to hCAII. Zn(II) coordination is represented by solid lines and hydrogen bonding is represented by dashed lines. Zn(II) ion and water molecules are shown as green and red spheres, respectively. Atom colors are: carbon (green for MBP, gray for protein), oxygen (red), nitrogen (blue), and sulfur (yellow).

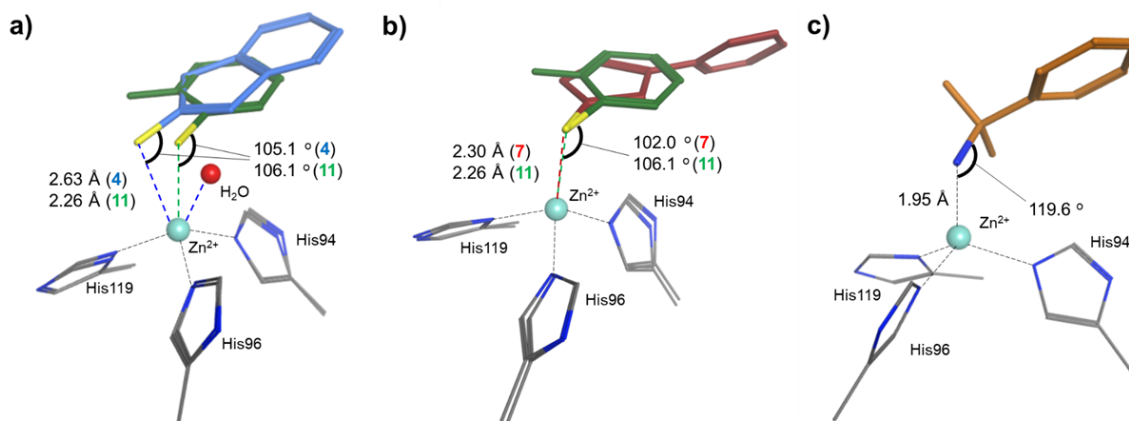


Figure 4.10. Structural superposition between compounds a) **4.4** (blue) and **4.11** (green) (PDB: 2OSM), b) **4.7** (red) and **4.11** (green) bound to the hCAII active site. c) Coordination mode of benzenesulfonamide (orange) bound to the hCAII active site (PDB: 2WEJ). Atoms participating in the Zn(II) coordination are colored: sulfur (yellow) and nitrogen (blue). Zn(II)-ligand bonds are represented by dashed lines.

4.7 Conclusion

In Chapter 4, several thioamide, thiourea, and thiocarbamate MBPs that are less reactive than free thiols, but still have enzymatic inhibition activity against Zn(II)-dependent metalloenzymes, including hCAII and MMP-2, have been identified. The Zn-S binding interaction of these compounds was investigated using bioinorganic model complexes and hCAII. Compounds **4.5** and **4.7** showed higher stability and better activity against hCAII compared to the known thiol-based inhibitor **4.11**. Given the selectivity of **4.7** toward hCAII over MMP-2 and the synthetic handle provided by the phenyl group, **4.7** can be an attractive starting point for developing new hCAII inhibitors. Based on the stability and comparable potency for hCAII and MMP-2, compound **4.4** may be among the more promising new MBPs from this study. This work demonstrates the potential utility of thioamide, thiourea, and thiocarbamate MBPs as fragments for developing metalloenzymes in FBDD campaigns.

4.8 Acknowledgements

Chapter 4 is a reprint of the material as it appears in “Masking thiol reactivity with thioamide, thiourea, and thiocarbamate-based MBPs.” *Chem. Comm.*, **2023**, 59, 2283. The dissertation author was a primary author of this paper and gratefully acknowledges the contributions of coauthors Alysia J. Kohlbrand, Ryjul W. Stokes, Jeewon Chung, and Seth M. Cohen.

4.9 Appendix: Supporting Information

General Experimental Details

All reagents and solvents were obtained from commercial sources (Sigma Aldrich, Alfa Aesar, TCI, Combi-Blocks etc.) and used without further purification. Compounds **4.1**, **4.2**, **4.3**, **4.4**, **4.5**, **4.6**, **4.7**, **4.8**, **4.11**, **4.12**, and **4.13** were purchased from commercial vendors. Compounds **4.5a**, **4.5b**, **4.9** and **4.10** were synthesized from widely available starting materials. $[(\text{Tp}^{\text{Ph,Me}})\text{Zn}(\text{MBP})]$ and $[\text{Zn}(\text{TPA})(\mathbf{5})]\text{BPh}_4$ complexes were prepared according to literature methods. High resolution mass spectrometry (HR-MS) analysis was performed using an Agilent 6230 accurate-mass liquid chromatography time-of-flight mass spectrometry LC–TOFMS at the Molecular Mass Spectrometry Facility (MMSF) in the Department of Chemistry and Biochemistry at the University of California, San Diego. For HPLC analysis, Agilent 1200 series degasser and pump system with an Agilent Eclipse XDB-C18 (5 μm 150 \times 4.6 mm) column was utilized in the Department of Chemistry and Biochemistry at the University of California, San Diego. ^1H NMR spectra were recorded at ambient temperature on 300 MHz Bruker, 400 MHz Jeol NMR instrument, or 500 MHz Varian NMR instrument in the Department of Chemistry and Biochemistry at the University of California, San Diego. Processing of the NMR data was performed using the MestReNova 14.2 program.

Compound Synthesis

3-Hydroxy-1,2-dimethylpyridine-4(1H)-thione (4.9). The compound was synthesized by using a modified literature procedure.²⁶ To a stirred solution of 3-hydroxy-1,2-dimethylpyridin-4(1H)-one (400 mg, 1 eq, 2.87 mmol) in toluene (50 mL), Lawesson's reagent (698 mg, 0.6 eq, 1.72 mmol) was added. The reaction mixture was left refluxing under nitrogen overnight followed by concentration in vacuo. The reaction mixture was diluted with NaHCO₃ (20 mL), extracted with EtOAc (3×20 mL), dried over anhydrous MgSO₄, and concentrated in vacuo. The crude product was purified via flash column chromatography (CH₂Cl₂:MeOH 0-5%) to give the purified product. Yield: 145 mg (32.5%). ¹H NMR (300 MHz, DMSO-*d*₆): δ 8.73 (s, 1H), 7.66 (d, *J* = 6.6 Hz, 1H), 7.28 (d, *J* = 6.6 Hz, 1H), 3.82 (s, 3H), 2.42 (s, 3H). HR-MS (ESI) (*m/z*): [M+H]⁺ calcd. for [C₇H₁₀NOS]⁺, 156.0478; found, 156.0479.

3-Hydroxy-2-methyl-4H-pyran-4-thione (4.10). The compound was synthesized by using a modified literature procedure.²⁷ To a stirred solution of 3-hydroxy-2-methyl-4H-pyran-4-one (500 mg, 1 eq, 3.96 mmol) in THF (30 mL), Lawesson's reagent (962 mg, 0.6 eq, 2.38 mmol) was added. The reaction mixture was heated to reflux under a nitrogen atmosphere for 4 h followed by concentration in vacuo. The crude product was purified via flash column chromatography (hexane:EtOAc 0-30%) to give the purified product as a yellow solid. Yield: 408 mg (72.4%). ¹H NMR (300 MHz, DMSO-*d*₆): δ 8.28 (s, 1H), 8.09 (d, *J* = 5.0 Hz, 1H), 7.34 (d, *J* = 5.0 Hz, 1H), 2.39 (s, 3H). HR-MS (ESI) (*m/z*): [M+H]⁺ calcd. for [C₆H₇O₂S]⁺, 143.0161; found, 143.0161.

1-Methylindoline-2-thione (4.5a). The compound was synthesized by using a modified literature procedure.²⁸ To a stirred solution of 1-methylindolin-2-one (400 mg, 1 eq, 2.72 mmol) in THF (10 mL), Lawesson's reagent (660 mg, 0.6 eq, 1.63 mmol) was added. The mixture was stirred at room temperature for 16 h followed by concentration in vacuo. The residue was purified via flash

column chromatography (hexane:EtOAc 0-50%) to give the purified product. Yield: 370 mg (83.4%). ¹H NMR (400 MHz, CDCl₃): δ 7.37 – 7.25 (m, 2H), 7.16 (td, *J* = 7.5, 1.0 Hz, 1H), 6.96 (d, *J* = 7.9 Hz, 1H), 4.09 (s, 2H), 3.62 (s, 3H). HR-MS (ESI) (*m/z*): [M+H]⁺ calcd. for [C₉H₁₀NS]⁺, 164.0528; found, 164.0530.

3,3-dimethylindoline-2-thione (4.5b). The compound was synthesized by using a modified literature procedure.²⁹ To a stirred solution of 3,3-dimethylindolin-2-one (400 mg, 1 eq, 2.48 mmol) in toluene (10 mL), Lawesson's reagent (552 mg, 0.55 eq, 1.36 mmol) was added. The reaction mixture was heated to reflux under a nitrogen atmosphere overnight followed by concentration in vacuo. The reaction mixture was diluted with H₂O (20 mL), extracted with EtOAc (3×20 mL), dried over anhydrous MgSO₄, and concentrated in vacuo. The crude product was purified by flash chromatography (hexane:EtOAc 0-20%) to give the purified product. Yield: 357 mg (81.2%). ¹H NMR (400 MHz, CDCl₃): δ 11.11 (s, 1H), 7.29 – 7.22 (m, 2H), 7.14 (td, *J* = 7.5, 1.0 Hz, 1H), 7.08 (dd, *J* = 7.7, 0.9 Hz, 1H), 1.45 (s, 6H). HR-MS (ESI) (*m/z*): [M+H]⁺ calcd. for [C₁₀H₁₂NS]⁺, 178.0685; found, 178.0687.

Preparation of [(Tp^{Ph,Me})Zn(MBP)] and [Zn(TPA)(5)]BPh₄ complexes

[(Tp^{Ph,Me})Zn(MBP)]. The complex was synthesized by using a modified literature procedure.³⁰ To obtain an X-ray structure of [(Tp^{Ph,Me})Zn(MBP)], [(Tp^{Ph,Me})K] and [(Tp^{Ph,Me})ZnOH] was prepared according to literature methods.³¹ [(Tp^{Ph,Me})ZnOH] (50 mg, 0.09 mmol) was dissolved in 15 mL of CH₂Cl₂ in a 50 mL round-bottom flask. Each compound (0.09 mmol, 1 eq) in 10 mL of MeOH was added, and the reaction mixture was stirred overnight under a nitrogen atmosphere. The resulting mixture was evaporated to dryness and subsequently dissolved in a minimal amount (~1 mL) of benzene. The solution was filtered using a syringe filter to remove any undissolved

solids. The resulting complex in benzene was recrystallized using vapor diffusion with pentane. Crystals typically formed within a few days. The resulting crystals are characterized by X-ray crystallography and HR-MS. [(Tp^{Ph,Me})Zn(**1**): HR-MS (ESI) (*m/z*): [M+H]⁺ calcd. for [C₃₇H₃₃BN₇OSZn]⁺, 698.1853; found, 698.1859. [(Tp^{Ph,Me})Zn(**2**): HR-MS (ESI) (*m/z*): [M+H]⁺ calcd. for [C₃₈H₃₆BN₈SZn]⁺, 711.2169; found, 711.2172. [(Tp^{Ph,Me})Zn(**3**): HR-MS (ESI) (*m/z*): [M+H]⁺ calcd. for [C₃₇H₃₄BN₈SZn]⁺, 697.2013; found, 697.2009. [(Tp^{Ph,Me})Zn(**4**): HR-MS (ESI) (*m/z*): [M+H]⁺ calcd. for [C₃₇H₃₃BN₇S₂Zn]⁺, 714.1624; found, 714.1624. [(Tp^{Ph,Me})Zn(**5**): HR-MS (ESI) (*m/z*): [M+H]⁺ calcd. for [C₃₈H₃₅BN₇SZn]⁺, 696.2060; found, 696.2054. [(Tp^{Ph,Me})Zn(**7**): HR-MS (ESI) (*m/z*): [M+H]⁺ calcd. for [C₃₉H₃₅BN₇S₂Zn]⁺, 740.1781; found, 740.1778.

[Zn(TPA)(5)]BPh₄. The complex was synthesized by using a modified literature procedure.¹ Zinc(II) acetate dihydrate (23 mg, 1 Eq, 0.10 mmol) was dissolved in MeOH (3 mL). Tris(pyridin-2-ylmethyl)amine (30 mg, 1 Eq, 0.10 mmol) was then dissolved in the vessel (yellowish transparent), sonicated and stirred for 10min. Indoline-2-thione (15 mg, 1 Eq, 0.10 mmol) was added to the vessel and stirred for 10min. Ammonium tetraphenylborate (35 mg, 1 Eq, 0.10 mmol) was added and stirred for 3h. After filtration and washing with methanol, the green precipitate precipitates were crystalized by vapor diffusion of Et₂O into a CH₃CN solution of the complex. The resulting crystal was characterized by X-ray crystallography.

DTNB Reactivity Analysis

Tested compounds (compounds **4.1** – **4.13**) were prepared as 50 mM DMSO stock solution and the stock solution was further diluted to 5, 2, and 1 mM. 0.5 mM DTNB (5,5'-dithio-bis-(2-nitrobenzoic acid)) was prepared in 50 mM tris sulfate buffer (pH 8). 10 μ L of each compound was incubated with 200 μ L of 0.5 mM DTNB for 90 min at 25° C and the absorbance at 412 nm was measured. All tested compounds were also incubated with buffer solution without DNTB for 90 min and no background signal at 412 nm was observed. Each measurement was triplicated, and their background absorbance was subtracted from the measurement. Their reactivity with DTNB was quantified based on the standard calibration curve of L-cysteine methyl ester.

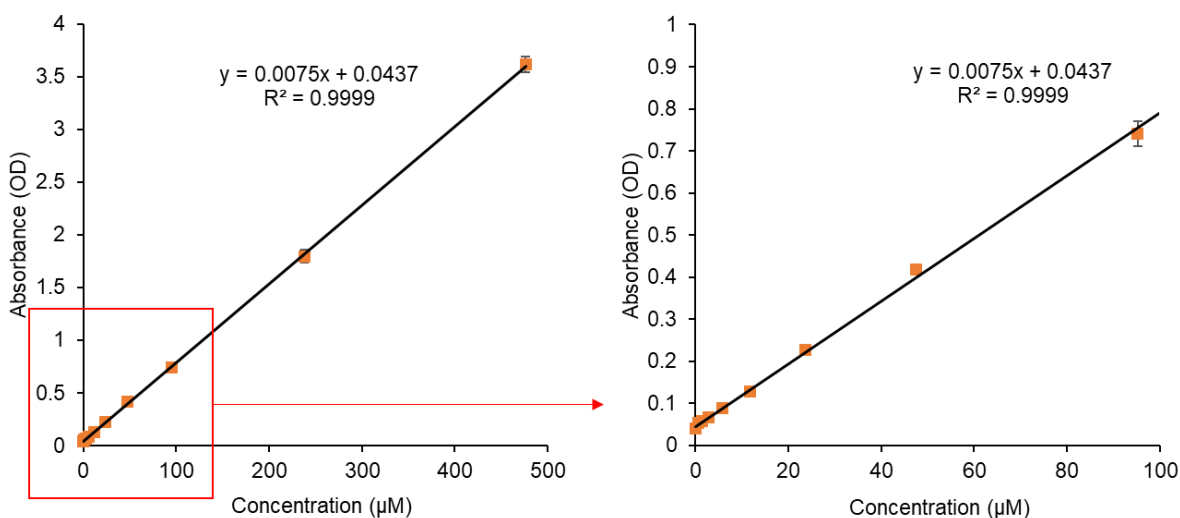


Figure 4.S1. Standard calibration curve of L-cysteine methyl ester. The final concentration range of L-cysteine methyl ester was between 1 and 500 μ M with the fixed concentration of DTNB (500 μ M). The whole concentration range (*left*) and the lower concentration range (*right*) of the standard calibration curve.

Table 4.S1. Percent reactivity of the proposed compounds with DTNB. Excess amount of DTNB was used with different molar ratios (1:2, 1:5, 1:10). 2-Mercapophenol (**4.11**), captopril (**4.12**), and L-cysteine methyl ester (**4.13**) were used as representative free thiol groups and showed almost 100% reactivity with DTNB.

Compound	Molar ratio (Compound/DTNB)		
	1:2	1:5	1:10
4.1 – 4.4, 4.6, and 4.8	2 (0)	3 (0)	5 (0)
4.5	35 (1)	36 (1)	33 (0)
4.7	23 (2)	19 (1)	19 (0)
4.9	50 (2)	50 (4)	52 (2)
4.10	51 (6)	74 (1)	64 (7)
4.11	98 (5)	98 (1)	97 (1)
4.12	101 (11)	104 (1)	105 (0)
4.13	100 (7)	100 (2)	100 (1)

Cysteine Reactivity Analysis

HPLC Analysis.

25 μ L of 50 mM compounds **4.1** – **4.11** dissolved in DMSO were mixed with 25 μ L of 50 mM L-cysteine methyl (1:1 molar ratio), and then the mixture were dissolved in 950 μ L of 10% ACN/ 90% H₂O (final concentration of each compound: 1.25 mM). The pH of the solution was adjusted to 7.4 and the mixture incubated for 24 h. The HPLC spectra were measured at 254 nm/280nm. The solvents (HPLC grade) were Millipore water (solvent A) and acetonitrile (solvent B). The following solvent gradient was used: 0-12 min: linear gradient from 95% A (5% B) to 5% A (95% B); 12-14 min: isocratic 5% A (95% B); 14-15 min: linear gradient from 5% A (95% B) to 95% A (5% B); 15-20 min: isocratic 95% A (5% B).

¹H NMR Analysis.

Compounds **4.1**–**4.11** were incubated in a 1:1 molar ratio with L-cysteine methyl ester in DMSO-*d*₆ for 24 h (final concentration of each compound was 25 mM). ¹H NMR spectra were measured for each compound, L-cysteine methyl ester, and the mixture after 24 h incubation.

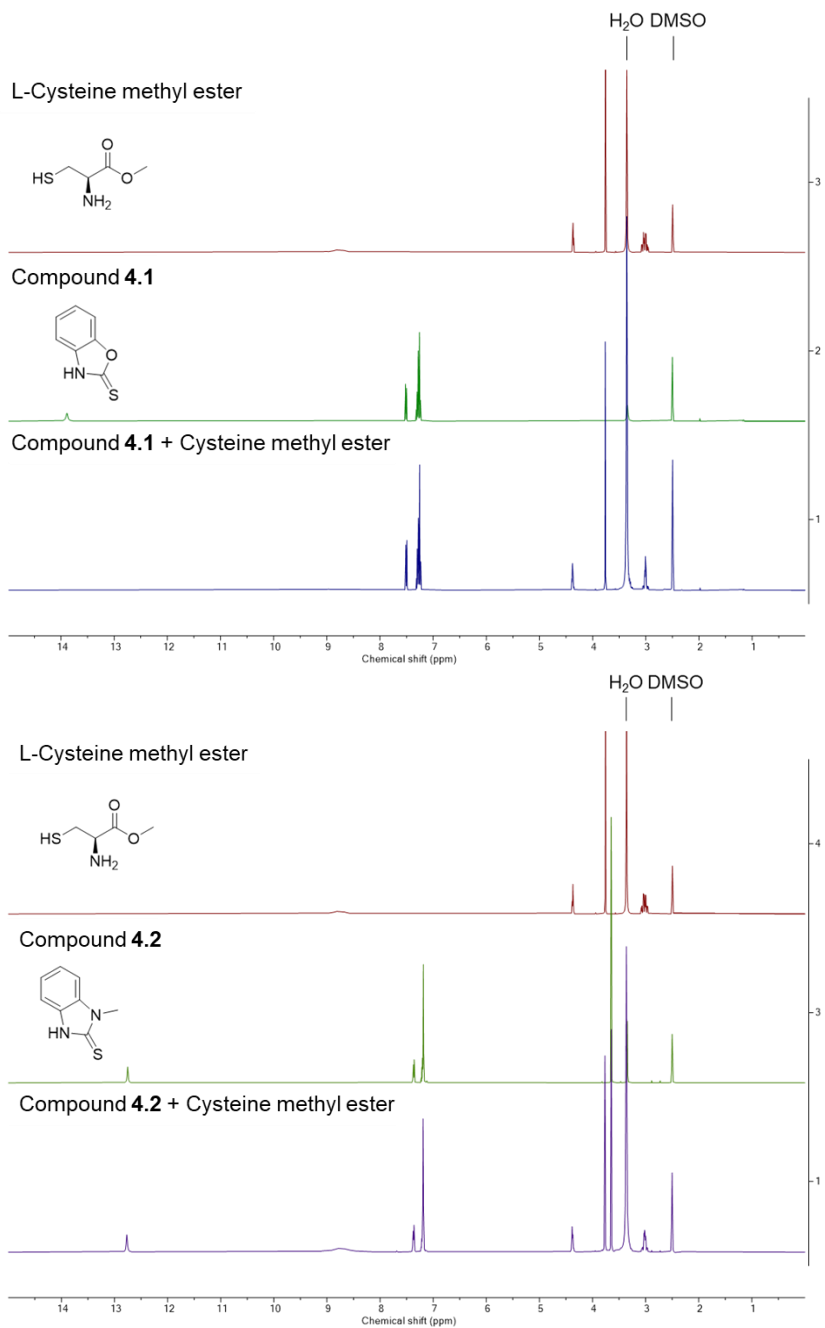


Figure 4.S2. ^1H NMR spectra of L-cysteine methyl ester (*top*), the proposed thioamide, thiourea, and thiocarbamate compounds (*middle*), and 1:1 molar mixture of the compounds and L-cysteine methyl ester after 24 h incubation (*bottom*).

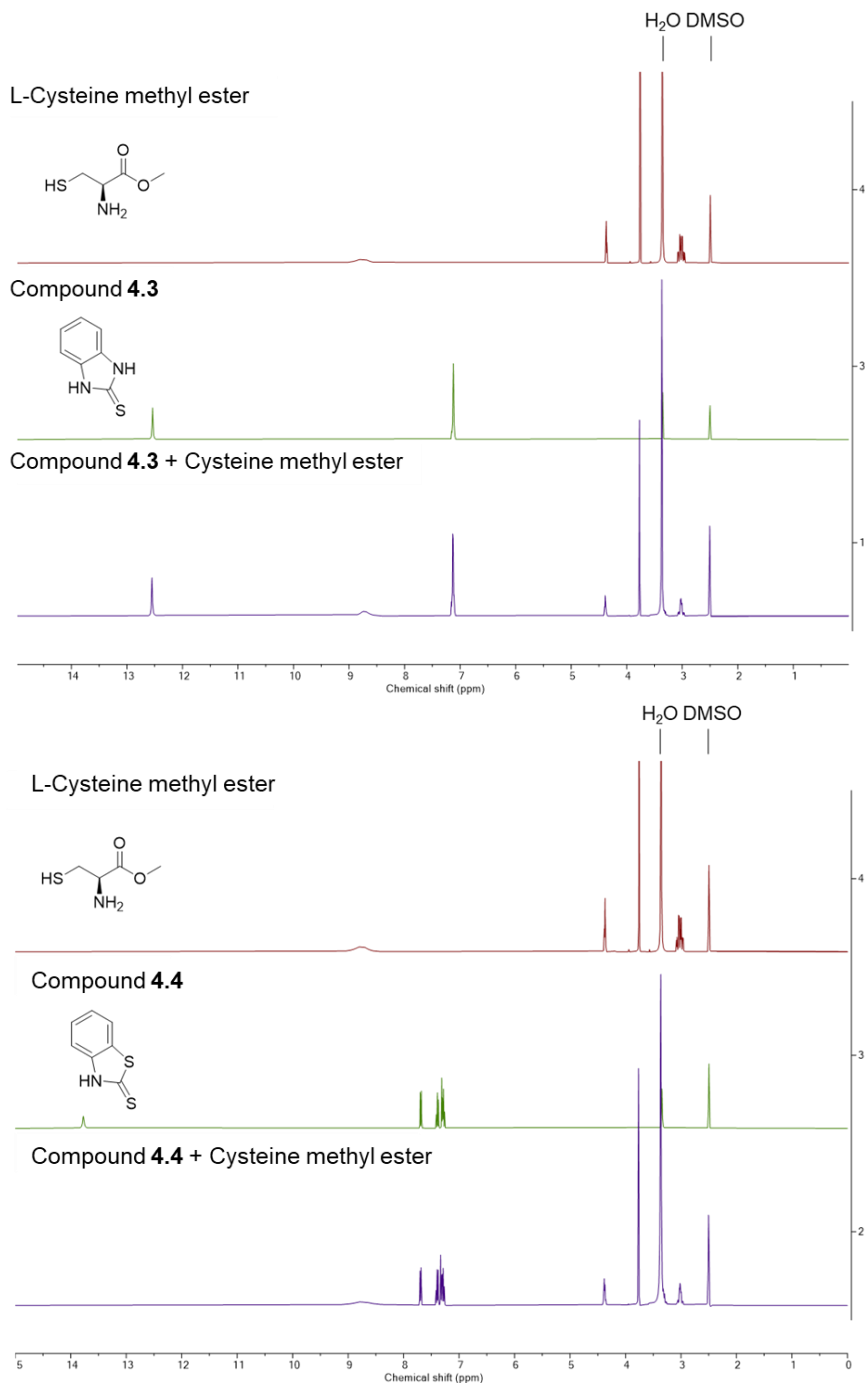


Figure 4.S2 (continued). ¹H NMR spectra of L-cysteine methyl ester (*top*), the proposed thioamide, thiourea, and thiocarbamate compounds (*middle*), and 1:1 molar mixture of the compounds and L-cysteine methyl ester after 24 h incubation (*bottom*).

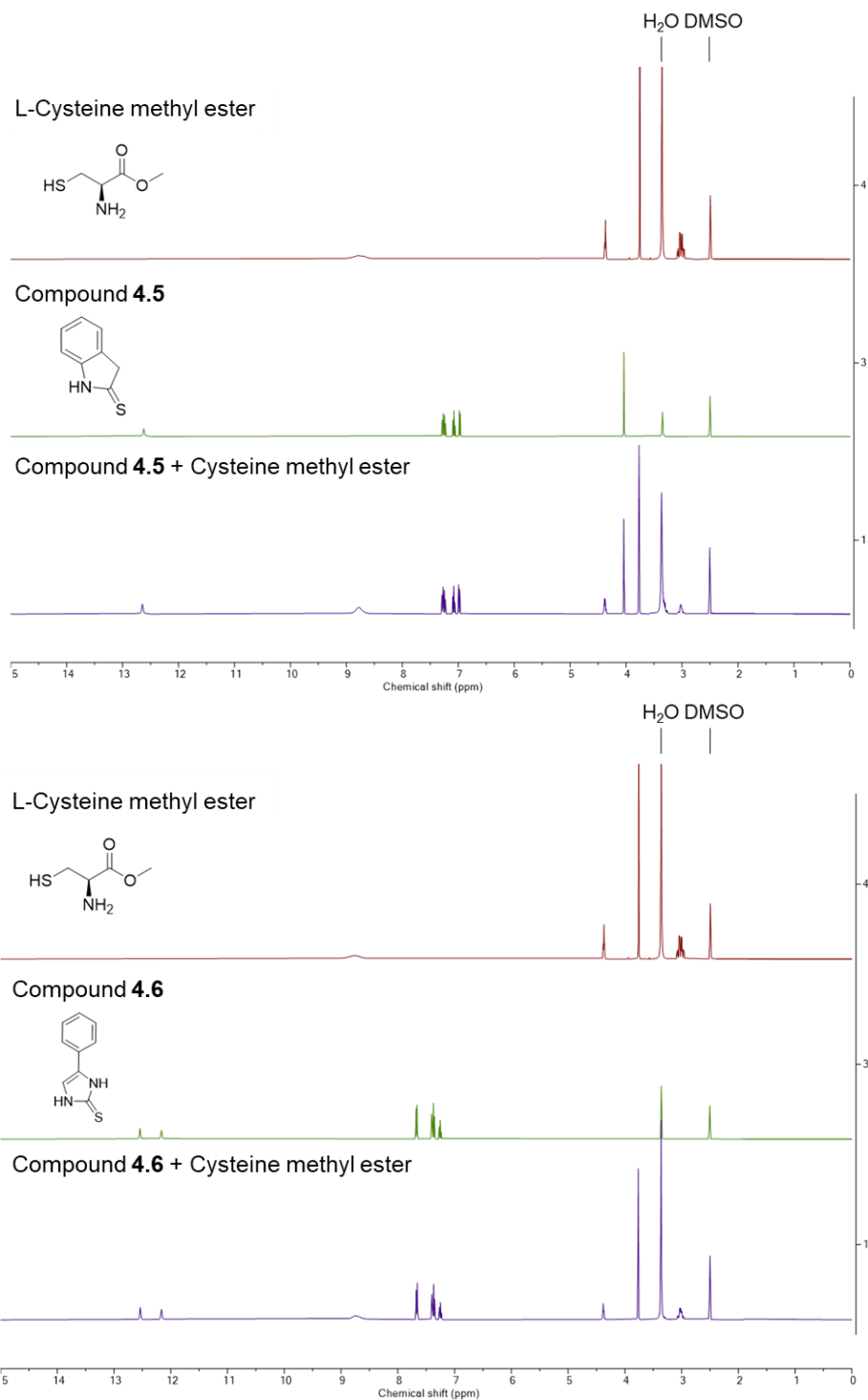


Figure 4.S2 (continued). ^1H NMR spectra of L-cysteine methyl ester (*top*), the proposed thioamide, thiourea, and thiocarbamate compounds (*middle*), and 1:1 molar mixture of the compounds and L-cysteine methyl ester after 24 h incubation (*bottom*).

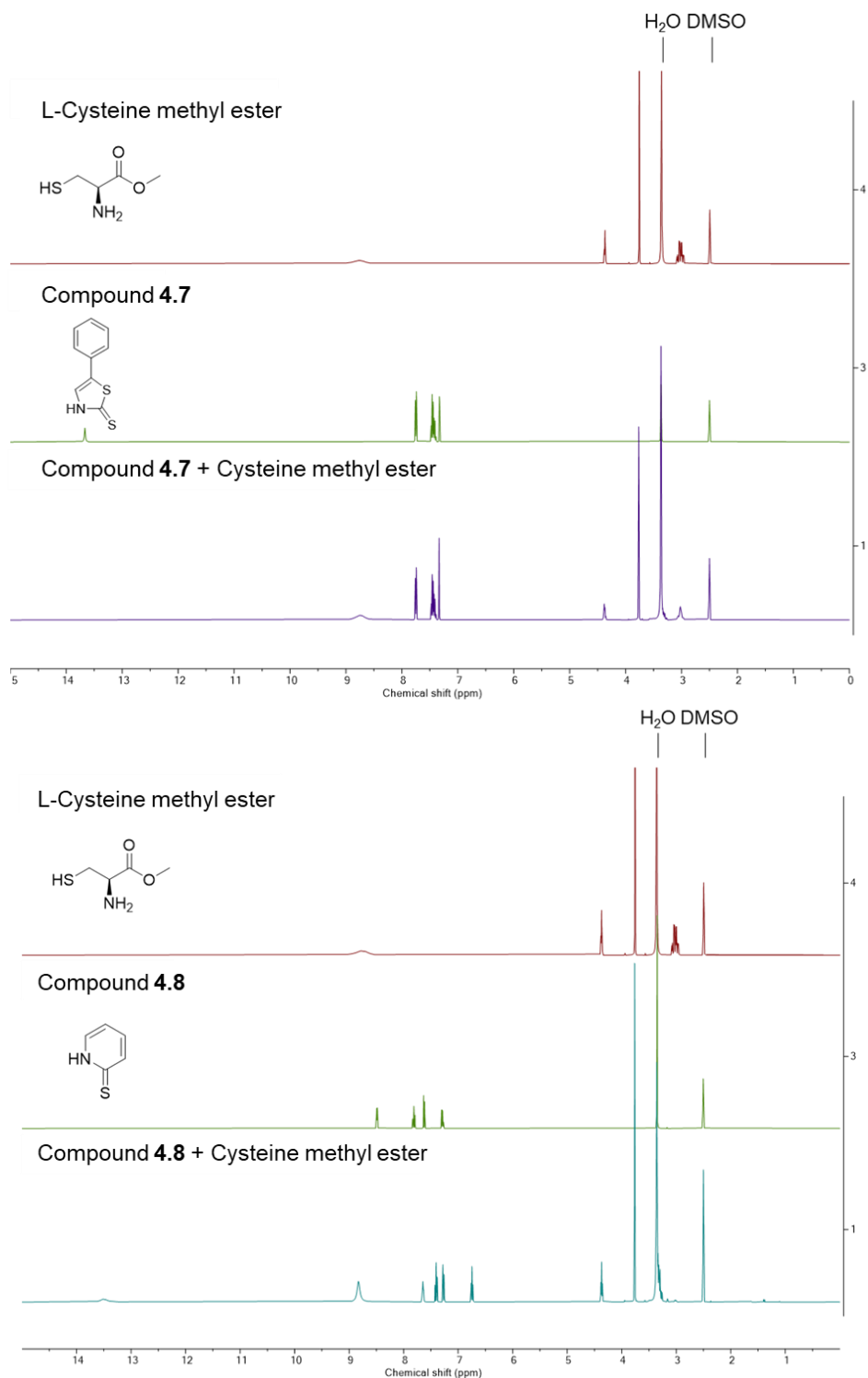


Figure 4.S2 (continued). ¹H NMR spectra of L-cysteine methyl ester (*top*), the proposed thioamide, thiourea, and thiocarbamate compounds (*middle*), and 1:1 molar mixture of the compounds and L-cysteine methyl ester after 24 h incubation (*bottom*).

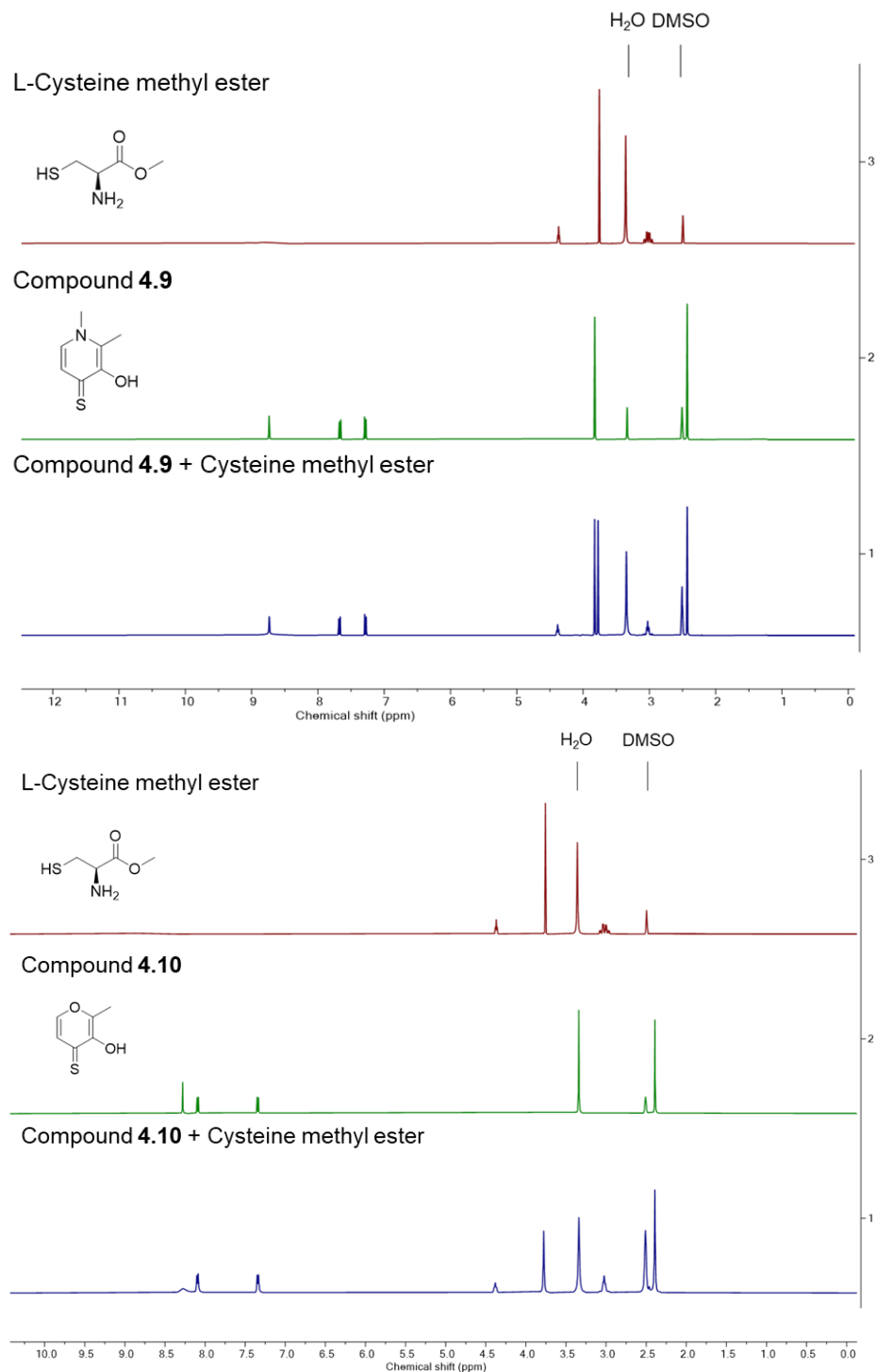


Figure 4.S2 (continued). ¹H NMR spectra of L-cysteine methyl ester (*top*), the proposed thioamide, thiourea, and thiocarbamate compounds (*middle*), and 1:1 molar mixture of the compounds and L-cysteine methyl ester after 24 h incubation (*bottom*).

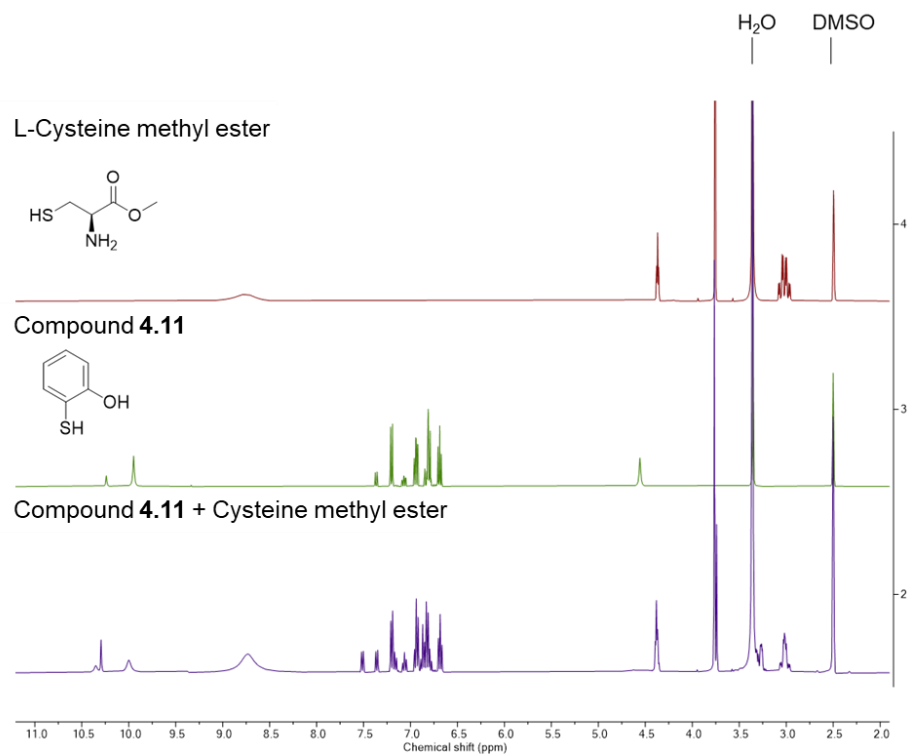


Figure 4.S2 (continued). ¹H NMR spectra of L-cysteine methyl ester (*top*), the proposed thioamide, thiourea, and thiocarbamate compounds (*middle*), and 1:1 molar mixture of the compounds and L-cysteine methyl ester after 24 h incubation (*bottom*).

Single Crystal X-ray Diffraction

Suitable crystals of $[(\text{Tp}^{\text{Ph,Me}})\text{Zn}(\mathbf{MBP})]$ ($\text{Tp}^{\text{Ph,Me}}$ = hydrotris(3,5-phenylmethylpyrazolyl)borate) were selected and data was collected at 100 K on a Bruker APEX-II Ultra diffractometer with a Mo-K α Microfocus Rotating Anode and a APEX-II CCD area detector or a Bruker Kappa diffractometer equipped with a Bruker X8 APEX II Mo sealed tube and a Bruker APEX-II CCD. The data were integrated using the Bruker SAINT Software program and scaled using the SADABS software program. The structure was solved with the ShelXT³² structure solution program using direct methods and refined with the XL³³ refinement package using least squares minimization using Olex2.³⁴ The crystal data files were deposited into the Cambridge Crystallographic Data Centre (CCDC).

Table 4.S2. Selected bond lengths and angles of $[\text{Tp}^{\text{Ph,Me}}\text{Zn}(\mathbf{MBP})]$ complexes. *Previously reported structure. Refcodes (entry ID) for the reported compounds are listed below.

	C-S (Å)	Adjacent C-N (Å)	Zn-S (Å)
4.1	1.7168 (3)	1.313 (2)	2.2831(4)
4.2	1.733 (2)	1.318 (3)	2.2438(7)
4.3	1.6908 (18)	1.364 (2) 1.357 (2)	- -
4.4	1.7284(16)	1.302 (2)	2.2915(4)
4.5	1.7654 (15)	1.3834 (19)	2.2513(4)
4.7	1.723 (11) 1.741 (14)	1.296 (15) 1.319 (16)	2.267 (3) 2.275 (3)
4.8* (LUZVEH)	1.754	1.340	2.351
4.9* (BIBDEW)	1.711 1.732 1.736	-	2.287 2.297 2.329
4.10* (BIBDIA)	1.707	-	2.340
4.11* (KEXPUZ)	1.770 1.777	-	2.279 2.248

Table 4.S3. Crystal data and structure refinement for [(Tp^{Ph,Me})Zn(MBP)] complexes.

Compound	[(Tp ^{Ph,Me})Zn(4.1)]	[(Tp ^{Ph,Me})Zn(4.2)]
Identification code	2211573	2211575
Empirical formula	C ₃₇ H ₃₂ BN ₇ OSZn	C ₃₈ H ₃₅ BN ₈ SZn
Formula weight	698.93	711.98
Temperature/K	100	100
Crystal system	monoclinic	monoclinic
Space group	P2 ₁ /n	P2 ₁ /c
<i>a</i> /Å	16.0769(5)	13.2565(10)
<i>b</i> /Å	12.0606(4)	16.8902(11)
<i>c</i> /Å	17.4588(5)	16.1386(13)
<i>α</i> /°	90	90
<i>β</i> /°	101.3210(10)	107.479(2)
<i>γ</i> /°	90	90
Volume/Å ³	3319.34(18)	3446.7(4)
<i>Z</i>	4	4
$\rho_{\text{calc}}/\text{cm}^3$	1.399	1.372
μ/mm^{-1}	0.845	0.814
F(000)	1448	1480
Crystal size/mm ³	0.1 × 0.06 × 0.06	0.1 × 0.1 × 0.1
Radiation	MoK α ($\lambda = 0.71073$)	MoK α ($\lambda = 0.71073$)
2 θ range for data collection/°	4.252 to 52.74	4.252 to 52.862
Index ranges	-20 ≤ <i>h</i> ≤ 20, -13 ≤ <i>k</i> ≤ 15, -21 ≤ <i>l</i> ≤ 21	-16 ≤ <i>h</i> ≤ 16, -20 ≤ <i>k</i> ≤ 21, -20 ≤ <i>l</i> ≤ 20
Reflections collected	81571	157697
Independent reflections	6749 [R _{int} = 0.0739, R _{sigma} = 0.0290]	7086 [R _{int} = 0.1189, R _{sigma} = 0.0407]
Data/restraints/parameters	6749/0/436	7086/0/446
Goodness-of-fit on F ²	1.043	1.054
Final <i>R</i> indexes [<i>I</i> ≥ 2 σ (<i>I</i>)]	R ₁ = 0.0281, wR ₂ = 0.0658	R ₁ = 0.0378, wR ₂ = 0.0918
Final <i>R</i> indexes [all data]	R ₁ = 0.0333, wR ₂ = 0.0698	R ₁ = 0.0496, wR ₂ = 0.1006
Largest diff. peak/hole / e Å ⁻³	0.33/-0.27	0.32/-0.67

Table 4.S3 (continued). Crystal data and structure refinement for [(Tp^{Ph,Me})Zn(MBP)] complexes.

Compound	[(Tp ^{Ph,Me})Zn(4.3)]	[(Tp ^{Ph,Me})Zn(4.4)]
Identification code	2211570	2211572
Empirical formula	C ₄₃ H ₃₉ BN ₈ SZn	C ₃₇ H ₃₂ BN ₇ S ₂ Zn
Formula weight	776.06	714.99
Temperature/K	100	100
Crystal system	triclinic	monoclinic
Space group	P-1	P2 ₁ /n
<i>a</i> /Å	12.2415(9)	16.2876(11)
<i>b</i> /Å	12.4061(9)	12.0580(8)
<i>c</i> /Å	14.3641(10)	17.5877(12)
<i>α</i> /°	84.4340(10)	90
<i>β</i> /°	67.5970(10)	101.4370(10)
<i>γ</i> /°	68.4550(10)	90
Volume/Å ³	1873.6(2)	3385.6(4)
<i>Z</i>	2	4
ρ _{calc} /cm ³	1.376	1.403
μ/mm ⁻¹	0.755	0.888
F(000)	808	1480
Crystal size/mm ³	0.1 × 0.1 × 0.1	0.1 × 0.1 × 0.1
Radiation	MoKα (λ = 0.71073)	MoKα (λ = 0.71073)
2Θ range for data collection/°	3.07 to 56.816	3.114 to 54.252
Index ranges	-16 ≤ <i>h</i> ≤ 16, -16 ≤ <i>k</i> ≤ 16, -17 ≤ <i>l</i> ≤ 19	-20 ≤ <i>h</i> ≤ 20, -14 ≤ <i>k</i> ≤ 15, -21 ≤ <i>l</i> ≤ 22
Reflections collected	24447	43464
Independent reflections	9398 [R _{int} = 0.0332, R _{sigma} = 0.0377]	7493 [R _{int} = 0.0409, R _{sigma} = 0.0263]
Data/restraints/parameters	9398/0/490	7493/0/436
Goodness-of-fit on F ²	1.016	1.03
Final <i>R</i> indexes [<i>I</i> >= 2σ(<i>I</i>)]	R ₁ = 0.0362, wR ₂ = 0.1215	R ₁ = 0.0271, wR ₂ = 0.0650
Final <i>R</i> indexes [all data]	R ₁ = 0.0429, wR ₂ = 0.1288	R ₁ = 0.0348, wR ₂ = 0.0688
Largest diff. peak/hole / e Å ⁻³	0.81/-0.66	0.35/-0.19

Table 4.S3 (continued). Crystal data and structure refinement for [(Tp^{Ph,Me})Zn(MBP)] complexes.

Compound	[(Tp ^{Ph,Me})Zn(4.5)]	[(Tp ^{Ph,Me})Zn(4.7)]	[Zn(TPA)(4.5)]BPh ₄
Identification code	2211571	2211576	2211574
Empirical formula	C ₃₈ H ₃₄ BN ₇ SZn	C ₄₂ H ₃₇ BN ₇ S ₂ Zn	C ₅₀ H ₄₄ BN ₅ SZn
Formula weight	696.96	780.08	823.14
Temperature/K	273.15	273.15	273.15
Crystal system	triclinic	monoclinic	monoclinic
Space group	P-1	P2 ₁ /n	P2 ₁ /c
<i>a</i> /Å	12.0736(3)	16.078(2)	11.7128(7)
<i>b</i> /Å	12.1394(4)	20.118(3)	9.8315(5)
<i>c</i> /Å	12.7540(4)	23.900(4)	35.780(2)
<i>α</i> /°	103.5020(10)	90	90
<i>β</i> /°	112.5280(10)	98.684(4)	95.106(2)
<i>γ</i> /°	92.3260(10)	90	90
Volume/Å ³	1661.25(9)	7642(2)	4103.9(4)
<i>Z</i>	2	8	4
$\rho_{\text{calc}}/\text{cm}^3$	1.393	1.356	1.332
μ/mm^{-1}	0.842	0.793	0.692
F(000)	724	3240	1720
Crystal size/mm ³	0.1 × 0.1 × 0.1	0.1 × 0.1 × 0.1	0.1 × 0.1 × 0.1
Radiation	MoK α (λ = 0.71073)	MoK α (λ = 0.71073)	MoK α (λ = 0.71073)
2 Θ range for data collection/°	4.994 to 53.444	4.96 to 50.526	5.378 to 52.988
Index ranges	-15 ≤ <i>h</i> ≤ 15, -15 ≤ <i>k</i> ≤ 15, -15 ≤ <i>l</i> ≤ 16	-19 ≤ <i>h</i> ≤ 19, -24 ≤ <i>k</i> ≤ 23, -28 ≤ <i>l</i> ≤ 28	-14 ≤ <i>h</i> ≤ 14, -12 ≤ <i>k</i> ≤ 12, -44 ≤ <i>l</i> ≤ 44
Reflections collected	24789	176725	80358
Independent reflections	6997 [R _{int} = 0.0370, R _{sigma} = 0.0409]	13706 [R _{int} = 0.3439, R _{sigma} = 0.0969]	8464 [R _{int} = 0.0965, R _{sigma} = 0.0478]
Data/restraints/parameters	6997/0/436	13706/0/961	8464/0/531
Goodness-of-fit on F ²	1.053	1.152	1.028
Final <i>R</i> indexes [<i>I</i> ≥ 2 σ (<i>I</i>)]	R ₁ = 0.0276, wR ₂ = 0.0675	R ₁ = 0.1325, wR ₂ = 0.3099	R ₁ = 0.0368, wR ₂ = 0.0803
Final <i>R</i> indexes [all data]	R ₁ = 0.0297, wR ₂ = 0.0688	R ₁ = 0.1546, wR ₂ = 0.3223	R ₁ = 0.0574, wR ₂ = 0.0874
Largest diff. peak/hole / e Å ⁻³	0.32/-0.28	1.21/-1.69	0.37/-0.36

hCAII Assay

The plasmid for recombinant expression of hCAII with a T7 RNA polymerase promoter and ampicillin resistance gene (pACA) was a gift from Thomas R. Ward (U. Basel, Switzerland). The protein for activity assays was expressed in BL21 Escherichia coli cells and purified as reported previously.³⁵ The Zn content of expressed hCAII was measured by inductively coupled plasma-mass spectrometry (ICP-MS). The metal-to-protein (Zn:protein) molar ratio was determined to be 0.951 ± 0.006 , indicating the holo enzyme (fully metalated) is was isolated (data not shown). Assays were carried out in clear-bottom Costar 96-well plates (catalog # 07-200-706) with a total volume of 100 μ L per well. The assay buffer was comprised of 50 mM HEPES pH 8.0 and 100 mM NaSO₄. MBIs were added from a 50 mM DMSO stock to a final concentration of 200 μ M and incubated with hCAII (40 nM final concentration) for 15 min at room temperature. *p*-Nitrophenyl acetate was used as the substrate (500 μ M final concentration), and the absorbance at 405 nM was monitored for 20 min at 1 min intervals using BioTek Synergy H4 plate reader. Percent inhibition was determined by comparing the activity of wells. A positive control (acetazolamide inhibitor, 50 μ M final concentration) showed complete inhibition under the assay conditions described above. Dose-response curves were generated, analyzed, and fitted to obtain IC₅₀ values of compounds using a concentration range of between 0.01 μ M and 1000 μ M depending on compound solubility.

MMP-2 Assay

Human recombinant MMP-2 catalytic domain was purchased from ENZO Life Sciences (catalog # BML-SE237-0010). Assays were carried out in clear Costar 96-well, half-area, flat-bottom assay plates (catalog # 80-2404). Each well contained a total volume of 100 μ L including buffer (50 mM MES, 10 mM CaCl₂, 0.05% Brij-35, pH 7.5), MMP-2 (1.16 U), and the fragment solution (200 μ M final concentration). After a 30 min incubation period at 37 °C, the reaction was initiated by the addition of 10 μ L of fluorogenic MMP-2 substrate (4 μ M final concentration, Mca-Pro-Leu-Gly-Leu-Dpa-Ala-Arg-NH₂·AcOH, ENZO Life Sciences, catalog # BML-P126-0001). Fluorescence was monitored at $E_x/E_m=328/420$ nm using BioTek Synergy H4 plate reader, and measurements were recorded every minute for 10 min. The rate of fluorescence increase was compared for samples versus negative controls (no inhibitor, arbitrarily set as 100% activity). A positive control (NNGH as inhibitor, 50 μ M final concentration) showed complete inhibition under the assay conditions described above. Dose-response curves were generated, analyzed, and fitted to obtain IC₅₀ values of compounds using a concentration range of between 1 μ M and 1000 μ M depending on compound solubility.

hCAII Expression & Purification

Plasmids encoding human carbonic anhydrase isozyme II and containing a T7 RNA polymerase promoter and an ampicillin resistance gene (pACA) were a generous gift from Carol A. Fierke, University of Michigan Medical School. Plasmids were introduced into BL21(DE3) *Escherichia coli* cells via heat-shock (45 s at 42 °C) and incubated in sterile SOC medium for 1 h at 37 °C with gentle shaking. The cells were then placed onto agar plates containing 60 µg /mL ampicillin and 34 µg/mL chloramphenicol and incubated overnight at 37 °C. Single colonies were transferred to 30 mL of autoclaved LB medium (10 g/L tryptone, 5 g/L yeast extract, 10 g/L NaCl) containing 100 µg /mL ampicillin and 34 µg/mL chloramphenicol and incubated overnight at 37 °C. Six pre-cultures were used to inoculate 6 L of autoclaved induction media (20 g/L tryptone, 10 g/L yeast extract, 5 g/L NaCl, 0.36×M9 salts solution, 0.4% glucose, 60 µM ZnSO₄, 100 µg/mL ampicillin and 34 µg/mL chloramphenicol). Cells were shaken (250 rpm) in induction media at 37 °C until OD₆₀₀ = 0.6 – 0.8. Addition of isopropyl-β-D-thiogalactopyranoside (IPTG, 250 µM final concentration) and ZnSO₄ (450 µM final concentration) induced protein expression and the temperature was lowered to 30 °C. The protease inhibitors phenylmethanesulfonyl fluoride (PMSF, 8 µg/mL) and *N*α-*p*-tosyl-L-arginine methyl ester hydrochloride (TAME, 1 µg/mL) were added to the induction media after 3 h. The cells were shaken for an additional 3 h after addition of protease inhibitors (for a total of 6 h induction) and pelleted via centrifugation (4,400 rpm at 4 °C) for 15 min. Carbonic anhydrase expression was confirmed via SDS-PAGE and Coomassie staining. Cell paste was flash frozen and stored at -80 °C prior to lysis. Cell paste was thawed in batches on ice for 2 h and resuspended in an equal volume of lysis buffer (1% Triton-X, 200 µM ZnSO₄, 2 mM DTT, 10-100 µg/mL DNase-1, 1 mg/mL lysozyme, and 1% glycerol with three EDTA free protease inhibitor tablets (Roche) added prior to resuspension) to cell pellet. Cells

were lysed using a probe sonicator (Fisherbrand model 120) with cycles of 25 second pulses and 59 second rest at 60% amplitude. Cell debris was then pelleted by centrifugation (10,000 rpm at 4 °C) for 45 min. The supernatant was decanted from the pellet and dialyzed against 4 L of activity buffer (50 mM Tris-sulfate (pH 8.0) and 0.5 mM ZnSO₄). Cell lysates were slowly mixed with DEAE-Sephacel ion exchange resin equilibrated with activity buffer (50 mM Tris-sulfate (pH 8.0) and 0.5 mM ZnSO₄) and 1 mM DTT for 1 h at 4 °C. The mixture was filtered using a Nalgene filter flask (0.45 µm) and the resin was washed three times with activity buffer. The eluent was combined and dialyzed in activity buffer overnight at 4 °C. The protein is then purified by affinity chromatography with 25 mL of 4-aminomethylbenzene sulfonamide agarose resin packed in a XK 16/20 column. Briefly, the column was equilibrated with 5 CV of activity buffer (50 mM Tris-sulfate (pH 8.0) and 0.5 mM ZnSO₄) or until absorbance reached a steady baseline. Dialyzed protein was loaded to the column from a 150 mL Superloop at a flow rate of 0.5 mL/min. The column was then washed with 5 CV of wash buffer (50 mM Na₂PO₄H, 50 mM KSCN, and 25 mM Tris at pH 8.8). The bound protein was then eluted with 10 CV of elution buffer (200 mM KSCN and 50 mM Na₂PO₄H at pH 5.6) at a flow rate of 2 mL/min collecting 2 mL fractions. hCAII eluted between fractions 13-41. SDS-PAGE analysis showed a band corresponding to hCAII running at ~29 kDa with only one small impurity at ~50 kDa. Pure fractions were pooled and dialyzed against 4 L of activity buffer for 24 h at 4 °C. A portion of this protein was then either concentrated to 80 nM for activity assays or 20 mg/ml for crystallography and flash frozen. The remaining protein was dialyzed against 4 L of DI water for 24 h at 4 °C and mQ water for 24 h at 4 °C and then lyophilized. All protein samples are stored at -80 °C.

hCAII Crystallography

Crystals of hCAII were obtained by the hanging-drop vapor diffusion method using 24-well pre-greased plates (Hampton) with siliconized glass slides (Hampton). The protein solution consisted of 20 mg/mL hCAII and 1 mM *p*-chloromercuribenzoic acid in 50 mM Tris-SO₄ (pH 8.0) supplemented with 0.5 mM ZnSO₄. Protein solution was incubated on ice with 1 mM compound for 1 h prior to setting the crystallization drops. The precipitant solution contained 2.6-3.0 M (NH₄)₂SO₄ in 50 mM Tris-SO₄ (pH 8). Drops consisting of 3 μL of protein solution and 2.5-4.0 μL of precipitant solution were equilibrated at room temperature against 500 μL of precipitant solution. Colorless crystals roughly 0.3×0.3×0.3 mm in size appeared after 7-10 days. Crystals formation occurred spontaneously, but streak crystal seeding with natural or artificial cat whiskers produced larger and more abundant single crystals. Crystals soaked by transferring crystals to a 5 μL drop of the corresponding reservoir solution that was supplemented with 5 μL of a 50mM DMSO compound stock for 4-48 h. Collected crystals were cryoprotected with perfluoroether (Hampton) prior to flash freezing and were stored in liquid nitrogen until data collection. All structures include a 4-mercuribenzoic acid ligand bound to Cys206. X-ray diffraction studies were carried out on a Bruker Microfocus Rotating Anode (MicroStar FR- 592) X-ray generator with a Bruker APEX II CCD detector at wavelength 1.54178 Å. Data was integrated, scaled, and merged using the Bruker APEX3 software package (Bruker, 2017). All crystals belong to the monoclinic space group *P*2₁. The data were phased by molecular replacement using a previously reported hCAII structure (PDB: 4E49), with water molecules removed, using PHASER. All structures were refined with Phenix version 1.19.2 and model building and visualized using Coot version 0.9.5.

Table 4.S4. X-ray crystallographic data collection and refinement statistics.

Compound	4.4	4.7
PDB	8FAL	8FAU
Resolution range	35.54- 1.37 (1.42-1.37)	35.53- 1.44 (1.49-1.44)
Space group	P2 ₁	P2 ₁
Cell dimensions a, b, c, (Å) α, β, γ (°)	42.009 41.143 71.915 90 104.556 90	42.144 41.316 71.919 90 104.541 90
Unique reflections	88780	75411
Completeness (%)	99	92.4
Mean I/sigma(I)	11 (1.5)	15 (2.2)
R-merge	0.060 (0.355)	0.045 (0.225)
R-measured	0.067 (0.476)	0.050 (0.312)
R-work	0.1903 (0.2997)	0.1756 (0.2544)
R-free	0.2224 (0.2772)	0.2086 (0.3072)
RMS(bonds)	0.012	0.007
RMS(angles)	1.25	1.02
Ramachandran favored (%)	95.69	96.06
Ramachandran outliers (%)	0	0
Average B-factor	18.1	19.6
Redundancy	4	4.1
CC1/2	0.999 (0.803)	0.999 (0.892)

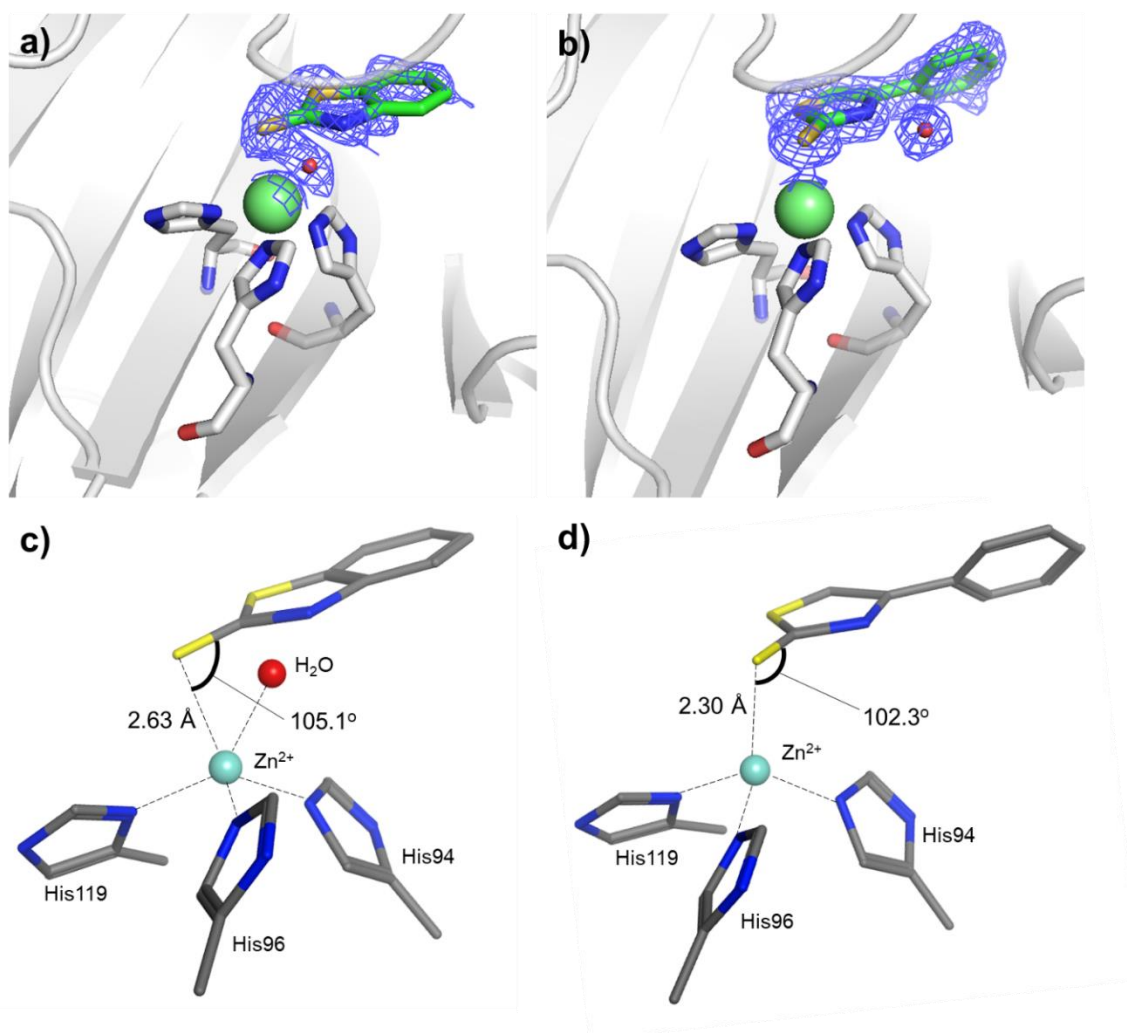


Figure 4.S3. Co-crystal structures of hCAII with a) **4.4** and b) **4.7**. Zn(II) ion and water molecules are shown as green and red spheres, respectively. Residues coordinating the Zn²⁺ ion is shown in sticks. Atom colors are: carbon (green for compound, gray for protein), oxygen (red), nitrogen (blue) and sulfur (yellow). Details of the coordination modes of c) **4.4** and d) **4.7** bound to the hCAII active site. Zn(II) coordination is represented by dashed lines.

4.10 References

1. Seo, H.; Prosser, K. E.; Kalaj, M.; Karges, J.; Dick, B.; Cohen, S. M. "Evaluating Metal–Ligand Interactions of Metal-Binding Isosteres Using Model Complexes." *Inorg. Chem.*, **2021**, *60* (22), 17161-17172.
2. Barrese, A. A.; Genis, C.; Fisher, S. Z.; Orwenyo, J. N.; Kumara, M. T.; Dutta, S. K.; Phillips, E.; Kiddle, J. J.; Tu, C.; Silverman, D. N.; Govindasamy, L.; Agbandje-McKenna, M.; McKenna, R.; Tripp, B. C., Inhibition of Carbonic Anhydrase II by Thioxolone: A Mechanistic and Structural Study. *Biochemistry* **2008**, *47* (10), 3174-3184.
3. Yamaguchi, Y.; Jin, W.; Matsunaga, K.; Ikemizu, S.; Yamagata, Y.; Wachino, J.-i.; Shibata, N.; Arakawa, Y.; Kurosaki, H., Crystallographic Investigation of the Inhibition Mode of a VIM-2 Metallo- β -lactamase from *Pseudomonas aeruginosa* by a Mercaptocarboxylate Inhibitor. *J. Med. Chem.* **2007**, *50* (26), 6647-6653.
4. Ondetti, M. A.; Rubin, B.; Cushman, D. W., Design of specific inhibitors of angiotensin-converting enzyme: new class of orally active antihypertensive agents. *Science* **1977**, *196* (4288), 441-4.
5. Natesh, R.; Schwager, S. L.; Evans, H. R.; Sturrock, E. D.; Acharya, K. R., Structural details on the binding of antihypertensive drugs captopril and enalaprilat to human testicular angiotensin I-converting enzyme. *Biochemistry* **2004**, *43* (27), 8718-24.
6. Irvin, J. D.; Viau, J. M., Safety profiles of the angiotensin converting enzyme inhibitors captopril and enalapril. *Am. J. Med.* **1986**, *81* (4, Supplement 3), 46-50.
7. Gavras, H.; Gavras, I., Angiotensin converting enzyme inhibitors. Properties and side effects. *Hypertension* **1988**, *11* (3_pt_2), 37-41.

8. Chauvin, J.-P. R.; Pratt, D. A., On the Reactions of Thiols, Sulfenic Acids, and Sulfinic Acids with Hydrogen Peroxide. *Angew. Chem.* **2017**, *56* (22), 6255-6259.
9. DeCollo, T. V.; Lees, W. J., Effects of Aromatic Thiols on Thiol–Disulfide Interchange Reactions That Occur during Protein Folding. *J. Org. Chem.* **2001**, *66* (12), 4244-4249.
10. Manna, D.; Roy, G.; Mugesh, G., Antithyroid Drugs and Their Analogues: Synthesis, Structure, and Mechanism of Action. *Acc. Chem. Res.* **2013**, *46* (11), 2706-2715.
11. Bozdog, M.; Supuran, C. T.; Esposito, D.; Angeli, A.; Carta, F.; Monti, S. M.; De Simone, G.; Alterio, V., 2-Mercaptobenzoxazoles: a class of carbonic anhydrase inhibitors with a novel binding mode to the enzyme active site. *Chem. Commun.* **2020**, *56* (59), 8297-8300.
12. Puerta, D. T.; Griffin, M. O.; Lewis, J. A.; Romero-Perez, D.; Garcia, R.; Villarreal, F. J.; Cohen, S. M., Heterocyclic zinc-binding groups for use in next-generation matrix metalloproteinase inhibitors: potency, toxicity, and reactivity. *J. Biol. Inorg. Chem* **2006**, *11* (2), 131-138.
13. Khan, H.; Badshah, A.; Shaheen, F.; Gieck, C.; Qureshi, R. A., 1-Methyl-1H-benzimidazole-2(3H)-thione. *Acta Crystallogr. E* **2008**, *64* (6), o1141.
14. Proj, M.; Sosič, I.; Gobec, S., Synthesis and NMR spectroscopic assignment of chlorinated benzimidazole-2-thione derivatives. *Tetrahedron Lett.* **2019**, *60* (39), 151078.
15. Balestrero, R. S.; Forkey, D. M.; Russell, J. G., ¹⁵N NMR: Iminothiol-thioamide tautomerism of 2-mercaptobenzazoles and 1-methyl-2-mercaptoimidazole. *Magn. Reson. Chem.* **1986**, *24* (8), 651-655.
16. Moran, D.; Sukcharoenphon, K.; Puchta, R.; Schaefer, H. F.; Schleyer, P. v. R.; Hoff, C. D., 2-Pyridinethiol/2-Pyridinethione Tautomeric Equilibrium. A Comparative Experimental and Computational Study. *J. Org. Chem.* **2002**, *67* (25), 9061-9069.

17. Kollár, L.; Gobec, M.; Szilágyi, B.; Proj, M.; Knez, D.; Ábrányi-Balogh, P.; Petri, L.; Imre, T.; Bajusz, D.; Ferenczy, G. G.; Gobec, S.; Keserű, G. M.; Sosič, I., Discovery of selective fragment-sized immunoproteasome inhibitors. *Eur. J. Inorg. Chem.* **2021**, *219*, 113455.
18. Hino, T.; Tsuneoka, K.; Nakagawa, M.; Akaboshi, S., Thiation of Oxindoles. *Chem. Pharm. Bull.* **1969**, *17* (3), 550-558.
19. Owczarzak, A. M.; Kubicki, M., 4-Phenyl-1H-imidazole-2(3H)-thione. *Acta Crystallogr. Sect. E* **2012**, *68* (Pt 6), o1686.
20. Kimblin, C.; Parkin, G., Comparison of Zinc and Cadmium Coordination Environments in Synthetic Analogues of Carbonic Anhydrase: Synthesis and Structure of {[PimPri,But]Cd(OH₂)(OCIO₃)}(ClO₄). *Inorg. Chem.* **1996**, *35* (24), 6912-6913.
21. Puerta, D. T.; Cohen, S. M., Examination of Novel Zinc-Binding Groups for Use in Matrix Metalloproteinase Inhibitors. *Inorg. Chem.* **2003**, *42* (11), 3423-3430.
22. Lovejoy, B.; Welch, A. R.; Carr, S.; Luong, C.; Broka, C.; Hendricks, R. T.; Campbell, J. A.; Walker, K. A.; Martin, R.; Van Wart, H.; Browner, M. F., Crystal structures of MMP-1 and -13 reveal the structural basis for selectivity of collagenase inhibitors. *Nat. Struct. Biol* **1999**, *6* (3), 217-21.
23. Eriksson, A. E.; Jones, T. A.; Liljas, A., Refined structure of human carbonic anhydrase II at 2.0 Å resolution. *Proteins* **1988**, *4* (4), 274-82.
24. Dołęga, A.; Becker, B.; Chojnacki, J.; Konitz, A.; Wojnowski, W., Formation, crystal and molecular structures of heteroleptic zinc(II) tri-tert-butoxysilanethiolates with ZnNO₂S₂ and ZnN₂S₂ coordination pattern. *Inorg. Chim. Acta* **2004**, *357* (2), 461-467.
25. Dołęga, A.; Baranowska, K.; Gudat, D.; Herman, A.; Stangret, J.; Konitz, A.; Śmiechowski, M.; Godlewska, S., Modeling of the Alcohol Dehydrogenase Active Site: Two

Different Modes of Alcohol Binding in Crystals of Zinc and Cadmium Tri-tert-butoxysilanethiolates Evidenced by X-ray Diffraction and Solid-State Vibrational Spectroscopy.

Eur. J. Inorg. Chem. **2009**, 2009 (24), 3644-3660.

26. Chaves, S.; Gil, M.; Canário, S.; Jelic, R.; Romão, J. M.; Trincão, J.; Herdtweck, E.; Sousa, J.; Diniz, C.; Fresco P.; Santos, M. A., Biologically relevant O,S-donor compounds. Synthesis, molybdenum complexation and xanthine oxidase inhibition. *Dalton Trans.* **2008**, 13, 1773-1782.

27. Hackl, C. M.; Schoenhacker-Alte, B.; Klose, M. H. M.; Henke, H.; Legina, M. S.; akupec, M. A. J; Berger, W.; Keppler, B. K., Brüggemann, O.; Teasdale, I.; Heffeter P.; Kandioller, W., Synthesis and *in vivo* anticancer evaluation of poly(organo)phosphazene-based metallodrug conjugates. *Dalton Trans.* **2017**, 46, 12114-12124.

28. Liang, H.; Liu, R.; Zhou, M.; Fu, Y.; Ni C.; Hu, J., Difluorocarbene-Triggered Cyclization: Synthesis of (Hetero)areneFused 2,2-Difluoro-2,3-dihydrothiophenes. *Org. Lett.* **2020**, 22 (17), 7047-7051.

29. Saputra, A.; Fan, R.; Yao, T.; Chen J.; Tan, J., Synthesis of 2-(Arylthio)indolenines via Chemoselective Arylation of Thio-Oxindoles with Arynes. *Adv. Synth. Catal.* **2020**, 362 (13), 2683-2688.

30. Seo, H.; Jackl, M. K.; Kalaj M.; Cohen, S. M., Developing Metal-binding Isosteres of 8-Hydroxyquinoline as Metalloenzyme Inhibitor Scaffolds. *Inorg. Chem.* **2022**, 61 (19), 7631-7641.

31. Puerta, D. T.; Cohen, S. M., Elucidating Drug-Metalloprotein Interactions with Tris(pyrazolyl)borate Model Complexes. *Inorg. Chem.* **2002**, 41 (20), 5075-5082.

32. Sheldrick, G. M. Crystal structure refinement with SHELXL. *Acta Crystallogr. A* **2015**, 71, 3-8.

33. Sheldrick, G. M. A short history of SHELX. *Acta Crystallogr. A* **2008**, 64, 112-122.

34. Dolomanov, O. V.; Bourhis, L. J.; Gildea, R. J.; Howard, J. A. K.; Puschmann, H., *OLEX2: a complete structure solution, refinement and analysis program. J. Appl. Crystallogr.* **2009**, *42*, 339-341.
35. Monnard, F. W.; Nogueira, E. S.; Heinisch, T.; Schirmer T.; Ward, T. R., Human carbonic anhydrase II as host protein for the creation of artificial metalloenzymes: the asymmetric transfer hydrogenation of imines. *Chem. Sci.* **2013**, *4* (8), 3269-3274.

Chapter 5: Developing Cu-only Superoxide Dismutase Inhibitors as Novel Antifungal Agents

5.1 Introduction

In the previous chapters, several efforts were made to broaden the scope of metal-binding pharmacophores (MBPs) and metal-binding isostere (MBIs) available for lead development for metalloenzyme inhibition. With the successful development of new MBPs and MBIs described, ~70 small molecules have been added to our fragment library. This has significantly enriched the chemical diversity of our fragment library, broadening the spectrum of physicochemical properties available for exploration in developing metalloenzyme inhibitors, as well as providing alternative scaffolds for mitigating potential liabilities of existing MBPs that might arise from hit-to-lead development. In total, the Cohen laboratory now houses a library comprising ~380 fragments, well-suited for targeting various metalloenzymes. The primary objective of Chapter 5 is to employ this augmented fragment library against a superoxide dismutase (SOD) enzyme that has been identified as a promising target for antifungal drug development.

SODs are metalloenzymes that disproportionate superoxide ($O_2^{\bullet-}$) produced by aerobic metabolism. SODs are found across a broad range of organisms, from fungi to humans, serving various functions in protecting against oxidative stress and in signaling processes that involve reactive oxygen species (ROS).¹ The eukaryotic intracellular Cu,Zn superoxide dismutase (Cu,Zn-SOD1) has been extensively studied, particularly in terms of its catalytic activity, structure, and overall function since it was first identified.¹ The laboratory of Prof. Valerie Culotta (Johns Hopkins University) has discovered a new class of extracellular, Cu-dependent SOD enzymes (Figure 5.1) that is unique to the fungal kingdom and structurally distinct from all other SODs, including the Cu,Zn-SOD1 found in humans.² These so-called ‘Cu-only’ SODs are highly conserved throughout the fungal kingdom and are exclusively extracellular, either tethered to the cell wall, or secreted into the environment.³⁻⁵ In pathogenic fungi, Cu-only SODs degrade $O_2^{\bullet-}$

produced by host phagocytes (Figure 5.1),^{3, 6-7} protect against phagocyte killing,^{3, 6-10} and are essential for fungal virulence in humans,^{3, 9, 11-12} plants,¹³⁻¹⁴ and insects.¹⁵ Early data strongly suggest that these Cu-only SODs are a promising new antifungal target. It is reported that deletion of just a single Cu-only SOD, called SOD5, of *C. albicans* is enough to completely inhibit fungal infection in a rat catheter model.¹²

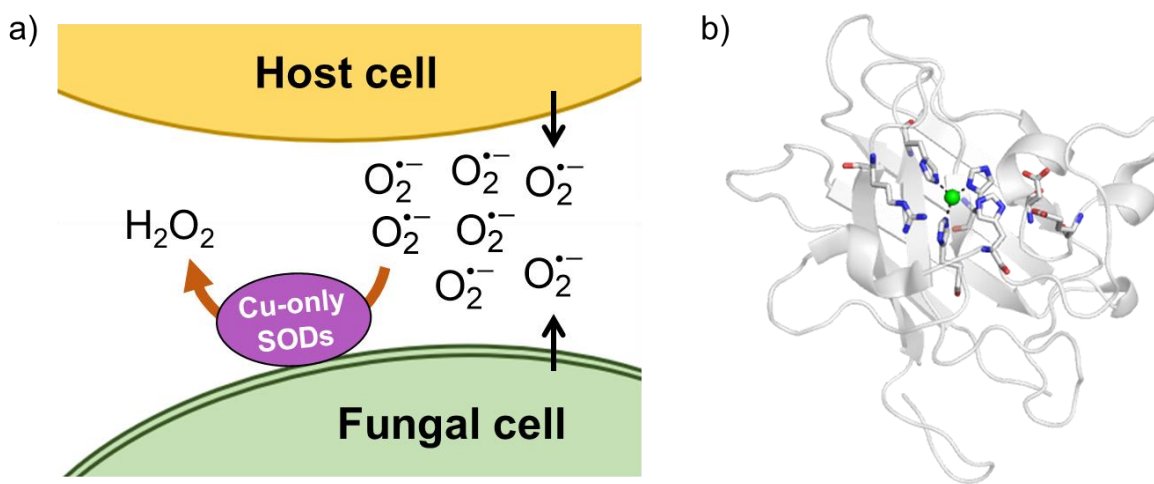


Figure 5.1. Fungal Cu-only SODs. a) Cu-only SODs can react with superoxide from both the host and fungal pathogen. b) Overall structure of *C. albicans* SOD5 (PDB: 4N3U). The Cu(II) ion is shown as a green sphere and select active site residues are shown as sticks colored by atom type (carbon, gray; nitrogen, blue; oxygen, red).

Structural and biochemical studies of Cu-only SODs demonstrate that these enzymes are unique in that they lack the Zn-binding residues and electrostatic loop that are hallmarks of the eukaryotic Cu,Zn-SOD1 (Figure 5.2). Figure 5.2 details structural differences between fungal Cu-only SOD (*C. albicans*) from a canonical Cu,Zn-SOD1 (*S. cerevisiae*). The result shows a more open active site in Cu-only SOD5 that makes them more susceptible to loss of the essential Cu cofactor compared to Cu,Zn-SOD1 in the presence of strong metal binders.^{2, 5, 12, 16} In Cu-only SOD5, the active site Cu(II) center is coordinated by four histidine residues (H75, H77, H93, and H153) in a distorted square planar geometry (Figure 5.2). Superoxide is oxidized in the first

catalytic step, and structural analysis shows a loss of connecting electron density between the copper ion and the nitrogen atom of the H93 residue is observed during upon reduction of Cu(II) to Cu(I), resulting in a pseudo-trigonal planar geometry in the Cu(I) state.² Additionally, residue H93 interacts with E110, promoting pH-independent catalysis and a hydrogen bonding network between H75 and D113 stabilizes the copper center (Figure 5.2).¹⁷

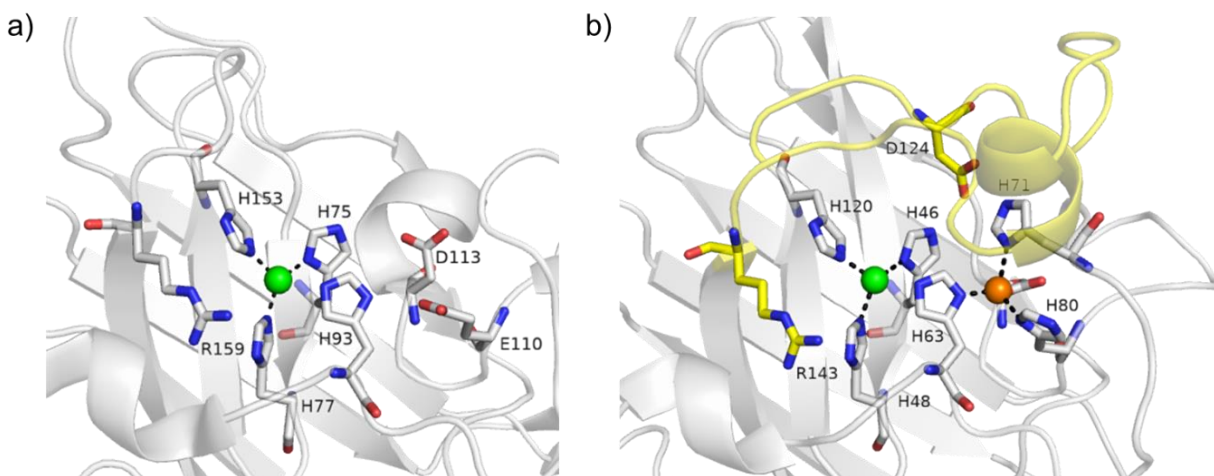


Figure 5.2. Active site structures of fungal Cu-only SOD5 and comparison with a canonical eukaryotic Cu,Zn-SOD1. a) Active site of *C. albicans* Cu-only SOD5 (PDB: 4N3U). b) Active site of *S. cerevisiae* CuZn-SOD1 (PDB: 1AZV). The electrostatic loop is shown in yellow, and the Zn(II) ion is shown as an orange sphere. Cu(II) ions are shown as green spheres and select active site residues are shown as sticks colored by atom type (carbon, gray/yellow; nitrogen, blue; oxygen, red).

Given the increasing prevalence of drug resistance resulting from prolonged use of antifungal medications and the natural evolution of resistance among pathogens like *Candida* sp. against current drugs such as fluconazole, there is a critical need for innovative therapeutic strategies. Despite attempts to repurpose or modify existing drugs and explore combination therapies, their success in overcoming resistance remains limited.¹⁸ Consequently, there is an urgent demand for a novel approach that goes beyond current antifungal treatments. In Chapter 5, we propose targeting the Cu-only SOD5 as a promising avenue for antifungal drug development.

5.2 Assay Protocol and Library Screening Results

Currently, there are few inhibitors known for Cu-only SOD5 (Figure 5.3a). These inhibitors were initially discovered by the Culotta laboratory,¹² and are listed in Figure 5.3a. Although they exhibit good inhibition of Cu-only SOD5, with IC₅₀ values ranging from 100 nM to 30 μM, most of the inhibitors identified in this screening effort are non-specific metal chelators. For instance, ammonium tetrathiomolybdate (TTM) and diethyldithiocarbamic acid (DETC) are known copper chelators and were previously reported as inhibitors of Cu,Zn-SOD1 by demetallation of its copper co-factor.¹⁹⁻²⁰ Similarly, bathophenanthroline sulfonic acid (BPS) was identified, a well-characterized iron chelator that has been studied for its ability to mitigate iron-related cellular stress by engaging iron homeostasis.²¹ The broad chelating properties of TTM, DETC, and BPS raise concerns about their selectivity toward Cu-only SOD5. Additionally, Zn-pyrithione, an FDA-approved microbicidal agent, inhibits Cu-only SOD5 by removing the copper co-factor.¹² This characteristic enables it to permeate the cell membrane, but results in non-selective effects on copper homeostasis.²² Indeed, in March 2022, the European Union (EU) classified Zn-pyrithione as a prohibited substance due to its potential to cause DNA damage and banned its use for all cosmetic products (e.g., anti-dandruff shampoos) in the EU.²³⁻²⁴ Given that only a few small molecules have been identified as potent inhibitors of Cu-only SOD5,^{12, 25} there is a need to discover additional SOD5 inhibitors. A biochemical assay was optimized based on a previously published protocol from the Culotta laboratory.¹² Specifically, Cu-only SOD5 activity is measured using 2-(4-iodophenyl)-3-(4-nitrophenyl)-5-(2,4-disulfo-phenyl)-2*H*-tetrazolium, monosodium salt (WST-1, Figure 5.3b). In this assay, superoxide is generated by xanthine oxidase and detected by reducing WST-1 tetrazolium salt to WST-1 formazan, which results in a bright yellow color that is detectable by UV-visible absorbance spectroscopy at 450

nm. The formation of WST-1 formazan is inhibited in the presence of Cu-only SOD. To increase the assay sensitivity, the concentration of xanthine, xanthine oxidase, and WST-1 were increased ~2-fold when compared to the reported protocol (0.2 mM xanthine, 0.1 mM EDTA, 0.75 mM WST-1, and 0.48 milliunits of xanthine oxidase) in a final volume of 200 μ L per reaction well. The detailed protocol can be found in the Appendix of this chapter. The known inhibitor Zn-pyrithione and 1-hydroxypyridine-2(1*H*)-thione (1,2-HOPTO) were used as positive controls (IC_{50} = 111 nM and 579 nM, respectively) (Figure 5.3c) and to validate the optimized assay protocol.¹²

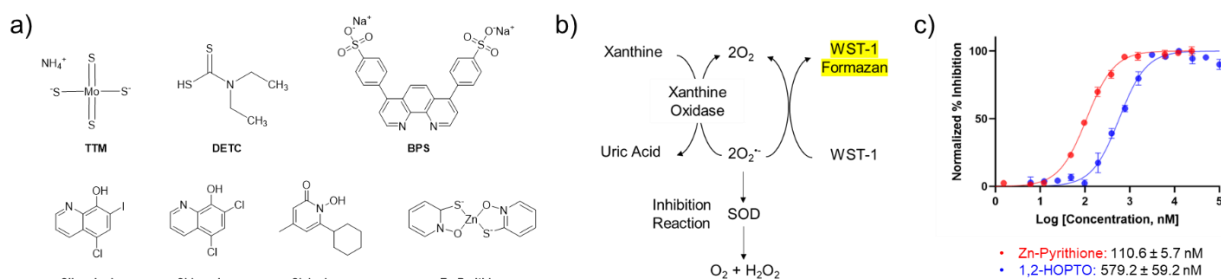


Figure 5.3. a) Reported SOD5 inhibitors. Ammonium tetrathiomolybdate (TTM), Diethyldithiocarbamic acid (DETC), bathophenanthroline sulfonic acid (BPS), Clioquinol, and Chloroxine are known Cu(II) chelators. Ciclopirox and Zn-pyrithione are FDA-approved antifungal drugs. b) Schematic showing the principle of the SOD assay. Superoxide produced by xanthine oxidase reduces WST-1 to WST-1 formazan showing yellow color. SOD can block the reaction and SOD inhibitors allow WST-1 formazan formation in a dose-dependent manner. Adapted from the cited reference. c) Titration curves for the reported SOD5 inhibitors, pyrithione zinc and 1-hydroxypyridine-2(1*H*)-thione (1,2-HOPTO). The IC_{50} values were determined under the optimized SOD assay condition and validated the assay.

With this assay in hand, our MBP and MBI libraries (~380 fragments, Figure 5.4) were screened against Cu-only SOD5 at a fragment concentration of 200 μ M and the screening results are shown in Figure 5.5. The screening campaign shows that a significant number of MBPs exhibited inhibitory activity toward Cu-only SOD5. From our library containing ~380 fragments, ~45 fragments showed >50% inhibition activity at a concentration of 200 μ M and ~20 fragments showed >50% inhibition activity when screened at a concentration of 50 μ M. Compounds that exhibited >90% inhibition activity at a concentration of 50 μ M were further evaluated to determine

their IC₅₀ values against SOD5. The top five hits were identified, giving excellent IC₅₀ values, as low as ~0.33 μM, and showing no inhibition for Cu,Zn-SOD1 at a concentration of up to 50 μM (Figure 5.6, Table 5.1). Notably, several previously unreported compounds were identified as hits for Cu-only SOD inhibition, which includes compounds **5.1** (7-(1*H*-tetrazol-5-yl)-1*H*-benzo[d][1,2,3]triazole), 8-hydroxyquinoline (8-HQ), **5.2** (*N*-hydroxypicolinamide), and **5.3** (2-(4,5-dihydrooxazol-2-yl)phenol). The reported inhibitor, 1,2-HOPTO, was also identified as an inhibitor in this screening, validating the assay. This initial screening of our MBP/MBI library was very encouraging and indicates that we will be able to identify several viable lead fragments to target Cu-only SOD5.

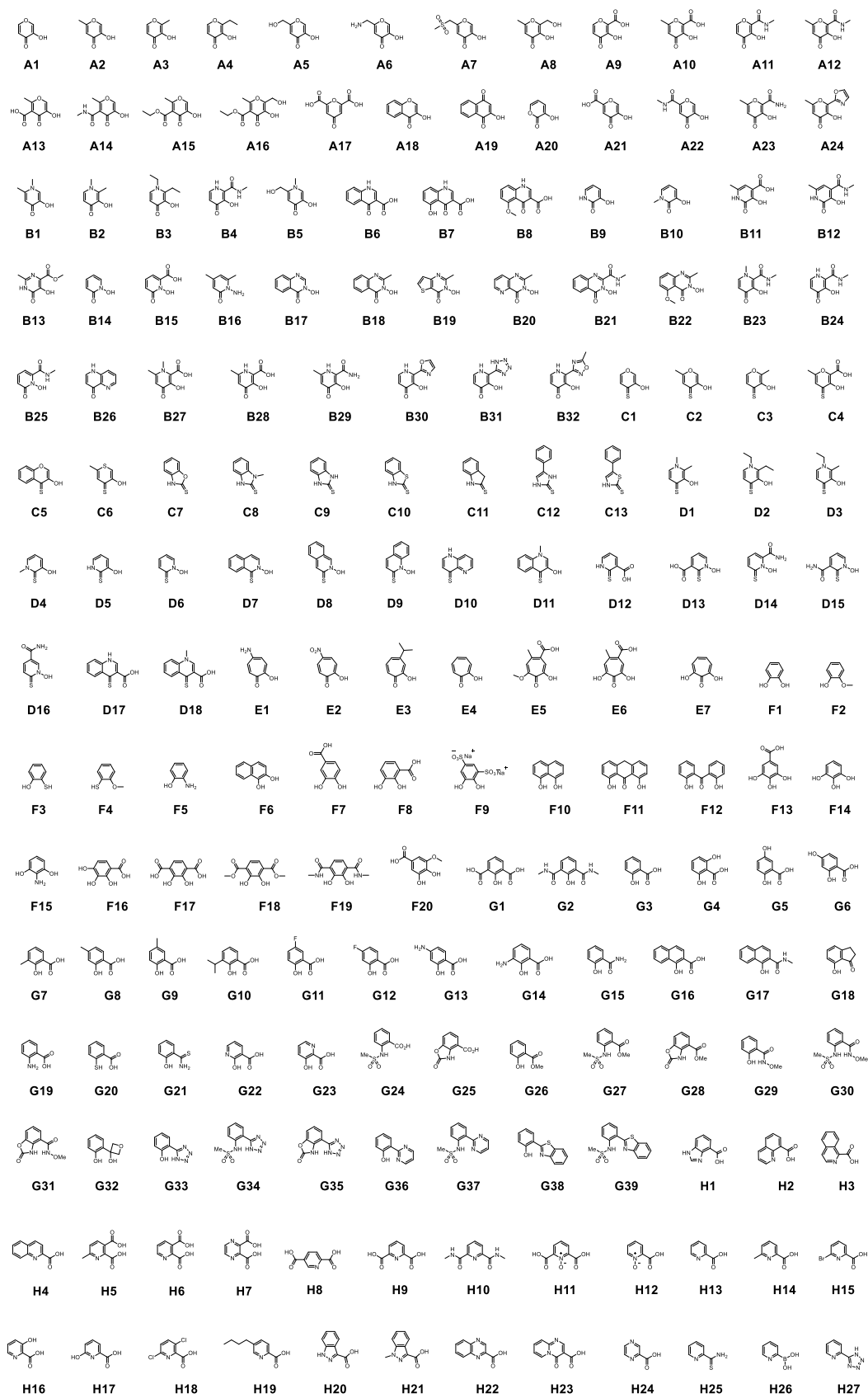


Figure 5.4. Structures of all fragments in the Cohen laboratory MBP/MBI library.

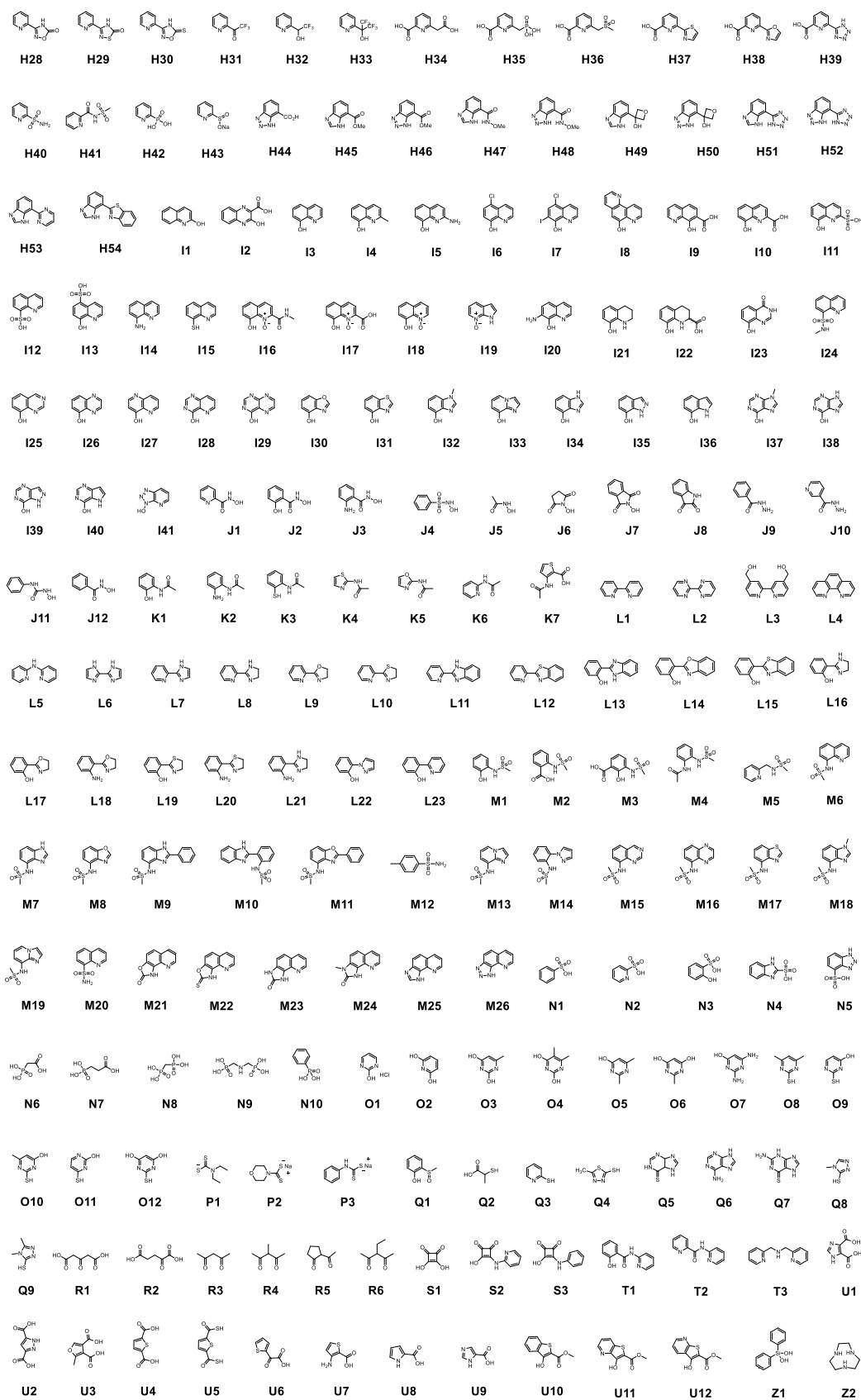


Figure 5.4 (continued). Structures of all fragments in the Cohen laboratory MBP/MBI library.

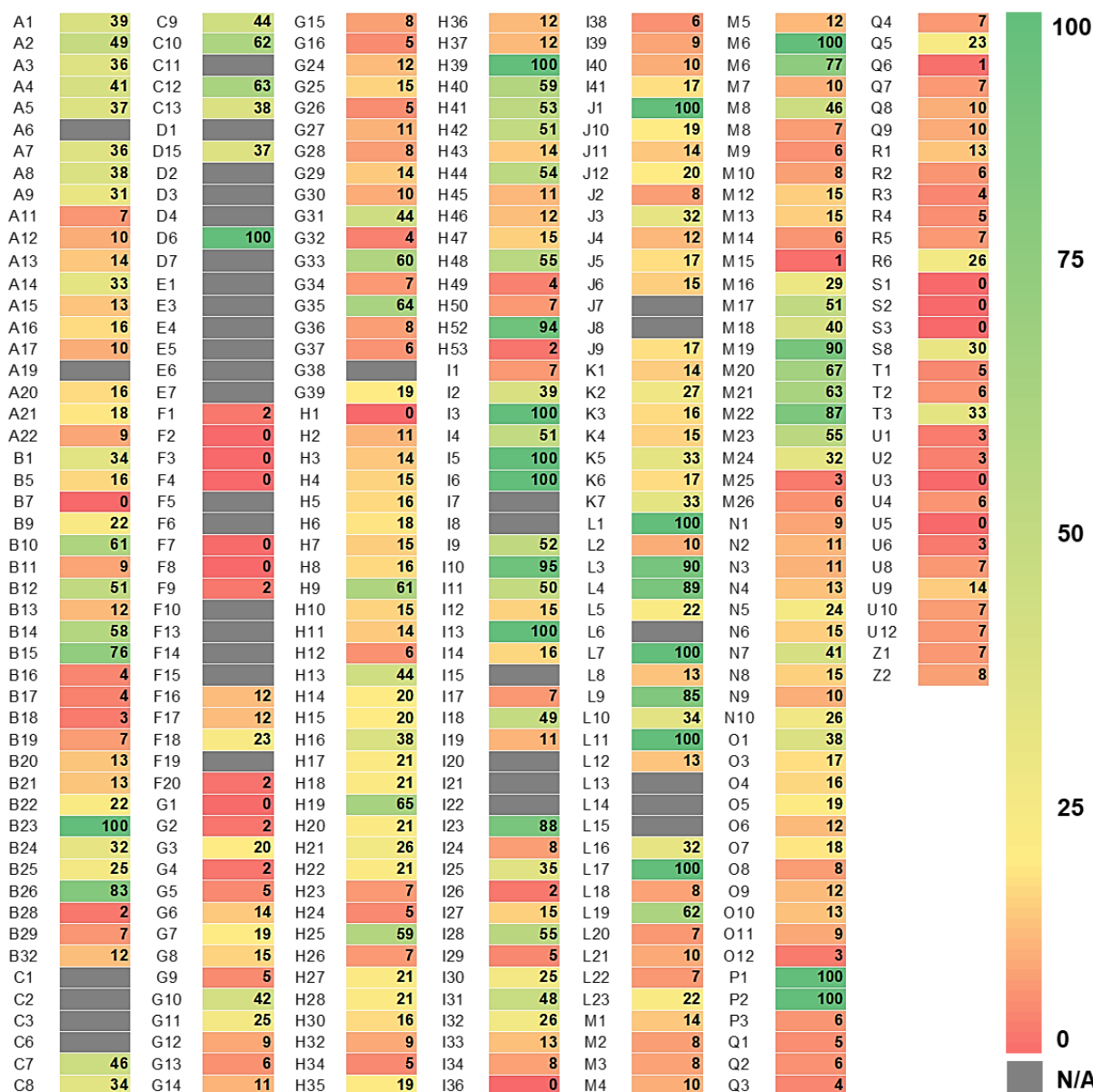


Figure 5.5. Screening of the MBP/MBI fragment library (~380 fragments) against Cu-only SOD5. Percent inhibition of SOD5 activity shown at a fragment concentration of 200 μ M. Fragments in green (~45) showed >50% inhibition activity. Grey cells are compounds that interfered with the assay, generally due to background signal resulting from its intrinsic UV-visible absorbance at 450 nm.

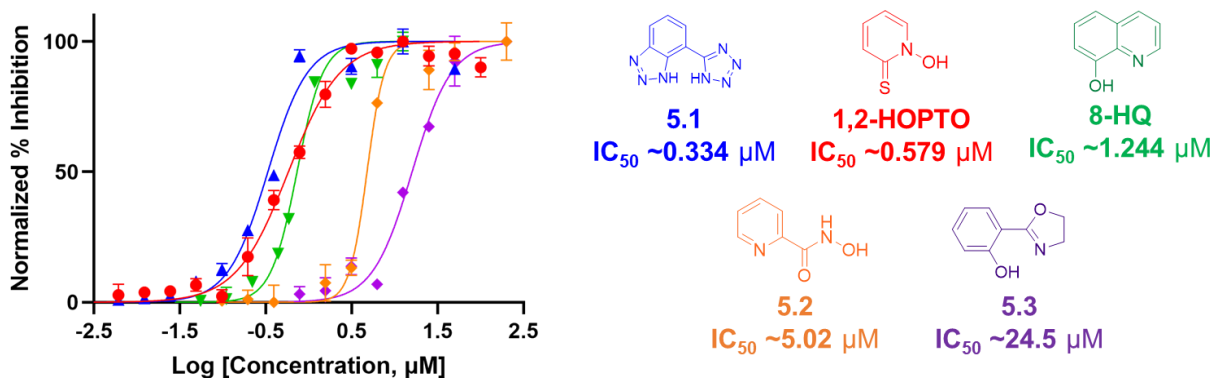


Figure 5.6. IC₅₀ curves for the representative hits (color-coded) from the MBP/MBI library screen (*left*). The structure and IC₅₀ values of the hits are listed (*right*). Chemical structure of compounds **5.1** (7-(1*H*-tetrazol-5-yl)-1*H*-benzo[d][1,2,3]triazole), 1,2-HOPTO, 8-HQ, **5.2** (*N*-hydroxypicolinamide), and **5.3** (2-(4,5-dihydrooxazol-2-yl)phenol) are shown in different colors corresponding to inhibition curves (*left*).

Table 5.1. IC₅₀ values of hit compounds against Cu-only SOD5 versus Cu,Zn-SOD1. IC₅₀ values reported in μM with the 95% confidence interval indicated. ND = Not Defined; IC₅₀ for Cu,Zn-SOD1 was not defined due to insufficient or absent inhibition of enzyme activity over the dose range of compounds tested (0.02 – 50 μM).

Compound	IC ₅₀ (μM)	
	Cu-only SOD5	Cu,Zn-SOD1
5.1	0.334±0.040	ND
1,2-HOPTO	0.579±0.060	ND
8-HQ	1.244±0.061	ND
5.2	5.019±0.581	ND
5.3	24.51±4.95	ND

5.3 Inhibitor Development Against Cu-only SOD5

The top three hits displaying the highest activity - compounds **5.1**, 1,2-HOPTO, and 8-HQ - were selected for lead development. To access available chemical space and identify amino acid residues that might be suitable for creating new interactions upon compound elaboration, computational docking was conducted using the Molecular Operating Environment (MOE) software (Figure 5.7, see Appendix to Chapter 5 for details). Notably, the active site of Cu-only SOD5 is quite open and solvent exposed. Each of the hit compounds was found by docking to form a hydrogen bonding interaction with His93 and coordination bonds with the Cu(II) ion in the active site. Moreover, compounds **5.1** and 1,2-HOPTO formed a hydrogen bond with Arg159. Gly157, which was identified in the solvent exposed regions near the active site, was found to make a noncovalent interaction with the aromatic moieties of compound **5.1**. Another polar amino acid residue, Asn156, was found close to the active site, which could be a potential residue to interact with hit compounds on the solvent-exposure regions.

Based on this docking analysis, there are limited opportunities to generate new interactions with amino acids in the active site due to the open and solvent-exposed nature of the receptor. However, some studies do suggest that exploiting solvent-exposed regions can be an effective strategy for ligand development, particularly when the traditional active site does not offer enough room or features for strong or specific interactions.²⁶ This approach not only increases affinity or selectivity for a target protein but also improves drug-like properties by targeting solvent-exposed regions. Consequently, a tailored synthetic approach for each hit compound was developed, the details of which are discussed in the subsequent sections.

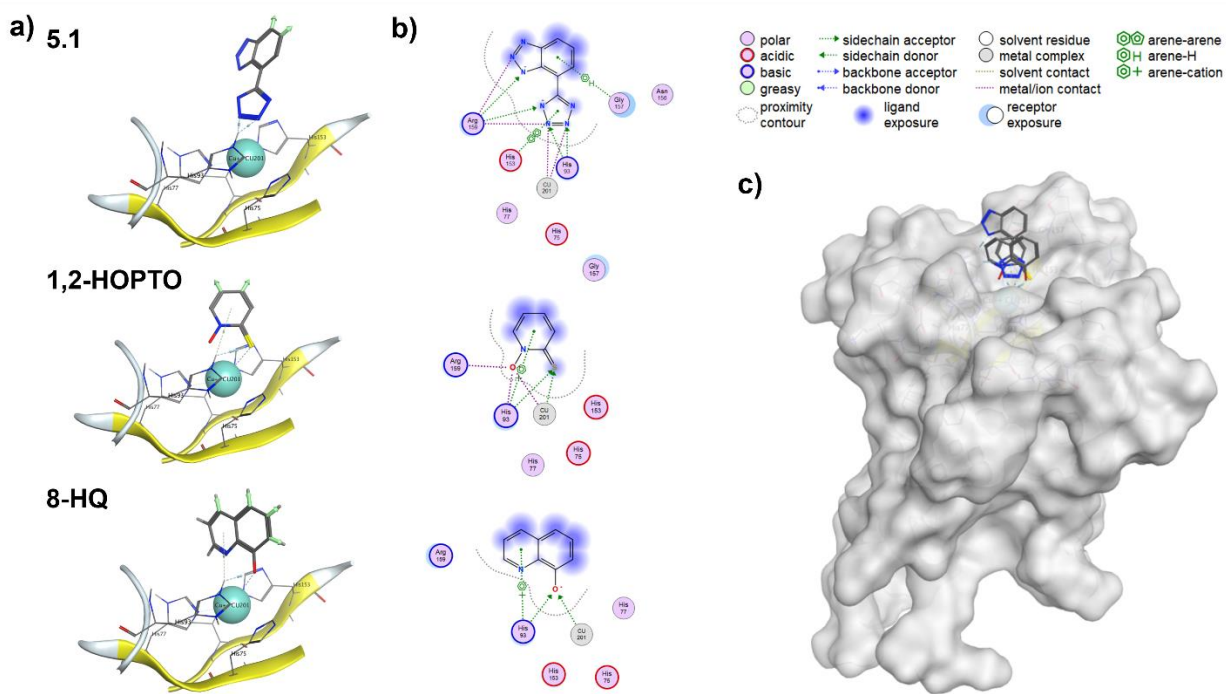


Figure 5.7. Binding modes of computationally derived poses for hit compounds (**5.1**, 1,2-HOPTO, and 8-HQ) upon docking with MOE. The docking models were prepared using the structure (PDB: 4N3U). a) Active site of Cu-only SOD5 with each MBP. Green arrows indicate positions on the ligand where a hypothetical methyl group can be added without inducing a conformational change or a clash. b) 2-Dimensional interaction diagram of each ligand in the Cu-only SOD5 active site and legend. The solvent exposure of each MBP is indicated by a blue cloud. c) Structure of Cu-only SOD5 with overlapping MBPs. Protein shown as gray surface, active site metals shown as cyan surface, and MBP shown as sticks colored by atom type; grey=carbon, blue=nitrogen, red=oxygen, and yellow=sulfur.

5.3.1 7-(1*H*-tetrazol-5-yl)-1*H*-benzo[d][1,2,3]triazole-based Inhibitors of Cu-only SOD5

Compound **5.1** exhibited the highest inhibition activity from the library screening with an IC_{50} value of 0.334 μ M. The synthetic scheme to prepare compound **5.1** is shown in Figure 5.8. Benzotriazole was synthesized through the reaction of nitrite with 2,3-diaminobenzene under acidic condition. Subsequently, the tetrazole moiety was prepared from nitriles via 1,3-dipolar cycloaddition. The detailed synthetic procedures and the complete characterization of compound **5.1** can be found in the Appendix to Chapter 5.

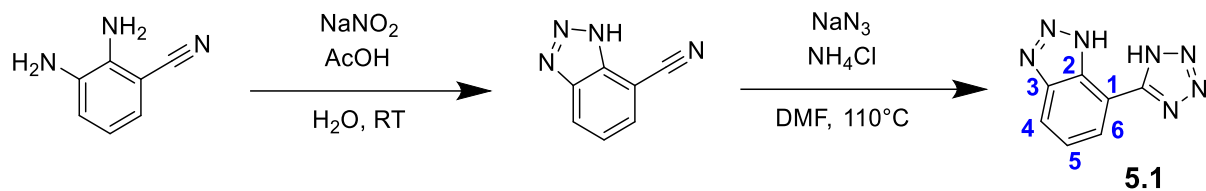


Figure 5.8. Synthetic scheme of compound **5.1**.

For derivatization, given that all three positions of the phenyl ring in compound **5.1** are solvent-exposed according to the docking results (Figure 5.7). Unfortunately, there are limited synthetic reports and few commercially available sources for making derivatives of **5.1**. Based on these limitations, we chose to expand on the 6-position of benzene in compound **5.1**. Specifically, we utilized 2,6-dichloro-3-nitrobenzonitrile as the starting material, as outlined in the suggested synthetic scheme (Figure 5.9). The successful synthesis of 2-amino-6-chloro-3-nitrobenzonitrile was achieved by reacting 2,6-dichloro-3-nitrobenzonitrile with NH_3 in ethanol, in a 70% yield. Unfortunately, the subsequent step to prepare derivatized 2-chloro-3-nitrobenzonitrile via Suzuki coupling reaction failed under various conditions. A major byproduct observed was biphenyl, likely resulting from the homocoupling of phenylboronic acid.²⁷

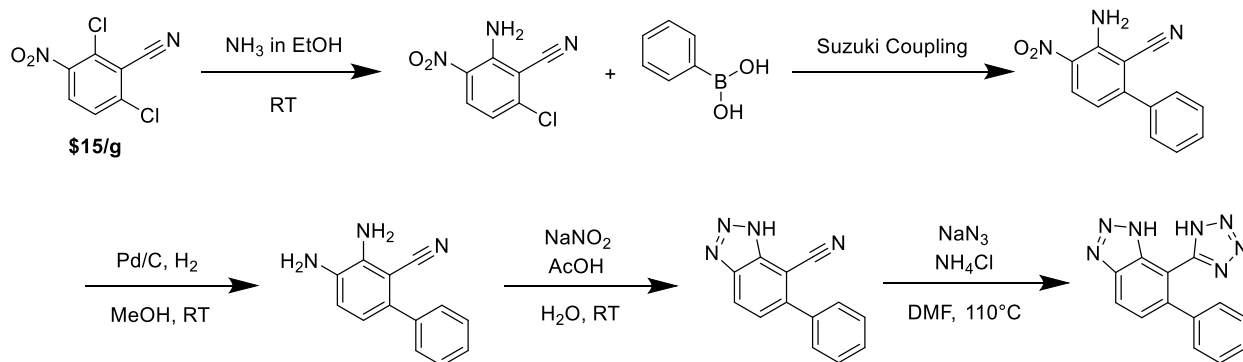


Figure 5.9. Proposed synthetic scheme for derivatization of compound **5.1** at the 6-position. The step for Suzuki coupling reaction did not work under different conditions: (1) $\text{Pd}(\text{PPh}_3)_4$, tetrakis(triphenylphosphine)palladium(0), Na_2CO_3 , (2) $\text{Pd}(\text{PPh}_3)_4$, SPhos Pd G3, Na_2CO_3 , (3) $\text{Pd}(\text{OAc})_2$, tri(*o*-tolyl)phosphine, CsF.

As we encountered challenges in preparing derivatives of compound **5.1**, we explored MBIs of compound **5.1** to identify alternative starting compounds. The tetrazole moiety was substituted by carboxylic acid, hydroxamic acid ester, and oxetane, while for the benzotriazole moiety, imidazole, carbamate, sulfonamide, and hydroxyl group were selected as isostere replacements (Figure 5.10). The MBIs of compound **5.1** were synthesized in a few steps from widely available starting materials using established synthetic methods reported by Jackl et al.²⁸ In addition, compounds **5.21** (1*H*-benzo[d][1,2,3]triazole) and **5.22** (5-phenyl-1*H*-tetrazole) were prepared as control compounds to assess the activity of each component part of compound **5.1** on Cu-only SOD5.

Initially, the MBIs of compound **5.1** were screened against Cu-only SOD5 at 200 μ M. The results indicated that MBIs **5.4** – **5.6** containing the tetrazole moiety showed high inhibition activity, except for MBI **5.7** containing the sulfonamide group, suggesting the necessity of the tetrazole moiety to maintain potency. Similarly, some MBIs with benzotriazole (**5.8** and **5.13**) exhibited significantly higher % inhibition (~55%) compared to those with imidazole, carbamate, hydroxyl, and sulfonamide groups. However, despite the presence of tetrazole or benzotriazole moieties in some MBIs, none of them demonstrated a better inhibition activity (<65% at 200 μ M) compared to compound **5.1** (100% at 200 μ M). Interestingly, the fragment parts of compound **5.1**, **5.21** (benzotriazole) and **5.22** (tetrazole), exhibited a significant loss of activity with <10% inhibition. This suggests that both moieties of compound **5.1**, benzotriazole and tetrazole, are necessary to retain high potency for Cu-only SOD5. Although we were unable to identify a better scaffold to substitute compound **5.1**, the structural novelty of compound **5.1** and its high activity ($IC_{50} = 0.334 \mu$ M) suggest that further investigation of the compound as a Cu-only SOD5 inhibitor is needed.

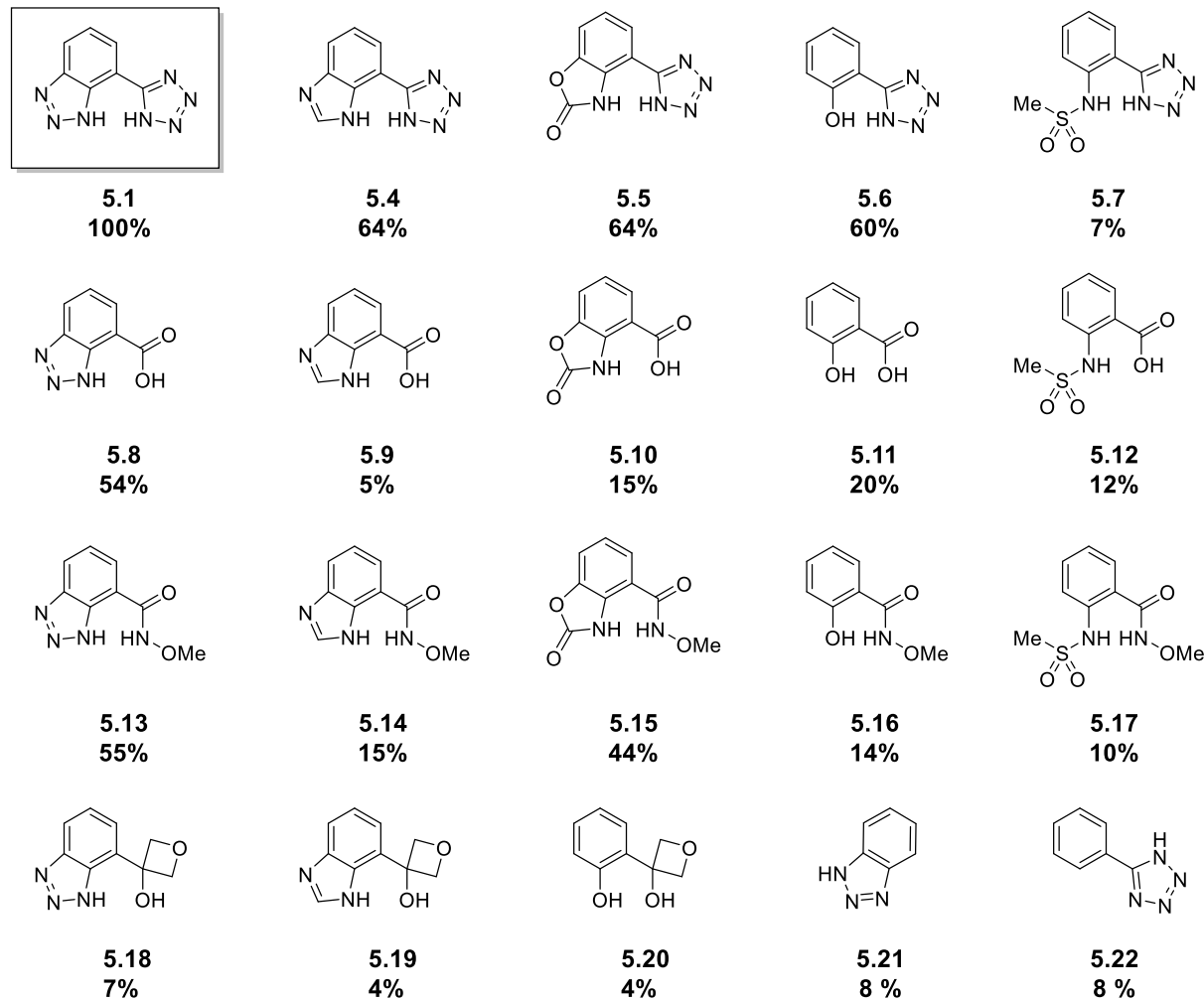


Figure 5.10. Chemical structures and labeling for MBIs of compound **5.1** (*top*) and percent inhibition against SOD5 at a concentration of 200 μ M (*bottom*). The tetrazole and benzothiazole moieties were replaced with their isosteres and their combinations were synthesized as MBIs. Fragment parts of compound **5.1**, 1*H*-benzo[d][1,2,3]triazole (**5.21**) and 5-phenyl-1*H*-tetrazole (**5.22**), were included in the library for screening.

5.3.2 1-Hydroxypyridine-2(1*H*)-thione (1,2-HOPTO)-based Inhibitors of Cu-only SOD5

1,2-HOPTO has been identified as an inhibitor for Cu-only SOD5;¹² however, its derivatives have not been extensively explored. The docking results shown in Figure 5.7 indicate that all positions are viable for modification, leading to further exploration of derivatization at 3-position of 1,2-HOPTO based on synthetic accessibility. Screening a sublibrary of 1,2-HOPTO

derivatives with substituents at the 3-position revealed that sulfonamide derivatives at the 3-position (**5.25** and **5.26**) significantly enhance activity compared to other functional groups such as amides (**5.23** and **5.24**) at the same position (Table 5.2). Consequently, sulfonamide derivatives of 1,2-HOPTO were further studied to identify suitable derivatives as warheads for Cu-only SOD5 inhibition.

The synthetic route for preparing sulfonamide derivatives of 1,2-HOPTO is detailed in Figure 5.11, and the procedure was modified from the work of Adamek et al.²⁹ The desired sulfonamide products were obtained by reacting sulfonyl chloride with 2-bromopyridin-3-amine in pyridine, using a microwave reactor. Note that disulfonamides (see Figure 5.12) were produced as a major byproduct in this reaction when an excess of sulfonyl chloride was used. To prevent this side reaction, an equimolar amount of sulfonyl chlorides (1.0 eq) was slowly added to a slight excess of 2-bromopyridin-3-amine (1.3 eq). The formation of disulfonamide byproducts was still observed and the formation of these byproducts was governed by the electrophilicity of the sulfonyl chloride used. In cases where disulfonamides were formed as byproducts, the final products were successfully isolated using column purification with a 100% DCM eluent system. Subsequent oxidation using mCPBA achieved selective oxidation at the pyridine nitrogen. This step required long reaction times, up to 108 hours. Two-steps column purification was employed to isolate the product, initially running a gradient from 100% hexanes to 50% ethyl acetate, followed by 100% DCM to 5% MeOH.

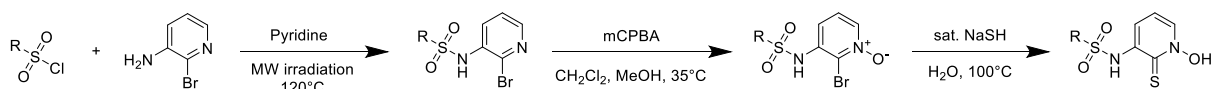


Figure 5.11. Synthetic scheme for sulfonamide derivatives of 1,2-HOPTO.

Subsequently, thionation of the oxidized products was accomplished by heating them in a freshly prepared saturated NaSH solution. The reaction mixture was quenched with aqueous HCl, followed by a subsequent work-up process. During this step, we found that products containing a 1-hydroxypyridin-2(1*H*)-one heterocycle (HOPOs, Figure 5.12), which possess a carbonyl (C=O) group instead of the desired thione (S=O), were generated as a major byproduct. The final desired products (HOPTOs) were isolated from the byproduct (HOPOs) by running reverse-phase column chromatography with a gradient of 100% H₂O to 100% acetonitrile with 0.1% formic acid. When necessary, the collected products underwent further purification via normal-phase column chromatography using a gradient from 100% DCM to 10% MeOH, or from 50% hexane to 100% ethyl acetate. Isolating the desired final products using column chromatography proved challenging for some compounds despite numerous attempts. Specifically, we observed that metal complexes formed on the column with the HOPTO compounds and co-eluted with the desired products (particularly during normal-phase column chromatography, Figure 5.12). The blue-colored metal complexes may have been formed by the final ligand eluting with trace amounts of metal present in the stationary phase (e.g., silica column), which impaired the complete isolation of the desired product. Furthermore, residual impurities were identified for some compounds after running reverse-phase column chromatography. It has been reported that pyridiones, including 1,2-HOPTO, could transform into copper- or iron-containing complexes or disulfide oxidized products, depending on the type of the stationary phase used in chromatographic analysis such as HPLC.³⁰ This behavior of pyridiones in chromatography may contribute to the complexity of the purification process. Ultimately, the combination of major byproducts such as HOPOs and a complicated purification process resulted in fewer compounds being prepared with a low yield (15-32%) for the sub-library of sulfonamide 1,2-HOPTOs than initially planned.

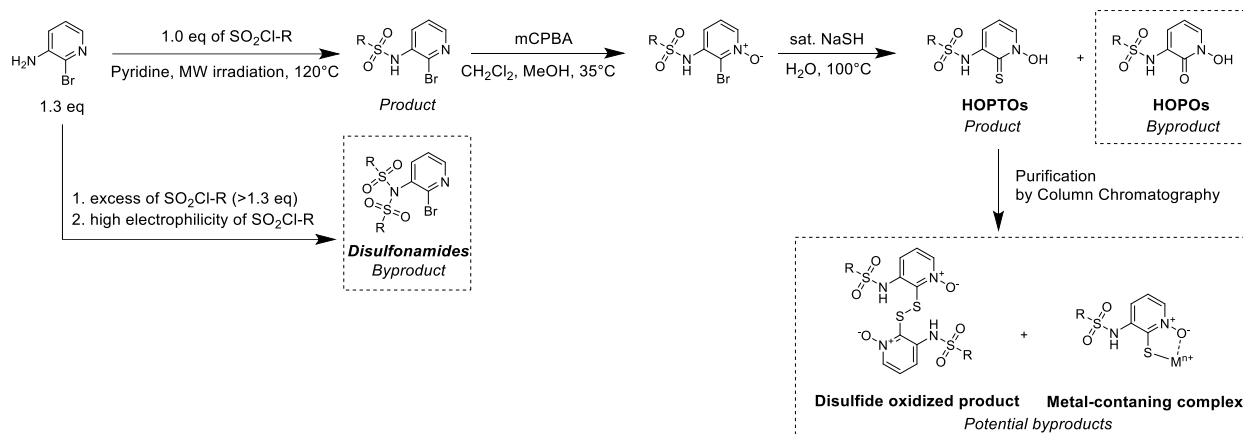
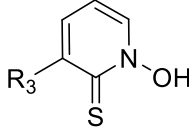
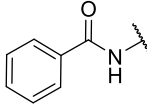
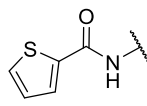
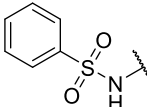
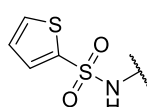
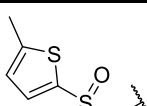
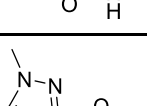
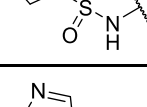
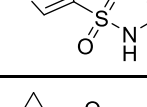


Figure 5.12. Synthetic pathway illustrating the challenges in the preparation of sulfonamide derivatives of 1,2-HOPTO. This figure outlines each reaction step, conditions, and the resulting products and byproducts.

Using the aforementioned synthetic method, six heterocyclic sulfonamide 1,2-HOPTO derivatives were prepared to identify heterocyclic substituents that enhanced the activity of the parent MBP (Table 5.2). Specifically, substitutions with thiophene, pyrazole, and cyclopropane were explored. Replacement of the benzyl group (**5.25**) with thiophene (**5.26**) resulted in about 2-fold increase in inhibition activity. Methyl thiophene (**5.27**) also exhibited enhanced activity, though not to the same extent as the thiophene moiety itself. Among the pyrazole derivatives, compound **5.28** demonstrated equivalent inhibition to the benzyl derivative, whereas compound **5.29** showed a decrease in activity by almost half, highlighting the impact of the methyl group and nitro atom on potency. Conversely, cyclopropane substitution (**5.30**) led to a significant loss of inhibition activity, underscoring the potential importance of an aromatic group in this position to maintain potency.

Table 5.2. IC₅₀ values of compound 1,2-HOPTO and its derivatives against Cu-only SOD5. IC₅₀ values reported in μM with the 95% confidence interval indicated.

		
Compound	R ₃	IC ₅₀ (μM)
1,2-HOPTO	H	0.579±0.059
5.23		>50 μM
5.24		>50 μM
5.25		0.191±0.016
5.26		0.110±0.013
5.27		0.165±0.011
5.28		0.197 ± 0.021
5.29		0.332 ± 0.020
5.30		0.676 ± 0.052

These findings suggest that sulfonamide derivatives of 1,2-HOPTO may prove useful as inhibitors for Cu-only SOD5. Among the compounds evaluated, compound **5.26** emerged as the most potent, achieving an IC₅₀ value of 0.110 μM, which is comparable to that of the known

inhibitor, Zn-pyrithione ($IC_{50} = 0.111 \mu M$). Furthermore, exploring modifications to compound **5.25** is a promising avenue for enhancing potency, based on the availability of more accessible synthetic approaches for expanding derivatives on the benzyl group. Nevertheless, it is crucial to address the existing challenges in synthesis and purification of sulfonamide HOPTOs to fully explore their potential as SOD5 inhibitors.

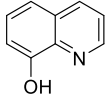
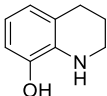
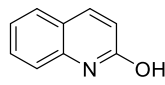
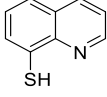
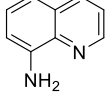
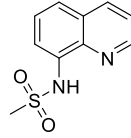
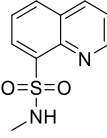
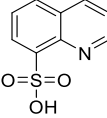
5.3.3 8-Hydroxyquinoline (8-HQ)-based Inhibitors of Cu-only SOD5

8-HQ demonstrated an IC_{50} value of $1.244 \mu M$ for Cu-only SOD5. Clioquinol and chloroxine (Figure 5.3) are FDA-approved antifungal drugs that are also reported to inhibit Cu-only SOD5; both of these compounds also possess a 8-HQ core. However, comprehensive SAR studies and further derivatization of 8-HQ for inhibitors of SOD5 have not been reported.

Initially, compounds **5.31** – **5.37** were introduced into the library to conduct preliminary SAR analysis (Table 5.3). They were screened to verify the metal binding interaction of 8-HQ with the copper ion in the active site and to validate the potency of the parent compound against Cu-only SOD5. The percent inhibition activity at $20 \mu M$ and IC_{50} values are presented in Table 5.3. Notably, replacing the pyridine part of quinoline with piperidine (**5.31**) resulted in a loss of activity, indicating the significance of maintaining the aromaticity of the parent compound. Compound **5.32**, which moved the hydroxyl group to the 2-position, completely lost activity, underscoring the crucial requirement of the hydroxyl group at the 8-position. Moreover, various substitutions of the hydroxyl group with other isosteric or different functional groups (**5.33** – **5.37**) also exhibited a loss of activity, highlighting the importance of the hydroxyl group which may contribute to the metal binding in the active site. These findings underscore the necessity for 8-

HQ to retain activity against Cu-only SOD5 as a core compound, reaffirming its potential as a promising scaffold for modification.

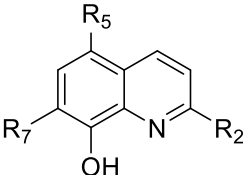
Table 5.3. Percent inhibition and IC₅₀ values of 8-HQ derivatives against Cu-only SOD5.

Compound	Compound	%Inhibition at 20μM, IC ₅₀ (μM)
8-HQ		100 % 1.244 ± 0.06 μM
5.31		0 %
5.32		0 %
5.33		41 %
5.34		5 %
5.35		100 % > 5 μM
5.36		7 %
5.37		13 %

To determine suitable positions for derivatization, a preliminary SAR analysis using a sublibrary of 8-HQ derivatives was performed (Table 5.4). The library encompasses small substituents at 2-, 5-, or 7-positions, including methyl, amine, carboxylic acid, and sulfonic acid. The screening result is detailed in Table 5.4 and Table 5.5. None of the compounds with

substituents at the 2-position (**5.38** – **5.41**) showed improved activity. Considering the possible steric constraints at this position of 8-HQ in the docking result (Figure 5.5), further derivatives at this site were not pursued. Similarly, no improvements were observed for compounds derived at the 7-position. Among the derivatives at the 7-position, the addition of a bromo group to the parent scaffold (**5.45**) exhibited greater activity compared to the other substituents at the 7-position (**5.42** – **5.44**), with IC₅₀ values ranging from 5 to 10 μM. By contrast, the introduction of an amine (**5.43**) and carboxylic acid group (**5.44**) resulted in complete loss of potency at 20 μM. This analysis suggests that solely adding substituents either at 2- or 7-positions does not lead to improved activity.

Table 5.4. IC₅₀ values of 8-HQ and its derivatives with 2- or 7-position substituents against Cu-only SOD5. IC₅₀ values reported in μM with the 95% confidence interval indicated.



Compound	R ₂	R ₅	R ₇	IC ₅₀ (μM)
8-HQ	H	H	H	1.244 ± 0.061
5.38	CH ₃	H	H	> 20
5.39	NH ₂	H	H	> 1.5
5.40	CO ₂ H	H	H	> 1.5
5.41	SO ₃ H	H	H	> 20
5.42	H	H	CH ₃	~ 10
5.43	H	H	NH ₂	> 20
5.44	H	H	CO ₂ H	> 20
5.45	H	H	Br	5 – 10

Evaluation of the sublibrary with substituents at the 5-position revealed improved inhibition activity, suggesting it as a promising position for modification (Table 5.5). Notably, amine substituent at the 5-position (**5.46**) abolished inhibition activity and nitro group (**5.50**) also affected the activity, with an IC₅₀ of ~5 μM. However, carboxylic acid (**5.47**) and chloride groups

(**5.49**) had no or only slight improvement on activity, while the addition of sulfonic acid (**5.48**) enhanced potency by ~2-fold, with an IC_{50} value of 0.575 μ M. Further analysis revealed that derivatives exhibiting improved or similar inhibition activity displayed decreased pK_a values for hydroxyl and nitrogen of the parent compound (Table 5.6), suggesting that substituents at the 5-position alter the electronic properties and enhancing acidity might improve potency. Notably, the introduction of a strong electron-withdrawing nitro group at the 5-position (**5.50**) led to increased acidity but did not correlate with improved potency, indicating the importance of maintaining optimal pK_a values (~8.5 for hydroxyl and ~3.5 for nitrogen) for enhanced activity.

Based on the preliminary SAR analysis, derivatives both at 5- and 7- positions were further explored. The addition of iodine at the 7-position of 5-chloro-8-hydroxyquinoline (**5.52**) doubled the inhibition activity compared to 5-chloro-8-hydroxyquinoline (**5.49**, $IC_{50} = 1.159 \mu$ M), resulting in high potency with an IC_{50} value of 0.408 μ M. Conversely, the introduction of an amino group (**5.53**) completely abolished the inhibition activity. This difference may be attributed to electronic disparities arising from different substituents. Upon adding iodine to the 7-position, the pK_a of both the hydroxyl and nitrogen groups decreased, while the addition of the amino group slightly increased the pK_a of both groups (Table 5.6). Hence, the increased acidity might positively impact the inhibition potency when substituents are placed at 7-position of 5-chloro-8-hydroxyquinoline (**5.49**).

Table 5.5. IC₅₀ values of compound **3** and its derivatives at 5- or 5,7-positions against Cu-only SOD5. IC₅₀ values reported in μM with the 95% confidence interval indicated.

No.	R ₂	R ₅	R ₇	IC ₅₀ (μM)
8-HQ	H	H	H	1.244 ± 0.061
5.46	H	NH ₂	H	> 20
5.47	H	CO ₂ H	H	1.050 ± 0.149
5.48	H	SO ₃ H	H	0.575 ± 0.041
5.49	H	Cl	H	1.159 ± 0.074
5.50	H	NO ₂	H	~ 5
5.51	H	SO ₃ H	I	0.617 ± 0.056
5.52	H	Cl	I	0.408 ± 0.021
5.53	H	Cl	NH ₂	> 20

Table 5.6. Calculated pK_a values of 8-HQ derivatives. Calculated pK_a values were obtained using Marvin (ChemAxon) software package. ND = Not Defined in the range of pH 0–14.

No.	R ₂	R ₅	R ₇	pK _{a1}	pK _{a2}
3	H	H	H	4.83	9.36
5.38	CH ₃	H	H	5.42	9.38
5.39	NH ₂	H	H	6.34	9.35
5.40	CO ₂ H	H	H	ND	9.35
5.41	SO ₃ H	H	H	ND	9.22
5.42	H	H	CH ₃	5.35	9.56
5.43	H	H	NH ₂	6.81	9.29
5.44	H	H	CO ₂ H	2.77	10.73
5.45	H	H	Br	4.06	7.59
5.46	H	NH ₂	H	5.45	9.20
5.47	H	CO ₂ H	H	2.63	8.97
5.48	H	SO ₃ H	H	3.55	8.45
5.49	H	Cl	H	4.01	8.37
5.50	H	NO ₂	H	1.92	6.89
5.51	H	SO ₃ H	I	2.82	7.42
5.52	H	Cl	I	3.28	7.34
5.53	H	Cl	NH ₂	6.06	8.73

In summary, our preliminary SAR study underscores the potential of 8-HQ as a scaffold for further lead development, suggesting synthetic modifications at the 5-position as particularly promising. The incorporation of halogen groups such as iodine at the 7-position could be a potential strategy to enhance activity. Among the derivatives, those with sulfonic acid at the 5-position exhibited superior potency. However, the sulfonic acids may have problems entering fungal cells due to its strongly acidic nature and the possibility of subsequent ionization at biological pH.³¹⁻³² Therefore, exploring sulfonamide derivatives as an alternative could mitigate this problem by acting as weak acids and offer a wide range of substituents with accessible synthetic routes,³³ paving the way for the development of effective Cu-only SOD5 inhibitors.

5.4 Future Work

Going forward, inhibitors developed in this effort will be tested using in vitro and animal infection models, in collaboration with the Culotta group at Johns Hopkins University. Details regarding the cell-culture and animal model-based evaluation of Cu-only SOD5 inhibitors are outlined as future work.

Fungal Cultures. Both *C. albicans* and *C. auris* secrete Cu-only SODs into the growth media and these SODs can be monitored by subjecting the growth media to immunoblots and a native gel assay for SOD activity.^{5, 16} Therefore, Inhibitor efficacy is defined by undetectable SOD activity in the native gel assay with no change in SOD protein levels by immunoblot, with Zn-pyridithione as a control for Cu-only SODs.¹² We will examine activity against intracellular Cu/Zn-SOD1³⁴ that should not be affected by selective inhibitors. These studies are expected to reveal inhibitors that effectively inactivate native, Cu-only SODs from live fungal cultures.

***C. albicans* Infection of Macrophages.** The Cu-only SODs of *C. albicans* have been shown in numerous studies to remove superoxide produced by macrophages and neutrophils and guard fungal killing by these phagocytes.^{6-8, 12, 35} The effect of fungal Cu-only SODs on phagocyte superoxide production can be monitored in a luminol assay for ROS. When J774A macrophages are infected with live fungal cells or incubated with zymosan (fungal cell wall material), they begin to produce ROS within minutes. The ROS production triggered by fungal cells is greatly enhanced when the macrophage is infected with a *sod4 sod5* mutant of *C. albicans*. This enhancement in ROS reflects the inability of the fungus lacking Cu-only SODs to remove superoxide produced by the macrophage. By comparison, loss of the intracellular fungal Cu/Zn-SOD1 has no effect on macrophage ROS. Only extracellular Cu-only SODs and not intracellular SODs of the fungus can remove superoxide from host immune cells. Therefore, macrophage ROS is a reliable functional assay for fungal Cu-only SOD activity. Using this assay, the efficacy of inhibitors will be tested to block Cu-only SODs during infection.

Animal Model of Infection. The efficacy of lead inhibitors will be further tested in mouse models. The mouse model of disseminated candidiasis is routinely used, whereby *C. albicans* is injected via lateral tail vein, and within 12 h, the pathogen disseminates to tissues with kidney as primary target.^{34, 36-38} The mouse succumbs to lethal candidiasis with a mean survival time of 7 d. Macrophages and neutrophils represent key host defenses in this model and it is therefore not surprising that Cu-only SODs are important for virulence.^{11, 39} The disseminated mouse model for candidiasis represents a good starting point to examine the effect of Cu-only SOD inhibitors on fungal infection in vivo.

5.5 Acknowledgements

Chapter 5 contains unpublished material that was written with Valeria Culotta and Seth M. Cohen. The dissertation author was the primary author of this chapter. We acknowledge Alysia J. Kohlbrand for the preparation of Cu-only SOD5 and the effort for X-ray crystallography. This chapter, in part, is a reprint of the material as it appears in “Salicylate metal-binding Isosteres as fragments for metalloenzyme Inhibition.” *Chem. Sci.* **2022**, 13, 7, 2128. The dissertation author was a primary author of this paper and gratefully acknowledges the contributions of coauthors Moritz K. Jackl, Mark Kalaj, and Seth M. Cohen.

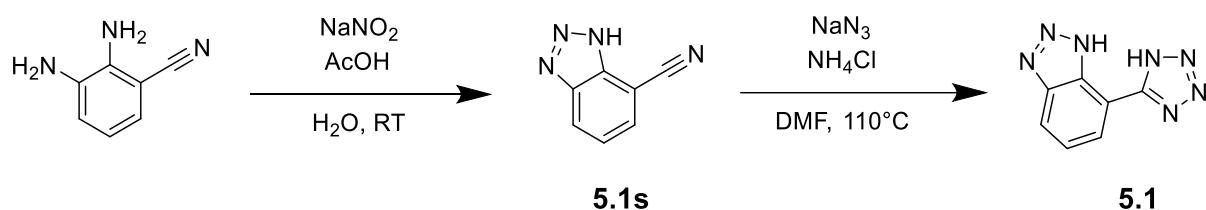
5.6 Appendix: Supporting Information

General Experimental Details

All solvents and reagents, unless otherwise noted, were obtained from commercial sources (Sigma Aldrich, Alfa Aesar, TCI, Combi-Blocks etc.) and used without further purification. All reactions, unless otherwise stated, were performed under a nitrogen atmosphere. Silica chromatography was performed using a CombiFlash Rf Teledyne ISCO system or Biotage® Selekt flash purification system using hexane, ethyl acetate, methylene chloride (DCM), or methanol (MeOH) as eluents. C₁₈ reverse phase chromatography was performed using the same instruments using 0.1% formic acid in acetonitrile or water as eluent. ¹H and ¹³C NMR spectra were recorded at ambient temperature on 300 MHz Bruker, 400 MHz Jeol NMR instrument, or 500 MHz Varian NMR instrument in the Department of Chemistry and Biochemistry at the University of California, San Diego. Processing of the NMR data was performed using the MestReNova 14.2 program. High resolution mass spectrometry (HRMS) analysis was performed using an Agilent 6230 accurate-mass liquid chromatography time-of-flight mass spectrometry

LC-TOFMS at the Molecular Mass Spectrometry Facility (MMSF) in the Department of Chemistry and Biochemistry at the University of California, San Diego.

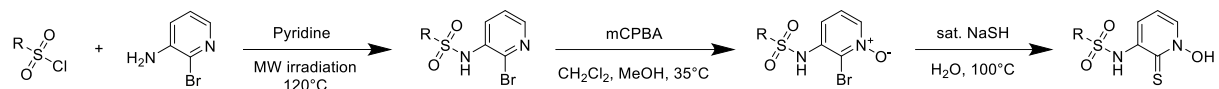
Synthesis of Compounds



1H-benzo[d][1,2,3]triazole-7-carbonitrile (5.1s). 2,3-diaminobenzonitrile (500 mg, 1 Eq, 3.76 mmol) was dissolved in water (3 mL) and AcOH (2 mL) and stirred for 5 min. A solution of sodium nitrite (311 mg, 1.2 Eq, 4.51 mmol) in water (2 mL) was added drop-wise to the stirring solution and the resulting suspension was stirred for 18 h at room temperature. The resulting brown solid was filtered off, washed with water, and dried under high vacuum. Isolated as a brownish solid. Yield: 332 mg (61%). ¹H NMR (300 MHz, DMSO-*d*₆): δ 8.28 (d, J = 8.0 Hz, 1H), 8.04 (d, J = 7.1 Hz, 1H), 7.63 (d, J = 7.2 Hz, 1H).

7-(1H-tetrazol-5-yl)-1H-benzo[d][1,2,3]triazole (5.1). 1H-benzo[d][1,2,3]triazole-7-carbonitrile (400 mg, 1 Eq, 2.78 mmol), ammonium chloride (297 mg, 2 Eq, 5.55 mmol) and sodium azide (361 mg, 2 Eq, 5.55 mmol) were suspended in DMF and the resulting mixture was stirred at 110 °C for 72 h. All volatiles were removed under reduced pressure. The resulting solid was suspended in water and dissolved partially. The solution was acidified to pH~3 resulting in larger amounts of solid crushing out. Yield: 444 mg (86%). ¹H NMR (300 MHz, DMSO-*d*₆): δ 8.19 – 8.11 (m, 2H), 7.61 (t, J = 7.9 Hz, 1H); ¹³C NMR (100 MHz, DMSO-*d*₆): δ 153.89, 125.18, 124.79, 122.51, 118.98, 116.08, 111.80; HRMS (ESI): calculated for [C₇H₄N₇]⁻: *m/z* = 186.0534, found: *m/z* = 186.0531.

General Synthesis for Sulfonamide HOPOs (5.23 – 5.30)



Sulfonamide coupling. The synthetic procedure was modified from the work of Adamek et al.²⁹ To a solution of starting amine (1.3 eq) in 2 mL dry pyridine, sulfonyl chloride (1.0 eq) was added. The mixture was placed in a microwave reactor and irradiated at 120 °C for 5-15 min. Upon cooling, the reaction mixture was diluted with 15 mL ethyl acetate, and washed with 2×15 mL 4M HCl. The combined organic phase was washed with brine, dried over magnesium sulfate, and the solids were filtered off and discarded. The filtrate was concentrated under reduced pressure, and the resulting crude was purified by column chromatography, running gradient from either 100 % hexane to 100 % ethyl acetate or 100% DCM. Fractions were combined and concentrated under reduced pressure to obtain the desired sulfonamide product that was used directly in the subsequent step.

Oxidation. To a solution of products from the sulfonamide coupling (1.0 eq) in 5 mL chloroform, a solution of mCPBA (3 eq) in 5 mL Chloroform was added. The reaction mixture was then stirred at RT for 72-108 h. Upon completion, the reaction mixture was concentrated under reduced pressure, and the resulting crude was purified by column chromatography, running gradient first from 100 % hexanes to 50 % ethyl acetate, and then from 100 % DCM to 5 % MeOH. Fractions were combined and concentrated under reduced pressure to obtain the desired oxidized product that was used directly in the subsequent step.

Thionation. The starting material was dissolved in 20 mL of water and 20 mL of saturated sodium hydrogen sulfide solution (excess). The reaction mixture was stirred at RT for 16 h. Upon reaction completion as indicated by TLC, the reaction mixture was slowly quenched with 6M HCl. CAUTION - The neutralization of NaSH using acid generates H₂S gas, which is both highly

flammable and highly toxic by inhalation; only perform neutralization in a well-vented fume hood. After waiting ~10 minutes to allow the resultant H₂S gas to evolve and disperse, the resulting mixture was extracted into organic using 3×15 mL ethyl acetate. Then the combined organic layer was washed with brine, dried over magnesium sulfate, and the solids were filtered off and discarded. The filtrate was concentrated under reduced pressure, and the remaining residue was then purified by reversed-phase column chromatography, using a gradient of 100 % H₂O to 100 % acetonitrile with 0.1% formic acid. When necessary, the collected products were further purified by normal-phase column chromatography, using a gradient from 100 % DCM to 10 % MeOH or from 50 % hexane to 100 % ethyl acetate. Yield: 15-32%.

N-(1-hydroxy-2-thioxo-1,2-dihydropyridin-3-yl)benzenesulfonamide (5.25). Following the above general synthesis for sulfonamide HOPOs. Yield: 27%. ¹H NMR (400 MHz, DMSO-*d*₆): δ 9.45 (s, 1H), 8.13 (dd, J = 6.9, 1.3 Hz, 1H), 7.87 (dd, J = 8.3, 1.3 Hz, 2H), 7.67 (s, 1H), 7.56 (ddd, J = 15.0, 7.4, 1.5 Hz, 3H), 6.83 (dd, J = 8.0, 6.9 Hz, 1H). ¹³C NMR (126 MHz, DMSO-*d*₆): δ 163.48, 138.30, 137.14, 133.99, 133.30, 129.62, 127.01, 118.44, 112.47. HRMS (ESI): calculated for [C₁₁H₉N₂O₃S₂]⁻: *m/z* = 281.0134, found: *m/z* = 281.0131.

N-(1-hydroxy-2-thioxo-1,2-dihydropyridin-3-yl)thiophene-2-sulfonamide (5.26). Following the above general synthesis for sulfonamide HOPOs. Yield: 28%. ¹H NMR (400 MHz, DMSO-*d*₆): δ 9.52 (d, J = 3.4 Hz, 1H), 8.19 (ddd, J = 6.8, 3.1, 1.5 Hz, 1H), 8.02 – 7.96 (m, 1H), 7.74 (tt, J = 3.7, 1.6 Hz, 1H), 7.60 (ddd, J = 7.8, 3.2, 1.5 Hz, 1H), 7.15 (td, J = 4.8, 2.6 Hz, 1H), 6.89 (ddt, J = 7.5, 4.4, 2.2 Hz, 1H). ¹³C NMR (126 MHz, DMSO-*d*₆): δ 164.04, 138.42, 137.20, 135.31, 134.38, 133.82, 128.43, 119.50, 112.85. HRMS (ESI): calculated for [C₉H₇N₂O₃S₃]⁻: *m/z* = 286.9624, found: *m/z* = 286.9626.

N-(1-hydroxy-2-thioxo-1,2-dihydropyridin-3-yl)-5-methylthiophene-2-sulfonamide (5.27).

Following the above general synthesis for sulfonamide HOPOs. Yield: 25%. ¹H NMR (400 MHz, DMSO-*d*₆): δ 12.94 (s, 1H), 9.45 (s, 1H), 8.18 (dd, *J* = 6.8, 1.4 Hz, 1H), 7.61 – 7.55 (m, 2H), 6.92 – 6.86 (m, 2H), 2.45 (d, *J* = 1.0 Hz, 4H). ¹³C NMR (126 MHz, DMSO-*d*₆): δ 163.66, 149.31, 136.99, 134.91, 134.39, 133.47, 126.65, 118.34, 112.46, 15.23. HRMS (ESI): calculated for [C₁₀H₉N₂O₃S₃]⁻: *m/z* = 300.9781, found: *m/z* = 300.9780.

N-(1-hydroxy-2-thioxo-1,2-dihydropyridin-3-yl)-1-methyl-1H-pyrazole-3-sulfonamide

(5.28). Following the above general synthesis for sulfonamide HOPOs. Yield: 30%. ¹H NMR (400 MHz, DMSO-*d*₆): δ 9.31 (s, 1H), 8.14 – 8.07 (m, 1H), 7.84 (d, *J* = 3.3 Hz, 1H), 7.54 – 7.48 (m, 1H), 6.83 (dq, *J* = 7.8, 4.5 Hz, 1H), 6.75 (d, *J* = 3.3 Hz, 1H), 3.86 – 3.81 (m, 4H). ¹³C NMR (126 MHz, DMSO-*d*₆): δ 162.84, 147.75, 137.29, 133.64, 132.76, 117.06, 112.50, 107.48. HRMS (ESI): calculated for [C₉H₉N₄O₃S₂]⁻: *m/z* = 285.0122, found: *m/z* = 285.0122.

N-(1-hydroxy-2-thioxo-1,2-dihydropyridin-3-yl)-1-methyl-1H-pyrazole-4-sulfonamide

(5.29). Following the above general synthesis for sulfonamide HOPOs. Yield: 32%. ¹H NMR (400 MHz, DMSO-*d*₆): δ 9.25 (d, *J* = 3.5 Hz, 1H), 8.48 – 8.43 (m, 1H), 8.15 (ddd, *J* = 6.8, 2.9, 1.5 Hz, 1H), 7.88 – 7.84 (m, 1H), 7.54 (ddt, *J* = 6.7, 3.0, 1.5 Hz, 1H), 6.87 (ddt, *J* = 9.9, 4.7, 2.3 Hz, 1H), 3.85 – 3.80 (m, 3H). ¹³C NMR (126 MHz, DMSO-*d*₆): δ 163.21, 138.46, 137.40, 133.61, 132.91, 119.58, 117.54, 112.65. HRMS (ESI): calculated for [C₉H₉N₄O₃S₂]⁻: *m/z* = 285.0122, found: *m/z* = 285.0121.

N-(1-hydroxy-2-thioxo-1,2-dihydropyridin-3-yl)cyclopropanesulfonamide (5.30).

Following the above general synthesis for sulfonamide HOPOs. Yield: 15%. ¹H NMR (400 MHz, DMSO-*d*₆): δ 12.88 (s, 1H), 8.96 (s, 1H), 8.23 (dd, *J* = 6.8, 1.4 Hz, 1H), 7.60 (dd, *J* = 7.9, 1.4 Hz, 1H), 6.91 (dd, *J* = 7.9, 6.8 Hz, 1H), 2.85 (tt, *J* = 7.8, 4.9 Hz, 1H), 1.08 – 0.95 (m, 5H). ¹³C NMR (126

MHz, DMSO-*d*₆): δ 163.32, 137.95, 132.70, 118.62, 112.57, 30.11, 5.53. HRMS (ESI): calculated for [C₈H₉N₂O₃S₂]⁻: m/z = 245.0060, found: m/z = 245.0061.

Fragment Docking

The hit compounds (**5.1**, 1,2-HOPTO, and 8-HQ) were docked using the Molecular Operating Environment (MOE, Chemical Computing Group ULC, Montreal, QC, Canada, 2019) software package. Cu-only SOD5 (PDB 4N3U) was downloaded from the Protein Data Bank (<https://www.rcsb.org/>) and prepared in MOE. Water molecules, other small molecules as well as ions were removed. Hydrogen atoms were added, and the side chains protonated at physiological pH. The pharmacophore models were created between the Cu ion at the active site and metal-binding donors of fragments considering their potential metal-binding interaction. The fragments were docked into the binding site with the pharmacophore model predicting 100 binding poses and the binding poses with the best score were shown in this work.

Expression and Purification of Cu-only SOD5

The protein was expressed and purified according to published procedures.² DNA encoding *C. albicans* superoxide dismutase 5 (SOD5) residues 27–181 lacking the N-terminal secretion sequence and C-terminal cell wall anchor, subcloned into expression vector pAG8H was a generous gift from Prof. Valaria Culotta (Johns Hopkins University). The plasmid was transformed into *E. coli* strain Lemo21 (DE3). Cells harboring the expression plasmid were grown at 37 °C until they reached an A₆₀₀ of 0.6 - 0.8; at that time, the temperature was lowered to 16 °C and expression was induced by the addition of isopropyl β -D-thiogalactoside to a final concentration of 1 mM. Cells were harvested by centrifugation 16 h after induction and frozen at

-20 °C. After thawing on ice, the cell paste was resuspended in 50 mM Tris (pH 8.0), 400 mM NaCl, and protease inhibitor mixture (Sigma); lysed through shearing methods such as microfluidization or pushing the suspension through an 18G needle on ice; and centrifuged. The supernatant was discarded, and the pellet was resuspended in the same buffer, followed by another round of centrifugation to remove all soluble proteins. The pellet was again resuspended at 4 °C in 50 mM Tris (pH 8.0), 8 M urea, and 1.5 mM reduced glutathione. The mixture was centrifuged, and denatured SOD5 protein was refolded by dialysis overnight against 50 mM Tris (pH 8.0) and 0.25 mM oxidized glutathione. During this step, the SOD5 protein partitioned into a major fraction of properly folded SOD5 and a minor fraction of misfolded/aggregated SOD5. The solution was filtered and loaded onto a Cytiva His-Trap FF nickel column, washed, and eluted with a linear imidazole gradient (0.1 – 0.5 M). SOD5-containing fractions were pooled, dialyzed against 50 mM Tris (pH 8.0), and incubated with His-tagged TEV protease (20:1 stoichiometric ratio) overnight. The solution was passed over the His-Trap FF column again, and the His tag-free protein was collected in the flow-through. The sample was then loaded on a HiTrap-Q column and eluted with a linear NaCl gradient (0.1–0.5 M). Pooled fractions of SOD5 were dialyzed against 50 mM Tris (pH 8.0) to remove the NaCl and to prepare for metal reconstitution experiments. To reconstitute with metals, the SOD5 sample was dialyzed against 50 mM sodium acetate (pH 5.5) and 0.25 mM CuSO₄, followed by dialysis against the same buffer without copper to remove metal ions in solution. The reconstituted protein was subsequently dialyzed against 25 mM Tris (pH 8.0), flash frozen in liquid nitrogen, and stored at -80°C.

SOD Assay for Library Screening

Copper-only *C. albicans* SOD5 and bovine Cu,Zn-SOD1 enzymatic activity was monitored using a WST-1 based reaction.^{12, 40-41} Assays were carried out in clear-bottom Costar 96-well plates (catalog # 07-200-706) with a total volume of 200 μ L per well. Tested fragment was stored as 50 mM aliquots in DMSO at 4 °C. Recombinant SOD5 and SOD1 were diluted in 50 mM KPO4 buffer to 0.06 mg/ml stocks and their aliquots were stored at -80°C. Each well contained a total volume of 200 μ L including 5 μ l of fragment solution, 5 μ l of 300 ng of SOD1 or SOD5 enzyme, 160 μ l of reaction buffer (50 mM KPO₄, pH 7.8, 0.2 mM xanthine, 0.1 mM EDTA, 0.75 mM WST-1 to a final volume of 200 μ l), and 30 μ l of xanthine oxidase (1 milliunits per well). The plates were incubated at 37 °C for 45 min, and then each well was measured for absorbance at 450 nm using BioTek Synergy H4 plate reader. 100% inhibition was set by subtracting SOD control from no SOD control. Percent inhibition of SOD activity was determined for all compounds by subtracting the A450 of the sample background (no xanthine oxidase) from sample A450 and then dividing by 100% inhibition. Inhibition values were plotted using Prism version 10 (GraphPad Software, Inc.), and nonlinear regression analysis was used to calculate an IC₅₀ value for each compound.

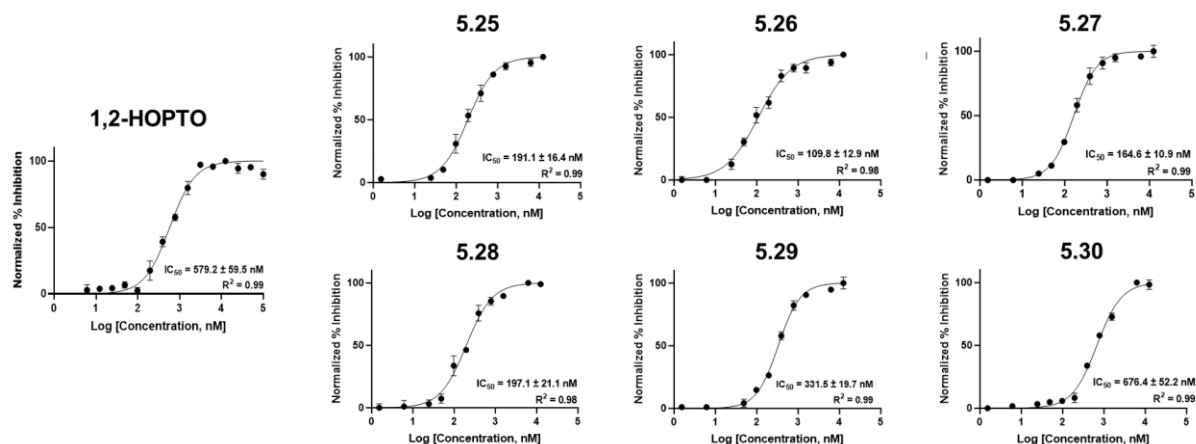


Figure 5.S1. IC₅₀ curves of sulfonamide derivatives of 1,2-HOPTO. The IC₅₀ values of each compound are listed in the curve. IC₅₀ values reported in log [nM] with the 95% confidence interval indicated.

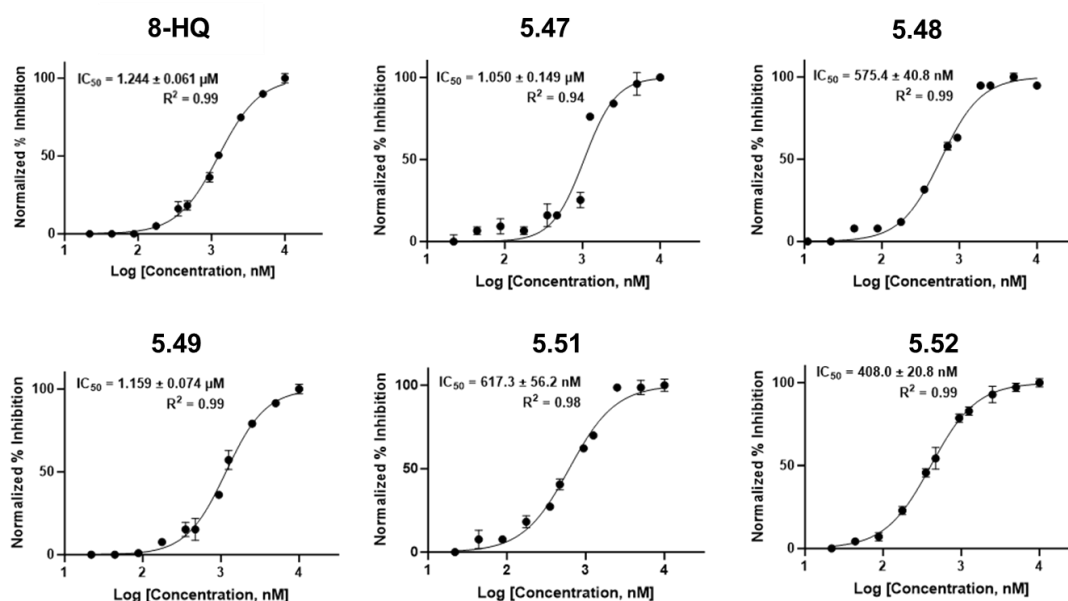


Figure 5.S2. IC₅₀ curves of sulfonamide derivatives of 8-HQ. The IC₅₀ values of each compound are listed in the curve. IC₅₀ values reported in log [nM] with the 95% confidence interval indicated.

5.7 References

1. Sheng, Y.; Abreu, I. A.; Cabelli, D. E.; Maroney, M. J.; Miller, A. F.; Teixeira, M.; Valentine, J. S., Superoxide dismutases and superoxide reductases. *Chem. Rev.* **2014**, *114* (7), 3854-3918.
2. Gleason, J. E.; Galaleldeen, A.; Peterson, R. L.; Taylor, A. B.; Holloway, S. P.; Waninger-Saroni, J.; Cormack, B. P.; Cabelli, D. E.; Hart, P. J.; Culotta, V. C., *Candida albicans* SOD5 represents the prototype of an unprecedented class of Cu-only superoxide dismutases required for pathogen defense. *PNAS* **2014**, *111* (16), 5866-5871.
3. Youseff, B. H.; Holbrook, E. D.; Smolnycki, K. A.; Rappleye, C. A., Extracellular superoxide dismutase protects histoplasma yeast cells from host-derived oxidative stress. *PLoS Pathog.* **2012**, *8* (5), e1002713.
4. Peterson, R. L.; Galaleldeen, A.; Villarreal, J.; Taylor, A. B.; Cabelli, D. E.; Hart, P. J.; Culotta, V. C., The Phylogeny and Active Site Design of Eukaryotic Copper-only Superoxide Dismutases. *J. Biol. Chem.* **2016**, *291* (40), 20911-20923.
5. Schatzman, S. S.; Peterson, R. L.; Teka, M.; He, B.; Cabelli, D. E.; Cormack, B. P.; Culotta, V. C., Copper-only superoxide dismutase enzymes and iron starvation stress in *Candida* fungal pathogens. *J. Biol. Chem.* **2020**, *295* (2), 570-583.
6. Frohner, I. E.; Bourgeois, C.; Yatsyk, K.; Majer, O.; Kuchler, K., *Candida albicans* cell surface superoxide dismutases degrade host-derived reactive oxygen species to escape innate immune surveillance. *Mol. Microbiol.* **2009**, *71* (1), 240-252.
7. Miramon, P.; Dunker, C.; Windecker, H.; Bohovych, I. M.; Brown, A. J.; Kurzai, O.; Hube, B., Cellular Responses of *Candida albicans* to Phagocytosis and the Extracellular Activities of

Neutrophils Are Critical to Counteract Carbohydrate Starvation, Oxidative and Nitrosative Stress. *PLoS One* **2012**, 7 (12), e52850.

8. Fradin, C.; De Groot, P.; MacCallum, D.; Schaller, M.; Klis, F.; Odds, F. C.; Hube, B., Granulocytes govern the transcriptional response, morphology and proliferation of *Candida albicans* in human blood. *Mol. Microbiol.* **2005**, 56 (2), 397-415.

9. Tamayo, D.; Munoz, J. F.; Lopez, A.; Uran, M.; Herrera, J.; Borges, C. L.; Restrepo, A.; Soares, C. M.; Taborda, C. P.; Almeida, A. J.; McEwen, J. G.; Hernandez, O., Identification and Analysis of the Role of Superoxide Dismutases Isoforms in the Pathogenesis of *Paracoccidioides* spp. *PLoS Negl. Trop. Dis.* **2016**, 10 (3), e0004481.

10. Staerck, C.; Yaakoub, H.; Vandeputte, P.; Tabiasco, J.; Godon, C.; Gastebois, A.; Giraud, S.; Guillemette, T.; Calenda, A.; Delneste, Y.; Fleury, M.; Bouchara, J. P., The Glycosylphosphatidylinositol-Anchored Superoxide Dismutase of *Scedosporium apiospermum* Protects the Conidia from Oxidative Stress. *J Fungi (Basel)* **2021**, 7 (7), 575.

11. Martchenko, M.; Alarco, A. M.; Harcus, D.; Whiteway, M., Superoxide dismutases in *Candida albicans*: transcriptional regulation and functional characterization of the hyphal-induced SOD5 gene. *Mol. Biol. Cell* **2004**, 15 (2), 456-467.

12. Robinett, N. G.; Culbertson, E. M.; Peterson, R. L.; Sanchez, H.; Andes, D. R.; Nett, J. E.; Culotta, V. C., Exploiting the vulnerable active site of a copper-only superoxide dismutase to disrupt fungal pathogenesis. *J. Biol. Chem.* **2019**, 294 (8), 2700-2713.

13. Zheng, P.; Chen, L.; Zhong, S.; Wei, X.; Zhao, Q.; Pan, Q.; Kang, Z.; Liu, J., A Cu-only superoxide dismutase from stripe rust fungi functions as a virulence factor deployed for counter defense against host-derived oxidative stress. *Environ. Microbiol.* **2020**, 22 (12), 5309-5326.

14. Wang, Q.; Pokhrel, A.; Coleman, J. J., The Extracellular Superoxide Dismutase Sod5 From *Fusarium oxysporum* Is Localized in Response to External Stimuli and Contributes to Fungal Pathogenicity. *Front. Plant Sci.* **2021**, *12*, 608861-608861.
15. Li, F.; Shi, H. Q.; Ying, S. H.; Feng, M. G., Distinct contributions of one Fe- and two Cu/Zn-cofactored superoxide dismutases to antioxidation, UV tolerance and virulence of *Beauveria bassiana*. *Fungal Genet. Biol.* **2015**, *81*, 160-171.
16. Chandler, C. E.; Hernandez, F. G.; Totten, M.; Robinett, N. G.; Schatzman, S. S.; Zhang, S. X.; Culotta, V. C., Biochemical Analysis of CaurSOD4, a Potential Therapeutic Target for the Emerging Fungal Pathogen *Candida auris*. *ACS Infect. Dis.* **2022**, *8* (3), 584-595.
17. Robinett, N. G.; Peterson, R. L.; Culotta, V. C., Eukaryotic copper-only superoxide dismutases (SODs): A new class of SOD enzymes and SOD-like protein domains. *J. Biol. Chem.* **2018**, *293* (13), 4636-4643.
18. Tu, J.; Liu, N.; Huang, Y.; Yang, W.; Sheng, C., Small molecules for combating multidrug-resistant superbug *Candida auris* infections. *Acta Pharm. Sin. B* **2022**, *12* (11), 4056-4074.
19. Chong, C. R.; Chen, X.; Shi, L.; Liu, J. O.; Sullivan, D. J., A clinical drug library screen identifies astemizole as an antimalarial agent. *Nat. Chem. Biol.* **2006**, *2* (8), 415-416.
20. Juarez, J. C.; Betancourt, O., Jr.; Pirie-Shepherd, S. R.; Guan, X.; Price, M. L.; Shaw, D. E.; Mazar, A. P.; Doñate, F., Copper Binding by Tetrathiomolybdate Attenuates Angiogenesis and Tumor Cell Proliferation through the Inhibition of Superoxide Dismutase 1. *Clin. Cancer Res.* **2006**, *12* (16), 4974-4982.
21. Jain, A.; Nilatawong, P.; Mamak, N.; Jensen, L. T.; Jensen, A. N., Disruption in iron homeostasis and impaired activity of iron-sulfur cluster containing proteins in the yeast model of Shwachman-Diamond syndrome. *Cell Biosci.* **2020**, *10* (105), 1-12.

22. Lamore, S. D.; Wondrak, G. T., Zinc pyrithione impairs zinc homeostasis and upregulates stress response gene expression in reconstructed human epidermis. *BioMetals* **2011**, *24* (5), 875-890.
23. Opinion on Zinc Pyrithione (ZPT) (P81) (CAS No 13463-41-7) – Submission III. *Scientific Committee on Consumer Safety (SCCS) March 2020, SCCS/1614/19*.
24. Commission Regulation (EU) 2021/1902 of 29 October 2021 amending Annexes II, III and V to Regulation (EC) No 1223/2009 of the European Parliament and of the Council as regards the use in cosmetic products of certain substances classified as carcinogenic, mutagenic or toxic for reproduction. *Official Journal of the European Union October 2021*.
25. Lockhart, S. R.; Chowdhary, A.; Gold, J. A. W., The rapid emergence of antifungal-resistant human-pathogenic fungi. *Nat. Rev. Microbiol.* **2023**, *21* (12), 818-832.
26. Jiang, X.; Yu, J.; Zhou, Z.; Kongsted, J.; Song, Y.; Pannecouque, C.; De Clercq, E.; Kang, D.; Poongavanam, V.; Liu, X.; Zhan, P., Molecular design opportunities presented by solvent-exposed regions of target proteins. *Med. Res. Rev.* **2019**, *39* (6), 2194-2238.
27. Lima, C. F. R. A. C.; Rodrigues, A. S. M. C.; Silva, V. L. M.; Silva, A. M. S.; Santos, L. M. N. B. F., Role of the Base and Control of Selectivity in the Suzuki–Miyaura Cross-Coupling Reaction. *ChemCatChem* **2014**, *6* (5), 1291-1302.
28. Jackl, M. K.; Seo, H.; Karges, J.; Kalaj, M.; Cohen, S. M., Salicylate metal-binding isosteres as fragments for metalloenzyme inhibition. *Chem. Sci.* **2022**, *13*, 2128-2136.
29. Adamek, R. N.; Suire, C. N.; Stokes, R. W.; Brizuela, M. K.; Cohen, S. M.; Leissring, M. A., Hydroxypyridinethione Inhibitors of Human Insulin-Degrading Enzyme. *ChemMedChem* **2021**, *16* (11), 1776-1788.

30. Doose, C. A.; Szaleniec, M.; Behrend, P.; Müller, A.; Jastorff, B., Chromatographic behavior of pyrithiones. *J. Chromatogr. A* **2004**, *1052* (1-2), 103-110.
31. Gershon, H.; Gershon, M.; Clarke, D. D., Antifungal activity of substituted 8-quinolinol-5- and 7-sulfonic acids: a mechanism of action is suggested based on intramolecular synergism. *Mycopathologia* **2003**, *155* (4), 213-217.
32. Pippi, B.; Reginatto, P.; Machado, G. d. R. M.; Bergamo, V. Z.; Lana, D. F. D.; Teixeira, M. L.; Franco, L. L.; Alves, R. J.; Andrade, S. F.; Fuentefria, A. M., Evaluation of 8-Hydroxyquinoline Derivatives as Hits for Antifungal Drug Design. *Med. Mycol. J.* **2017**, *55* (7), 763-773.
33. Joaquim, A. R.; Pippi, B.; de Cesare, M. A.; Rocha, D. A.; Boff, R. T.; Staudt, K. J.; Ruaro, T. C.; Zimmer, A. R.; de Araújo, B. V.; Silveira, G. P.; Martins, A. F.; Teixeira, M. L.; dos Santos, F. P.; Fuentefria, A. M.; de Andrade, S. F., Rapid tools to gain insights into the interaction dynamics of new 8-hydroxyquinolines with few fungal lines. *Chem. Biol. Drug Des.* **2019**, *93* (6), 1186-1196.
34. Li, C. X.; Gleason, J. E.; Zhang, S. X.; Bruno, V. M.; Cormack, B. P.; Culotta, V. C., *Candida albicans* adapts to host copper during infection by swapping metal cofactors for superoxide dismutase. *PNAS* **2015**, *112* (38), E5336-42.
35. Rossi, D. C. P.; Gleason, J. E.; Sanchez, H.; Schatzman, S. S.; Culbertson, E. M.; Johnson, C. J.; McNees, C. A.; Coelho, C.; Nett, J. E.; Andes, D. R.; Cormack, B. P.; Culotta, V. C., *Candida albicans* FRE8 encodes a member of the NADPH oxidase family that produces a burst of ROS during fungal morphogenesis. *PLoS Pathog.* **2017**, *13* (12), e1006763.

36. Culbertson, E. M.; Bruno, V. M.; Cormack, B. P.; Culotta, V. C., Expanded role of the Cu-sensing transcription factor Mac1p in *Candida albicans*. *Mol. Microbiol.* **2020**, *114* (6), 1006–1018.
37. Culbertson, E. M.; Khan, A. A.; Muchenditsi, A.; Lutsenko, S.; Sullivan, D. J.; Petris, M. J.; Cormack, B. P.; Culotta, V. C., Changes in mammalian copper homeostasis during microbial infection. *Metallomics* **2020**, *12* (3), 416-426.
38. Besold, A. N.; Gilston, B. A.; Radin, J. N.; Ramsoomair, C.; Culbertson, E. M.; Li, C. X.; Cormack, B. P.; Chazin, W. J.; Kehl-Fie, T. E.; Culotta, V. C., The role of calprotectin in withholding zinc and copper from *Candida albicans*. *Infect. Immun.* **2018**, *86* (2), e00779-17.
39. Netea, M. G.; Joosten, L. A.; van der Meer, J. W.; Kullberg, B. J.; van de Veerdonk, F. L., Immune defence against *Candida* fungal infections. *Nat. Rev. Immunol.* **2015**, *15*, 630-642.
40. Peskin, A. V.; Winterbourn, C. C., Assay of superoxide dismutase activity in a plate assay using WST-1. *Free Radic. Biol. Med.* **2017**, *103*, 188-191.
41. Peskin, A. V.; Winterbourn, C. C., A microtiter plate assay for superoxide dismutase using a water-soluble tetrazolium salt (WST-1). *Clin. Chim. Acta.* **2000**, *293* (1), 157-166.